Biomagnetic sensors based on spin electronics

Chloé Chopin

Thèse de doctorat

NNT: 2020UPASP022

université PARIS-SACLAY

Biomagnetic sensors based on spin electronics

Thèse de doctorat de l'université Paris-Saclay

École doctorale n° 564, Physique en Ile-de-France (PIF)
Spécialité de doctorat: Physique
Unité de recherche: université Paris-Saclay, CEA, CNRS, SPEC, 91191, Gif-sur-Yvette, France.
Référent: Faculté des sciences d'Orsay

Thèse présentée et soutenue à Gif-sur-Yvette, le 17/12/2020, par

Chloé CHOPIN

Composition du jury:

Henri JAFFRES Directeur de recherche, Laboratoire CNRS/Thalès	Président
Gilles GAUDIN Directeur de recherche, SPINTEC	Rapporteur & Examinateur
Laurence MECHIN Directrice de recherche, GREYC ENSICAEN	Rapportrice & Examinatrice
Nicolas BIZIERE Chargé de recherche, CEMES	Examinateur
Timo VAN KERKOERLE Chargé de recherche, Neurospin	Examinateur
Myriam PANNETIER-LECOEUR Directrice de recherche CEA, SPEC	Directrice de thèse

Remerciements

Je tiens à remercier Myriam Pannetier-Lecoeur pour m'avoir accompagnée tout au long de cette thèse. Merci à toi Myriam, j'ai beaucoup apprécié le soutien que tu m'as apporté tant sur un plan scientifique que humain. Mes remerciements vont également à Aurélie Solignac et Claude Fermon avec lesquels j'ai énormément travaillé. Tous les deux avez fait preuve d'une grande disponibilité et j'ai beaucoup appris à vos côtés que soit grâce au nombre impressionnant d'outils qu'Aurélie maîtrise ou grâce aux compétences de Claude en électronique pour ne citer que ces deux exemples. De même, je remercie Gregory Cannies de son aide pour des manips, l'utilisation des machines et pour toutes les fois où il m'a aidé et ce dans des domaines très variés. Merci également à Élodie Paul avec qui j'ai passé beaucoup de temps en salle blanche pour fabriquer des échantillons et des magnétrodes. Le temps passé au laboratoire aurait été aussi très différent sans mon co-bureau Julien Moulin. Nous avons tous les deux commencé notre thèse au même moment et ça a été un grand plaisir que de partager mon bureau avec lui que ce soit pour parler physique, théâtre, film ou de tant d'autres choses ! Je n'oublie pas Vincent Trauchessec que j'ai croisé en stage alors qu'il finissait sa thèse avant de reprendre j'en prenne la suite. J'espère que l'on se reverra à Arkose pour faire un peu d'escalade ! Je pense aussi à tous les post-docs, thésards et stagiaires qui ont survécu au trajet en RER B pour un afterwork sur Paris.

De manière générale, j'aimerai remercier le LNO et le SPEC de m'avoir aussi bien accueillie. J'y ai rencontré des chercheurs, des post-docs, des stagiaires et tant d'autres personnes interessantes. J'ai apprécié de travailler avec vous tous au jour le jour, de discuter en salle café, d'aller courir le midi ou faire de l'escalade et même une fois une partie de foot unique. Cette thèse a été plus qu'un moment de travail et d'étude pour obtenir le grade de docteur, ça a été une tranche de vie partagée avec des personnes exceptionnelles et c'est avec une grande émotion que je quitte le SPEC pour de nouvelles aventures. J'espère garder le lien avec vous tous et j'ai de grands espoirs de vous revoir au détour d'une conférence ou d'un passage sur le plateau de Saclay.

J'ai eu envie de travailler dans la physique assez tôt, au collège pour être précise, en lisant le magasine Science et Vie Junior au CDI. Cette envie a ensuite été confirmée par un stage de troisième avec Julien Gabelli au LPS et je me suis assez vite imaginée travailler dans les nanotechnologies. Cette envie m'a guidée pendant toutes mes études et m'a emmenée jusqu'à la thèse. Julien, je ne te remercierais jamais assez pour cela.

J'aimerais remercier également les membres du jury Henry Jaffres, Gilles Gaudin, Laurence Méchin, Nicolas Bizière et Timo van Kerkoerle qui ont pris le temps d'étudier mon travail et de maîtriser les outils nécessaires pour une thèse en visio. Je remer-

cie Aurélie qui s'est occupé à la perfection de la partie technique de la soutenance. Et surtout je remercie Patrice Roche et Myriam Pannetier Lecoeur qui ont permis à cette soutenance de se tenir en comité restreint avec Henry Jaffres qui a accepté d'être président du jury, mes parents Isabelle et Emmanuel Chopin, ma sœur Océane et mon compagnon Alexandre Bruneau. J'ai pu soutenir dans des conditions inespérées en ces temps de COVID 19. Je remercie tous ceux qui se sont connectés : familles, amis, collègues et curieux et tous ceux qui ne le pouvant m'ont envoyé un mot d'encouragement ou qui y ont pensé.

Résumé

Le cerveau est intensivement étudié que ce soit pour comprendre les principes de fonctionnement de cet organe fondamental ou pour comprendre les maladies qui y sont liées comme la maladie de Parkinson ou l'épilepsie. Certaines cellules spécifiques du cerveau comme les neurones font l'objet de nombreuses recherches car elles sont les éléments de base de la transmission d'information. L'activité neuronale est associée à des courants ioniques qui circulent à l'intérieur et à l'extérieur des neurones, générant des champs électriques et magnétiques. L'objectif de cette thèse est de développer un instrument pour mesurer l'activité magnétique d'un neurone à l'échelle locale et plus précisément de mesurer un potentiel d'action magnétique dont l'amplitude est attendue entre 10 et 100 pT [1] pour une fréquence de l'ordre du kHz.

Mesurer l'activité électrique des neurones à différentes échelles est possible grâce à différents outils, comme des électrodes pour l'électroencéphalographie (EEG) par exemple, qui vont détecter un signal avec une amplitude de l'ordre du µV au mV. Cependant les différences de conductivité entre les tissus entraînent la déformation des signaux électriques lors de leur propagation et induisent une forte dépendance à la localisation de la sonde électrique dans les tissus. Une électrode de référence est également nécessaire et sa localisation a un impact sur les signaux mesurés. De plus, la mesure électrique est uniquement scalaire, c'est à dire que seule l'amplitude du signal est mesurée. L'accès au signal magnétique permet d'une part de réaliser une mesure vectorielle (si le capteur le permet) et donc de mesurer à la fois l'amplitude du signal ET sa direction, ce qui permettrait de réaliser une cartographie des courants neuronaux. D'autre part, un signal magnétique n'est pas déformé par les tissus car ils ont une perméabilité magnétique constante et donc est moins dépendant de la location de la sonde magnétique et l'électrode de référence n'est plus nécessaire. Cependant la mesure d'un signal magnétique est complexe du fait que l'amplitude des signaux magnétiques est très faible (0,1 pT – nT) ce qui nécessite des capteurs magnétiques avec une limite de détection, qui est le champ magnétique le plus faible que le capteur puisse détecter, extrêmement basse.

Cette thèse doit répondre à de nombreux challenges. En effet, le capteur magnétique à utiliser pour la mesure doit pouvoir mesurer un potentiel d'action magnétique dont la fréquence est de l'ordre du kHz et doit donc avoir une limite de détection extrêmement faible à ces fréquences. Comme l'amplitude du signal est très faible, le capteur magnétique va être placé au plus proche des neurones pour réaliser une mesure *in-vivo* et il doit donc fonctionner à température physiologique et être miniaturisé pour pouvoir être inséré dans les tissus. Le capteur est embarqué sur une sonde qui doit être le

moins invasive possible afin de limiter les dommages lors de l'insertion de la pointe dans le cerveau. Cette sonde est appelée magnétrode et possède également des électrodes afin de mesurer simultanément l'activité électrique et magnétique du cerveau. Cette thèse poursuit les travaux réalisés par Laure Caruso et Vincent Trauchessec [2, 3] afin de proposer un nouvel outil pour les neurosciences. En effet, la mesure simultanée de l'activité locale avec des magnétrodes et de l'activité à une échelle macroscopique grâce à la MEG permettrait de définir le lien entre les différentes échelles de l'activité neuronale, c'est à dire le lien entre l'activité neuronales et l'activité des aires cérébrales par exemple. Les magnétrodes ont déjà permis de réaliser une mesure de l'activité d'un ensemble de neurones [2] et l'objectif de cette thèse est d'aller plus loin en mesurant l'activité magnétique d'un neurone unique appelée potentiel d'action.

Ce manuscrit est découpé en 4 chapitres. Le premier chapitre présente un rapide état de l'art des techniques qui peuvent être utilisés pour l'étude du cerveau à différentes échelles spatiales et temporelles. On peut notamment distinguer l'imagerie structurelle qui cherche à définir les différentes parties et structures du cerveau de l'imagerie fonctionnelle qui vise à mesurer l'activité du cerveau. Il existe un très grand nombre d'outils au service de l'imagerie fonctionnelle et ici, nous nous intéressons à ceux qui permettent de faire une mesure directe de l'activité neuronale comme la mesure de l'activité électrique et magnétique du cerveau. La mesure de l'activité électrique des neurones est bien maîtrisée, cependant mesurer l'activité magnétique du cerveau présente des avantages en plus d'apporter une mesure complémentaire à la mesure électrique. Il existe différents outils qui permettent de réaliser des mesures non-invasives comme l'électroencéphalographie (EEG) et la magnétoencéphalographie (MEG). L'EEG est réalisée à l'aide d'un grand nombre d'électrodes posées sur le scalp tandis la MEG est réalisée à l'aide capteur magnétique et plus précisément des dispositifs supraconducteurs à interférences quantiques (SQUIDs) qui ont besoin d'être refroidis à l'hélium liquide [4]. Pour protéger le patient, une isolation thermique entre les SQUIDs et le patient est nécessaire, ce qui les éloigne des sources des signaux magnétiques. Pour remédier au problème de refroidissement à des températures cryogéniques, des magnétomètres atomiques [5] peuvent remplacer les SQUIDs ce qui permet de placer les capteurs magnétiques directement sur le scalp du patient.

Il existe un grand nombre d'électrodes pour mesurer l'activité électrique des neurones à l'échelle locale mais peu pour mesurer l'activité magnétique. Une preuve de concept a été réalisée grâce à magnétomètre basé sur les lacunes d'azote dans le diamant : un potentiel d'action magnétique a pu être mesuré sur un invertébré (ver marin) qui possède un axone géant par Barry et al [6]. Un type de capteur magnétique avec une limite de détection plus haute mais miniaturisable est nécessaire pour réaliser des mesures *in-vivo* sur des mammifères et les capteurs basés sur la magnétorésistance géante (GMR) sont de bons candidats. En effet, ces capteurs ont une limite de détection de l'ordre de 1 nT à 1 kHz pour une taille réduite (4*200 μm^2) ce qui est un bon compromis entre taille et limite de détection. Ces capteurs ont une structure de type vanne de spin, c'est à dire qu'ils sont composés de deux couches ferromagnétiques séparées par un espaceur conducteur non magnétique. La première couche ferromagnétique a une aimantation dont la direction suit le champ magnétique externe, c'est la couche libre, tandis que la deuxième couche ferromagnétique a sa direction d'aimantation fixée dans une direction. C'est la couche dure ou couche de référence. Pour avoir un comportement de type capteur, les directions d'aimantation de la couche dure et de la couche

libre doivent être perpendiculaires à champ nul. Pour cela, la direction d'aimantation de la couche libre à champ nul est déterminée grâce à l'anisotropie de forme. En effet, la largeur du capteur est très supérieure à sa longueur. La direction d'aimantation de la couche dure est déterminée par un recuit à 180°C pendant une heure sous un champ magnétique externe de 1 T qui oriente les couplages magnétiques (couplage d'échange [7]) dans la couche dure. La réponse du capteur à un champ magnétique est alors composée de deux parties saturées séparées par une partie linéaire centrée autour de zéro champ. Au niveau de la partie linéaire, la résistance du capteur est proportionnelle à l'angle entre les directions d'aimantation des deux couches ferromagnétiques grâce au transport polarisé en spin [8].

Les capteurs GMR ont donc une limite de détection de l'ordre du nT pour une empreinte spatiale réduite en plus de fonctionner à température physiologique. Ils sont donc sélectionnés pour être embarqué sur une magnétrode. Elle possède également des électrodes électriques pour diminuer la limite de détection en moyennant les mesures magnétiques grâce aux signaux de référence électriques mesurés par les électrodes.

Dans le chapitre 2, plusieurs études pour diminuer la limite de détection des capteurs GMR sont présentées ainsi que les deux méthodes de caractérisation utilisées pendant cette thèse. La première est une mesure de magnétotransport qui permet de déterminer la résistance du capteur, son ratio de magnétorésistance (MR), sa sensibilité, la présence d'un offset et d'hystérésis. La deuxième est une mesure de bruit qui permet de déterminer le niveau de bruit du capteur, sa sensibilité grâce à un signal de calibration et enfin sa limite de détection. Trois types de bruit ressortent de ces mesures. Un bruit thermique dû au mouvement brownien des électrons qui dépend de la température et de la résistance du capteur, un bruit en 1/f qui a une composante électrique et une composante magnétique. Ce bruit dépend du volume du capteur et de sa tension d'alimentation. Le troisième bruit est un bruit télégraphique aléatoire (ou Random Telegraphic Noise). La présence de ce bruit rend le capteur instable et donc difficilement utilisable.

Les capteurs utilisés lors de ces études sont définis suivant une forme en yoke. Cette forme particulière permet de stabiliser les domaines magnétiques le long du capteur [9]. Un rapport d'aspect de 50:1 est utilisé pour que la résistance des capteurs soit indépendante de leur taille ($\sim$700Ω). Il peut être tentant de diminuer le bruit thermique en diminuant leur résistance mais la résistance impacte la tension de sortie du capteur qui doit être, d'une part, assez grande pour être supérieure au bruit de la chaîne d'acquisition et d'autre part, une résistance trop faible nécessite un courant important pour avoir une tension de sortie suffisamment élevée (ce que l'on cherche à éviter pour limiter la consommation des capteurs GMR mais également pour limiter le chauffage par effet Joule, voir chapitre 4).

La première étude cherche à augmenter la sensibilité du capteur tout en diminuant son bruit en jouant sur la largeur du capteur. La sensibilité augmente linéairement avec la largeur jusqu'à ce que l'offset et l'hystérésis décentre la partie linéaire. Or, comme on cherche à mesurer des champs magnétiques très faible, seule la sensibilité autour du champ nul nous intéresse. De ce fait, lorsque la partie linéaire est décentrée, la sensibilité diminue. De plus, lorsque l'hystérésis apparaît, la sensibilité dépend alors le l'histoire magnétique du capteur ce qui le rend instable. Augmenter la largeur du capteur et donc son volume permet de diminuer le bruit en 1/f jusqu'à atteindre le

bruit thermique qui est le bruit plancher. Cependant, pour des largeurs importantes, du RTN réapparaît ce qui augmente le bruit du capteur et le rend instable. Augmenter la sensibilité et diminuer le bruit en jouant sur la largeur est possible mais cette méthode est limitée par l'apparition d'hystérésis et de RTN et présente donc une largeur optimale.

La deuxième étude vise à limiter le RTN en diminuant l'hystérésis en jouant sur la composition des capteurs GMR et plus précisément en augmentant l'épaisseur de NiFe dans la couche libre. En effet, le NiFe a une coercivité faible et cela peut diminuer le RTN car des études (dont certaines réalisées au laboratoire) ont montré un lien entre hystérésis et RTN. La sensibilité et l'hystérésis sont mesurées pour différents capteurs GMR selon l'épaisseur de NiFe et la largeur de ces capteurs. Un optimum de sensibilité et un minimum d'hystérésis apparaissent pour des épaisseurs de NiFe entre 5 nm et 8.8 nm. Pour une épaisseur de 6.3 nm et une largeur de 8-9 µm la sensibilité est de 2.8 %/mT ce qui est presque de 2 fois plus élevé que pour le capteur de référence (tNiFe= 5nm avec une largeur de 4 µm pour une sensibilité de 1,5 %/mT). Ce qui signifie que pour un rapport signal sur bruit équivalent il faut faire une moyenne sur 4 fois moins d'évènements avec le capteur optimisé pour obtenir la même limite de détection ce qui permet de diviser le temps d'autant. C'est un avantage non négligeable pour des mesures *in-vivo*. Cependant, les mesures de bruit montrent qu'il y a du RTN pour de telles largeurs. Il y a donc un compromis entre sensibilité et RTN. Les capteurs GMR embarqués sur les magnétrodes ont une largeur de 4 µm et l'épaisseur optimal de NiFe pour cette largeur est de 6.3 nm. Le capteur optimisé a une limite de détection de 1 nT à 1 kHz à 1 V sans RTN et ne présente pas de RTN à 1.5 V.

Pour des raisons de compacités, les capteurs GMR embarqués sur des magnétrodes sont des méandres. Ce qui permet de diminuer la longueur du capteur tout en gardant un volume magnétique important afin de limiter le bruit en 1/f pour une résistance de l'ordre de 700 Ω pour une largeur de 4 µm. Il a été vérifié que les méandres et les yokes ont les mêmes caractéristiques à 4 µm pour la couche GMR optimisée.

Une quatrième étude [10] est mentionnée ici car elle vise à diminuer le bruit en augmentant le volume des capteurs en superposant des capteurs GMR les uns sur les autres. A la fois la sensibilité et le bruit sont impactés par l'empilement des GMR. La limite de détection de ce type de capteur est trop haute pour être utilisée pour les mesures *in-vivo* mais leur grande stabilité, leur large gamme de linéarité et l'absence de RTN jusqu'à 3 V en font des capteurs de choix notamment à haute fréquence quand le régime thermique est atteint.

Ce chapitre a permis de déterminer un capteur optimal à embarquer sur des magnétrodes qui a une limite de détection de l'ordre de 1 nT et sans RTN jusqu'à 1.5 V.

Le troisième chapitre présente les magnétrodes en détaillant notamment les étapes de fabrication et la méthode d'amincissement utilisée pour obtenir une pointe d'une épaisseur de 25 µm, ce qui est 10 fois plus fin que pour les magnétrodes épaisses fabriquées auparavant qui ont une pointe d'une épaisseur de 270 µm. Une épaisseur réduite permet de diminuer l'invasivité des magnétrodes ce qui a un impact sur la réponse des neurones comme on le verra au chapitre 4. Les magnétrodes sont évaluées et présentent des caractéristiques similaires indépendamment de leur épaisseur et de l'année de fabrication (2018 ou 2019). Le processus de fabrication est très bien maîtrisé

et est reproductible. Afin de réaliser des cartographies en 2D des courants neuronaux, certaines magnétrodes ont un design particulier. En effet, elles possèdent deux capteurs GMR dont un qui est tourné à 90° dans le plan de la sonde afin d'avoir deux capteurs GMR avec des axes de sensibilités orthogonaux. Après le recuit qui permet de fixer la direction d'aimantation de la couche dure des deux capteurs simultanément, le premier capteur a une réponse linéaire. Cependant, pour le deuxième capteur, l'aimantation de la couche libre et l'aimantation de la couche dure sont parallèles à champ nul ce qui ne permet pas de l'utiliser comme capteur. Un recuit local est donc nécessaire pour réorienter la couche dure du deuxième capteur à 90° sans que cela ait un impact sur le premier capteur. Un pulse de tension est envoyé dans le deuxième capteur afin de générer un chauffage par effet Joule sous un champ magnétique externe et de retourner l'aimantation de la couche dure du deuxième capteur. Après le recuit local, les deux capteurs ont des axes de sensibilité orthogonaux. La méthode de recuit local peut être améliorée puisque la sensibilité résultante est plus faible. Plusieurs magnétrodes pour réaliser des mesures 2D sont ainsi fabriquées. Nous avons mesuré une sensibilité parasite perpendiculaire à l'axe de sensibilité principal des capteurs GMR. Cette sensibilité ne peut pas être négligée et pour reconstruire le champ magnétique externe, il faut utiliser une matrice de sensibilité avec des termes non diagonaux. Pour tester les capacités de reconstruction des magnétrodes 2D, un fantôme a été fabriqué. Il permet de générer un champ local à 0°, à 90° ou une combinaison des deux champs simultanément ainsi qu'un champ à 45°. Pour un champ approximativement à 0°, l'amplitude et l'angle du champ externe est reconstruit pour des amplitudes importantes. Cependant, la sensibilité parasite limite la précision lors de la reconstruction. Il serait intéressant de rapprocher les deux capteurs pour améliorer les capacités de reconstruction des magnétrodes 2D. Ce fantôme a également été utilisé pour déterminer la limite de détection la plus basse que l'on puisse atteindre après une moyenne sur 40 000 évènements et une mesure sur une bande passante réduite (300Hz-3kHz), soit les conditions typiques des expériences *in-vivo*. Elle est donc de 480 pT pic à pic [11] pour un capteur GMR après un recuit. Ce chapitre présente également l'état de l'art des électrodes car les électrodes embarquées sur les magnétrodes sont moins performantes. En effet, fabriquer des électrodes est un champ de recherche à part entière. Trois types d'électrodes commerciales ont été sélectionnées : des électrodes de tungstène et deux réseaux d'électrodes. Ces électrodes sont collées manuellement sur les magnétrodes par Patrick Jendritza (ESI).

Le quatrième chapitre présente les mesures *in-vivo* réalisés avec des magnétrodes en collaboration avec notamment Patrick Jendritza et Pascal Fries à l'ESI (Francfort) ainsi que les résultats associés [9]. Les mesures sont réalisées sur des rats anesthésiés. Les constantes vitales de l'animal sont surveillées pendant toute la durée de l'expérience. Les challenges ainsi que les avancées depuis les travaux de L. Caruso et V. Trauchessec sont détaillées. Une grande attention est portée à la détection d'artéfacts, pendant la mesure. La tension d'alimentation des capteurs GMR est alternativement mise en situation "on" (capteurs alimentés) et "off" (capteurs non alimentés) afin de vérifier qu'ils mesurent uniquement des signaux d'origines magnétiques et de détecter d'éventuels artéfacts. Les magnétrodes et les électrodes sont insérées au niveau de l'hippocampe afin de mesurer l'activité spontanée importante de cette structure. Ce type de mesure ne nécessite donc pas de stimulus comme dans le cas des mesures précédentes dans le cortex visuel. Deux résultats importants peuvent être présentés dès à présent. Le premier est l'impact de l'épaisseur de la pointe des magnetrodes sur l'activité neuronale. L'activité électrique mesurée avec des magnétrodes affinées dont la pointe ne fait que

25 µm d'épaisseur (contre 270 µm pour les sondes précédentes), mesurent une fréquence d'activité 12 fois plus importante. Cela est dû à l'invasivité décrue des magnétrodes affinées qui endommagent moins les tissus lors de l'insertion, ce qui augmente le nombre de neurones intacts et donc présentant une activité fonctionnelle. Le deuxième résultat concerne la tension d'alimentation des capteurs GMRs, si les capteurs GMR n'ont pas d'impact sur la mesure de l'activité neuronale alors on s'attend à mesurer le même nombre de potentiel d'action dans l'état on et off. Cependant, on observe que lorsque les capteurs GMR sont alimentés à 2 V, le nombre d'évènements mesurés dans l'état "on" est bien plus important que dans l'état "off". Ceci peut s'expliquer par un effet de chauffage des capteurs GMR qui impacte la température locale autour des neurones et modifie leur fonctionnement. Les mesures suivantes ont donc été limitées à 1V afin de supprimer cet effet. L'objectif est de mesurer un potentiel d'action dont l'amplitude est attendue entre 10 et 100 pT. Comme les magnétrodes ont une limite de détection à 1 kHz de 1 nT, il faut faire une moyenne sur au moins 40 000 évènements pour atteindre une limite de détection autour de 250 pT (0-pic). Les spikes, qui sont la signature extracellulaire d'un potentiel d'action, sont visibles sur le signal électrique et sont utilisées pour réaliser une moyenne à la fois sur la mesure électrique et sur la mesure magnétique correspondante. Trois méthodes sont utilisées pour, d'une part, sélectionner les spikes et, d'autres part, les classer. La première méthode est une méthode de seuil. En effet, si les spikes dépassent un certain seuil alors elles sont utilisées pour moyenner le signal magnétique et électrique. Cependant, il est important de placer ce seuil assez bas pour sélectionner un nombre important de spikes mais il ne faut pas qu'il soit trop bas, sinon du bruit peut être interprété comme un signal neuronal ce qui diminuerait la qualité du moyennage. La deuxième méthode reprend la détermination d'un seuil mais, en plus, l'amplitude des spikes est mesurée par deux électrodes de part et d'autre du capteur GMR, puis elles sont comparées ce qui permet de réaliser un premier tri et de sélectionner manuellement les spikes qui sont regroupées en clusters. La troisième méthode utilise un réseau d'électrode ainsi qu'un algorithme appelé Kilosort pour classer un très grand nombre de spikes et les associer à un neurone unique. Plusieurs enregistrements sont réalisés en 2018 et en 2019. Pour l'un des enregistrements, un signal ambigu est mesuré et apparaît à la fois avec la méthode 1 et 2. Ce signal est peut-être un potentiel d'action magnétique car le signal est centré et il n'apparaît que quand le capteur GMR est alimenté entre autre. Cependant, il a une amplitude ∼2,5 nT, ce qui est bien supérieur au signal attendu par les modélisations. Comme tous les artéfacts connus ont été écartés, il est possible que ce soit un potentiel d'action magnétique malgré une amplitude plus grande qu'attendue. La méthode 3 a permis de faire une moyenne sur un très grand nombre d'évènement (>100 000 évènements) pour un niveau de bruit ∼ 250 pT. De fait, un signal magnétique d'une amplitude supérieur à 250 pT peut-être détecté.

En conclusion, les capteurs GMR sont de bons candidats pour la mesure de l'activité magnétique des neurones à l'échelle locale. Une première partie d'optimisation a permis de réaliser des capteurs stables et sans RTN jusqu'à une tension de 1.5 V. Ces capteurs ont ensuite été intégrés sur des sondes destinées aux mesures *in-vivo* appelées magnétrodes. Des magnétrodes affinées (pointe de 25 µm d'épaisseur) permettent de mesurer une activité neuronale jusqu'à 12 fois plus fréquente que pour une sonde épaisse (270 µm d'épaisseur). Des magnétrodes pour la mesure 2D ont également été réalisé et la limite de détection d'un capteur GMR standard après une moyenne sur 40 000 évènements pour une mesure sur une bande de fréquence réduite permet d'atteindre

une limite de détection de 480 pT p-p. Ces magnétrodes ont été utilisées *in-vivo* et un signal ambigu a été mesuré. L'expérience est très contrôlée, notamment pour la réduction du bruit, et après une moyenne sur un grand nombre d'évènement ($>$ 100 000) un niveau de bruit d'une amplitude $\sim$ 250 pT a été atteint *in-vivo*.

Bibliography

[1] Francesca Barbieri. "magnetrodes" project 600730 - fp7-ict-2011-9, 2015. *unpublished*. v

[2] Francesca Barbieri, Vincent Trauchessec, Laure Caruso, Josué Trejo-Rosillo, Bartosz Telenczuk, Elodie Paul, Thierry Bal, Alain Destexhe, Claude Fermon, Myriam Pannetier-Lecoeur, et al. Local recording of biological magnetic fields using giant magneto resistance-based micro-probes. *Scientific reports*, 6(1):1–10, 2016. vi

[3] Laure Caruso, Thomas Wunderle, Christopher Murphy Lewis, Joao Valadeiro, Vincent Trauchessec, Josué Trejo Rosillo, Jose Pedro Amaral, Jianguang Ni, Patrick Jendritza, Claude Fermon, et al. In vivo magnetic recording of neuronal activity. *Neuron*, 95(6):1283–1291, 2017. vi

[4] S Della Penna, C Delgratta, C Granata, A Pasquarelli, V Pizzella, R Rossi, M Russo, K Torquatiand, and SN Erne. Biomagnetic systems for clinical use. *Philosophical Magazine B*, 80(5):937–948, 2000. vi

[5] E Boto, N Holmes, J Leggett, G Roberts, V Shah, SS Meyer, and MJ Brookes. Moving brain imaging towards real-world applications using a wearable meg system. *Nature*, pages 17–19, 2018. vi

[6] John F Barry, Matthew J Turner, Jennifer M Schloss, David R Glenn, Yuyu Song, Mikhail D Lukin, Hongkun Park, and Ronald L Walsworth. Optical magnetic detection of single-neuron action potentials using quantum defects in diamond. *Proceedings of the National Academy of Sciences*, 113(49):14133–14138, 2016. vi

[7] Josep Nogués and Ivan K Schuller. Exchange bias. *Journal of Magnetism and Magnetic Materials*, 192(2):203–232, 1999. vii

[8] Bernard Dieny, Virgil S Speriosu, Serhat Metin, Stuart SP Parkin, Bruce A Gurney, Peter Baumgart, and Dennis R Wilhoit. Magnetotransport properties of magnetically soft spin-valve structures. *Journal of Applied Physics*, 69(8):4774–4779, 1991. vii

[9] C Fermon, M Pannetier-Lecoeur, Nicolas Biziere, and B Cousin. Optimised gmr sensors for low and high frequencies applications. *Sensors and Actuators A: Physical*, 129(1-2):203–206, 2006. vii

[10] J Torrejon, A Solignac, C Chopin, J Moulin, A Doll, E Paul, C Fermon, and M Pannetier-Lecoeur. Multiple giant-magnetoresistance sensors controlled by additive dipolar coupling. *Physical Review Applied*, 13(3):034031, 2020. viii

[11] Chloé Chopin, Jacob Torrejon, Aurélie Solignac, Claude Fermon, Patrick Jendritza, Pascal Fries, and Myriam Pannetier-Lecoeur. Magnetoresistive sensor in two-dimension on a 25 μm thick silicon substrate for in vivo neuronal measurements. *ACS sensors*, 5(11):3493–3500, 2020. ix

Contents

Introduction

The brain activity can be recorded by various tools depending on the nature of the signal (magnetic, electrical, oxygenation level of the blood, etc.), and on the conditions of the recordings through *in-vivo*, in-vitro or ex-vivo experiments. Also, the scale of the recording impacts the choice of the instrument, for example, a recording at large scale can be made with electrodes placed on the scalp and a recording at local scale can be realized with another type of electrodes implanted inside the brain to record the activity of precise area of the brain like in the cortex or in the hippocampus. Recording the *in-vivo* activity at local scale allows to measure the activity of a localized area of the whole brain of a living animal.

Neurons are one type of the cells composing the brain and measuring their activity is crucial to understand the working principle of the brain both by understanding neurons themselves and how they interact and transmit information across the different parts of the brain. The neuronal activity generates ionic currents flowing inside and outside neurons which create both an electrical and a magnetic field. Recording the electrical activity of neurons is an important research field which is addressed by numerous probes and software to measure and analyze this electrical neuronal activity both at global and at local scale. Recording the magnetic field is more challenging because the magnetic amplitude of the neuronal activity is extremely weak (between 1nT down to 10-100 fT) and, hence, ultra-sensitive magnetometers are needed. However, recording the magnetic component of neuronal activity has several advantages. First, the magnetic recordings can be made without galvanic contacts on the contrary of an electrical measurement. Second, the brain's tissues have the same magnetic permeability as vacuum, hence, magnetic field are not distorted by the brain's tissues on the contrary of the electric field, which is deformed because of the various conductivities of tissues. Third, measuring the magnetic field allows to do a vectorial recording of the neuronal activity by recording simultaneously the amplitude and the direction of the magnetic field. Recording the magnetic field generated by the neurons can lead to the mapping of the neuronal activity.

SQUIDSs (Superconducting QUantum Interference Devices), which are state-of-the-art of ultra-sensitive magnetometers, can detect magnetic field with an extremely low amplitude (down to a few fT) but to reach such level of detection, they need to be helium-cooled at 4 K, have a large volume or surface or need additional equipment which prevent them from being used *in-vivo* at local scale. The physical principles of spin electronics (or spintronics) allow to build magnetometer with a low limit of detection, working at room temperature and with a small footprint. Magnetic sensors

based on spintronics and more precisely on giant magnetoresistance (GMR) or tunnel magnetoresistance are good candidates.

Biological magnetic fields have been recorded previously with GMR sensors in-vitro on rodent muscles to realize of proof-of-concept. Then, collective response of neurons have been recorded with an amplitude of few nT at low frequencies (under 500 Hz). The next step would be to record the magnetic activity of a single neuron called which an action potential. The amplitude of this signal is expected between 10 to 100 pT with frequency around 1 kHz.

To record the magnetic field generated by neurons, at local scale and during *in-vivo* experiments, several challenges need to be addressed. First, the extremely low amplitude of the magnetic signal needs to be recorded either by a probe with an ultra-low limit of detection or by a probe with a low limit of detection which is stable over all the duration of the recording to allow the averaging of the magnetic signal to extract a magnetic action potential from the noise. An electrical reference is needed to average the magnetic signal so the probe used *in-vivo* must embed both magnetic sensors and electrodes. Second, the probe is inserted inside the brain during *in-vivo* experiments, as it is an invasive measurement, damages induced during the insertion of the probe must be reduced in order to have a high number of responding neurons in close vicinity of the probe. Third, to realize a recording of a magnetic field in two directions, two magnetic sensors with perpendicular axis of sensitivity are needed on the same probe. To achieve this, one of the two sensors have it sensitive axis forced perpendicularly. When working on solutions for the last two challenges, it is important to keep a similar limit of detection.

This manuscript is organized in four chapters.

The first chapter presents the basic working principles of the brain and the methods used to study the brain for medical use or to increase our knowledge about the brain including the cells composing the brain or the cognition process. Then ultra-sensitive magnetic sensors are presented, and their ability to be used for local *in-vivo* recordings are challenged. Finally, magnetic sensors based on magneto resistance are presented and sensors based on Giant Magnetoresistance (GMR) are selected to be inserted on a probe called magnetrode for biomagnetic recordings at local scale.

The second chapter introduces the fabrication process of GMR sensors followed by the characterisation methods. To lower the limit of detection of GMR sensors, four axes are studied:

- The impact of the sensor width
- The impact of the NiFe thickness in the free layer
- The comparison of the optimal width and thickness for two different shapes: yokes which are used for GMR optimization and meanders which are used for *in-vivo* recording.
- The impact of the number of GMR stack deposited on top of another.

The third chapter summarizes previous biological recordings made with GMR sensors before presenting the fabrication process of magnetrode including the magnetrode's tip thinning procedure. Then, the characteristics of the new magnetrodes are presented

and compared to the previous generation on thick substrates. Finally, magnetrodes designed for recording a magnetic field along two directions are presented and tested in a phantom experiment to challenge their reconstruction ability. The different type of electrodes for recording the electrical neuronal signal are quickly presented.

The fourth and final chapter relates the *in-vivo* experiments. The set-up is described as well as the different method used to average the magnetic signal in order to extract a magnetic action potential from the noise level.

Conclusions and perspectives are finally given.

Chapter 1

Magnetic sensors and their applications for brain imaging

Contents

Magnetic sensors can detect different characteristics of a magnetic signal (magnetic field amplitude and/or direction, flux density, etc.) and are based on various techniques and physical principles. They are used in several fields in industry and research and we will see in this chapter how magnetic sensors can be applied to brain imaging.

There are several approaches to study the brain including recording an electric field and a magnetic field. These fields are generated by ionic movements at the cellular level and, depending on the source-to-sensor distance [1], the magnetic field can be in the range of 10 to 100pT $/\sqrt{\text{Hz}}$ at a few microns, to 100 fT $/\sqrt{\text{Hz}}$ at a few centimeters, with a frequency range from a few Hz to few kHz. Therefore, in order to study the magnetic activity of the brain, an ultra-sensitive magnetic sensor which is able to detect weak magnetic signals at low frequencies is required. The lowest magnetic field a magnetic sensor can detect is referred to as the limit of detection (LOD).

In this chapter, we will first introduce the brain and the origin of the biological magnetic signals we aim to record. Then we will present several magnetic sensors with ultra-low limit of detection at low frequencies and their limitation for *in-vivo* application. Finally, we will study how sensors based on magnetoresistance can be a competitive alternative for local magnetic *in-vivo* imaging despite a higher limit of detection compared to other types of sensors.

1.1 Brain imaging

The brain is intensively studied to understand cognition processes and to understand and potentially cure neuronal diseases like Parkinson, Alzheimer or epilepsy. There are several ways to study the brain and we will focus on structural imaging and functional imaging. Structural imaging is used to investigate the brain anatomy and structure, it needs a good spatial resolution. Functional imaging allows to study the brain activity for linking a function to a brain structure or a brain area defined by structural imaging, to understand the way these areas communicate and more. It needs both a good spatial resolution and a good temporal resolution.

First, we will see the main features of the neuronal activity of the brain and then the differences between structural and functional imaging.

1.1.1 Neuronal activity of the brain

The brain is the main part of the central nervous system with the spinal cord. It is composed of several types of cells including excitable cells such as neurons. A human brain has around 100 billions neurons [2].

A neuron is composed of dendrites, a cellular body called soma and an axon along which an electrical signal can propagate (fig 1.1b). The connection between two neurons is made by a synapse and a neuron can have around 1 000 synaptic connections [2]. A synapse is a small space between the end of the pre-synaptic neuron axon (axon terminal) and a dendrite of a post-synaptic neuron. A dendrite is a prolongation of a neuron which propagates electrochemical stimulation received from other neurons.

When a neuron receives information from other neurons through the dendrites, the potentials are summed up and if a threshold is reached then an **Action Potential** (AP) is

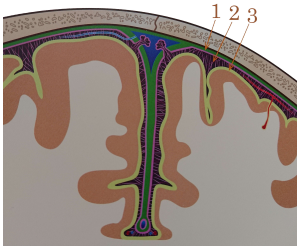

(a) Brain protection layers: skull and meninges.[2]

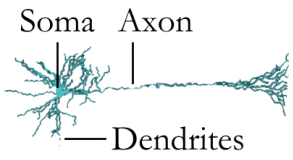

(b) Neuron scheme.

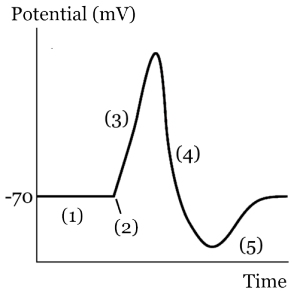

(c) Action potential

Figure 1.1: (a) The brain is protected by the skull and the meninges. The meninges are composed of three membranes : (1) the dura mater, (2) the arachnoid mater and (3) the pia mater. (b) Neuron scheme [3]. (c) Description of membrane potential during an action potential: 1) Neuron at rest 2) Stimulation 3) Depolarization 4) Re-polarization 5)Refractory period. Adapted from [1].

fired. Otherwise, the potential of the cell slowly returns to the resting potential. This is an all-or-none process as, in addition to the threshold condition, the strength of the action potential is independent of the amplitude of the summed potentials. The AP propagates along the axon by membrane depolarization and re-polarization followed by a refractory period (fig 1.1c). During this period the neuron cannot generate another action potential. The depolarization and re-polarization typically last 1ms (for a corresponding frequency of 1kHz) and the refractory period is around 2ms. The depolarization and re-polarization are the result of the opening of Na+ and K+ ion-channels in the neuron membrane and movement of Na+ from outside of the neuron (extra-cellular medium) to the inside (intra-cellular medium) during depolarization and the opposite transfer of K+ ion during re-polarization. Once the action potential reaches the axon terminals, it releases neurotransmitters from the pre-synaptic neuron to the dendrites of the post-synaptic neurons *via* synapses (cf fig 1.2b). These neurotransmitters induce the opening of ion-channels and a transfer of ions from the extra-cellular medium to the intra-cellular medium of the post-synaptic neuron. Action potentials can have a particular shape on temporal recording which is called a spike.

These movements of ions lead to two main current sources in the brain which generate a magnetic field. The first one is located in the synapses with ionic currents flowing within dendrites (cf fig 1.2b). They last tens of milliseconds and are called synaptic currents or primary currents. The second includes the two intracellular currents generated in an axon during an action potential: the forward current generated by the depolarization of the membrane and the backward current generated by the re-polarization of the membrane (cf fig 1.2a). These two currents are opposites and last around 1 ms. There are also transmembrane currents (due to ionic transfer between the intra- and extra-cellular medium) which are not expected to generate any measurable magnetic field because of their cylindrical symmetry.

At lower frequencies ($\leqslant$500Hz), **Local Field Potentials** (LFP) can be measured. LFPs are electric potential variations in the extracellular space. They are measured with intracranial microelectrodes which record activity from several neurons in the volume surrounding the electrodes. LFP response can be triggered by a stimulus, leading to

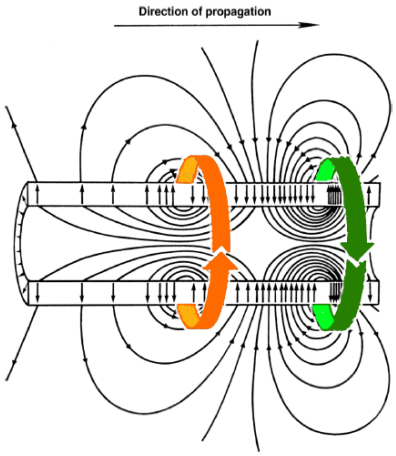

(a) Cross section of a nerve axon

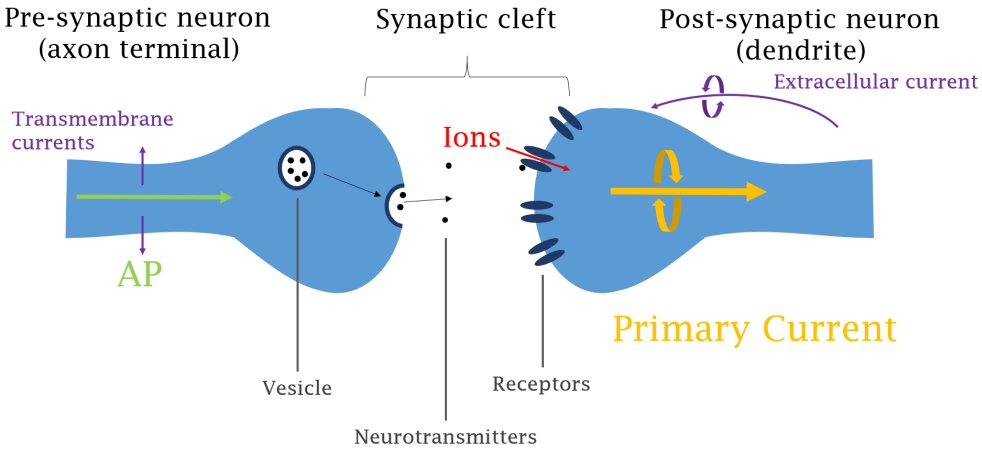

(b) Scheme of a synapse

Figure 1.2: (a) Cross section of a nerve axon with transmembrane currents symbolized by black arrows, the propagating magnetic field associated to forward current is represented by a green arrow and the magnetic field associated to backward current is illustrated by an orange arrow. Colourized from [4] (b) Scheme of a synapse. The primary current is illustrated in yellow with the associated magnetic field.

the recording of an Evoked Response Potential (ERP). AP and LFP are biological signals widely studied as they give valuable information about the working principles of the brain.

The brain can be studied with several approaches and we will focus on two of them. The first one is a reductionist (or bottom-up) approach where cells are studied separately to understand the working principle of these cells. The second is an holistic (or top-down) approach to study mental functions and make links between an ability and the brain area or the cells needed. A present challenge is to bring these two approaches together to understand the role of the brain components (like neurons) for a given function.

1.1.2 Structural and functional imaging

To study the brain, independently of the chosen approach, structural or functional imaging can be used. They can be used together to enhance the quality and the

understanding of the results.

Structural imaging

A high spatial resolution is required to study in details all parts of the brain. The first possibility to study the brain was *post-mortem* study. In the 1970's scanners with X-rays were used until tomography and Magnetic Resonance Imaging (MRI) replaced them. Tomography has a spatial resolution of a few mm and uses radiotracer. MRI has a resolution from a few mm to sub-mm scale. MRI is non-invasive and does not need radiotracer for basic uses. Nonetheless, it is possible to use tomography in combination with MRI [5]. MRI is based on nuclear magnetic resonance and requires a strong magnetic field. The external magnetic field aligns the magnetic moments of hydrogen atoms into an equilibrium position. Then this equilibrium is disturbed by radio-frequency pulses and the magnetic moments of hydrogen nuclei emit an electromagnetic signal while returning to the equilibrium. In general MRI uses magnetic fields from 1.5 T to 3 T for an optimal spatial resolution around 2 mm. Some MRI (for human brain study) can have magnetic field up to 7 T for a sub-millimeter resolution and even 11.7 T (since 2019 with the magnet Iseult for research purpose).

The amplitude of the magnetic field needs to be as high as possible to have the best spatial resolution (cf fig 1.3) but people with magnetic implants cannot benefit from it as well as overweight patients or patients suffering from claustrophobia. Indeed the magnetic field needs to be homogeneous which is difficult to achieve on large volume and thus the space inside the MRI is limited. Also to reach high magnetic field, MRI magnets are made with superconducting materials which need helium cooling. MRI is an expensive device with a high running cost. It is a powerful device with great advantages (non-invasive, non-contact technique, good spatial resolution) and few limitations (high magnetic field, limited space and expensive technique).

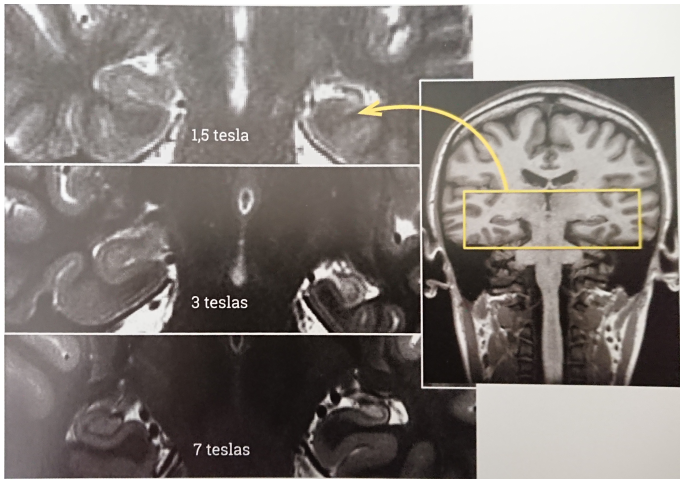

Figure 1.3: MRI at different magnetic field amplitudes. [2]

Functional imaging

It needs both a high spatial and temporal resolution as it aims to study the brain activity. In the 19th century, Paul Broca studied the brain (*post-mortem*) of people who had lost the ability to speak and he discovered the brain area involved in speaking.

It is now called the Broca area. Nowadays, MRI can be used for functional imaging (f-MRI) with Blood Oxygen Level Dependent (BOLD) imaging. As neurons do not have a reserve of energy, when they are active they need to be sustained quickly which results in a variation of oxygen concentration in the blood of the active area. This change can be detected by MRI and through statistical procedure, a brain area can be associated to a mental function. f-MRI has several limitations, first it is an indirect measurement of the brain activity, second it has a low temporal resolution (a few seconds when neuronal activity lasts around one millisecond). To do a direct-imaging of brain activity, the electrical or magnetic activity of the brain can be measured by neurophysiological techniques in real time.

The electrical activity of the brain can be measured at different scales: at macroscopic scale with an ElectroEncephaloGraphy (EEG) device and at mesoscale and microscale with intracranial electrodes. EEG is non-invasive (electrodes are placed on the scalp) with an excellent temporal resolution in the order of ms and a spatial resolution in the order of the cm. Also electric signals are distorted because of the difference of conductivity between tissues. Intracranial electrodes are invasive but they allow to record the electrical activity inside the brain. Electrodes are inserted in close vicinity of neurons and depending on the frequency, they can record activity from several neurons like LFP or from single neuron like action potential. Another technique is patch-clamp which is mostly used *in-vitro*. A pipette filled with an electrolyte solution is inserted into the brain close to a neuron, inside it or enclosing an ionic channel. This technique allows to record an electrical potential inside or outside a neuron or the potential of an ionic channel.

(a) EEG (Christine Doublé ©CEA NeuroSpin)

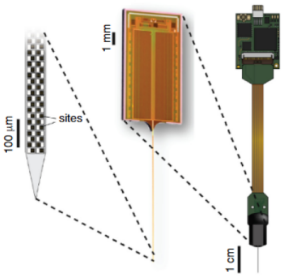

(b) Intracranial electrode (Neuropixel) from [6]

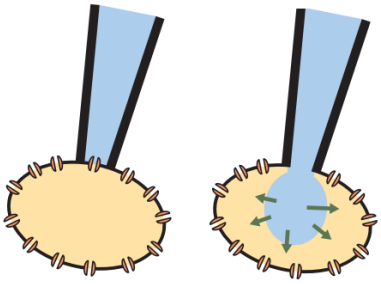

(c) Patch clamp from[7]

Figure 1.4: Neurophysiological techniques to record an electric signal generated by the brain at different scales. At macrocale with EEG (a), at meso-scale with an electrode called neuropixel with 960 recording sites on a 70x20 shank (b) and at micro-scale with the patch clamp technique (c). On the left, the pipette measures the potential of an ionic channel and on the right, the pipette measures a potential inside the cell.

Magnetic activity can only be recorded at macroscale by MagnetoEncephaloGraphy (MEG) at this time. MEG measures the magnetic activity on the surface of the brain like EEG and it has a similar spatial and temporal resolution.

The cortex is folded and the magnetic field generated by neurons located in sulci are perpendicular to the brain surface when neurons in gyri are parallel to the brain surface. The neurons can be associate to a magnetic dipole and generate a magnetic field parallel

to the brain surface (cf fig 1.5a). MEG is only sensitive to magnetic field perpendicular to the brain surface. MEG uses magnetic sensors which are called SQUIDs. These sensors are described more precisely in section 1.2.1. They measure the magnetic flux trapped inside a superconducting loop and this loop is placed in parallel to the brain surface (cf fig 1.5a), as close as possible to the brain as the amplitude of a magnetic dipole decreases quickly with the distance ($\sim 1/r^3$). Typically, the distance between the thermal isolation and the subject is about 2 cm [8]. Thus, MEG is only sensitive to magnetic field generated by neurons in sulci. On the contrary EEG is sensitive to electric signal generated by neurons locally perpendicular to the scalp surface located on gyri. These magnetic signals are in the order of a few fT which is 1 billion time lower than the Earth magnetic field (50 µT). To reduce strongly the Earth magnetic field and all magnetic fields from metallic pieces in movement (car,...), a Magnetic Shielded Room (MSR) and an active magnetic shielding are needed. MEG uses an array of SQUIDs which are helium-cooled at 4.2K. An isolation is needed between the head of the patient and the cryostat. This adds a distance between SQUIDs and magnetic sources and as magnetic field decreases quickly with distance ($1/r^3$), the magnetic amplitude measured by SQUIDs decreases as well.

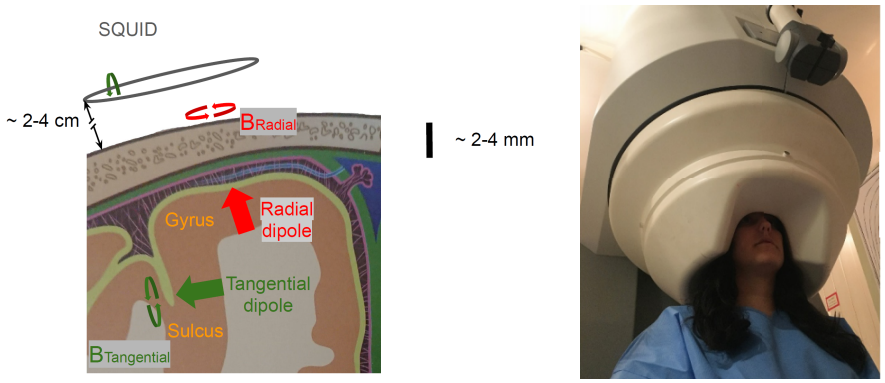

(a) MEG source. Adapted from [2] (b) from [9]

Figure 1.5: (a) MEG detects magnetic fields from tangential equivalent current dipole located in sulci. The resulting magnetic field is picked-up by a coil and then measured by SQUIDs. (b) Picture of a commercial MEG device.

MEG has a lot of advantages: the magnetic permeability is the same for all tissues in the brain (*ie* the magnetic signal is not distorted), MEG is non-invasive and contact-less but neuronal magnetic fields are weak and the magnetic amplitude is decreased due to the distance between neuronal sources and SQUIDs. In addition, magnetic shielding is needed to reduce the magnetic noise.

EEG and MEG face the same problems; it is difficult to determine the location of electrical sources at the origin of the electric field for the EEG and the magnetic field for MEG. This is called the "inverse problem". EEG and MEG can be used simultaneously [10] and as they do not record exactly the same signal, they are complementary. EEG and MEG recordings can be made in addition to an MRI to have both structural and functional information.

1.1.3 Local recording of neuronal magnetic activity

Recording the magnetic field in addition to the electric potential has several interests. First, the magnetic field is not disturbed by magnetic permeability of tissues as their magnetic permeability is the same as vacuum. Second, recording a magnetic field is reference free which makes experiments more reproducible as they do not depend on the position of a reference like an electrode does. Third, it is contactless as it does not require a galvanic contact to measure the magnetic field. For example, for *in-vitro* imaging, to record an electric potential on different locations on a cell, an electrode is placed on different parts of the cell which can be damaged in the process. For a magnetic recording, the contact-less sensor is simply moved without having an impact on the cell. Finally the results of an electric recording is a scalar measurement while a recording of a magnetic signal leads to a vectorial measurement which allows to have information both about the amplitude and the direction of the signal. This is why a magnetic equivalent of an electrode is a device of interest.

For now only macro-scale magnetic field can be recorded by MEG with an array of SQUIDs. Recording the magnetic counterpart of an electrical signal like LFP or AP would be of great interest but in order to access the local magnetic fields generated by neurons, a biocompatible magnetic sensor is needed. It is challenging and requires ultra-sensitive magnetometer as the magnetic field generated by neurons is estimated between 10 to 100 pT. Also, such a magnetic sensor should be compatible with an insertion in the brain.

A magnetic sensor for *in-vivo* magnetic recording must:

- work at biological temperature
- have a small footprint to reduce damage during the insertion
- have a low limit of detection (weak magnetic field detection)
- have a high spatial resolution
- and a high temporal resolution.

Magnetic sensors can be differentiated depending on their working principle and the recorded components of the magnetic field (amplitude, direction, flux, ...). We will present in the following section a state of the art of ultra-sensitive magnetic sensors with limit of detection low enough to be used for neuronal recordings.

1.2 State of the art of ultra-sensitive magnetic sensors

In this section, three magnetic sensors with ultra-low limits of detection at low frequencies (< 10 kHz) are presented: Superconducting QUantum Interference Devices (SQUIDs), Optically Pumped Magnetometers (OPMs) and Nitrogen Vacancy (NV) centers.

We will investigate their operating principles, their responses to an external magnetic field, their spatial resolutions and limits of detection to understand their advantages and limits. Then their applications for neuronal recordings are presented.

1.2.1 SQUID

Introduction to SQUID

SQUIDs are magnetometers with a limit of detection of 2-3 fT/$\sqrt{\text{Hz}}$ down to few Hz. There are two main types of SQUID: Direct Current (DC)-SQUID and Radio-Frequency (RF)-SQUID. A simple description of DC-SQUID is given here and for more information about SQUID physics and applications see [11]. DC-SQUIDs are based on superconducting loops with two Superconductor-Insulator-Superconductor Josephson junctions in parallel as shown in fig 1.6a.

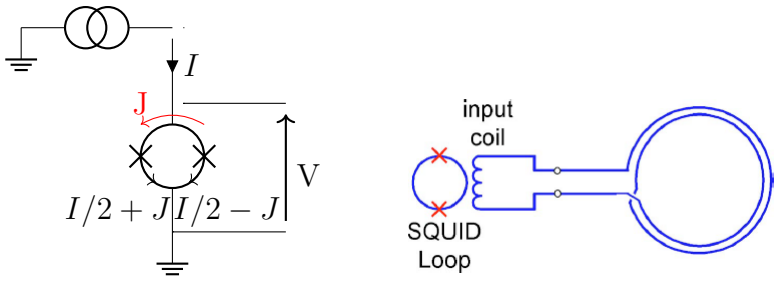

(a) DC-SQUID. From [12]

(b) DC-SQUID with a two turns pick-up coil. From [13]

Figure 1.6: (a) Principle of a DC-SQUID. Crosses represent Josephson junctions. A current I is applied to a superconducting loop and a voltage is measured due to a magnetic flux inside the junction. (b) A pick-up coil is coupled to a DC-SQUID to increase its sensitivity.

First let's investigate the physics of superconducting loop, then we will present the Josephson effect [14] and finally we will introduce how Josephson junctions are integrated in a SQUID.

It is important to recall that, below a critical temperature T_c, a superconducting material shows a complete loss of electrical resistance and a perfect diamagnetism. Below a temperature T_c, the magnetic flux is expelled from a superconducting material by Meissner effect.

When the superconducting material forms a loop, a screening current J appears due to Meissner effect and the magnetic flux is trapped inside the loop. The total flux inside the loop is:

$$\phi_{total} = \phi_{ext} + LJ = n.\phi_0 \tag{1.1}$$

with L the inductance of the junction, $\phi_0 = h/2e$ is the magnetic flux quantum with h the Planck's constant and e the electronic charge, n is the number of flux quanta trap into the loop.

If a non-superconducting material (either a conductor or an insulator) is inserted in between two superconducting parts, then electrons will travel through the non superconducting part by tunneling. This is called the Josephson effect. Josephson junctions are based on this effect and are either Superconducting-Insulator-Superconducting (SIS) junction or Superconducting-Normal-Superconducting (SNS) junction.

In a DC-SQUID, two SIS Josephson junctions are inserted in parallel in a superconducting loop (fig 1.6a). The loop is powered by a current I and a critical current I_c defines the current above which the junction loses its superconductivity effect leading to the apparition of an electrical resistance at the junctions. As long as I is inferior to I_c, Cooper pairs can travel through the insulator barrier without voltage drop and there is no difference of potential and thus no voltage across the Josephson junctions. When I is superior to I_c, a voltage depending on the external magnetic flux can be measured, therefore a SQUID is powered with I slightly superior to I_c. A SQUID response is non-linear and ϕ_0 periodic. The SQUID is sensitive to the field component perpendicular to the plane of the loop and its sensitivity is limited by its loop area. To increase its sensitivity, a pick-up coil can be used to couple the externally detected flux into the SQUID loop[13].

SQUID constraints SQUIDs need to be cooled below a critical temperature, T_c, which depends on the material used for the superconducting loops, in a cryostat. Niobium loops have a T_c around 9.2 K and thus need to be cooled by liquid helium, which has a boiling point of 4.2 K. Liquid helium is expensive and to limit losses due to helium evaporation the cryostat must be isolated. This increases the distance between SQUID and magnetic sources. High-T_c superconducting material like Yttrium Barium Copper Oxide (YBCO) with a T_c of 90 K allows to replace liquid helium by liquid nitrogen with a boiling point of 77 K, leading to high-T_c SQUID. However they exhibit an increased noise level around 30 fT/$\sqrt{\text{Hz}}$ at 1Hz [15].

In conclusion, SQUIDs are magnetic flux sensors with a non-linear response and do a vectorial measurement in real-time, they need an helium-cooling. They can have a spatial resolution as low as 10 µm [16] for a limit of detection of 41 pT/$\sqrt{\text{Hz}}$ (for a noise level of $2.10^{-6}\phi_0/\sqrt{\text{Hz}}$) and even sub-micrometer [17]. To reach a limit of detection of ∼fT/$\sqrt{\text{Hz}}$, the loop area of the pick-up coil can be increased. For MEG measurements, pick-up coils can have a surface of 81 mm^2 for a limit of detection of 5 fT/$\sqrt{\text{Hz}}$ [18].

1.2.2 Optically Pumped Magnetometers (OPMs)

OPMs have several direct advantages compared to SQUIDs. First, they measure directly the magnetic field amplitude. Second, they work at room temperature and thus are helium-free.

An OPM is made of a glass cell containing a vapor of alkali metals (Cesium, Rubidium or Potassium), two laser diodes and an optical detector.

The first laser diode emits a circular polarized light to align alkali atoms spin parallel to the optical beam axis. This is called optical pumping [19] and works by transferring the

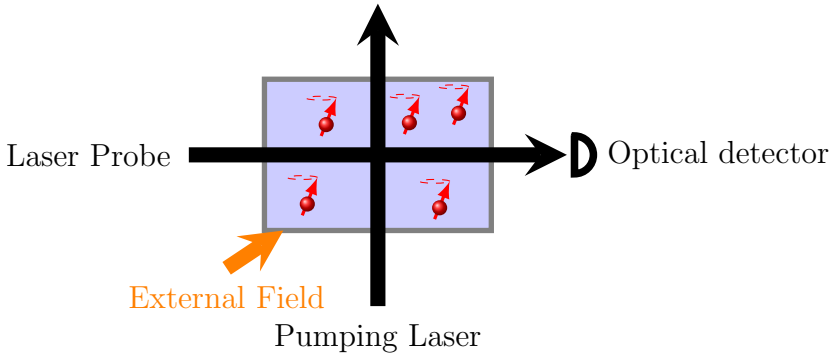

Figure 1.7: Principle of an OPM.

photon's momentum to the alkali atoms by absorption. The external field $\overrightarrow{B}$ induces a precession of the alkali magnetic moments at the Larmor frequency $\omega_0 = \gamma B$ with ω_0 the Larmor frequency, γ the gyromagnetic ratio of the atomic species and B the magnitude of the magnetic field.

The second laser diode probes the polarization rotation induced by the external magnetic field. The light is linearly polarized and is shined through the alkali atoms vapor. Either the change in polarization or in intensity can be measured. The polarization is deflected by an angle proportional to the external magnetic field due to Faraday effect and the light intensity is decreased by absorption.

The fundamental noise limit of an OPM is the shot noise. It is described by:

$$\delta B = \frac{1}{\gamma\sqrt{nT_2Vt}} \tag{1.2}$$

with γ the gyromagnetic ratio, n the number density of atoms, T_2 the transverse spin relaxation time, V the measurement volume and t the measurement time. To reduce the shot noise, some atomic magnetometers have a high volume and a low density of atoms. In practice, OPMs are limited by spin relaxation which prevents them from reaching lower limit of detection. Spin relaxation depends on thermal relaxation (due to atom-atom collisions or atom-wall collisions). To prevent atom-atom collision a buffer gas [20] can be used and the walls of the glass cell can be chemically treated or covered with paraffin [21].

Typically, OPMs have a noise floor of 1 pT/$\sqrt{\text{Hz}}$ at 1Hz which is much higher than SQUIDs and they perform a scalar measurement of the external magnetic field. A noise floor of 180 fT/$\sqrt{\text{Hz}}$ for a volume of 2,4 cm^3 has been achieved [22].

OPMs in Spin-Exchange Relaxation-Free (SERF) regime can have a noise level similar to SQUIDs with a small volume. To suppress the spin-exchange relaxation, the SERF OPM is used close to zero magnetic field with a high density of alkali metal [23]. With a cell of 7 cm^3, a SERF magnetometer can achieve a limit of detection of 10 fT/$\sqrt{\text{Hz}}$ [24]. In this example, the sensitivity is limited by the magnetic noise from the magnetic shielding and the authors estimate the theoretical shot-noise limit to be in the order of 2.10^{-18} T/$\sqrt{\text{Hz}}$.

To decrease further the limit of detection, it is possible to use a gradiometer configuration. Dang et al [25] have reached a noise level of 160 aT/$\sqrt{\text{Hz}}$ at 40 Hz with a

SERF magnetometer in a gradiometer arrangement and a sensing volume of 0.45 cm^3. Weakly magnetized rocks have been measured with this SERF magnetometer up to a temperature of 420 °C.

OPMs usually perform scalar measurements and they can also realize vectorial measurements in special configuration, like near a zero magnetic field or by adding a magnetic modulation in three orthogonal directions with a lock-in detection [26]. A magnetometer was developed for space application and the author reported a sensitivity of 1 $pT/\sqrt{Hz}$ in scalar mode and 1 $nT/\sqrt{Hz}$ in vectorial mode [27].

1.2.3 Nitrogen Vacancy (NV)-center

An NV center is a defect in a diamond lattice which can be used as a magnetometer. A diamond is a semi-conductor with a gap of 5.5 eV and the insertion of defects can add either electron giver or receiver levels in the gap, leading to interaction with light in the visible range (400-800nm). The nature of the defect (bore, nitrogen, etc.) gives a distinct color to the diamond and these defects are called color centers. When two adjacent carbon atoms are replaced by a nitrogen atom and by a vacancy, the defect behaves like an artificial atom with a spin S=1 from two non-bonded electrons. This artificial atom can be used in various fields like quantum electronic [28] or biology [29].

An NV center has two levels of energy: a ground state and an excited state. Each level is divided in two sub-levels: $|0\rangle$ and $|\pm 1\rangle$. In the absence of a magnetic field, $|\pm 1\rangle$ is degenerated. A NV center is excited by a green laser with a wavelength of 532 nm and electrons decay either by producing photo-luminescence (PL) in the red around $\lambda = 670nm$ from the excited state $|0\rangle$ to the ground state or by non-radiative decay from the excited state $|\pm 1\rangle$ to the ground state $|0\rangle$ as shown on fig 1.8a. After a few PL cycles, electrons are optically pumped to the ground state $|0\rangle$.

A microwave field at the frequency 2.87 GHz forces transition in the ground level from $|0\rangle$ to $|\pm 1\rangle$ leading to a PL decay of 20 %. When a magnetic field is applied, it lifts the degeneracy of $|\pm 1\rangle$ state because of Zeeman splitting. This splitting is proportional to the external field and this property is used to turn an NV center into a magnetometer. The axis of sensitivity of a magnetometer is along the alignment of the vacancy and the nitrogen atom.

An NV-center is a vectorial atomic-sized magnetometer which operates at room temperature. A single NV-center can have a limit of detection 18 $nT/\sqrt{Hz}$ with a nanoscale resolution [30]. By increasing the number of NV centers, the noise can be decreased by a factor $1/\sqrt{N}$ with N the number of NV centers [30]. For a sensing volume of (13x200x2000 μm^3) with a high density of NV centers ($3*10^{17}$ cm^{-3}), a limit of detection of 15 $pT/\sqrt{Hz}$ can be achieved [31].

These three magnetometers are highly sensitive and their main characteristics are summarized in table 1.1.

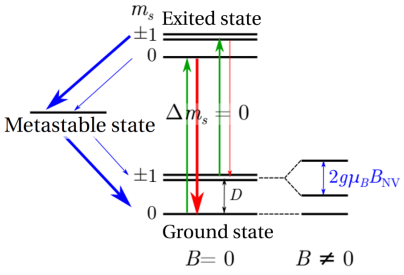

(a) Energy levels

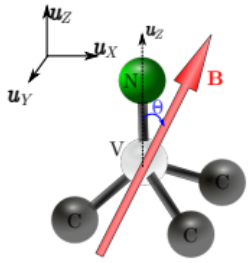

(b) Scheme of an NV center

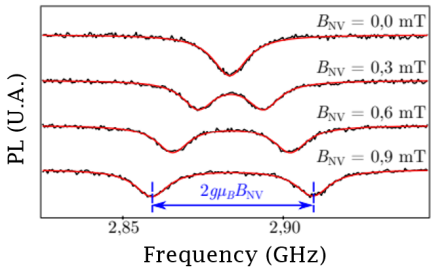

(c) PL response of an NV center

Figure 1.8: NV-center principles from [32]

Sensor	SQUID	OPM (SERF regime)	NV center	
			Single	Ensemble
LOD	5 fT/$\sqrt{\text{Hz}}$	10 fT/$\sqrt{\text{Hz}}$	18 nT/$\sqrt{\text{Hz}}$	15 pT/$\sqrt{\text{Hz}}$
Sensor size	81 mm^2	7 cm^3	Atomic	13*200*2000 μm^3
Sensitivity	Flux	Field	Field	Field
Mode	Vectorial	Scalar/Vectorial	Vectorial	Scalar
Working Temp.	4.2 K	Room temperature		
Reference	[18]	[24]	[30]	[31]

Table 1.1: Comparison of SQUIDs,OPMs and NV-centers characteristics.

1.2.4 Application of ultra-sensitive magnetic sensor to neuronal recording

We have seen that SQUIDs, OPMs and NV-center have a limit of detection low enough for biomagnetic recordings. In this section we will evaluate the possibility to adapt these sensors for an insertion in the brain to record magnetic neuronal activity in close vicinity of neurons.

As previously mentioned, SQUIDs are used for MEG but they cannot be miniaturised to be inserted in the brain as its sensitivity depends on the area of the SQUIDs and, in addition, it need cryogenic cooling which is incompatible with an insertion in the brain.

It is interesting to mention that solutions based on OPMs are tested as an alternative to SQUIDs for MEG to suppress the need of helium cooling. Indeed they have a very high sensitivity at room temperature and can be positioned directly on the scalp(cf fig 1.9a) which increases the recorded magnetic signal compared to SQUID. Also MEG with OPMs allows the patient to move and a huge number of OPMs over the brain

area to study and less OPMs elsewhere to reduce the total number of sensors with a good resolution in the zone of interest. Helmet for MEG with OPMs can be designed for the patient's head and 3d printed which allows a precise positioning of sensors [9].

OPMs have been miniaturized to increase their spatial resolution for *in-vitro* biomagnetic recording of a frog sciatic nerve [33], but the resulting size of the OPMs and of the equipment needed (laser beam and probe, detector, ...) prevent them from being used for recording local *in-vivo* magnetic activity of neurons.

NV-centers have also been used for *in-vitro* and *in-vivo* biomagnetic recording of a crayfish axon [31]. NV-centers are atomic scale magnetometers but the need of optical equipment prevent NV-center from being used as a local magnetic probe and inserted inside the brain.

SQUIDs, OPMs and NV-centers are state of the art magnetometer because of their ultra-low limit of detection but they cannot be used for *in-vivo* recording because of their working temperature, size or needed equipment.

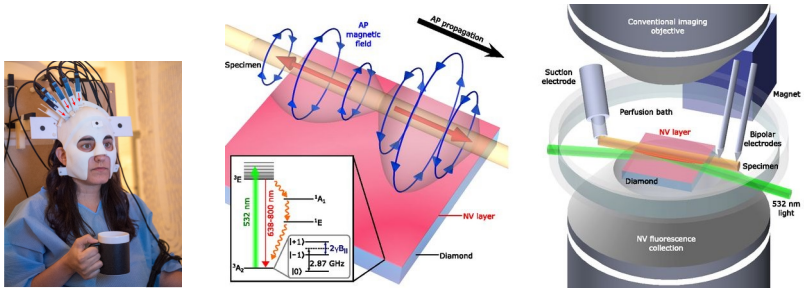

(a) MEG with OPMs instead of SQUIDs. From [9]

(b) NV center for *in-vitro* magnetic action potential detection. From [31]

Figure 1.9: Application of OPMs and NV-center to neuronal imaging.

1.2.5 Conclusion

Recording the magnetic neuronal activity inside the brain is challenging both because of the small amplitude of the expected magnetic signal and by the *in-vivo* constraints (temperature, size). Ultra-sensitive sensors have the possibility to record magnetic signal with such a small amplitude but their working temperature, size and recording equipment prevent then from being inserted in the brain.

Another possibility is to use sensors with a higher limit of detection ($\sim$nT) but with a footprint in the micrometer range, a simple readout electronics and which work at room temperature. Magnetoresistive sensors can fulfill these conditions and are presented in the next section.

1.3 Magnetoresistive sensors

The resistance of magnetoresistive (MR) sensors varies with the external magnetic field. We will focus on three types of MR sensors: Anisotropic Magnetoresistance (AMR), Giant Magnetoresistance (GMR) and Tunnel magnetoresistance (TMR) sensor.

1.3.1 Anisotropic Magnetoresistance

In 1857, the AMR effect was discovered by William Thomson [34], it corresponds to the variation of a ferromagnetic metal resistance as a function of the angle between its magnetization and the bias current direction (cf fig 1.10). In an AMR sensor, a magnetic anisotropy is induced either by annealing the ferromagnetic material under a strong magnetic field or by shaping the device with a high aspect ratio to force the magnetization along the length of the device due to shape anisotropy. In the presence of a magnetic field $\overrightarrow{H}$, the magnetization $\overrightarrow{M}$ aligns with $\overrightarrow{H}$ and the resistance is proportional to $\cos^2(\theta)$ with θ the angle between the magnetization and the current direction [35].

The MR ratio is calculated as follow:

$$MR_{AMR} = \frac{R(H) - R_{H=0}}{R_{H=0}} * 100 \tag{1.3}$$

AMR sensors have an MR ratio of 2-3 % and can typically reach a limit of detection of a 2 nT at 1Hz [36]. The best AMR sensors can reach a limit of detection of 23 $\mathrm{pT}/\sqrt{\mathrm{Hz}}$ [37]. This noise level is low enough for *in-vivo* magnetic recording. However, as AMR sensors need a minimal volume to prevent electron scattering (pT levels are reached for mm^2 surfaces sensors), this is too large for an insertion in the brain and we will not use AMR sensor for local recording of magnetic neuronal activity.

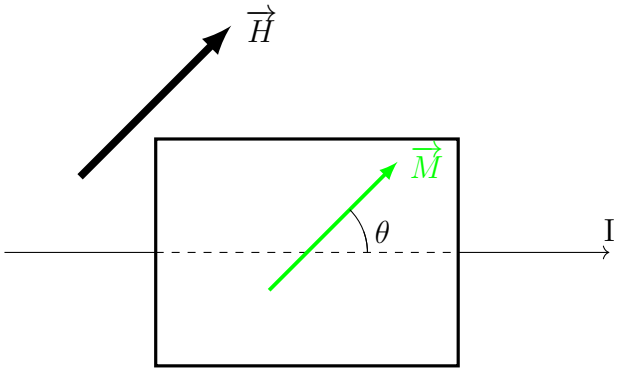

Figure 1.10: Scheme of an AMR sensor. The magnetization of the ferromagnetic material $\overrightarrow{M}$ is aligned with the external field $\overrightarrow{H}$. θ is the angle between the direction of the current I and $\overrightarrow{M}$.

1.3.2 Giant Magneto-Resistance (GMR)

In 1988, GMR was simultaneously observed by Albert Fert [38] in France and by Peter Grünberg [39] in Germany. This discovery generated an important technological development in the field of magnetic sensors and data storage. As a consequence, these

two scientists received the Nobel Prize in 2007. GMRs replaced AMRs in data storage technology with a quick transition ($\sim$ 10 years) from research laboratories to industry before being replaced by TMR.

The emergence of microfabrication techniques like Molecular Beam Epitaxy (MBE) allowed such a discovery. Indeed, before MBE spin manipulation was only possible at macroscopic scale *via* material's magnetization. MBE allows to deposit ultra-thin layers in the order of nanometers and grants access and control of the spin of conduction electron. Nowadays, GMR and TMR can also be deposited by sputtering.

Introduction to spintronics

An electron has both a charge and a spin. The first one is usually described by classical physics and the second through quantum physics framework. In classical electronic only the charge is used when in spintronics both properties are exploited. The spin is the angular momentum of the electron and can have two values: +1/2 (spin-up) and -1/2 (spin-down).

For the GMR effect a conduction electron has two properties of interest which are the mean free path λ_l and the spin diffusion length λ_s. λ_l is the average distance travelled by the electron in a crystal before scattering and λ_s is the average distance before spin-flip *ie* before the spin is inverted. Electrons can carry information *via* their spin state.

The spin diffusion length is around a few tens of nm (50 nm for Fe, 40 nm for CO and 10 nm for Ni) [40]. MBE and sputtering allow to deposit a superposition of ultra-thin layer with a thickness inferior to λ_s, enabling the spin information to be transported through the stack.

GMR effect

A GMR stack is a superposition of ferromagnetic (Co, Ni, Fe or alloys) and conductive non magnetic materials which separate two ferromagnetic layers (spacer). Initially, the GMR effect was observed in a superposition of ferromagnetic layer separated by a spacer with a thickness designed to create an anti-ferromagnetic coupling between two adjacent ferromagnetic layers by an RKKY-like coupling (cf fig 1.11a). It is an oscillatory coupling and depending on the thickness of the spacer it is either a ferromagnetic or antiferromagnetic coupling. The resistance of the GMR stack is maximum when the ferromagnetic layers have an anti-parallel configuration at zero field and minimal when they are parallel (cf fig 1.11b). As the GMR ratio is much higher than AMR (up to 80% for a multilayer of iron and chromium [38]) it is called "Giant" magnetoresistance.

There are two effects to take into consideration to explain GMR.

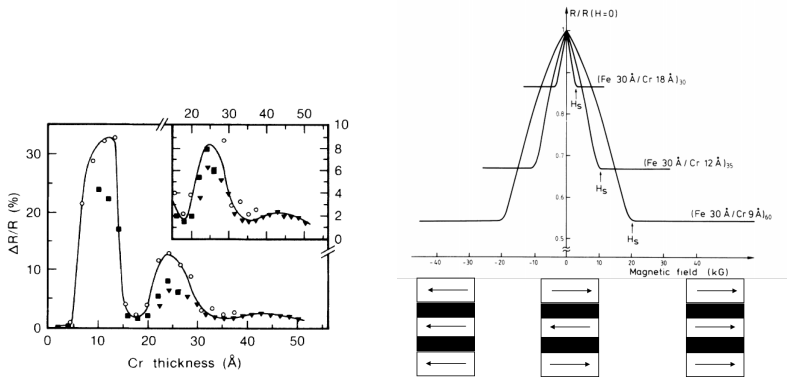

(a) GMR ratio as a function of the spacer thickness

(b) R/R(H=0) as a function of the external magnetic field

Figure 1.11: (a) GMR ratio as a function of Cr thickness in a Fe/Cr multilayer at 4.2K. The GMR oscillations are correlated with the oscillations between antiferro- and ferromagnetic coupling. From [41] (b) GMR effect. Ferromagnetic layers are anti-ferromagnetically coupled without an external magnetic field. With an external magnetic field, magnetization starts to rotate until all ferromagnetic layers are parallel for $H \geq H_s$. Adapted from [38]

First, as suggested in 1936 by Mott [42], there are two conduction channels in a ferromagnetic material which do not mix. One channel is for spin-up electrons and the second is for spin-down electrons leading to two independent conduction channels. It is supposed that during scattering, the spin is conserved.

Second, the scattering rate of spin-up and spin-down electrons is different in a ferromagnetic material. It is explained by the band splitting of ferromagnetic material leading to a different density of space at the Fermi level for spin-up and spin-down electrons. When the electrons have the same spin as the magnetization of the ferromagnetic layer they are referred to as spin-up and when the electron have a spin anti parallel they are referred as spin-down. The scattering is more important for spin-down electron and thus the resistivity of spin-down electrons is more important than spin-up electrons resistivity ($\rho_\downarrow > \rho_\uparrow$).

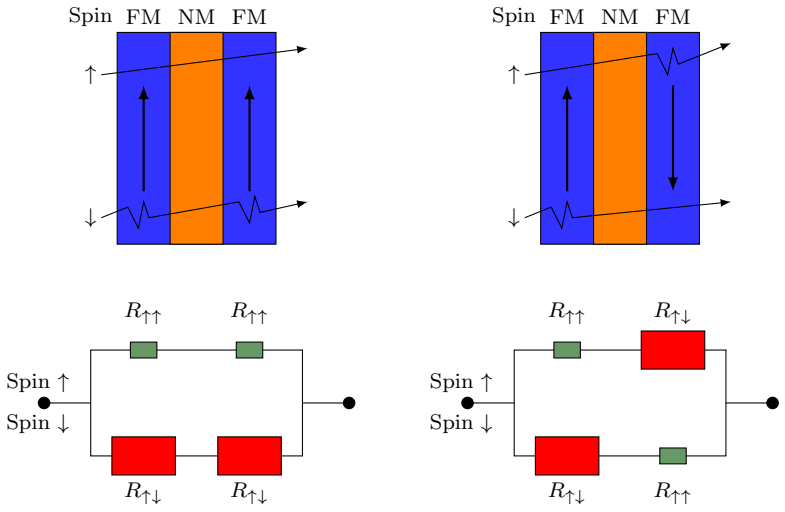

Figure 1.12: Sandwich of two ferromagnetic layers separated by a non magnetic layer and the corresponding circuit equivalent in parallel and antiparallel configuration.

By applying these two effects to two ferromagnetic layers separated by a spacer (fig 1.12), there are two conduction channels (one for spin ↑ and one for spin ↓). The resistance of spin-up and spin-down electrons conduction channels depends on the magnetization of each ferromagnetic layer. When the spins of the electrons are aligned with the magnetization of the ferromagnetic layer, the scattering is reduced and the resistance is noted $R_{\uparrow\uparrow}$. And inversely, when the spins of the electrons are antiparallel to the magnetization of the ferromagnetic layer, the scattering is increased and the resistance is noted $R_{\uparrow\downarrow}$, with $R_{\uparrow\downarrow} > R_{\uparrow\uparrow}$. Depending on the external field, the magnetization of the two ferromagnetic layers can be in either parallel or antiparallel configuration.

In the parallel configuration, the spin-up channel (↑) has a lower resistance than the spin-down channel (↓) for a total resistance $R_P \sim 2R_{\uparrow\uparrow}$ because as the two FM layers are parallel, the electrons in the spin ↑ channel will cross easily while the electrons in the spin ↓ channel will be strongly scattered in both FM layers.

In the antiparallel configuration, both channels have a similar resistance and $R_{AP} \sim \frac{R_{\uparrow\downarrow}}{2}$ because both channels are strongly scattered in one FM layer and goes easily through the other one.

In the parallel state the resistance is lower than in the antiparallel state. This difference of resistance depending on the magnetization of the ferromagnetic layers explains qualitatively the GMR effect.

In 1991, Dieny et al [43] proposed a device called a spin -valve composed of only two ferromagnetic layers separated by a spacer. One of the ferromagnetic layer is free to follow the external field when the second has its magnetization fixed in one direction by an exchange coupling with a antiferromagnetic material to raise its coercivity. It is massively used in hard-disk drive read-heads and magnetic sensors as a small magnetic field can move the magnetization of one ferromagnetic layer (a few mT) from anti parallel to parallel state when for previously mentioned multilayer a high field around 1T is needed.

Spin-valve

A spin-valve have three components:

- **A free layer** which is composed of a ferromagnetic layer with a low coercivity. The free layer is easily aligned with the external magnetic field. As we will see later, it can be composed of a bilayer of NiFe/CoFe.
- **A spacer** which is either a conducting material for GMR sensor or an insulator for TMR sensor. It decouples the free layer and the hard layer. Depending on its thickness, the two ferromagnetic layers have either a ferro- or antiferromagnetic coupling or a minimal coupling strength. This is an oscillatory coupling like RKKY coupling [44, 45, 46]. One wants a weak coupling so the free layer rotates freely with a low external field and a small thickness to prevent spin-flip and losing the information carried by spins of conduction electrons. Due to the roughness at the interfaces, a Néel coupling (or "orange-peel" coupling) arises [47]. This coupling is a weak ferromagnetic coupling and the spacer thickness can be designed to compensate this ferromagnetic coupling by the RKKY-like coupling.
- **A hard (or pinned) layer** which is composed of a ferromagnetic layer pinned by

an antiferromagnetic (IrMn or PtMn) by direct exchange coupling [48] to prevent the rotation of its magnetization with the external field. The hard layer acts as a reference layer. We will see later that a hard layer can be a synthetic antiferromagnet (SAF) to enhance its stability and suppress the stray field generated by the ferromagnetic layer. Typically, the ferromagnetic layer is made of CoFe.

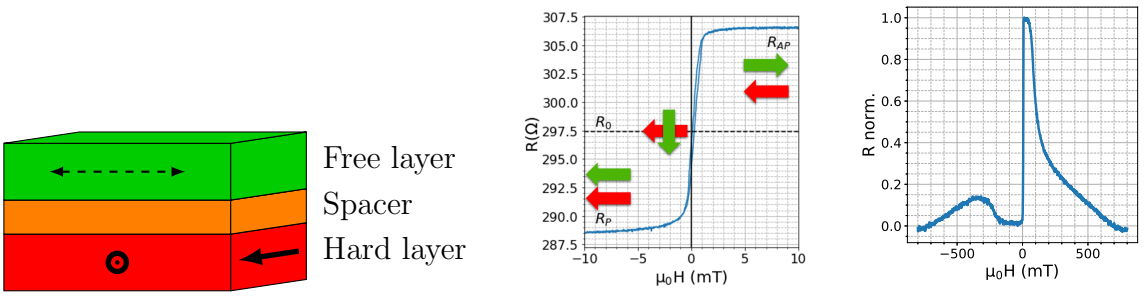

(a) GMR stack

(b) Hysteresis cycle of the free layer

(c) Hysteresis cycle of the entire GMR stack

Figure 1.13: (a) Schematic of a spin-valve. The dash arrow represents magnetization of the free layer which is able to rotate with the external field and the plain arrow the fixed magnetization of the hard layer. (b) Spin-valve resistance as a function of the external field H. Red arrows represent the hard layer magnetization and green arrows represent the magnetization direction of the free layer from top view. One can see that upward curve from +10mT to -10mT and backward curve from -10mT to +10mT do not superpose. This phenomenon is called hysteresis. (c) Resistance of the spin-valve at high-field. The hard layer is a SAF and at -350mT the external field is strong enough to break the SAF coupling.

To have a linear response centered at zero field, the free layer and the hard layer magnetization have to be perpendicular at zero field. This is achieved by inducing an easy axis for the free layer either by adding a permanent magnet to the spin-valve, by weakly coupling the free layer to an AF or by shape anisotropy. As described earlier, the spin-valve is shaped with a high aspect ratio and without an external field, the free layer magnetization is parallel to the length of the sensor as shown in fig 1.13a.

The response of a spin-valve with crossed anisotropy as a function of the external field is shown in fig 1.13b and three regimes can be differentiated. When the magnetization of the free layer and of the hard layer are either parallel or anti-parallel, the resistance is equal to R_P and R_{AP} respectively. These parts are called saturated states. The third part is the linear part in between and R is proportional to $cos(\theta)$ with θ the angle between the magnetization of the hard layer and of the free layer.

To increase the MR ratio, one can use a free layer composed of a bilayer of CoFe/NiFe. The CoFe layer is in contact with the spacer to increase the spin polarization and thus increase the MR ratio but it has a high coercivity which creates hysteresis. The NiFe layer has a low coercivity which decreases the hysteresis. This layer rotates with the external magnetic field and drags the CoFe layer by direct exchange coupling. The selection of NiFe and CoFe thickness is a compromise between MR ratio and hysteresis.

The hard layer magnetization can be set by an annealing under a magnetic field. The annealing can be made in an oven, by Joule effect with a voltage pulse or by a laser. The device is heated over the blocking temperature of the antiferromagnetic so the ferromagnetic layer in contact with the antiferromagnetic can be repinned. As a high

magnetic field is applied, the magnetization of the ferromagnetic layers are aligned in parallel to the magnetic field. By exchange coupling, anti-ferromagnetic (AF) is dragged by the ferromagnetic layer. The device is then cooled under this magnetic field. After the annealing the ferromagnetic layer of the hard layer is "pinned" by the AF and only a strong magnetic field can have an impact on the hard layer magnetization, as shown in fig 1.13c. The blocking temperature must be high enough so the hard layer is stable at high temperature and low enough to allow an easy repinning. Also the blocking temperature must be low enough to prevent diffusion at the interface.

The hard layer pinning can be enhanced by adding an additional ferromagnetic layer coupled to the ferromagnetic layer in contact with the antiferromagnetic by RKKY-like coupling through a non-magnetic conductive spacer like ruthenium. The thickness of the spacer is chosen to create an antiferromagnetic coupling between the two ferromagnetic layers. This is called a SAF and, as mentioned earlier, it increases the stability of the hard layer to high magnetic field as the coercivity of the hard layer is increased. As the two ferromagnetic layers are anti-parallel the resulting stray field is supposed to be zero and thus the hard layer should not have an impact on the free layer.

In the whole stack, other layers are used. The first one is the seed layer. It is used, in particular, to control the roughness of the surface on which the other materials are deposited. The second is a cap layer added on top of the layer. It is used to enhance contacts between GMR stack and contacts pads, it also protects the GMR stack from oxidation. The seed and cap layer can decrease the GMR ratio by creating a short-cut on the GMR stack depending on the configuration of measurement of the spin-valve.

A spin-valve can have two configurations of measurement: Current Perpendicular to Plane (CPP) or Current in Plane (CIP). CPP configuration increases the GMR effect as all the electrons go through the entire GMR stack when in CIP the current is short-cut by the conductive non magnetic layers (spacer, seed layer, cap layer,...). Indeed, to reach a measurable resistance the lateral size of the GMR device has to be in the nanometer range. Otherwise, a GMR used in CPP configuration would have a resistance too low and would need a high current to have a sufficient output voltage. Furthermore, very small volume GMR exhibits a high low frequencies noise (see sec.1.3.2), so for our application, we did not use CPP configuration. For TMR, on the other hand, the CPP configuration is mandatory as the TMR effect is measured through the insulating barrier of magnetic tunnel junctions (MTJs) (see sec. 1.3.3). As TMR have a high resistance due to the insulating barrier, a small current is sufficient to have a recordable output voltage. Furthermore, the biasing current should not be too high to prevent any damage to the insulating barrier.

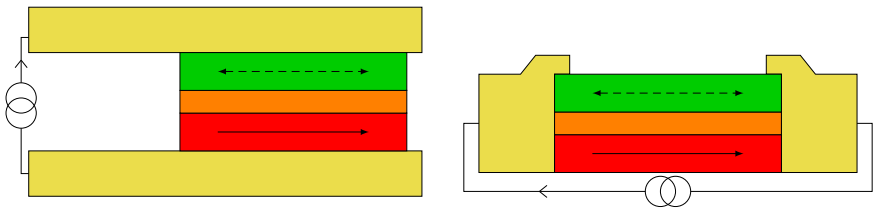

(a) CPP configuration (b) CIP configuration

Figure 1.14: Schemes of the two configurations used to measure the voltage of a spin-valve powered by a current source.

GMR sensors

GMR sensors are fabricated in three steps. First, the GMR stack is etched to define the sensor shape. Then, the contacts are deposited on each side of the device. GMR sensors can be easily connected in serial with another device if needed. Finally, GMR sensors and contacts are passivated. It is very easy to fabricate GMR sensors.

A spin-valve GMR sensor has an MR ratio around 10% which is defined as follow:

$$MR_{GMR} = \frac{R_{AP} - R_P}{R_0} \tag{1.4}$$

with R_{AP} the resistance in the anti-parallel state, R_P the resistance in the parallel state and $R_0 = \frac{R_{AP}+R_P}{2}$. The size of the GMR sensors fabricated in our group varies from few millimeters down to the nanometer scale.

Noise GMR sensors exhibit two types of noises: frequency independent noise (thermal noise) and frequency dependent noises (1/f noise and Random Telegraphic Noise (RTN)). They can have an electric and/or magnetic origin.

- **Thermal noise:** The origin of the thermal noise is the Brownian motion of electrons in a conductor. It is an electric noise independent of the applied voltage. It is also called Johnson noise or Nyquist Noise.

  $$\sqrt{S_{v,thermal}} = \sqrt{4k_BTR} \tag{1.5}$$

  with k_B the Boltzmann constant, T the temperature and R the resistance of the sensor. Thermal noise increases with the resistance and the temperature.

- **1/f noise:** The 1/f noise has both an electric and a magnetic origin and is phenomenologically described by the Hooge formula [49]:

  $$\sqrt{S_{V,1/f}} = \sqrt{\frac{\gamma}{n_c.Volume.f^\alpha}}RI \tag{1.6}$$

  with γ the Hooge constant which depends on the device, R the resistance, I the current, n_c the carrier density and f the frequency. α is usually close to one and in this thesis, we will consider $\alpha = 1$. 1/f noise has several origins. For the electric part it is due to conductivity fluctuations because of charge trapping by defects. 1/f noise also has a magnetic part due to magnetic domains configuration which is partly removed by using a "yoke" shape [50] as we will see in chapter 2. The yoke shape has an impact on the magnetic configuration and is used to stabilize the magnetic domains.

  This noise is dominant at low frequencies and is the main limitation in term of noise level of the GMR at low frequencies. The frequency at which the 1/f noise becomes smaller than thermal noise is called frequency corner. The 1/f noise increases when the volume, and thus the number of carriers, decreases. It also increases with the voltage. If the 1/f noise is smaller than the thermal noise, then it is interesting to increase the voltage as long as the thermal noise is dominant. This increases the signal to noise (SNR) ratio as the output tension increases for a constant noise. When the 1/f noise is dominant then it is not always interesting to increase the applied voltage, especially if there is Random Telegraphic Noise.

- **Random Telegraphic Noise (RTN):** comes from fluctuations of unstable magnetic domains. These unstable magnetic domains are located in the free layer. As for 1/f noise, a yoke shape is interesting for stabilizing the magnetic domain and prevent RTN. The RTN noise can also be prevented by optimizing the free layer composition and in particular the NiFe thickness. For a simple top-IrMn spin-valve, the optimal thickness for a low coercivity and thus a low RTN is 5 nm [51]. RTN is thermally activated and the size of the magnetic domains responsible for these sudden changes of resistance can be estimated [52].

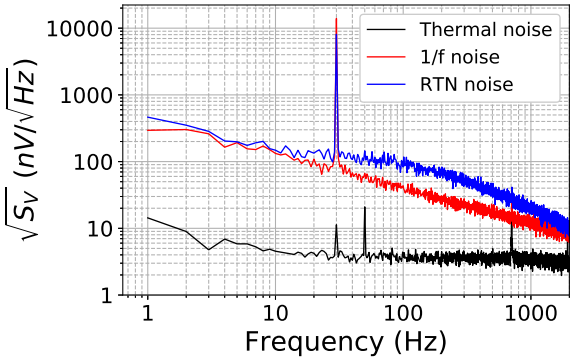

Figure 1.15: Noise Power Spectral Density *vs* Frequency. The 1/f noise at 1kHz is 12 nV/$\sqrt{\text{Hz}}$. This measurement was made on a device called meander (see chapter 2.5) with 5 segments with a width of 5 µm and a length of 30 µm.

GMR sensors vary in composition, shape and applications. Their sensitivity can be increased by flux concentrator, a reduction in the limit of detection from 47 nT/$\sqrt{\text{Hz}}$ to 2 nT/$\sqrt{\text{Hz}}$ at 10 Hz has been reported [53] with a flux guide with a relative magnetic permeability of 853 and a size in the order of 100 µm (which is too large to be used for *in-vivo* application). Flux concentrator can also be used with superconducting material at cryogenic temperature [54] and another method is to use a modulated flux concentrator to displace the sensing field at higher frequency in the thermal regime. It can be done by using a Microelectromechanical systems (MEMS) oscillator in addition to the flux concentrator [55]. GMR sensors sensitivity can also be increased by placing a GMR sensor in the constriction of a flux to field transformer made with a superconducting material (either high-Tc or low-Tc material). This type of device is called mixed sensor [56] and can reach a limit of detection of 32 fT/$\sqrt{\text{Hz}}$ at 4.2K in the thermal noise.

GMRs are used for several applications from biological tests for neural magnetic recording [57] or "lab on chip equipments" [58] to 3d magnetic sensors [59] or non-destructive testing at small scale.

The main assets of GMR sensors are: they are easy and cheap to fabricate, they work at room temperature and can be miniaturized. But for micrometer size they have a noise level of 1nT/$\sqrt{\text{Hz}}$ at 1kHz and their performances at low frequencies (under 1kHz) are limited by 1/f noise. GMRs are good candidates for *in-vivo* application despite a limit of detection of 1 nT at 1kHz.

1.3.3 Tunnel Magneto-Resistance (TMR) sensors

The first TMR experimental demonstration was made by Jullière in 1975 [60] at cryogenic temperature and it was in 1995 [61] that the TMR effect was observed at room

temperature. As a difference with the GMR sensor, the spacer in a TMR sensor is an insulator (MgO in general). TMRs need to be measured in CPP configuration as it is based on electrons tunnelling through the insulator barrier. TMRs typically have a MR ratio of 150-200% and TMR up to ∼600% at 300k have been reported [62].

$$MR_{TMR} = \frac{R_{AP} - R_P}{R_P} \tag{1.7}$$

The fabrication of TMR sensors is slightly different from GMR fabrication (cf fig 1.16). Indeed, a CPP configuration is mandatory to observe the tunneling through the insulating barrier. Also TMR are fragile and to prevent breaking due to discharge, several TMRs are connected in serial. The connection between TMRs is made in two different manners for bottom and top contacts. The bottom contact is ensured by a ferromagnetic layer (either the hard or the free layer). The top contact is made by the deposition of a metal on top of the free layer of two independent TMRs. TMR are connected in serial, in the bottom by the hard layer and in the top by a metal. First, a TMR stack is deposited on the wafer with the hard-layer in contact with the wafer. Then, the TMR stack is entirely etched into several ovals. The free layer and the barrier are etched into circles at the sides of the oval. Each circle is a TMR and two circles in the same oval are connected in serial by the hard layer. The sample is then passivated on the walls to prevent short-circuits during contact deposition. Then contacts are deposited, they connect TMRs *via* the top electrode (either the free or the hard layer). The side of TMRs are passivated to ensure the metallic contacts are only made at the top of the TMRs. As the free layer magnetization direction cannot be driven by shape anisotropy in this configuration, the crossed anisotropy between the free layer and the hard layer is induced by an external magnet or the pinned layer is weakly pinned by an AF.

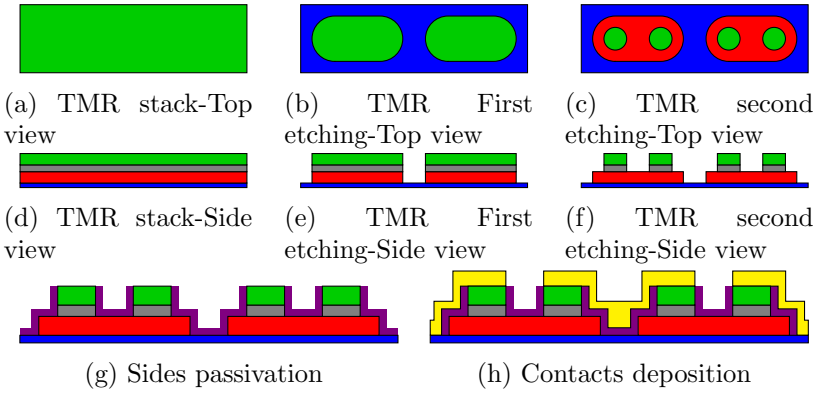

Figure 1.16: TMR fabrication process. The silicon wafer with a thin insulating layer is in blue, the hard layer is in red, the insulating spacer is in grey, the free layer is in green, the passivation is in a darker green and contacts are yellow.

TMR ratio is one order of magnitude higher than GMR which is important for the performance of a sensor. However, there is also an increase of 1/f noise due to the tunneling barrier, which is the main limitation for the use of TMR sensors at low frequencies. TMR are used in hard drive as read-heads, as high frequency sensors or for Magnetic Random Access Memory (MRAM).

Noise TMRs exhibit the same noise as GMR sensor in addition to shot noise.

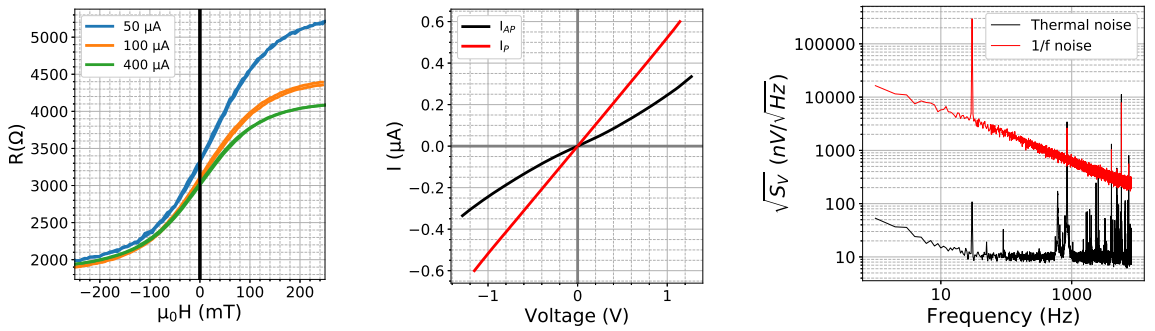

(a) R(H) (b) I(V) (c) Noise Power Spectral Density *vs* Frequency.

Figure 1.17: Measurements of a TMR with 4 pillars with a diameter of 5 µm in series. (a) TMR response depending on the current applied to the device. (b) Current through the TMR sensor as a function of the applied voltage depending on the magnetic configuration. Here we can observe two different curves, one for parallel state (I_P) and the second for antiparallel state (I_{AP}). (c) Noise measurement of a TMR sensors. The thermal noise (in black) and the 1/f noise (in red) are plotted as a function of the frequency. The 1/f noise at 1kHz is 666 nV/$\sqrt{\text{Hz}}$. It is much higher than the GMR 1/f noise for the same frequency (12 nV/$\sqrt{\text{Hz}}$) for a meander with 5 segments with a size of 5*30 µm^2 cf fig 1.15.

Shot-noise is due to fluctuation of the number of carriers and is directly proportional to the electric current. It is frequency independent.

$$S_{V,Shot} = \sqrt{2eI} \tag{1.8}$$

TMRs have a higher MR ratio than GMRs but the 1/f noise is much higher and TMRs can have equivalent limit of detection at low frequencies. In the thermal regime, TMRs can be highly competitive against GMR. Also, the high resistance of TMR allows to feed TMR with a low current and still have an important output voltage leading to low consumption devices.

TMR and GMR have the same stack deposition process but GMR sensors are easier to process as they are measured in a CIP configuration when TMR requires a CPP configuration.

1.3.4 Conclusion

For *in-vivo* magnetic signal recording by inserting a magnetic sensor into the brain (in close vicinity of neurons) a magnetic sensor which works at physiological temperature (37°C) with a small size (µm range) to limit damages during insertion in the brain and ensure a good spatial resolution, a low limit of detection to record biomagnetic signal in the range of 10-100pT at low frequencies, and stable to have the opportunity to average data and extract the magnetic signal output of the noise is what is needed.

MR sensors can work at room temperature and have a limit of detection in the nT range and even below depending on working temperature, size and noise canceling additional technologies. AMR sensors are too bulky for *in-vivo* application, GMRs present just enough sensitivity and can be as small as a few nanometers. TMRs exhibit a 1/f noise

which is too important at low frequencies. In conclusion, GMR sensors are a good option for *in-vivo* neuronal magnetic recording.

1.4 Conclusion

For now, developing tools for recording the magnetic activity of neurons at local scale is very challenging. This can be explained by the numerous challenges such as the low amplitude of the targeted magnetic field (from 10 pT to 100 pT for an action potential) and its low frequencies. Also the constraints due to the *in-vivo* environment are numerous: sensors must be bio-compatible, must work at 37 °C and must have a small size for limiting the damage in the brain during the insertion and to ensure a good spatial resolution.

Sensor		LOD	Size	Sensitivity	Mode	Working Temp.	Ref.
SQUID		5 fT/$\sqrt{\text{Hz}}$	81 mm^2	mag. flux	vectorial	4.2 K	[18]
OPM (SERF regime)		10 fT/$\sqrt{\text{Hz}}$	7 cm^3	mag. field	scalar/ vectorial	Room Temp.	[24]
NV center	single	18 nT/$\sqrt{\text{Hz}}$	atomic	mag. field	vectorial	Room Temp.	[30]
	ensemble	15 pT/$\sqrt{\text{Hz}}$	13*200*2000 µm^3	mag. field	scalar	Room Temp.	[31]
GMR		1 nT/$\sqrt{\text{Hz}}$*	5*(4*30µm^2)	mag. field	vectorial	Room Temp.	[63]
TMR		10 nT/$\sqrt{\text{Hz}}$*		mag. field	vectorial	Room Temp.	**

Table 1.2: Comparison of SQUIDs,OPMs, NV-centers GMR and TMR characteristics.* Measured at 1 kHz. ** To be published.

To respond to the necessity of an ultra-low limit of detection, SQUIQs, OPMs and NV-centers are good candidates but their limitations (working temperature, sensor size, size of needed equipment for measurement) prevent them from being used *in-vivo*. Thus, sensors with a smaller footprint and easier electronics are interesting despite a lower limit of detection.

GMRs and TMRs fulfill these criterion and are good candidates for local magnetic recording in the brain. TMRs have a higher MR ratio but also a higher noise at low frequencies than GMRs so we chose GMR sensors. GMR sensors are interesting sensors due to their micrometer size, easy fabrication and low limit of detection. But the important 1/f noise at low frequencies challenges the recording of neural signal in the frequency range of interest (DC-1kHz).

GMR sensors have previously been used for *in-vitro* recording biological magnetic field generated by muscles [64] and to record *in-vivo* magnetic signals generated by synchronous neurons [57]. The aim of this thesis is to determine if GMRs can be optimized to reach a limit of detection low enough for local *in-vivo* recording of the magnetic signal of an action potential generated by a single neuron.

Bibliography

[1] Matti Hämäläinen, Riitta Hari, Risto J Ilmoniemi, Jukka Knuutila, and Olli V Lounasmaa. Magnetoencephalography—theory, instrumentation, and applications to noninvasive studies of the working human brain. *Reviews of modern Physics*, 65(2):413, 1993. 2, 3

[2] ICM. *Le grand Atlas du Cerveau*. Glénat, 2018. 2, 3, 5, 7

[3] "magnetrodes" project 600730 - fp7-ict-2011-9, 2015. 3

[4] Ranjith S Wijesinghe. Magnetic measurements of peripheral nerve function using a neuromagnetic current probe. *Experimental Biology and Medicine*, 235(2):159–169, 2010. 4

[5] Hossein Jadvar and Patrick M Colletti. Competitive advantage of pet/mri. *European journal of radiology*, 83(1):84–94, 2014. 5

[6] Nicholas A Steinmetz, Christof Koch, Kenneth D Harris, and Matteo Carandini. Challenges and opportunities for large-scale electrophysiology with neuropixels probes. *Current opinion in neurobiology*, 50:92–100, 2018. 6

[7] Jacques Teulon. Le patch-clamp en bref. *M/S: médecine sciences*, 20(5):550–550, 2004. 6

[8] Joonas Iivanainen, Matti Stenroos, and Lauri Parkkonen. Measuring meg closer to the brain: Performance of on-scalp sensor arrays. *NeuroImage*, 147: 542 – 553, 2017. ISSN 1053-8119. doi: https://doi.org/10.1016/j.neuroimage.2016.12.048. URL http://www.sciencedirect.com/science/article/pii/S1053811916307704. 7

[9] E Boto, N Holmes, J Leggett, G Roberts, V Shah, SS Meyer, and MJ Brookes. Moving brain imaging towards real-world applications using a wearable meg system. *Nature*, pages 17–19, 2018. 7, 14

[10] Marie-Therese Horstmann, Stephan Bialonski, Nina Noennig, Heinke Mai, Jens Prusseit, Jörg Wellmer, Hermann Hinrichs, and Klaus Lehnertz. State dependent properties of epileptic brain networks: Comparative graph–theoretical analyses of simultaneously recorded eeg and meg. *Clinical Neurophysiology*, 121(2):172–185, 2010. 7

[11] John Clarke and Alex I Braginski. *The SQUID handbook. Vol. 1, Fundamentals and technology of SQUIDs and SQUID systems*. Wiley-VCH, 2004. 9

[12] Hedwige Polovy du Souich. *Capteurs mixtes pour applications médicales*. Theses, 2010. URL http://www.theses.fr/2010PA066087. 9

[13] RL Fagaly. Superconducting quantum interference device instruments and applications. *Review of scientific instruments*, 77(10):101101, 2006. 9, 10

[14] Brian Josephson. Possible new effect in superconducting tunneling. *Phys. Lett.*, 1:251–253, 1962. 9

[15] R Cantor, LP Lee, M Teepe, V Vinetskiy, and J Longo. Low-noise, single-layer yba/sub 2/cu/sub 3/o/sub 7-x/dc squid magnetometers at 77 k. *IEEE Transactions on Applied Superconductivity*, 5(2):2927–2930, 1995. 10

[16] JR Kirtley, MB Ketchen, KG Stawiasz, JZ Sun, WJ Gallagher, SH Blanton, and SJ Wind. High-resolution scanning squid microscope. *Applied Physics Letters*, 66 (9):1138–1140, 1995. 10

[17] John R Kirtley, Lisa Paulius, Aaron J Rosenberg, Johanna C Palmstrom, Connor M Holland, Eric M Spanton, Daniel Schiessl, Colin L Jermain, Jonathan Gibbons, Y-K-K Fung, et al. Scanning squid susceptometers with sub-micron spatial resolution. *Review of Scientific Instruments*, 87(9):093702, 2016. 10

[18] S Della Penna, C Delgratta, C Granata, A Pasquarelli, V Pizzella, R Rossi, M Russo, K Torquatiand, and SN Erne. Biomagnetic systems for clinical use. *Philosophical Magazine B*, 80(5):937–948, 2000. 10, 13, 26

[19] William Happer. Optical pumping. *Reviews of Modern Physics*, 44(2):169, 1972. 10

[20] M. Arditi. Gas cell "atomic clocks" using buffer gases and optical orientation. In *12th Annual Symposium on Frequency Control*, pages 606–622, 1958. 11

[21] SJ Seltzer, DJ Michalak, MH Donaldson, MV Balabas, SK Barber, SL Bernasek, M-A Bouchiat, A Hexemer, AM Hibberd, DF Jackson Kimball, et al. Investigation of antirelaxation coatings for alkali-metal vapor cells using surface science techniques. *The Journal of chemical physics*, 133(14):144703, 2010. 11

[22] EB Aleksandrov, MV Balabas, AK Vershovskii, AE Ivanov, NN Yakobson, VL Velichanskii, and NV Senkov. Laser pumping in the scheme of an mx-magnetometer. *Optics and Spectroscopy*, 78(2):292–298, 1995. 11

[23] W. Happer and H. Tang. Spin-exchange shift and narrowing of magnetic resonance lines in optically pumped alkali vapors. *Phys. Rev. Lett.*, 31:273–276, Jul 1973. doi: 10.1103/PhysRevLett.31.273. URL https://link.aps.org/doi/10.1103/PhysRevLett.31.273. 11

[24] JC Allred, RN Lyman, TW Kornack, and Michael V Romalis. High-sensitivity atomic magnetometer unaffected by spin-exchange relaxation. *Physical review letters*, 89(13):130801, 2002. 11, 13, 26

[25] HB Dang, Adam C Maloof, and Michael V Romalis. Ultrahigh sensitivity magnetic field and magnetization measurements with an atomic magnetometer. *Applied Physics Letters*, 97(15):151110, 2010. 11

[26] SJ Seltzer and Michael V Romalis. Unshielded three-axis vector operation of a spin-exchange-relaxation-free atomic magnetometer. *Applied physics letters*, 85 (20):4804–4806, 2004. 12

[27] Jean-Michel Leger, François Bertrand, Thomas Jager, Matthieu Le Prado, Isabelle Fratter, and Jean-Claude Lalaurie. Swarm absolute scalar and vector magnetometer based on helium 4 optical pumping. *Procedia Chemistry*, 1(1):634–637, 2009. 12

[28] Jörg Wrachtrup and Fedor Jelezko. Processing quantum information in diamond. *Journal of Physics: Condensed Matter*, 18(21):S807, 2006. 12

[29] M Bonnauron, S Saada, L Rousseau, Gaelle Lissorgues, C Mer, and P Bergonzo. High aspect ratio diamond microelectrode array for neuronal activity measurements. *Diamond and related materials*, 17(7-10):1399–1404, 2008. 12

[30] JM Taylor, P Cappellaro, L Childress, L Jiang, D Budker, PR Hemmer, A Yacoby, R Walsworth, and MD Lukin. High-sensitivity diamond magnetometer with nanoscale resolution. *Nature Physics*, 4(10):810–816, 2008. 12, 13, 26

[31] John F Barry, Matthew J Turner, Jennifer M Schloss, David R Glenn, Yuyu Song, Mikhail D Lukin, Hongkun Park, and Ronald L Walsworth. Optical magnetic detection of single-neuron action potentials using quantum defects in diamond. *Proceedings of the National Academy of Sciences*, 113(49):14133–14138, 2016. 12, 13, 14, 26

[32] Loïc Rondin. *Realisation of a NV coulour centre based magnetometer*. Theses, École normale supérieure de Cachan - ENS Cachan, November 2012. URL https://tel.archives-ouvertes.fr/tel-00824468. 13

[33] Kasper Jensen, Rima Budvytyte, Rodrigo A Thomas, Tian Wang, Annette M Fuchs, Mikhail V Balabas, Georgios Vasilakis, Lars D Mosgaard, Hans C Stærkind, Jörg H Müller, et al. Non-invasive detection of animal nerve impulses with an atomic magnetometer operating near quantum limited sensitivity. *Scientific reports*, 6(1):1–7, 2016. 14

[34] William Thomson. Xix. on the electro-dynamic qualities of metals:—effects of magnetization on the electric conductivity of nickel and of iron. *Proceedings of the Royal Society of London*, (8):546–550, 1857. 15

[35] T McGuire and RL Potter. Anisotropic magnetoresistance in ferromagnetic 3d alloys. *IEEE Transactions on Magnetics*, 11(4):1018–1038, 1975. 15

[36] P Ripka, M Vopálenskỳ, A Platil, M Döscher, K-MH Lenssen, and Hans Hauser. Amr magnetometer. *Journal of Magnetism and Magnetic materials*, 254:639–641, 2003. 15

[37] Egon Zimmermann, Arre Verweerd, Walter Glaas, Axel Tillmann, and Andreas Kemna. An amr sensor-based measurement system for magnetoelectrical resistivity tomography. *IEEE Sensors Journal*, 5(2):233–241, 2005. 15

[38] Mario Norberto Baibich, Jean Marc Broto, Albert Fert, F Nguyen Van Dau, Frédéric Petroff, P Etienne, G Creuzet, A Friederich, and J Chazelas. Giant magnetoresistance of (001) fe/(001) cr magnetic superlattices. *Physical review letters*, 61(21):2472, 1988. 15, 16, 17

[39] Grünberg Binasch, Peter Grünberg, F Saurenbach, and W Zinn. Enhanced magnetoresistance in layered magnetic structures with antiferromagnetic interlayer exchange. *Physical review B*, 39(7):4828, 1989. 15

[40] John MD Coey. *Magnetism and magnetic materials*. Cambridge university press, 2010. 16

[41] SSP Parkin, N More, and KP Roche. Oscillations in exchange coupling and magnetoresistance in metallic superlattice structures: Co/ru, co/cr, and fe/cr. *Physical review letters*, 64(19):2304, 1990. 17

[42] Nevill Francis Mott. The electrical conductivity of transition metals. *Proceedings of the Royal Society of London. Series A-Mathematical and Physical Sciences*, 153 (880):699–717, 1936. 17

[43] Bernard Dieny, Virgil S Speriosu, Serhat Metin, Stuart SP Parkin, Bruce A Gurney, Peter Baumgart, and Dennis R Wilhoit. Magnetotransport properties of magnetically soft spin-valve structures. *Journal of Applied Physics*, 69(8):4774–4779, 1991. 18

[44] Melvin A Ruderman and Charles Kittel. Indirect exchange coupling of nuclear magnetic moments by conduction electrons. *Physical Review*, 96(1):99, 1954. 18

[45] Tadao Kasuya. A theory of metallic ferro-and antiferromagnetism on zener's model. *Progress of theoretical physics*, 16(1):45–57, 1956. 18

[46] Kei Yosida. Magnetic properties of cu-mn alloys. *Physical Review*, 106(5):893, 1957. 18

[47] JCS Kools, W Kula, Daniele Mauri, and Tsann Lin. Effect of finite magnetic film thickness on néel coupling in spin valves. *Journal of Applied Physics*, 85(8): 4466–4468, 1999. 18

[48] Josep Nogués and Ivan K Schuller. Exchange bias. *Journal of Magnetism and Magnetic Materials*, 192(2):203–232, 1999. 19

[49] Friits N Hooge. 1/f noise is no surface effect. *Physics letters A*, 29(3):139–140, 1969. 21

[50] C Fermon, M Pannetier-Lecoeur, Nicolas Biziere, and B Cousin. Optimised gmr sensors for low and high frequencies applications. *Sensors and Actuators A: Physical*, 129(1-2):203–206, 2006. 21

[51] HR Liu, BJ Qu, TL Ren, LT Liu, HL Xie, CX Li, and WJ Ku. High-sensitivity gmr with low coercivity in top-irmn spin-valves. *Journal of magnetism and magnetic materials*, 267(3):386–390, 2003. 22

[52] J Moulin, A Doll, E Paul, M Pannetier-Lecoeur, C Fermon, N Sergeeva-Chollet, and A Solignac. Optimizing magnetoresistive sensor signal-to-noise via pinning field tuning. *Applied Physics Letters*, 115(12):122406, 2019. 22

[53] A Guedes, JM Almeida, S Cardoso, R Ferreira, and PP Freitas. Improving magnetic field detection limits of spin valve sensors using magnetic flux guide concentrators. *IEEE transactions on magnetics*, 43(6):2376–2378, 2007. 22

[54] M Pannetier-Lecoeur, L Parkkonen, N Sergeeva-Chollet, H Polovy, C Fermon, and C Fowley. Magnetocardiography with sensors based on giant magnetoresistance. *Applied Physics Letters*, 98(15):153705, 2011. 22

[55] SB Patil, A Guedes, PP Freitas, S Cardoso, V Chu, and JP Conde. On-chip magnetoresistive detection of resonance in microcantilevers. *Applied Physics Letters*, 95(2):023502, 2009. 22

[56] Myriam Pannetier, Claude Fermon, Gerald Le Goff, Juha Simola, and Emma Kerr. Femtotesla magnetic field measurement with magnetoresistive sensors. *Science*, 304(5677):1648–1650, 2004. 22

[57] Laure Caruso, Thomas Wunderle, Christopher Murphy Lewis, Joao Valadeiro, Vincent Trauchessec, Josué Trejo Rosillo, Jose Pedro Amaral, Jianguang Ni, Patrick Jendritza, Claude Fermon, et al. In vivo magnetic recording of neuronal activity. *Neuron*, 95(6):1283–1291, 2017. 22, 26

[58] Manon Giraud, François-Damien Delapierre, Anne Wijkhuisen, Pierre Bonville, Mathieu Thévenin, Gregory Cannies, Marc Plaisance, Elodie Paul, Eric Ezan, Stéphanie Simon, et al. Evaluation of in-flow magnetoresistive chip cell—counter as a diagnostic tool. *Biosensors*, 9(3):105, 2019. 22

[59] Fawaz Hadadeh, Aurélie Solignac, Myriam Pannetier-Lecoeur, Natalia Sergeeva-Chollet, and Claude Fermon. 3d magnetic imaging with gmr sensors. *IEEE Sensors Journal*, 19(22):10403–10408, 2019. 22

[60] Michel Julliere. Tunneling between ferromagnetic films. *Physics letters A*, 54(3): 225–226, 1975. 22

[61] Terunobu Miyazaki and N Tezuka. Giant magnetic tunneling effect in fe/al2o3/fe junction. *Journal of magnetism and magnetic materials*, 139(3):L231–L234, 1995. 22

[62] S Ikeda, J Hayakawa, Y Ashizawa, YM Lee, K Miura, H Hasegawa, M Tsunoda, F Matsukura, and H Ohno. Tunnel magnetoresistance of 604% at 300 k by suppression of ta diffusion in co fe b/ mg o/ co fe b pseudo-spin-valves annealed at high temperature. *Applied Physics Letters*, 93(8):082508, 2008. 23

[63] Chloé Chopin, Jacob Torrejon, Aurélie Solignac, Claude Fermon, Patrick Jendritza, Pascal Fries, and Myriam Pannetier-Lecoeur. Magnetoresistive sensor in two-dimension on a 25 μm thick silicon substrate for in vivo neuronal measurements. *ACS sensors*, 5(11):3493–3500, 2020. 26

[64] Francesca Barbieri, Vincent Trauchessec, Laure Caruso, Josué Trejo-Rosillo, Bartosz Telenczuk, Elodie Paul, Thierry Bal, Alain Destexhe, Claude Fermon, Myriam Pannetier-Lecoeur, et al. Local recording of biological magnetic fields using giant magneto resistance-based micro-probes. *Scientific reports*, 6(1):1–10, 2016. 26

Chapter 2

Magnetoresistive sensors

Contents

2.1 Introduction

This chapter presents the fabrication process of GMR sensors and the different studies to lower their limit of detection. The main objective is to have a sensor able to detect magnetic fields below nano Tesla range and ultimately in the order of pico Tesla, while taking into account the constraints of *in-vivo* applications. These constraints are to have a probe width in the order of 200 µm to minimize damages during insertion and a bio-compatible sensor with a surface of 50*50 μm^2 to allow insertion in the brain with a good spatial resolution.

This chapter is organized in five sections:

- The first section presents the fabrication of GMR sensor and the characterization methods.

Sections two to five present the results of the different studies realized on GMR sensors:

- The second section presents the impact of the width on the sensitivity, noise and limit of detection for yokes with an aspect ratio of 50:1 (cf fig. 2.1a).
- The third section introduces the impact of the composition layer and more precisely the impact of the NiFe thickness which is one component of the free layer which the CoFe layer and aims at determining both an optimal width and NiFe thickness (cf fig. 2.1a).
- The fourth section shows the comparison of the optimized GMR stack for yokes and meanders. Yokes are used to optimized GMR sensors in the laboratory while meanders are used for *in-vivo* recordings (cf fig. 2.1c).
- The fifth section summarizes the work made on GMR sensors deposited on top of another to increase the magnetic volume while keeping a small footprint. These sensors are called multi-GMR sensors (cf fig. 2.1d).

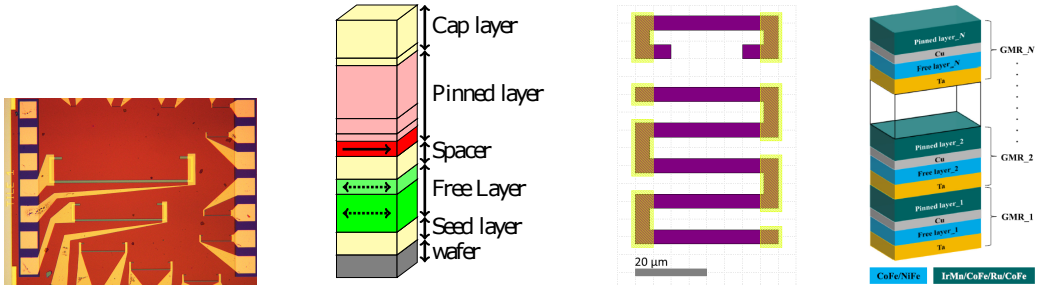

(a) Impact of width

(b) GMR composition.

(c) Yoke (top) Meander (bottom).

(d) Multi-GMR.

Figure 2.1: Illustration of the different studies presented in sections 2 to 5. (a) Yokes with different width w and length l =50*w. (b) GMR composition. The hard layer is in red and the free layer is in green.(c) Scheme of a yoke (top) and a meander (bottom). (d) Composition of a multi GMR with N GMRs.

2.2 Fabrication and characterization of GMR sensors

GMR sensors fabrication is made in the laboratory, from GMR stack deposition to sensors packaging. After fabrication, the sensor is characterized by magnetotransport and noise measurements and information about sensitivity, noise and limit of detection are extracted. These information are essential to compare GMR sensors and to improve their characteristics for *in-vivo* applications.

2.2.1 Fabrication

Wafer selection and GMR stack deposition

GMR sensors are deposited on various substrates depending on their application. There is a wide range of substrates like glass which is used because it is transparent, inert and it is an insulating material. Sapphire is strong and silicon allows to etch the substrate in various shape. Also silicon is used to develop Complementary Metal Oxide Semiconductor (CMOS) compatible devices and it is possible to integrate directly some electronics into the silicon wafer. In chapter 4, we will present a wafer of silicon with a layer of SiO_2in between two silicon layers which have interesting properties for *in-vivo* probes. It is a Silicon On Insulator (SOI) wafer. In this thesis, GMR stacks are deposited on a 270 µm thick silicon wafer with an insulating layer of 500 nm made of SiO_2.

The GMR stack deposition is made by sputtering (Rotaris deposition chamber from Singulus). Table 2.1 describes the composition of the GMR stack which is the most used in the laboratory. It will then be named reference stack.

Seed layer	Free layer		Spacer	Hard layer				Cap layer	
Ta	NiFe	CoFe	Cu	CoFe	Ru	CoFe	IrMn	Ru	Ta
3.00	5.00	2.10	2.90	2.10	0.85	2.00	7.50	0.40	5.00

Table 2.1: GMR reference stack composition with the thickness in nm.

Fabrication of GMR is based on photolithography process and needs 3 steps of fabrication:

- **Etching** to define the sensor shape
- **Contact deposition** to connect the GMR
- **Passivation** to protect the GMR

2.2.2 Step 1: Etching

As seen in chapter 1, to have a linear response, a magnetic anisotropy is imposed, perpendicularly to the hard layer's magnetization, to the free layer. There are several methods to induce such an anisotropy like shape anisotropy, adding an external magnet close to the GMR sensor or by weakly pinning the free layer thanks to an internal coupling with an anti-ferromagnetic layer. As these sensors are meant to be used for *in-vivo* experiments, the magnetic anisotropy is induced by shape anisotropy. Sensors

can be shaped as bars, yokes or meanders. The impact of the shape is studied in section 2.3.

Sensor shape definition The photolithography is realized in a clean room with a class 10 000. Clean rooms are classified depending on how clean the air is, and more precisely on the number of particles with a diameter ≥ 0.5 µm present in 1 ft^3 of air. A class 10 000 corresponds to less than 10 000 particles with a diameter ≥ 0.5 µm per ft^3 of air and a class 1 clean room has less than 1 particle per ft^3 of air. Our clean room is a class 10 000, it is sufficient to fabricate samples with low defects with an easy access to the clean room. When the class of the clean room is lower, the access conditions are more restrictive. To enter the clean room, the user needs to use gloves, hair cover, shoe covers and clean room garment to avoid skin flakes, hair or dust from user's garment or shoes to enter the clean room.

A photolithography step is decomposed is several sub-steps:

1. **Cleaning**: The sample is cleaned in an acetone bath with ultra-sound and the acetone is removed by an isopropanol bath, also with ultra-sound.
2. **Photoresist deposition**: A photoresit is used to define a pattern on the GMR layer like S1813 or S1818. It is a polymer resin which reacts towards UV light. A photoresist can either be positive or negative. When a positive photoresist is exposed to UV light, polymers are degraded and on the contrary, when a negative photoresist is exposed, polymers are strengthened by the light exposition. After exposition, the photoresist is washed away with a remover. In the case of a positive photoresist, only protected part stays after the remover part as the degraded polymers are washed away. It is the opposite for a positive photoresist, only the exposed photoresist stays after the development in a remover. The clean room part dedicated to lithography is protected from natural light by UV filtering to prevent photoresist reaction.
3. **Spin coating**: The photoresist is spin-coated on the sample to have an homogeneous distribution. The wafer is put on a platform and maintained by vacuum. The photoresist is deposited on the wafer surface, then the platform starts spinning. At the end of the spin-coating, the number of rotations per second increases to prevent an excess of photoresist on the edges of the wafer. This excess would lower the quality of the lithography by adding a space between the mask with the sensor's pattern and the sample. Finally, the sample is placed on a hot plate at 110°C during 3 minutes to evaporate the solvents.
4. **Exposure**: The sample with the photoresist is put in a mask aligner (MJB 4). A mask in quartz with a chromium pattern is inserted between the wafer and the UV light source. The maximum resolution we can achieve is 1 µm. When the mask is properly positioned, sample and mask are illuminated for a few seconds by a UV light.
5. **Developing**: Finally, the photoresist is removed by placing the sample in a basic solution called a remover. The remaining photoresist protects the GMR stack underneath. The sample is ready for etching. The lithography steps are schematized in fig. 2.2 for a yoke shape.

There are two more steps which are etching (for this step) and lift-off.

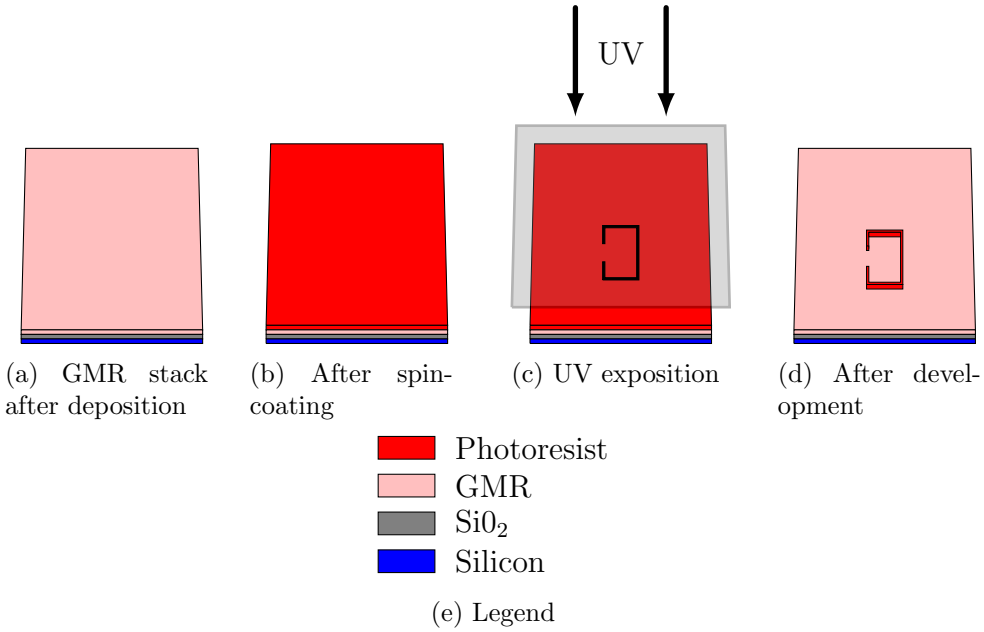

(a) GMR stack after deposition (b) After spin-coating (c) UV exposition (d) After development

(e) Legend

Figure 2.2: Optical lithography. (a) Scheme of a GMR stack (in pink) deposited on top of a silicon wafer (in blue) with an insulating layer (in grey). (b) A positive photoresist (in red) is homogeneously distributed by spin-coating. (c) A mask is positioned on top of the sample with a yoke structure. The sample is then illuminated with UV light. (d) After development, a yoke shape of photoresist protects the GMR stack beneath it.

Etching There are several types of etching including wet and dry etching. During wet etching, the wafer is immersed in a chemical solution (for example KOH), it is a chemical etching of silicon which can be either isotropic or anisotropic. For dry etching, the sample can be etched mechanically by the impact of high energy ions on the sample surface, this method is called Ion Beam Etching (IBE). A dry etching can also combine a mechanical and chemical actions by selecting chemical species which would react with the sample surface. It increases the etching speed and selectivity. A high selectivity means that some species (for example silicon) are etched when other material (for example SiO_2) present a much smaller etching rate.

Here, an IBE is used because the etchant is a beam of high-energy ions directed towards the sample, it is a universal etchant and thus it can etch multilayer like GMR stacks. IBE etching rates can be different depending on the material to etch. As the GMR stack thickness is around 30 nm, the etching process lasts only 24 minutes in our lab.

The unprotected part of the GMR layer is etched by an argon plasma at a pressure of 10×10^{-4} mbar. An argon gaz is used so the Ar atoms do not react with the sample surface but only have a mechanical action on the sample surface. A plasma is used to ionized the Ar atoms, then the ions are accelerated by grids and directed towards the sample. Finally, AR+ ions are neutralized to prevent any charging of the sample. The ar atoms transfer their momentum to the surface atoms which are then ejected from the sample. The wafer is rotated by 90° every six minutes to ensure an homogeneous etching of the GMR stack.

Lift-off After the etching, the photoresist is removed by an acetone and isopropanol cleaning. The sample is ready for contacts deposition.

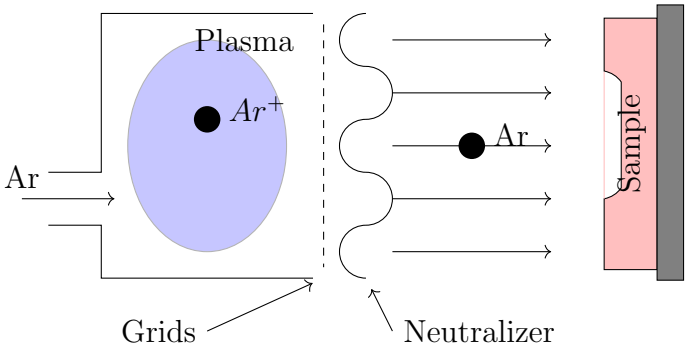

Figure 2.3: Ion Beam Etching

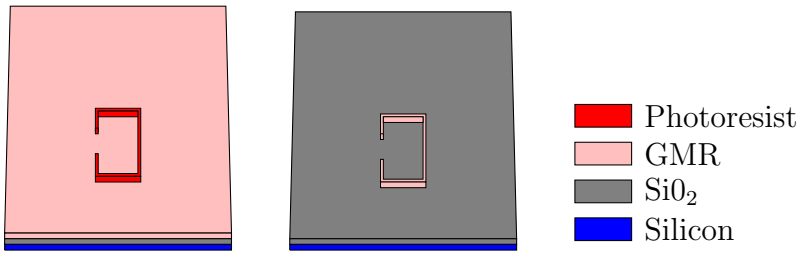

(a) Before etching (b) After etching and lift-off (c) Legend

Figure 2.4: After etching and lift-off, there is a yoke made of GMR stack (pink) on the substrate (grey).

2.2.3 Step 2: Contacts deposition

After the sensor patterning, contacts are deposited on the sample. There are several methods to deposit materials on a sample and in this fabrication process two methods are used: evaporation and sputtering. Contacts are deposited by evaporation and sputtering is used for passivation.

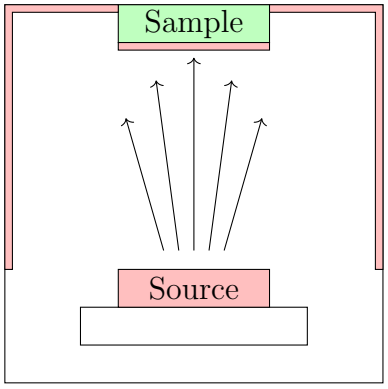

Figure 2.5: Evaporation

During evaporation (cf fig. 2.5), the sample is placed over the source material. The source material is heated by an electron beam under vacuum to increase the mean-free path of evaporated atoms which condensate on the substrate. To have an homogeneous deposition, the sample continuously rotates. Evaporation allows the deposition of material without a plasma but if the melting point of the material is too high or if an alloy needs to be deposited, then it is better to use sputtering techniques.

The deposition of contacts needs four steps (cf fig. 2.6):

1. **Photolithography**: contacts are patterned like GMR sensors with the difference that here we want to deposit material only in the unprotected area. To prevent any problem with the lift-off, the photoresist must be 3 times thicker than the contact thickness.

2. **Pre-etching**: the sample is etched by IBE during 30 seconds to clean the surface of the sample.

3. **Evaporation**: Contacts are made of a trilayer of Ti (15nm)/ Au (150nm)/Ti (15 nm). Ti is used to improve gold adhesion to the substrate and to improve passivation adhesion.

4. **Lift-off**: the sample is put in an acetone bath with ultra-sound. The photoresist will leave the sample with the deposited trilayer on top, leaving only the unprotected parts with contacts.

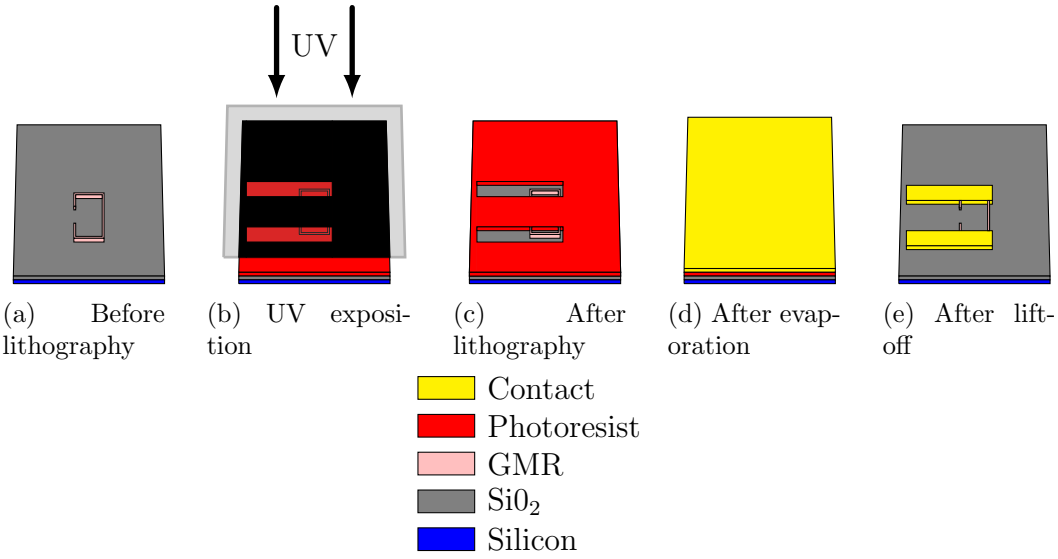

(a) Before lithography (b) UV exposition (c) After lithography (d) After evaporation (e) After lift-off

(f) Legend

Figure 2.6: (a) The sample is cleaned before lithography. (b) A mask with contacts patterns is used during UV exposition. (c) There are two holes in the photoresist (red) for contacts deposition. (d) A trilayer of Ti/Au/Ti is deposited all over the sample and the photoresist. (e) After lift-off, there is only Ti/Au/Ti on contacts area (yellow).

2.2.4 Step 3: Passivation

To avoid oxidation of the GMR sensor, a passivation layer is deposited on all the sample, except on contact pads. This passivation layer is a bilayer composed of Al_2O_3 (150 nm)/Si_3N_4 (150 nm). The alumina layer prevents any leakage between GMR sensor and contacts to the external medium and the Si_3N_4 layer ensures biocompatibility [1]. The bilayer has been previously optimized for *in-vivo* experiment.

An additional lithography step protects the contact pads from passivation deposition. The bilayer is then sputtered in two steps. First, Al_2O_3 is deposited directly on the sample from a target of Al_2O_3 as sputtering allows alloys deposition. It is similar to

IBE but here the material source is placed on the cathode, the sample is placed on the anode. The material source is bombarded by high energy ions and the ejected atoms from the target surface coat directly the sample.

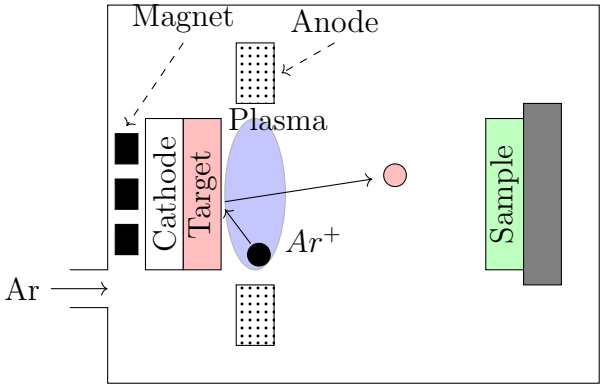

Figure 2.7: Sputtering

A magnetron is used to increase the deposition rate of the sputtering by trapping electrons close to the target with a magnetic field parallel to the target. This increases the probability of an ionizing collision between an electron and a gas atom (here argon atom). It increases the ion current density onto the target which is proportional to the erosion rate of the target and thus to the deposition rate. For conductive material, a DC sputtering is used, and for non conductive material, a RF sputtering is used instead to prevent any charging of the target material.

After the insulator deposition, the sample is immersed in acetone with an ultra-sound bath to remove the photoresist on the contact pad. The sample needs then to be cut and packaged.

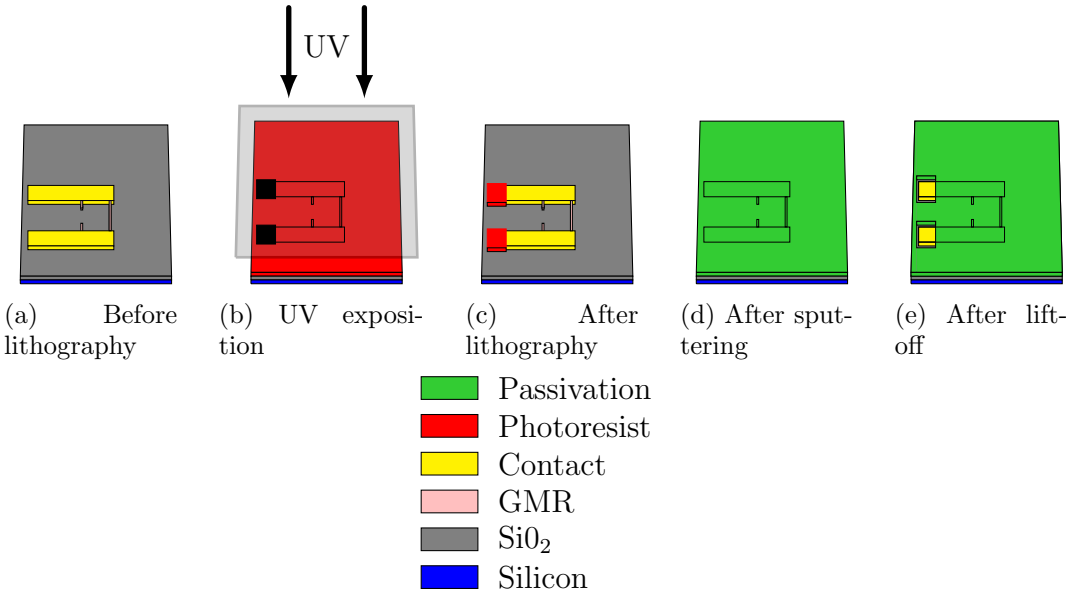

(a) Before lithography (b) UV exposition (c) After lithography (d) After sputtering (e) After lift-off

(f) Legend

Figure 2.8: Passivation steps: (a) The sample is cleaned before spin-coating. (b) During exposition a mask with passivation patterns is used. (c) After lithography, only the ends of contacts are protected to connect the sensor to a printed circuit board. (d) Passivation bilayer (green) is sputtered on all the sample. (e) After lithography, there is passivation on all the sample, except on contact pads.

Sample cutting and packaging

The fabrication process for GMR sensors designed for optimization is similar to the fabrication process of GMR sensors mounted on a probe for *in-vivo* experiments. The latter is called magnetrode and has a complex shape. GMR sensors are located on the probe's tip which is thinner than the probe's body. A thin tip allows to minimize damage during insertion in the brain and a thick body increases the robustness of the probe during manipulation. This particular process is described in chapter 3.

GMR sensors are designed for an easy and quick characterization. Several GMR sensors are grouped into dies (square of 20 mm^2 with around 10 GMR sensors) with their contact pads in the outside of the die for an easy wire bonding. A wafer have several dies which can be identical to have several sample of the same design and repeat the measurement on different sample or to have sensors which vary in size or design with the same GMR stack and fabrication parameters.

There are several methods to cut a wafer into several pieces and two of them were used:

- **Laser cutting** It allows to cut any form in the silicon wafer, it is a quick method but the edges are sloppy. There is an excimer laser in the laboratory with a wavelength of 193 nm (UV).
- **Dicing saw** This tool arrived later in the laboratory. It has a high positioning precision: 2 µm in X and Y direction and a rotation speed of 30,000 turns/min. It is a very quick and clean method but it can only cut straight lines.

Once the sample is cut into dies, they are micro-bounded on Quad Flat No-leads packages (QFN). A QFN connects integrated circuits to printed circuit board (PCB).

Dies contact pads are connected to QFN by micro-bounding with a 25 µm aluminum welded by ultrasound.

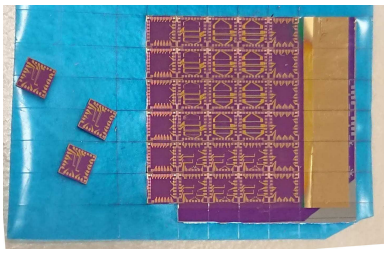

(a) Cut wafer with several dies

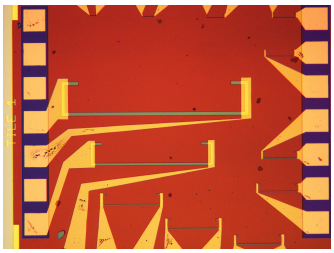

(b) Sample with several GMR sensors

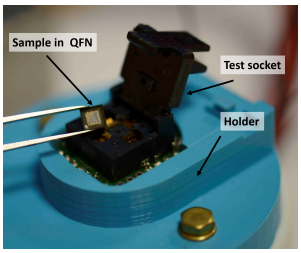

(c) Sample packaged in a QFN

Figure 2.9: ((a) Cut wafer with several dies ready to be packaged. The wafer is placed on a blue tape so that the saw cuts entirely the silicon wafer and 1/3 of the tape thickness. (b) Die with several yokes with the same aspect ratio (50:1) and different sizes. (c) Sample packaged in a QFN (square chip) ready to be mounted on a sample holder (photography by J. Moulin).

Using a QFN package allows to study GMR sensors more efficiently. A unique QFN holder is printed by a 3D-printer and hosts the QFN test socket. The test socket is wired for magnetotransport and noise measurements and, assuming that all dies have the same electronic design, to study another sample, only the QFN needs to be changed.

A summary with all fabrication parameters can be found in the annex A.

2.2.5 Characterization

To study a GMR sensor, two types of measurements are performed: magnetotransport measurements and noise characterization. The first one measures the response of a GMR depending on an external magnetic field, it is called R(H). It is mainly used to characterize the sensor sensitivity, MR ratio, linearity and saturating field. As we will see in the rest of this chapter, other characteristics are extracted from this measurement.

The second measures the noise of the sensor depending on the frequency. With an additional AC magnetic field, the sensitivity can also be extracted and one can compute the lowest magnetic field the sensor can detect, depending on the frequency. This is the limit of detection and we will see why it is an important feature of a GMR sensor.

R(H)

To measure the variation of resistance of the GMR sensor depending on the external field, the sensor is placed between two Helmholtz coils. They are powered by a current supply interfaced with a computer through an acquisition card driven by a home-made software based on Lazarus. The GMR sensor is powered by 1mA and the output voltage is filtered by a low-pass filter with a cutting frequency of 30Hz and amplified. A Standford Research (SR560) preamplifier is used for both the filtering and amplification. The output voltage is then sent to the acquisition card and the resistance of the sensor can be plotted as a function of the external field (fig. 2.10). This allows to extract R_0 the mean resistance, R_{AP} the resistance in the anti-parallel state, R_P the resistance in the parallel state, the MR ratio and the sensitivity.

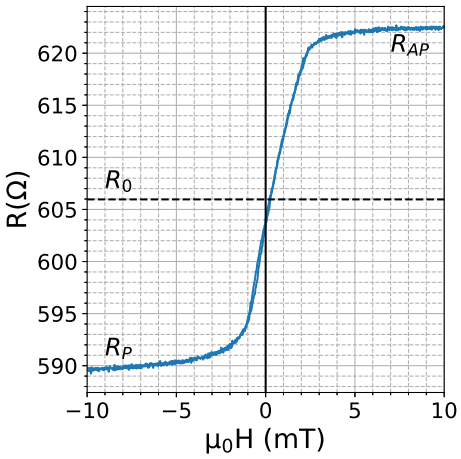

Figure 2.10: R(H) measurement

R_0, MR ratio and sensitivity are computed as follows:

$$R_0 = \frac{R_{AP} + R_P}{2} \tag{2.1}$$

$$GMR = \frac{R_{AP} - R_P}{R_0} \tag{2.2}$$

$$S = \frac{R_2 - R_1}{(R_2 + R_1)/2} * \frac{1}{H_2 - H1} = \frac{\Delta R}{\Delta H} \tag{2.3}$$

H1 and H2 are chosen close to zero-field and in the linear part of the R(H) curve. R1 (resp. R2) is the resistance associated to H1 (resp. H2). The characteristics of this sensor are: MR=5.5%, R_0=606 Ω and the sensitivity is 1.51 ± 0.08 %/mT. The sensitivity is computed in the linear part and around zero field (cf fig. 2.10). It is computed with H1=-0.2 mT and H2=0.2 mT.

Noise

During noise measurement, output voltage fluctuations are measured. The GMR is inserted in a Wheatstone bridge to suppress the DC component and center the fluctuations around 0V. The output of the bridge is amplified a first time by a low noise amplifier (LNA) INA 103 with a 500 gain. The signal is then amplified a second time with a 20 gain and filtered by an SR560 with a pass band filter (0.3 Hz-3 kHz). The whole set-up is placed inside a magnetic shielded room to avoid any external residual magnetic field (fig. 2.11).

The magnetic shielded room is made of mu-metal and aluminum layers. There are seven layers: 4 of mu-metal with a layer of aluminum between each layer of mu-metal (for total of 3 layers of aluminum). The aluminum layers act as a Faraday cage. Mu-metal is an alloy of nickel-iron with a very high permeability which allows to condensate the external magnetic field inside the walls, leaving a residual static magnetic field of 0.02 fT $/\sqrt{\text{Hz}}$ at 100 Hz inside the chamber, which is far below the sensor limit of detection.

To avoid any 50Hz contamination, the bridge is powered by an external battery and the INA 103 and the SR560 are powered on battery as well.

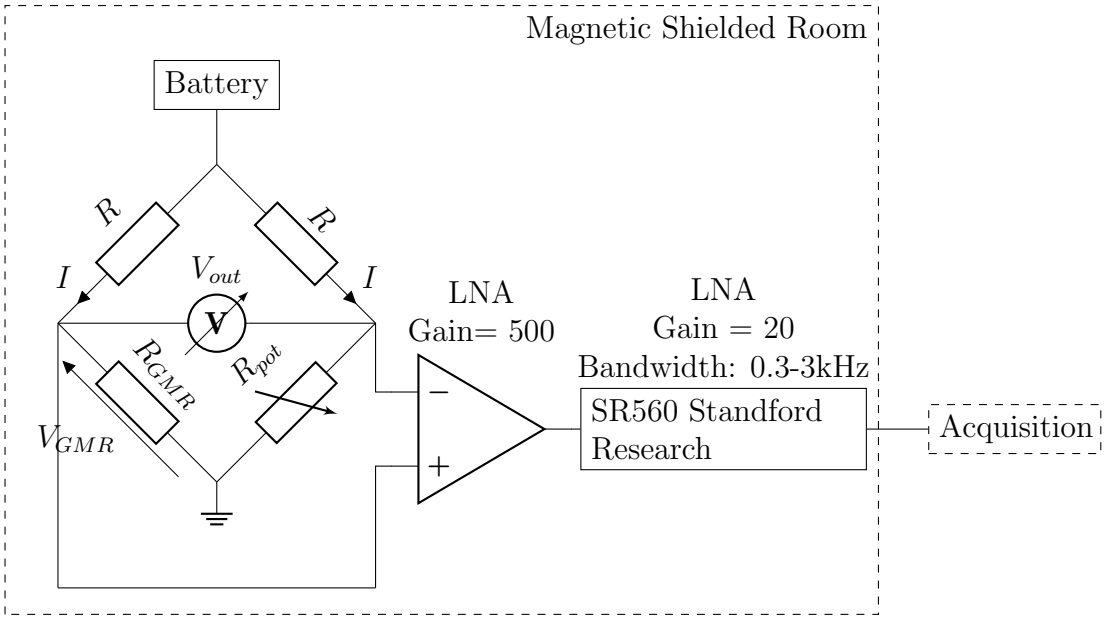

Figure 2.11: Noise set-up schematics.

The Wheatstone bridge is composed of four resistances:

- The GMR sensor (R_{GMR})
- A variable resistance to balance the bridge (R_{pot}).
- Two resistances with a low noise (R) and a high precision.

The bridge output is $V_{out} = V_{GMR} - V_{pot}$ and the battery delivers a voltage V.

By applying a voltage divider, we have:

$$V_{GMR} = \frac{R_{GMR}}{R + R_{GMR}} V \tag{2.4}$$

The resistances R of the bridge are higher than R_{GMR} to have a current I independent of any variation of R_{GMR} with the external field.

A Fourier transform is applied to the recorded signal. A typical noise measurement is shown in fig. 2.12a. At 0 V, there is only the thermal noise of the sensor and the acquisition chain then for V=0.5 V 1/f noise appears at low frequencies and one can see Random Telegraphic Noise (RTN) for V=1V. A coil placed around the sensor's holder is used to generate a calibration signal at 30Hz to compute the sensitivity and the limit of detection of the sensor. When the sensor is not powered, a small peak appears at 30 Hz. It comes from the coupling between the coil and the GMR sensor.

Sensitivity can be extracted with the following method:

1. The coil is powered with a current I of 10mA at a frequency of 30Hz. The coil is calibrated and for a current of 10mA a magnetic field with an amplitude of 850 nT RMS is generated.

2. The Wheatstone bridge is balanced and the output of the bridge is recorded after a first amplification by a low noise amplifier (LNA) with a gain of 500 then the

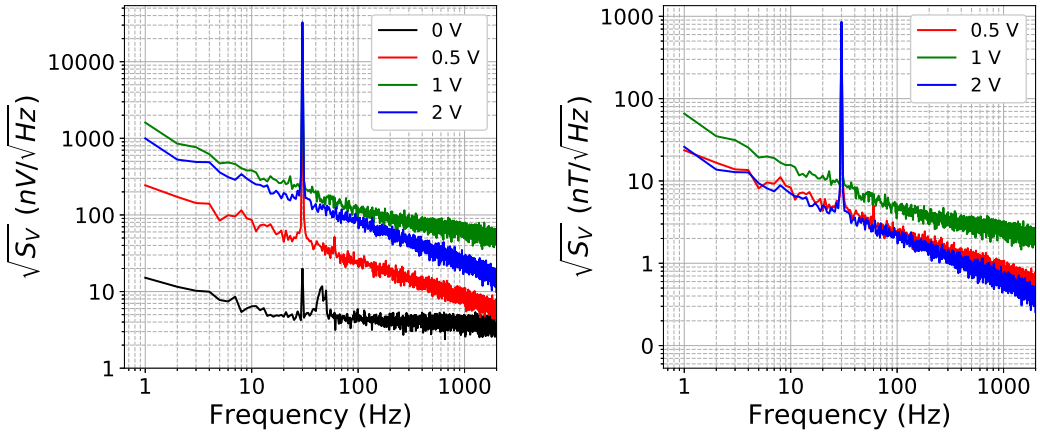

(a) Noise measurement

(b) Equivalent field

Figure 2.12: (a) Power spectral density as a function of frequency. (b) Equivalent field as a function of frequency.

signal is filtered with a pass-band filter in the frequency range: [0.3-3k Hz] and amplified for the second time by a gain of 20 by the SR560. Finally, the signal is recorded by an acquisition card.

3. The temporal data are then processed by a Fourier Transform to have the output voltage depending on the frequency and then divided by a factor $Gain_{LNA} * Gain_{Standford}$.

4. The value of the peak at 30 Hz is extracted and used to compute the sensitivity. The peak value (V_{peak}) is approximated on 1Hz to have a value in V instead of V/$\sqrt{\text{Hz}}$

$$S_{V/V/T} = \frac{V_{peak}}{V_{GMR}} . \frac{1}{H_{coil}} \tag{2.5}$$

with V_{GMR} the bias of the GMR sensor and $H_{coil} = 850$ nT RMS the amplitude of the magnetic field generated by the coil. The sensitivity is in V/V/T and we want to convert this sensitivity in %/mT:

$$S_{\%/mT} = S_{V/V/T} * \frac{100}{1000} \tag{2.6}$$

The limit of detection (LOD) or the lowest magnetic field the sensor can detect is computed as follows:

$$LOD = \frac{Noise}{Sensitivity} \tag{2.7}$$

The noise curve (fig. 2.12a) is multiplied by $\frac{H_{coil}}{Peak_{30Hz}}$ to have the equivalent field as a function of frequency (fig. 2.12b). The LOD is then extracted on a bandwidth of 1 Hz. The problem of the difference between sensitivity computed by R(H) and by noise is addressed later.

In conclusion, we have seen how to fabricate a GMR sensor and how to characterize it. Now, we will see what the characteristics of optimized sensors are.

2.2.6 An optimized sensor

In order to detect a very low magnetic field, a sensor needs to respect some requirements which are to be linear and centered around zero field with no or a negligible hysteresis and to have a low noise and high sensitivity to reach a low limit of detection. We will introduce how sensitivity can be impacted by offset and hysteresis, then we will present strategies to reduce the sensor's noise and finally see the impact of both sensitivity and noise on the limit of detection.

Sensitivity

When the sensor is linear, well centered and with no hysteresis the sensitivity can be defined by:

$$S = \frac{GMR}{2\mu_0 H_A} \tag{2.8}$$

with GMR, the MR ratio in % and $2\mu_0 H_A$ the anisotropy field in mT. The anisotropy field is the width of the linear part, extended until it crosses the saturated state (cf fig. 2.13a).

When there is an hysteresis like in 2.13b, depending on the magnetic history, the sensor can have two different sensitivities (one branch of the hysteresis is well centered and has a higher sensitivity than the other branch which is in the transition zone between linear part and saturation).

If a sensor exhibits an offset which pushes the linear part away from zero field then the sensor sensitivity decreases and can be close to zero as we can see in fig. 2.13c. So in

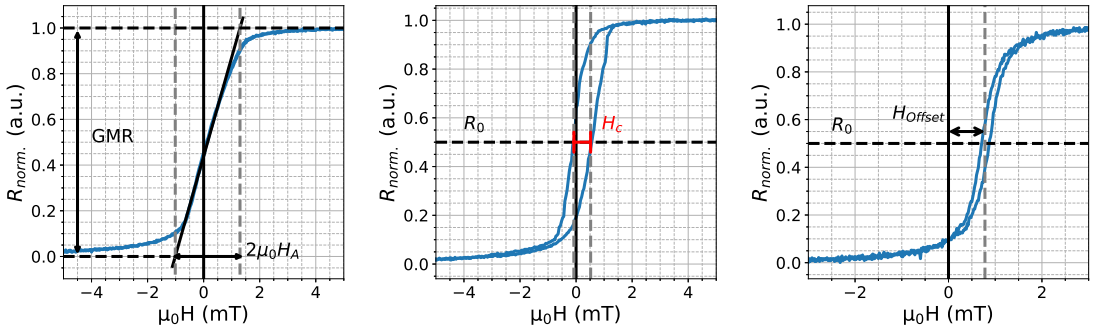

(a) without hysteresis or offset (b) with hysteresis (c) with hysteresis and offset

Figure 2.13: Magnetotransport curve of GMR sensor with and without defects. The curves are experimental curves with the resistance normalized between 0 and 1.

order to have a sensor with an optimized sensitivity, the GMR response needs to be well centered (no offset) and to have no or a negligible hysteresis. Then the sensitivity can be increased by increasing MR ratio or decreasing the anisotropy field.

Noise

As mentioned in chapter 1, GMR sensors exhibit two main noises: thermal noise and 1/f noise. We will see the strategies to decrease thermal noise and then 1/f noise.

Thermal noise can be decreased by either lowering the temperature or decreasing the sensor's resistance.

$$\sqrt{S_{V,th}} = \sqrt{4.k_b.T.R} \tag{2.9}$$

Sensors are designed for *in-vivo* application and more precisely for insertion into the brain so T is around 37 °C which is equivalent to 310 K. the resistance can be decreased to reduce thermal noise but if the resistance is too low then two aspects must be taken into consideration:

- First the output voltage of the sensors has to be higher than the noise of the acquisition chain, so we can have a high Signal to Noise Ratio (SNR). The electronics noise should be lower than the sensor noise.
- Second, according to Ohm's law: $U = R.I$ and the power generated by sensor is $P = U.I = R.I^2$ Therefore, to have a sufficient output voltage, GMR sensors need to be powered by an important current. This heats the GMR sensor by Joule effect and can have an impact on the surrounding medium as we will see in chapter 4 and increases the consumption of the sensor.

Therefore the sensor resistance is chosen around 700 Ohms, which leads to a thermal noise at operating temperature of 3.5 nV.

1/f noise can be decreased in several ways, including by increasing the GMR sensors volume by either increasing its length or width or by depositing several GMR stacks on top of each other (cf 2.6).

$$\sqrt{S_{V,1/f}} = \sqrt{\frac{\gamma}{n_c.Volume.f}}RI \tag{2.10}$$

This can have unwanted impacts on MR ratio, sensitivity, resistance, offset, hysteresis and saturating magnetic field [2]. As we will see in section 2.3 there is a compromise between sensitivity and noise related to the sensor's width. The superposition of GMR stack on top of another, depending on the width and the number of stacks (section 2.6), also have an impact both on sensitivity and noise.

Signal to noise ratio (SNR) is the ratio between the measured signal and the noise of the sensor. To be able to do a recording, SNR must be > 1. For a GMR sensor we have:

$$SNR = \frac{V}{N} = \frac{\Delta R.I}{\sqrt{4.k_b.T.R.\Delta f + \sqrt{\frac{\gamma.\Delta f}{N_c.V.f}(RI)^2}}} \tag{2.11}$$

With V the output signal, N the noise on the bandwidth Δf and ΔR the resistance variation of the GMR sensor for the measured magnetic field. When 1/f noise is dominant, both the output signal and the noise increase with I. When the thermal noise is dominant, only the output signal increases with I and the SNR is increased, leading to a higher quality recording as the output signal amplitude can be several times higher than noise amplitude.

Limit of detection

We have seen previously that the lowest magnetic field a sensor can detect is characterized by the limit of detection and that the limit of detection is the noise divided by sensitivity. Thus to have a lower limit of detection the sensitivity needs to be increased and/or the noise needs to be decreased. Otherwise, if the sensitivity and the noise are both increased or decreased, it is difficult to have a huge impact on the limit of detection to be below the nT range. In the next sections we will investigate different strategies to lower the limit of detection.

2.2.7 Conclusion

As seen previously, changing one parameter (width, composition, etc.) may have an impact on both noise and sensitivity and in the rest of this chapter we will try to find a compromise between sensitivity, noise, offset, hysteresis, etc. to reach the lowest limit of detection that a GMR sensor can achieve at low frequencies and determine if GMR sensors are the right tools for recording unique *in-vivo* action potential.

2.3 Impact of width

The shape of the sensor can have multiple impacts on the sensor properties like sensitivity, noise and limit of detection. As mentioned previously, the sensitivity can be increased by lowering the anisotropy field H_A which depends on the width of the sensors. The impact of the width on noise and limit of detection is also presented.

2.3.1 Anisotropy field

The anisotropy field comes from magnetic anisotropy interactions which have contributions from bulk, interfaces and surfaces [3]. It can be expressed as:

$$\mu_0 H_A = \frac{2K_{eff}}{M_s} \tag{2.12}$$

with $\mu_0 H_A$ the anisotropy field in T, K_{eff} the effective magnetic anisotropy in Jm^{-3} and M_s the saturation magnetization in Am^{-1}.

2.3.2 Magnetic anisotropy

The magnetic anisotropy defines the tendency of a ferromagnetic or antiferromagnetic axis to lie in a fixed direction called easy-axis [4]. Magnetic anisotropy has three main origins which are:

- **Magnetocrystalline anisotropy** which arises from the crystal structure (spin-orbit interaction)
- **Shape anisotropy** which comes from the sample shape and the associated demagnetizing field
- **Induced anisotropy** which is originated partly from atomic or micro-scale structure of the sample or applied stress on the sample.

The effective magnetic anisotropy constant can be described by the contribution of volume, surface and interfaces.

Here, we will consider only the volume contribution from magnetocrystalline anisotropy and shape anisotropy (which is also called magnetic dipolar anisotropy). As we are interested in the impact of the width on the anisotropy field, we separate the dipolar anisotropy contribution from the others, leading to the following equation:

$$K_{eff} = K_{v'} + K_d \tag{2.13}$$

with K_d, the volume contribution of shape anisotropy and $K_{v'}$ the volume contribution from other magnetic anisotropies. For a thin film K_d can be expressed as [5]:

$$K_d = \mu_0 \frac{M_s^2 t}{2w} \tag{2.14}$$

With t the layer thickness and w the width of the sample. By injecting 2.14 in 2.12, the anisotropy field $\mu_0 H_A$ is described by:

$$\mu_0 H_A = \mu_0 H_{v'} + \frac{\mu_0 M_s t}{w} \tag{2.15}$$

From 2.15 one can see that $\mu_0 H_A$ is inversely proportional to w. As a result, by considering only the impact of shape anisotropy, the sensitivity is intended to be proportional to the width:

$$S \propto GMR * \frac{w}{2\mu_0 M_s t} \tag{2.16}$$

As the sensitivity is proportional to the width, we will study GMR with a yoke shape and width from 1 µm and up to 30 µm to study its impact on the sensitivity and verify that we increase the sensitivity of our GMR sensor by decreasing the anisotropy. We will also investigate the impact of the width on the hysteresis and on the offset as offset limits the sensitivity and hysteresis can create magnetic instabilities in the sensor. The relation between noise and width is also examined as an increase of width leads to an increase of volume and thus we can expect to decrease the 1/f noise. Finally, the impact on the limit of detection is presented and we expecte to have a lower limit a detection for an increased width as both the sensitivity should increase and the 1/f noise should decrease.

2.3.3 Experimental results

We will first see the impact of width on the sensitivity, then we will investigate the effect on the GMR sensor's noise and finally the influence on the limit of detection to determine if there is an optimal width for the sensor's pattern.

Sensitivity

As expected, the MR ratio is constant and the slope of the linear part steepens. The results on yoke with an aspect ratio of 50:1 and width from 1 µm to 30 µm are shown in fig. 2.14. For a width of 30 µm the characteristics are similar to unpatterned thin film response.

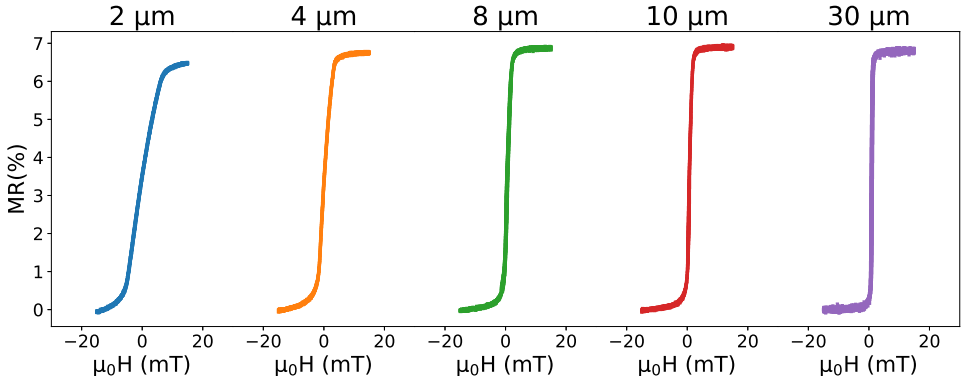

Figure 2.14: R(H) for yokes with various width (w=2 to 30 µm), the length being l=50w.

From fig. 2.15, we can see that the sensitivity increases with the width, as expected. However, the sensitivity is different if the external magnetic field goes from -5 mT to 5mT (*ie* from the parallel state to the antiparallel state) or from 5 mT to -5 mT (*ie* from the anti-parallel sate to the parallel state). The parallel state is referred to as P state and the anti-parallel state as AP state.

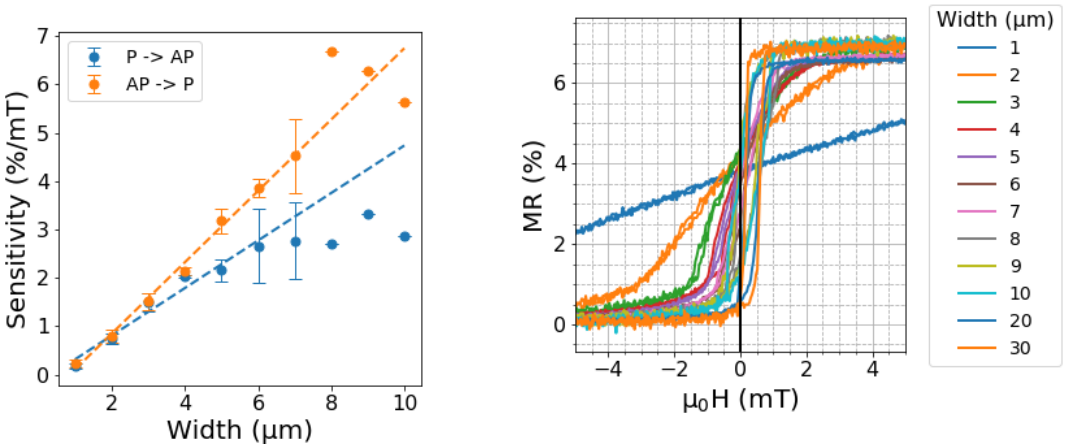

(a) Sensitivity vs width

(b) Magnetotransport curves for samples with different width.

Figure 2.15: (a) Sensitivity as a function of the external magnetic field. For each magnetic history, the sensitivity is fitted with a linear regression. (b) R(H) for yokes with an aspect ratio of 50:1.

The sensitivity plot can be separated in three zones:

- **Width≤3 µm** the sensitivities are similar for each configuration
- **4≤Width≤6 µm** the sensitivities are different but both increase with the width
- **Width≥7 µm** the sensitivity computed when the free layer rotates from P state to AP state starts to decrease.

This phenomenon can be explained by the hysteresis and the offset. The hysteresis implies that the sensitivity is computed for both branches with the free layer in different states, which explains that sensitivities are different for 4 ≤ Width ≤ 6 µm.

When the width is superior to 7 µm, the offset (in addition to the hysteresis) pushes the linear part of one branch of the hysteresis away. The curve foot is in the zero-field region which decreases the sensitivity despite a curve with a steeper linear region.

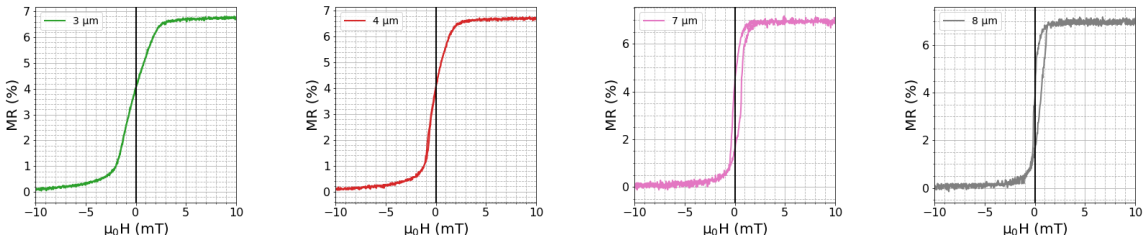

(a) Width = 3 µm (b) Width = 4 µm (c) Width = 7 µm (d) Width = 8 µm

Figure 2.16: R(H) for different yokes with different widths and an aspect ratio of 50:1.

Noise

The noise is then measured and results are plotted in fig. 2.17.

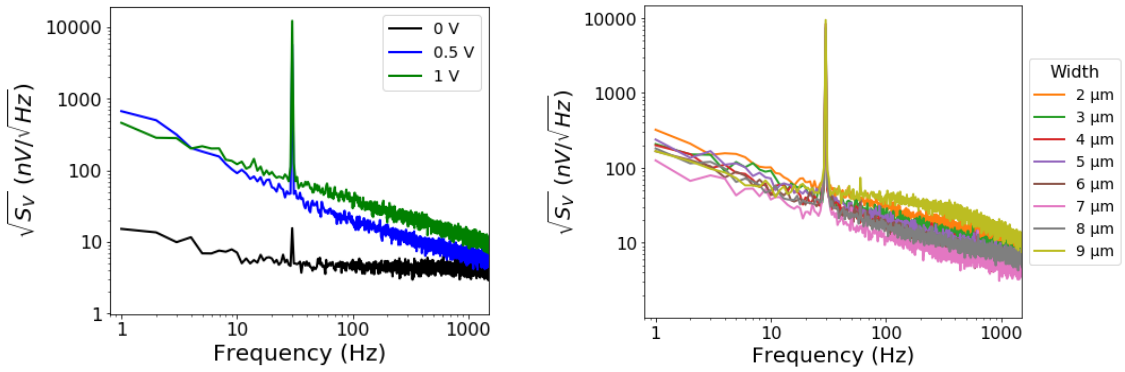

(a) Width=4µm (b) V_{GMR}=0.5V

Figure 2.17: Noise (a) for a given GMR sensor at different voltages. The noise increases with the voltage as 1/f noise is dominant. There is no RTN at 4 µm. (b) at a given voltage for different widths. From 2 µm to 7µm there is no RTN at 1 kHz. RTN arises for 8 µm and 9 µm which increases the noise.

The GMR sensors exhibit 1/f noise and sometimes RTN. For each width, the noise at 1kHz is extracted as well as the sensitivity. These results are plotted in fig. 2.18. The frequency of 1kHz is chosen because it is in the frequency range of interest for *in-vivo* application. The frequency corner of our GMR sensors for a voltage superior to 0.5 V is around a few kHz. As we have seen before, the 1/f noise depends on the applied voltage. To have a sensor noise independent from the applied voltage around 1kHz, we would need a sensor with a corner frequency lower than 1kHz. In this case, the thermal noise is dominant and it does not depend on the applied voltage, thus allowing us to increase the signal to noise ratio by increasing the voltage.

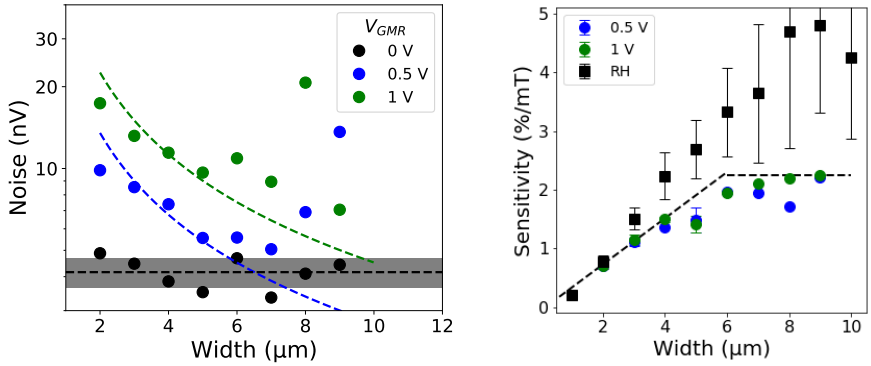

(a) Noise at 1kHz. (b) Sensitivity

Figure 2.18: (a) Noise at 1kHz as a function of width. The y-axis is plotted with a log scale. The 1/f noise decreases until a width of 6 µm. Then the presence of RTN increases the noise. For a voltage of 0.5V, the thermal noise should have been reached for w $\geq$ 6 µm without RTN. (b) Comparison of sensitivity computed from R(H) or noise measurements.

By increasing the width and therefore the sensor volume, one can expect to lower 1/f noise by a factor $1/w$. Indeed, increasing the width has an impact on the volume V=l*w*h=50*w*w*h. The volume only increases with w because of the aspect ratio (l=50w) and the composition of the GMR is the same for all the samples so h is constant.

The data on fig. 2.18 are fitted with a function f(w)=a/w and one can see that the noise tends to decrease. However, for w$\geq$ 8 µm there are a discrepancy because of the presence of RTN. Therefore, increasing the width is interesting to reduce 1/f noise as long as there are no RTN.

By comparing the sensitivity computed by R(H) and noise measurements, one can see that up to a width of 3µm, the sensitivity extracted with the noise set-up is similar to the mean sensitivity on each branch of the hysteresis. For the sake of simplicity, the difference of sensitivity for each branch of the hysteresis is symbolized by the error bar. One can differentiate two parts:

- Up to a width of 3 µm, the mean sensitivity of each branch is similar to the sensitivity computed by noise measurement for each voltage.
- For a width of 5 µm or 6 µm, the sensitivity is a bit lower than expected from a fit on sensitivity from 2 µm to 4 µm.
- For a width superior or equal to 4 µm, the noise computed sensitivity is close to the lowest sensitivity computed by R(H).

Also, up to 6 µm, the sensitivity increased linearly and for w $\geq$ 6 µm, the sensitivity reaches a plateau.

Limit of detection

As we can see in fig. 2.19a, the limit of detection decreases with the width up to 5 µm. Up to 5 µm, the limit of detection can be fitted by the function f(w)=a/(w^2). For 6 µm and 7 µm, the data and the fit are different because the sensitivity reaches a plateau. At 5 µm and for w > 8 µm, there is RTN because the free layer is no longer stabilized by the shape anisotropy.

The limit of detection can reach a value as low as 200 pT for a width of 9 µm. However, at such a width, the sensor exhibits RTN which prevents this sensor from being used for *in-vivo* neuronal magnetic recording. Indeed, the sensor needs to be stable to realize a recording with a good quality with the possibility to be averaged.

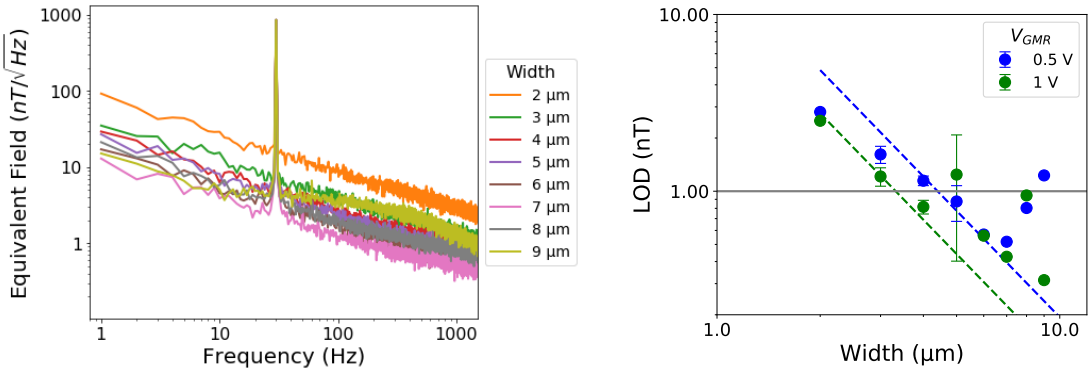

(a) $V_{GMR} = 0.5V$ (b) Limit of detection at 1kHz

Figure 2.19: Limit of detection (a) for a voltage of 0.5 V (b) Limit of detection at 1kHz depending on width and voltage

Conclusion

In conclusion, shape anisotropy plays an important role for stabilizing the free layer. When the shape anisotropy is strong, the free layer is stable (no RTN) but it has a low sensitivity. When the shape anisotropy decreases, the sensitivity increases until it reaches a plateau. The sensitivity is then independent from the sensor width until the hysteresis and offset shift completely the linear part from zero-field and thus become the limitation factors of the sensitivity. As long as the free layer is stabilized by the shape anisotropy, the noise decreases with the 1/f noise until it reaches the thermal noise. When the free layer is no longer stabilized by the shape anisotropy, RTN appears and increases both the noise and the limit of detection.

The optimal width is a compromise between sensitivity and RTN. For this GMR stack, the optimal width is 4 µm for a sensitivity of 1.5%/mT, a limit of detection below 1 nT without RTN. The reference stack needs to be optimized to prevent RTN at higher width and allows to have sensors that reach higher sensitivity and lower noise without RTN.

2.3.4 Other linearization techniques

As mentioned previously, to have a linear response, the free layer magnetization must be perpendicular to the reference layer magnetization when there is no external field. To achieve this, several techniques are available [6] (cf fig. 2.20) like using the shape anisotropy to force the magnetization of the free layer parallel to the length of the sensor like in the previous section (sec. 2.3). Then an annealing is used to reorient the hard layer magnetization. The perpendicular configuration of magnetization directions of the free and hard layer is called crossed anisotropy.

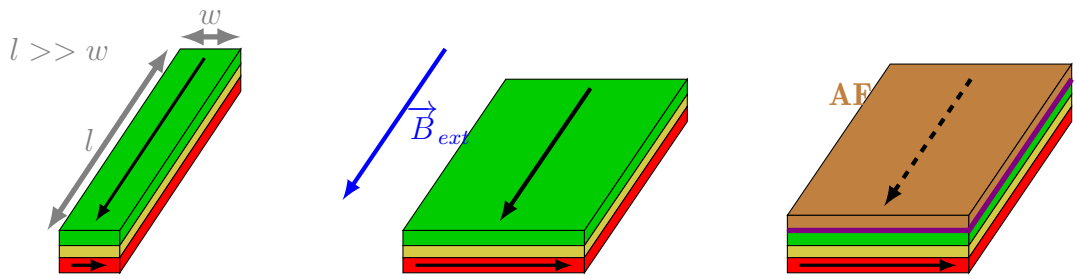

(a) Shape anisotropy (b) External pinning (c) Pinned free layer

Figure 2.20: Three techniques to fix the free layer magnetization at zero field. The free layer is in green, the spacer in yellow and the reference layer in red. The magnetization direction of the free and the hard layer are represented by black arrows. (a) The shape anisotropy forced the free layer magnetization along the length of the sensor. (b) An external magnetic field (magnet, current line, ...) is used to orient the free layer magnetization. (c) An anti-ferromagnetic layer (in brown) is deposited on top of the free layer with a non-magnetic spacer (in violet) in between. The strength of the RKKY-like coupling depends on the spacer thickness.

A second way is to apply a pinning field either externally, with a coil or a permanent magnet, or by an internal coupling. The strength of the internal coupling is then controlled by an RKKY-like coupling and tuned with the thickness of a spacer inserted between the ferromagnetic and the anti-ferromagnetic layers composing the free layer.

A second annealing is then needed to orient the free layer pinning at 90 ° from the magnetization of the reference layer.

The pinning field of the free layer can be optimized to decrease the magnetic noise due to 1/f magnetic part and RTN faster than the sensitivity leading to an optimal limit of detection increased by a factor up to 10 as it has been shown in the laboratory [7]. By increasing the pinning field, the magnetic domains are stabilized, leading to a lower magnetic noise but it also decreases the sensitivity as the anisotropy field increases. There is an optimum for a pinning field of a few mT which varies with the GMR composition.

2.3.5 Conclusion

In conclusion, there are several ways to have a spin-valve with a linear response. We are working with the shape anisotropy induced by the self-demagnetizing field (also called dipolar field) to force the free layer magnetization direction perpendicularly to the reference layer magnetization direction.

The shape anisotropy varies with the width of the GMR sensor and it has an impact on the sensitivity, noise and limit of detection. The optimal width is the width with the lower limit of detection and no RTN (4 µm from the previous measurements). However, the limit of detection can be decreased by stabilizing the magnetic domains of the free layer responsible for RTN. In order to achieve this goal and have GMR sensor without RTN, the composition of the free layer is studied and in particular the thickness of the NiFe layer.

2.4 Free layer composition

In order to reduce RTN and increase the sensor stability, we choose to work on the free layer composition to stabilize the magnetic domains. The objective is to reach an homogeneous magnetization of the free layer and a minimal hysteresis for a width w $\geq$ 4 µm. The RTN comes from fluctuations of magnetic domains, by stabilizing them the RTN is reduced. The diminution of the hysteresis increases the stability of the GMR sensor as the sensitivity is independent from the sensor's magnetic history.

As mentioned earlier, the free layer is a bi-layer of NiFe and CoFe. The CoFe layer has a higher coercivity than NiFe but it also has a higher spin polarization which leads to an increased MR ratio. The NiFe layer has a low coercivity which reduces the hysteresis. To reduce RTN by reducing the hysteresis, we studied the impact of several NiFe thicknesses between 0 and 15 nm. The CoFe thickness does not change (t_{CoFe}=2.10nm).

First, we will study the impact of the NiFe thickness on MR ratio and linearity, then we will investigate the impact on the noise and limit of detection. Finally, we will conclude on an optimal thickness for the realization of our *in-vivo* probe.

2.4.1 Magnetotransport measurement

To study the impact of NiFe thickness, several GMR stacks are deposited in addition to the reference stack and patterned following the fabrication steps described in section 2.2. They are shaped into yokes with an aspect ratio of (50:1) to keep a resistance around 700 Ω for a width between 1 µm to 30 µm. For this study, we used seven stacks with a composition described in table 2.2 and we measured for each stack 10 yokes with widths from 1 µm to 20 µm.

Seed layer	Free layer		Spacer	Hard layer				Cap layer	
Ta	NiFe	CoFe	Cu	CoFe	Ru	CoFe	IrMn	Ru	Ta
3.00	x	2.10	2.90	2.10	0.85	2.00	7.50	0.40	5.00

Table 2.2: GMR composition (in nm) with x= 0, 5 (reference layer), 6.3, 7.5, 8.8, 10 and 15 nm.

Impact on sensitivity and hysteresis

In fig. 2.21, sensitivity and hysteresis are plotted as a function of width and NiFe thickness from 0 nm to 15 nm. The sensitivity has an optimum for a NiFe thickness of 6.3 nm and a width of 9 µm. The hysteresis is lower for a NiFe thickness greater than 5 nm. We decided to realize an analysis on NiFe thickness between 5.0 nm and 8.8 nm to study GMR stacks with a low hysteresis and a reasonable sensitivity ($>$ 1%/mT).

Comparison of R(H) of GMR stack width NiFe thickness between 5 nm and 8.8 nm.

Fig. 2.22, compares R(H) measurement depending on the GMR stack and width. For a width of 4 µm, the hysteresis is small, independently from NiFe thickness. The MR is similar for the thicknesses t_{NiFe} = 5 nm and 6.3 nm, but for t_{NiFe} = 7.5 nm and 8.8 nm the MR is lower NiFe is a conductive material and by increasing its thickness

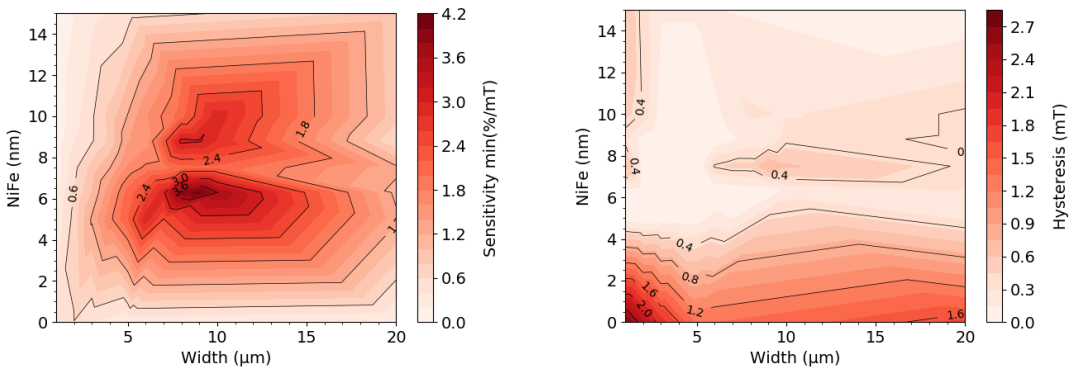

(a) Sensitivity (b) Hysteresis

Figure 2.21: Colormap of (a) Sensitivity from R(H) (lower estimation cf fig. 2.22) and (b) hysteresis as a function of width and NiFe thickness.

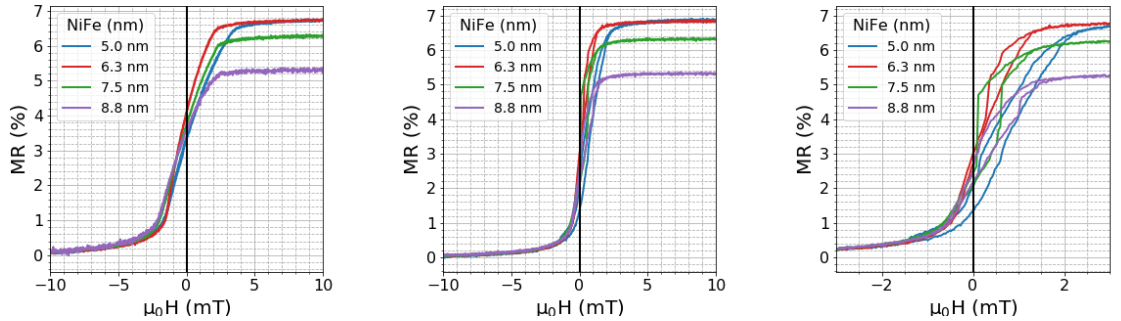

(a) Width = 4 µm (b) Width = 8 µm (c) Width = 8 µm (zoom)

Figure 2.22: (a) R(H) plots for a width of 4 µm. (b) R(H) plots for a width of 8 µm and (c) is the same figure zoomed around zero-field.

the resistance of the GMR stack is lower. It has an impact on the MR as some spin polarized electrons are only transported through the NiFe layer and do not cross the spacer and the reference layer. Thus, these electrons do not participate to the GMR effect which decreases the MR ratio (cf fig. 2.23 and table 2.3).

For a width of 8 µm, the reference stack ($t_{NiFe} = 5$ nm) exhibits hysteresis. For higher thickness, the hysteresis is decreased but jumps appear along the R(H) curve. Also, the linearity for $t_{NiFe} > 5$nm is degraded. Because of the presence of hysteresis and sudden changes of resistance in R(H) curve, it can be difficult to estimate the sensitivity from R(H) curve.

t_{NiFe} (nm)	MR (%)	R_0 (Ω)
5.0	6.8 ± 0.0	733.0 ± 18.3
6.3	6.7 ± 0.1	688.0 ± 16.1
7.5	6.1 ± 0.2	644.6 ± 17.4
8.8	5.1 ± 0.0	608.1 ± 15.4

Table 2.3: MR and R_0 values depending on the NiFe thickness for yokes with a width between 3 µm and 30 µm. The yokes have an aspect ratio 50:1 to ensure a resistance value around 700 Ω.

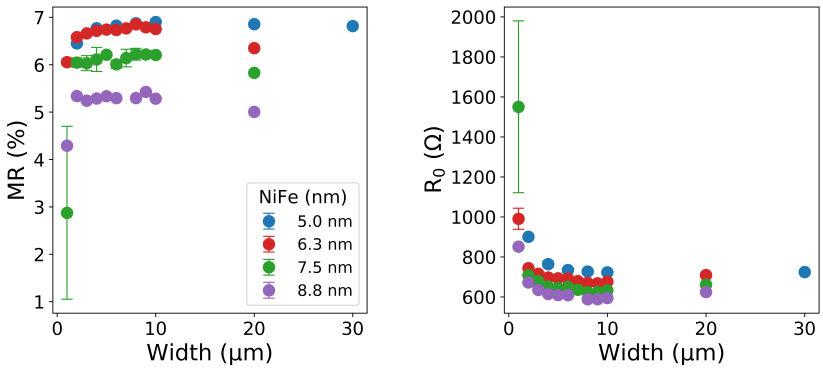

(a) MR (b) R_0

Figure 2.23: MR ratio and R_0 depending on the width and NiFe thickness. Yokes have a constant aspect ratio to have a resistance around 700 Ω independently from the sensor size. At lower width, defaults from the fabrication process can have a high impact on the resistance.

In fig. 2.23 the MR ratio and the resistance are plotted as a function of the GMR stack and sensor width. The MR ratio and resistance are averaged for each stack and for widths $\geq$ 3 µm in table 2.3. The MR ratio and resistance are independent from the sensor size and any variation for width $\leq$ 2 µm are assumed to come from the fabrication process or because the field used to saturate the GMR sensor for R(H) measurement is not sufficient (cf fig. 2.24). When the NiFe thickness increases by 1 nm, R_0 is decreased by around 32 Ω. GMR stack with NiFe thickness 5.0 nm , 6.7 nm and 8.8 nm were processed at the same time and for an increase of 1 nm, the MR is decreased by around 0.53 %. For a NiFe thickness of 5.0 and 6.3 nm the MR ratio is similar (6.8 % and 6.7 % respectively).

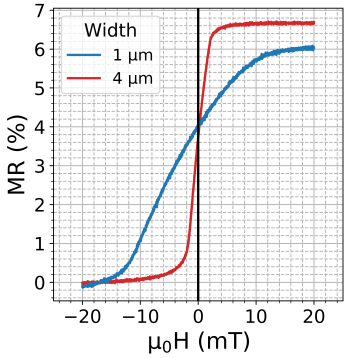

Figure 2.24: R(H) curves for yokes with an aspect ratio of 50:1. The GMR stack has a NiFe thickness of 6.3 nm. For a width of 1 µm, the AP state is reached for H≈15mT but the P state is not fully attained. Thus the computed R_P is underestimated . To reach the P state, a higher external field amplitude is needed. On the contrary, for a width of 4 µm, both AP and P states are reached, thus the true MR can be computed.

The MR is slightly lower for small sizes because the saturating field in P and/or AP state is not reached during R(H) measurement as seen in fig. 2.24.

2.4.2 Noise measurements

To study the impact of the NiFe thickness on the RTN, 1/f noise and the limit of detection, the power spectral density, for each stack and for width from 1 to 10 µm are measured.

Sensitivity comparison

By comparing sensitivity computed from noise and R(H) measurements, we can see that up to a width of 5 µm, both sensitivities are similar (fig. 2.25). The sensitivity measured by the noise is lower than the one measured by magneto-transport measurement for a width $>$ 5 µm. This can be explained by the apparition of the hysteresis when w increases. The curve presents jumps centered at zero-field which can artificially increase the sensitivity measured from a R(H) curves.

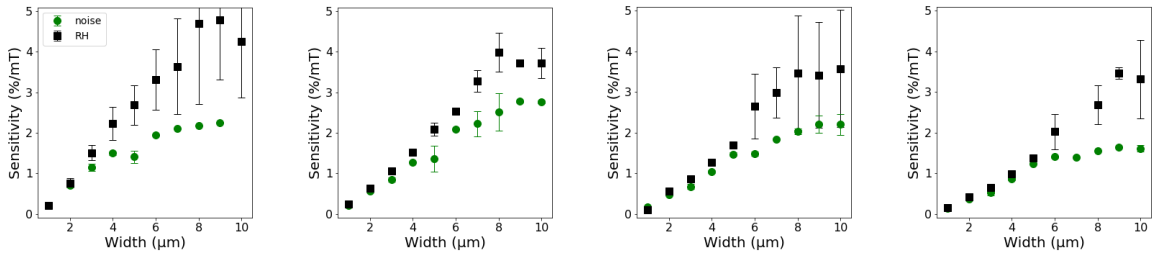

(a) t_{NiFe} = 5 nm (reference stack) (b) t_{NiFe} = 6.3 nm (c) t_{NiFe} = 7.5 nm (d) t_{NiFe} = 8.8 nm

Figure 2.25: Sensitivity computed from R(H) with a current of 1 mA (black squares) and noise measurements for a bias voltage of 1 V (green circles) for each stack.

By comparing the colormap of the sensitivity depending on the measurement method (cf fig. 2.26), the optimum sensitivity is for a thickness of 6.3 nm, and a width of 8 µm from R(H) and a width of 9 µm from noise measurement. However, the maximal sensitivity computed from R(H) is around 4%/mT when with the noise measurement the sensitivity drops down to 2.5%/mT. By increasing the NiFe thickness, the sensitivity is only slightly increased compared to the reference GMR sensor (t_{NiFe} = 5nm and w = 4 µm) which has a sensitivity of 2.2 ± 0.4 %/mT from R(H) and 1.5 %/mT from noise measurement.

The optimal sensitivity is lower than expected from R(H) measurement. We need to compare the noise and limit of detection to determine the optimal width and NiFe thickness.

Noise and limit of detection

By increasing the NiFe thickness we intend to stabilize the magnetic domains and reduce RTN. The magnetic volume of the GMR stack increases when the NiFe thickness increases but the impact on the electric part of 1/f noise is expected to be negligible. The NiFe layer is increased either by 1.2 or 1.3 nm. For a yoke of 4 µm with a NiFe thickness of 5 nm, an increase of 1.3 nm of the free layer corresponds to a volume variation of 4.2%. By comparison, when the width is increased by 1 µm, from 4 to 5

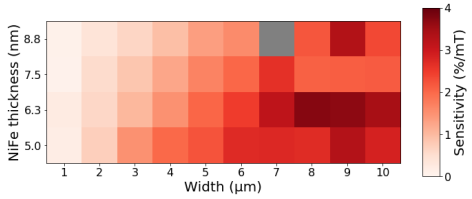

(a) Mean sensitivity computed from R(H) on the branch with the lowest sensitivity.

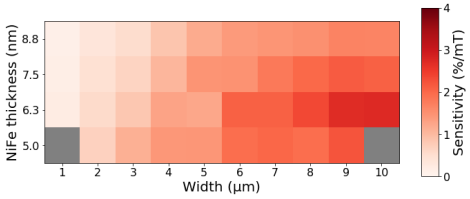

(b) Mean sensitivity computed from noise measurements at 0.5V and 1V.

Figure 2.26: Heat map of the sensitivity computed from (a) R(H) measurements and (b) noise measurements. The highest sensitivity from R(H) measurement is for a NiFe thickness of 6.3 nm and a width of 8. From noise measurement, the sensitivity is also higher for a NiFe thickness of 6.3 nm and a width of 9 µm but the increase of sensitivity is lower than expected from R(H) measurements.

µm, the volume increases by 56.2%. Therefore, we expect the impact of NiFe thickness on the 1/f noise to be negligible. Fig 2.27 (a) and (c) show the noise measurements.

In fig. 2.27, for these samples with a width of 4 µm, there are no RTN and the noise is similar for all NiFe thicknesses as expected. As the sensitivity of the reference layer is higher at 4µm and the three other stacks have similar sensitivity, the limit of detection at 4 µm is lower for the reference stack. But despite a lower sensitivity and a similar 1/f noise, an increased NiFe thickness can be interesting when there is RTN for the reference stack and no RTN for the stack with a modified free layer. Indeed, the objective is to reduce the RTN by increasing the NiFe thickness without sacrificing the limit of detection which has to remain around 1nT at 1kHz. This is illustrated for one sample with a width of 7 µm, for a NiFe thickness of 5nm, the limit of detection for a NiFe thickness of 7.5 nm is lower than the reference stack's limit of detection.

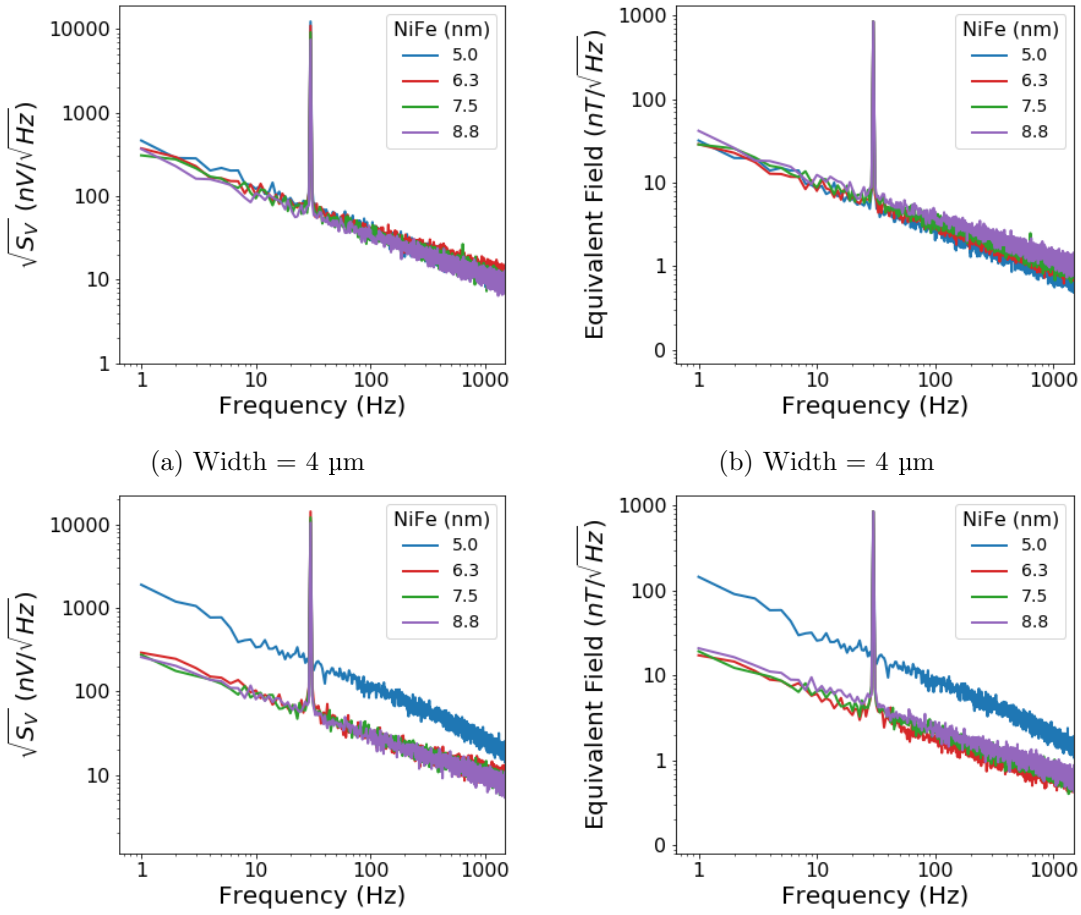

(a) Width = 4 µm

(b) Width = 4 µm

(c) Width = 5 µm

(d) Width = 5 µm

Figure 2.27: Comparison of noise and limit of detection for V_{GMR}= 1 V. (a),(b) Power spectral density and limit of detection for a width of 4 µm. (c),(d) Power spectral density and limit of detection for a width of 5 µm. At 4 µm, the 4 GMR stacks have a similar noise so only the change of sensitivity has an impact on the limit of detection. As the reference stack has the highest sensitivity, it is the stack with the lowest limit of detection at 4 µm. For a width of 5 µm, RTN arises for the reference stack and the lowest limit of detection is reached for a NiFe thickness of 6.3 nm.

The noise at 1kHz is extracted and fitted for each stack (fig. 2.28). From this figure, the NiFe thickness t_{NiFe}=7.5 nm seems to have the lowest RTN. These data are plotted for one sample. Two samples were studied.

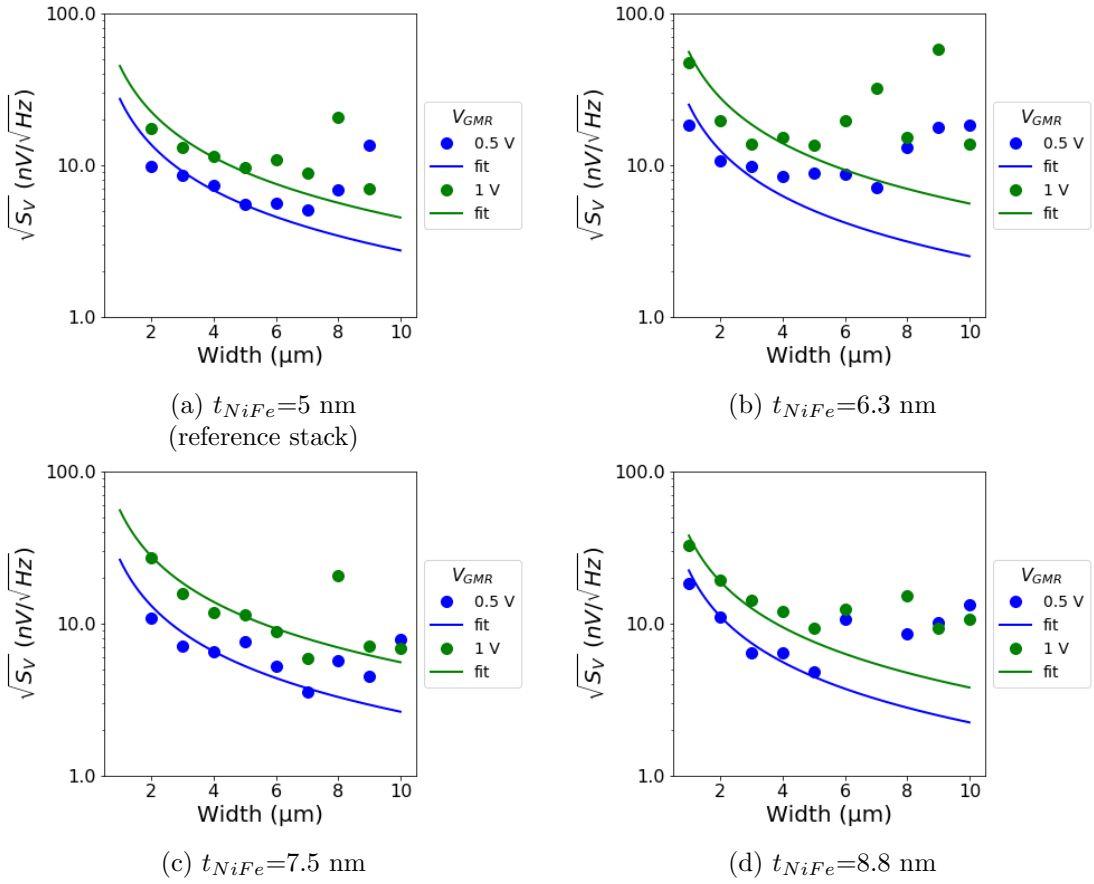

(a) t_{NiFe}=5 nm (reference stack)

(b) t_{NiFe}=6.3 nm

(c) t_{NiFe}=7.5 nm

(d) t_{NiFe}=8.8 nm

Figure 2.28: 1/f noise at 1kHz for each stack from a single sample.

In fig. 2.29, the noise decreases with the increase of NiFe thickness but as the RTN decreases as well, there is an optimum for the lowest limit of detection without RTN depending both on the width and the free layer composition. For a width superior to 5 µm, RTN cannot be avoided with this technique.

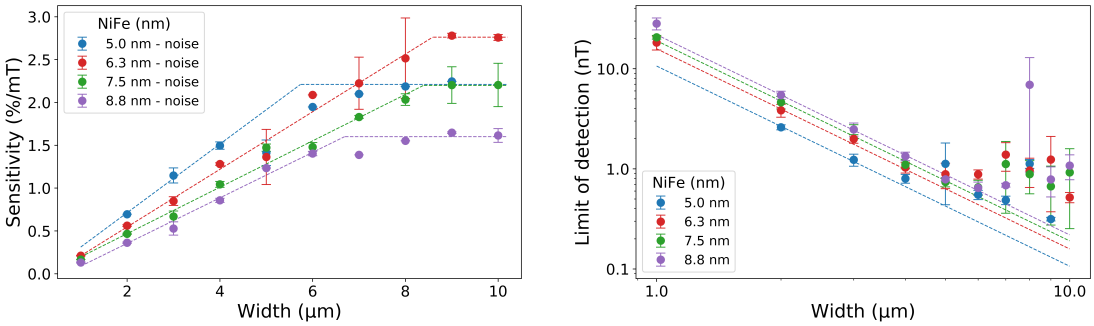

(a) Sensitivity

(b) Limit of detection

Figure 2.29: (a) Sensitivity and (b) limit of detection for each stack depending on the width.The limit of detection is fitted and divergences from the fit are explained by 2 phenomenon. First, the sensitivity is proportional to width up to a certain width. For higher width, the fit needs to be changed from $1/w^2$ to $1/w$ with w the width. Second, the RTN increases with the width and creates important variations.

The maximal width without RTN is described in table 2.4:

NiFe thickness (nm)	5.0	6.3	7.5	8.8
Upper width without RTN (µm)	3	4	5	5

Table 2.4: Upper width without RTN for each stack.

The optimal NiFe thickness is the thickness without RTN and presenting the lowest limit of detection. For each width, the optimal thickness is:

- **for w $\leqslant$ 3 µm**: $t_{NiFe,optimal}$ = 5.0 nm (There is RTN at lower frequency than 1kHz)
- **for w = 4 µm**: $t_{NiFe,optimal}$ = 6.3 nm
- **for w = 5 µm**: $t_{NiFe,optimal}$ = 7.5 nm

2.4.3 Conclusion

In conclusion on the free layer thickness study, for a width larger than 5 µm, the RTN cannot be prevented by NiFe thickness optimization on this reference stack. For *in-vivo* probes, previous GMR sensor masks have a width of 4 µm so the corresponding optimal NiFe thickness is 6.3 nm. There is a loss on the limit of detection but as the stability of the sensor is increased, this is the optimal configuration.

2.5 Differences between yokes and meanders

So far, yoke shapes (2.30 top) have been used for GMR stack optimization. For *in-vivo* probe, the shape used is a meander (2.30 bottom), which reconciles both a compact footprint and a reasonable volume, while keeping a mean resistance of the element in the kOhm range. From previous studies, an optimal configuration for a yoke of 4 µm is a single element with an NiFe thickness of 6.3 nm.

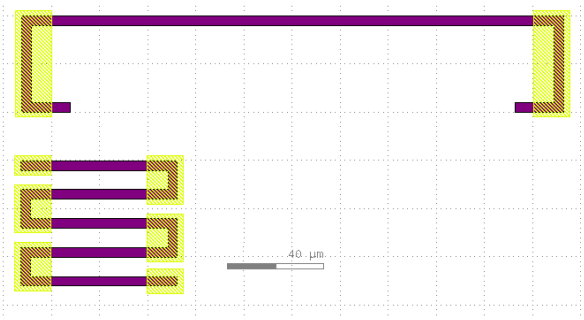

Figure 2.30: Comparison of the footprint of a yoke (top) and a meander (bottom) with the same active length (200 µm) and the same width (4 µm). The active length of the meander is divided in 5 segments of 40 µm each. Dashed squares have a length of 20 µm.

It is therefore important to study the difference of performance between a yoke and a meander in order to validate the optimized stack for *in-vivo* experiments.

For GMR optimization and *in-vivo* experiment, GMR sensors are shaped into yokes and meanders respectively. A yoke shape allows to stabilize magnetic domains but for *in-vivo* experiment, the width of the tip is limited to 200 µm to minimize damages during insertion and the surface occupied by the sensor is limited to approximately 50*50 μm^2. Having one shape for optimization allows to compare the impact of different strategies studied by different teams inside the laboratory with a good efficiency. Meanders have the advantages of a lower length with an increased volume compared to a single segment and a stabilization of magnetic domains similar to yoke. In this section, we want to know if optimizations on yokes have the same results on meanders.

We have seen previously, that yokes have an aspect ratio of 50:1 to keep a resistance around 700 Ω independently from the width. So a yoke with a width of 4 µm has a length of 200 µm which is too long for *in-vivo* application. One strategy to keep a small footprint while having a reasonable resistance, volume and a stabilization of magnetic domains, is to fold the length along a meander (cf fig. 2.30). With our present design, a meander with a width of 4 µm has five segments of 30 µm for a total width of 150 µm.

It should be noted that the segments of a meander need to have a sufficient distance between them. Indeed, if the GMR segments are too close to each other, then after the contact evaporation, it would be difficult to remove the contacts between two GMR segments and the meander might be short-circuited.

We will first comment on magnetic domains stabilization according to the shape of the element, then we will compare magnetotransport measurements of yokes and meanders with the same GMR stack and finally study noise measurements for both shapes.

2.5.1 Magnetic domains stabilization

At low frequencies, GMR sensor noise is dominated by 1/f noise and sometimes RTN. The 1/f noise can have an electric and a magnetic origin. As we have seen, for small width, magnetic domains can be stabilized by shape anisotropy. The yoke shape is used to increase domains stabilization by shape anisotropy, especially at the corners. Fig. 2.31 shows a simulation of magnetic domains configuration at the end of a sweep of the external field from saturated state to zero external field. One can see that magnetic domains in the arms are oriented in the same directions and only rotate in the corners. All magnetic domains of the main bar are aligned parallel to the length. To suppress contribution of unstable magnetic domains to 1/f noise and RTN, the corners need to be short-circuited by contacts. This reduces the active length of the sensor but lower the magnetic part of 1/f noise [8]. The stabilization of magnetic domains also prevents RTN.

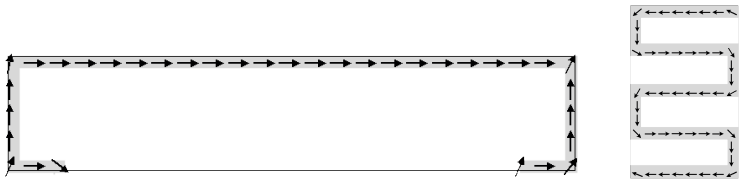

(a) Yoke (b) Meander

Figure 2.31: OOMMF simulation of magnetic domains configuration at zero external field for (a) a yoke, (b) a meander.

To reduce the length of the sensor and conserve a minimal magnetic volume, several GMR segments are placed in parallel. To keep the magnetic domains stabilization of a yoke shape, all segments are connected in series to create a meander (cf fig. 2.31b) and the connections are also short-circuited by contacts deposition to suppress the impact of corner's unstable magnetic domains.

2.5.2 R(H) comparison

As can be seen in fig. 2.32d R(H) curves of yoke and meander with the same GMR stack are quite similar. The deposition of the GMR stack is made at the same time for yokes and meanders. The fabrication of meanders follows the same lithographic process as for yokes. The MR ratio is lower for meander. Both yokes and meander start to have hysteresis and resistance jumps for w $\geq$ 5µm.

From these R(H) curves, MR and sensitivity are extracted (cf fig. 2.33). MR for meanders are lower for every width but the slope around zero-field is similar, thus a similar sensitivity for yoke and meander is expected despite a lower MR ratio.

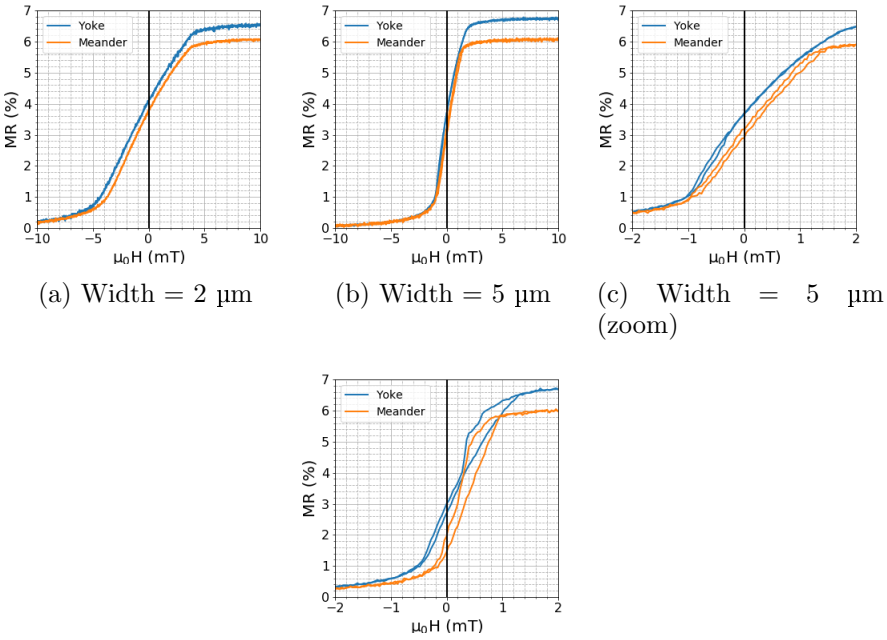

(a) Width = 2 µm (b) Width = 5 µm (c) Width = 5 µm (zoom)

(d) Width = 8 µm

Figure 2.32: (a)-(d) R(H) curves for different widths.

Due to an aspect ratio of 50:1, yokes have a resistance around for a width $\geq$ 3 µm of 688 $\pm$ 16 Ω while the meander resistance is strongly impacted by the width and varies as a function of 1/w as you can see in fig. 2.23. The yoke and the meander with a width of 3 µm have the same length (150 µm) which is why they have the same resistance.

Sensitivity for yoke and meander are similar up to 6 µm and the lower sensitivity starts to decrease at 8 µm for the meander. The loss of sensitivity for one branch for a width of 8 µm is more important for the meander because of a larger hysteresis and offset, as we can see in fig. 2.32d.

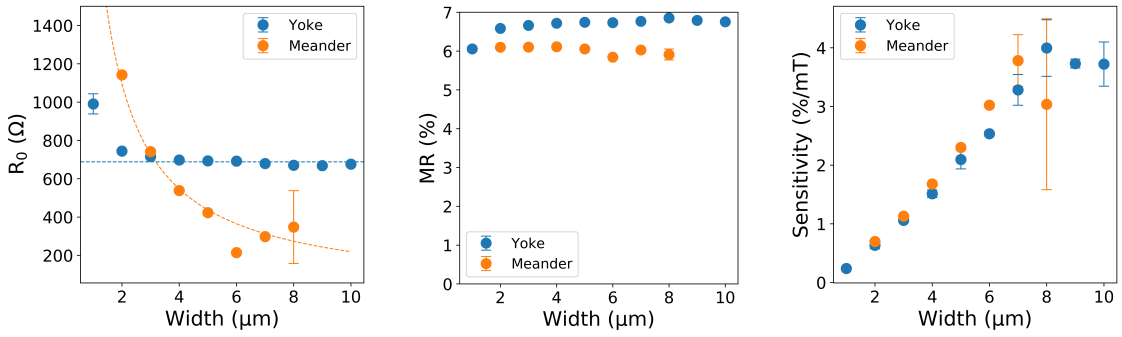

(a) R_0 (b) MR ratio (c) Sensitivity

Figure 2.33: (a) R_0, (b) MR ratio and (c) sensitivity extracted from R(H) as a function of width for yokes and meanders. In (a) the blue dashed line represents the mean resistance for w $\geq$ 3 µm, R_{mean}= 688 Ω and the dashed blue line represents the fit of the meander resistance.

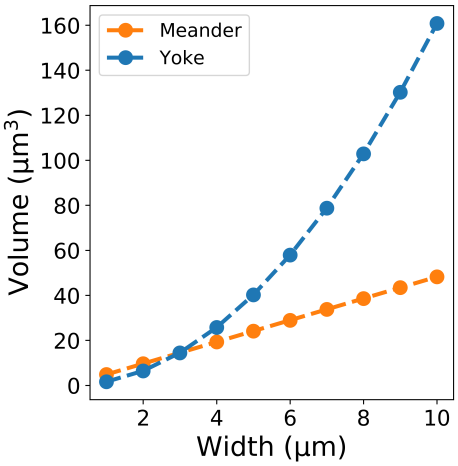

(a) Volume for yokes and meander as a function of width

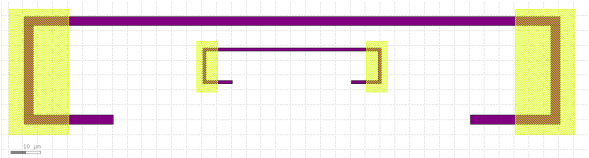

(b) Comparison of yokes with a width of 3 µm (external) and 1 µm (internal)

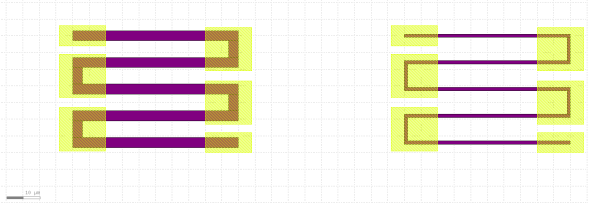

(c) Comparison of meanders with a width of 3 µm (left) and 1 µm (right)

Figure 2.34: Comparison of yokes and meanders volume as a function of the width (a) and examples of yokes (b) and meanders (c) with a width of 1 and 3 µm.

2.5.3 Noise comparison

The volume for yoke and meander except for w = 3 µm as you can see in fig. 2.34a. For yoke, the volume is computed as follows: $V_{yoke} = h * w * l = h * 50w^2$ and for meander we use: $V_{meander} = h * l * w * N$ with l = 30 µm and N = 5 (5 segments). The stack is the same for yoke and meander and h, the thickness of the optimized GMR stack, is equal to 32.15 nm.

For w $\leq$ 3 µm, meanders have a volume superior to yokes so we can expect a lower noise for meanders. For w = 3 µm, yokes and meanders have the same volume so we can assume that the 1/f noise is similar for both shapes. Finally, for w $\geq$ 4 µm, we assume that yokes have a slightly lower noise than meanders.

In fig. 2.35, noise measurements at different widths are plotted as a function of frequency. We can see that noise levels are similar for meanders and yokes and at larger width (for example 7 µm), there are RTN for both yokes and meanders .

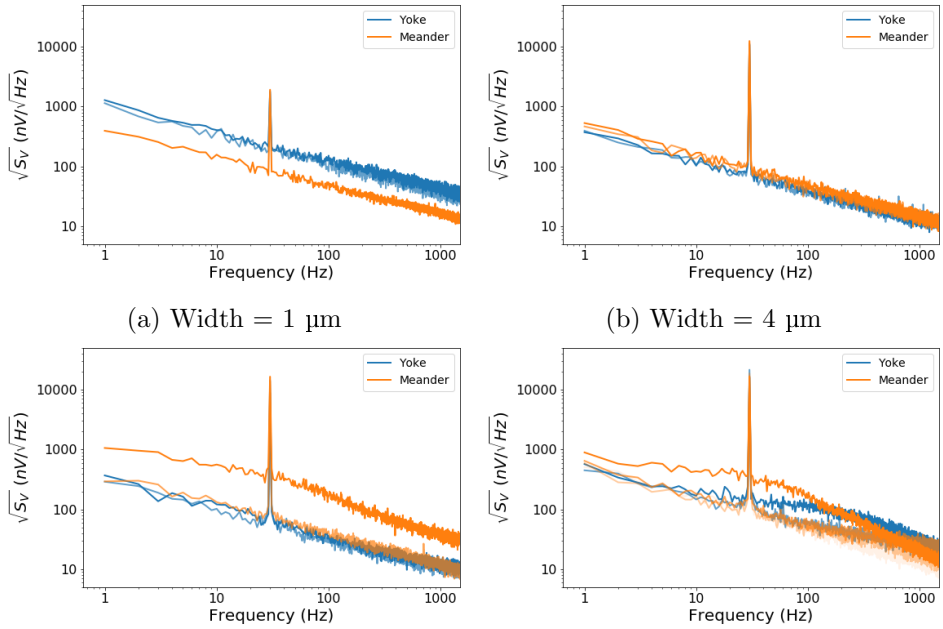

(a) Width = 1 µm

(b) Width = 4 µm

(c) Width = 5 µm

(d) Width = 7 µm

Figure 2.35: Power spectral density as a function of frequency for various widths for a bias voltage of 1 V. Several devices are measured and are differentiated by different shades of blue for yokes and orange for meanders.

Noise at 1kHz is extracted and plotted as a function of width (fig2.36). Meander's sensitivity is a bit higher than yoke's sensitivity up to 5 µm.

The limit of detection is a bit lower for meanders for a width of 3 µm. For a width of 4 µm, the limit of detection is the same and for w $\geq$ 5 µm, RTN is present for yoke and meander.

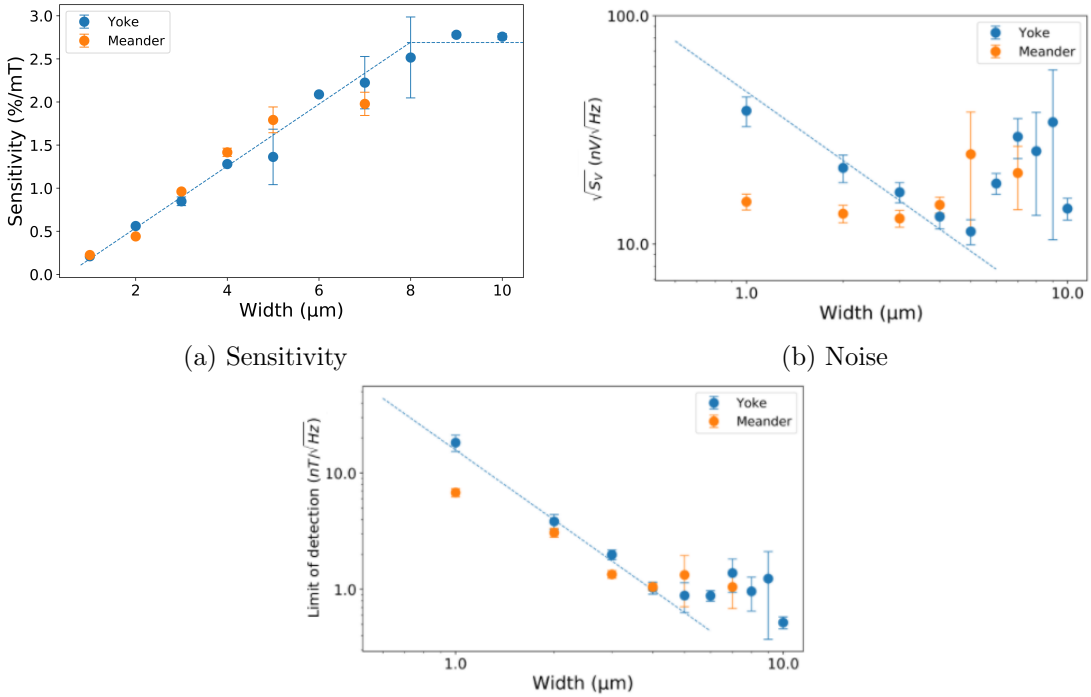

(a) Sensitivity

(b) Noise

(c) LOD

Figure 2.36: (a) Sensitivity and (b) limit of detection of yoke and meander as a function of width. Sensors are composed of the optimized GMR stack.

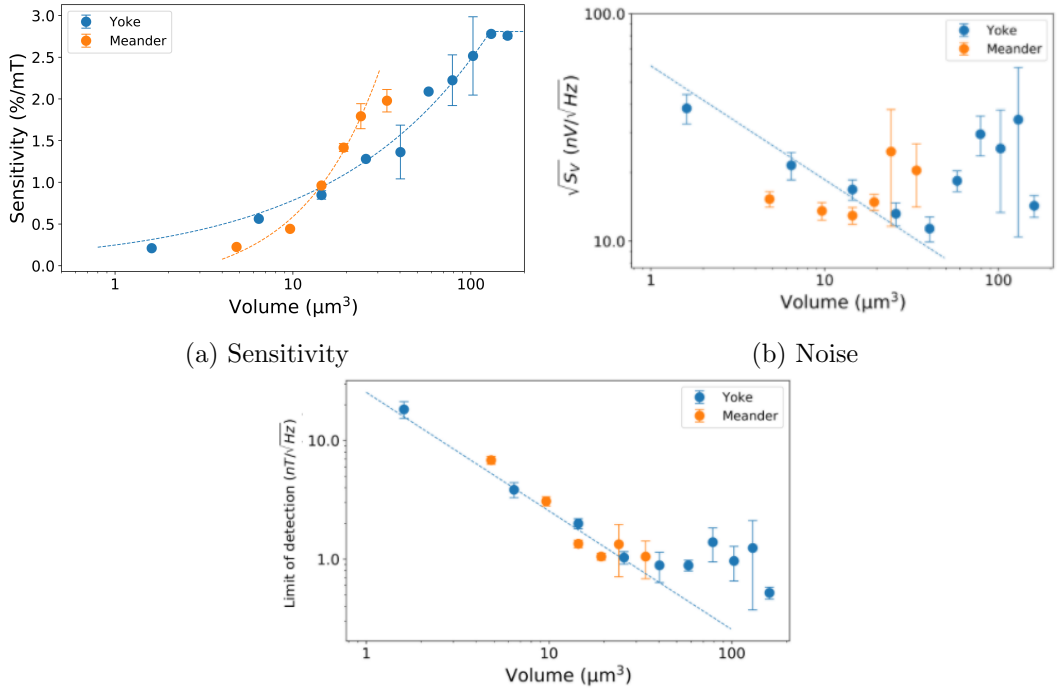

(a) Sensitivity

(b) Noise

(c) Limit of detection

Figure 2.37: (a) Sensitivity computed from noise measurements. (b) Noise at 1kHz as a function of volume. (c) Limit of detection at 1kHz for a voltage of 1V as a function of volume.

The sensitivity depends on the width of the sensor and is similar for yoke and meander as shown in fig. 2.36. In fig. 2.37, yoke and meander sensitivity, noise and limit of detection at 1kHz for a supply voltage of 1V are shown. The sensitivity is different for yoke and meander depending on the volume. As said before, the sensitivity depends on the width. The noise of yoke as a function of the volume can be fitted with a function $\propto 1/\sqrt{V}$ from the Hooge formula: $\sqrt{S_{V,1/f}} = \sqrt{\frac{\gamma}{n_c.Volume.f}}RI$. The noise is almost constant for the meander until RTN appears. However, the limit of detection as a function of volume, is almost the same for yokes and meanders. Meanders start to be unstable at a lower volume than yokes. This is explained by the fact that in the noise graph, RTN appears for a lower width and thus a lower volume than yokes (cf fig. 2.35).

In conclusion, LOD of yokes and meanders are very similar and an optimized stack studied with a yoke shape can be used with a meander shape with similar LOD .

2.6 Multi-GMR

Another way to investigate the reduction of noise while keeping the same footprint is to increase the sensor volume by a superposition of GMR sensors on top of each other. The vertical packaging of GMR sensors have been theoretically proposed [9]. It has the main advantage of increasing the volume while keeping the same footprint as a single element. It has an impact both on the 1/f noise due to the volume increase and also on the thermal noise as the resistance decreases with the number of stacked spin-valves. Indeed, the spin-valves are stacked in parallel so the total resistance is in theory $R_N = \frac{R_1}{N}$ with R_1 the resistance of a single element leading to a thermal noise: $\sqrt{S_{V,th}} = \sqrt{\frac{4k_bTR_1}{N}} \propto \frac{1}{\sqrt{N}}$.

This study was conducted by Jacob Torrejon and is reported here as it is an important study for GMR optimization. Details can be found in [10].

The composition of the spin-valves is described in table 2.1. We tested experimentally the impact with a superposition of N spin-valves (cf fig. 2.38) with N varying from 1 to 12. Between each spin-valve, a spacer of 3 nm of Ta is deposited to maintain a low roughness. The sensor width is chosen between 3 and up to 5 µm depending on the composition of the free layer (cf sect. 2.4), to be in the range where RTN is prevented. Sensors performance (sensitivity, noise and limit of detection) was extensively studied and main outputs in term of interest for *in-vivo* probe are given below.

Free layer		Spacer	Hard layer			
NiFe	CoFe	Cu	CoFe	Ru	CoFe	IrMn
5.00 nm	2.10 nm	2.90 nm	2.10 nm	0.85 nm	2.00 nm	7.50 nm

Table 2.5: top-SAF IrMn spin-valve composition

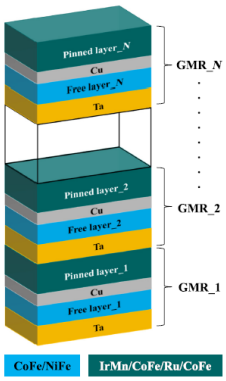

Figure 2.38: Composition of a multi-GMR device. From [10].

2.6.1 Main results

The reversal mechanisms of multi-GMR are complex and depend on the number of spin-valve N. The behavior of multi-GMR is demonstrated to be mainly driven by the competition between the Néel coupling and the additive dipolar coupling which occur between the free layers in the stack. Crossovers can appear according to N (number of repetition) but also with the width, as it strongly impacts the dipolar coupling.

These parameters have an impact on the sensitivity and the noise. In fig. 2.39, we can see that the sensitivity is strongly reduced with N: $S \propto \frac{w}{N}$ for small widths (w<7-8um) then is constant. The 1/f noise is decreasing as expected as $S_{V,1/f} \propto \frac{1}{w\sqrt{N}}$. This leads to a limit of detection larger on small widths multi-GMR than for single element. Therefore for our application, where the element width is small, single stack are preferable considering the LOD. One may also observe that for N $\geq$ 4, the RTN is strongly reduced and the stability of the GMR device is increased. Multi-GMR are in general more robust against RTN at higher voltages, and are therefore of interest for application in the frequency range of thermal noise (>1kHz) where the output voltage can be driven much higher than in a single element.

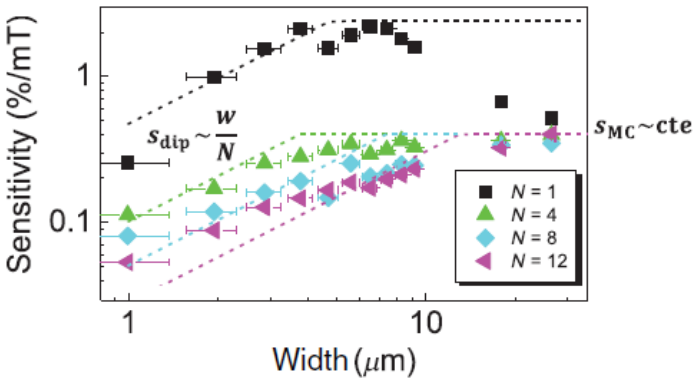

(a) Sensitivity

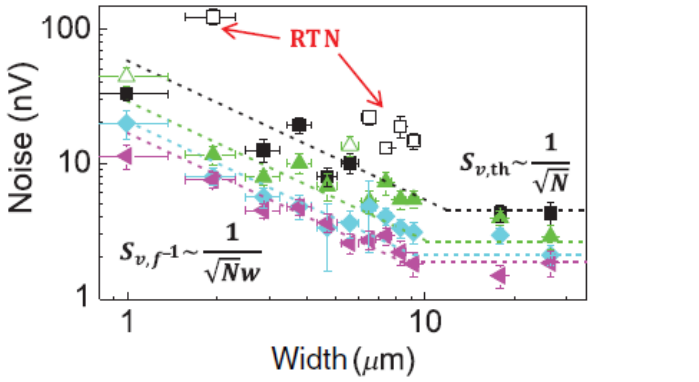

(b) Noise

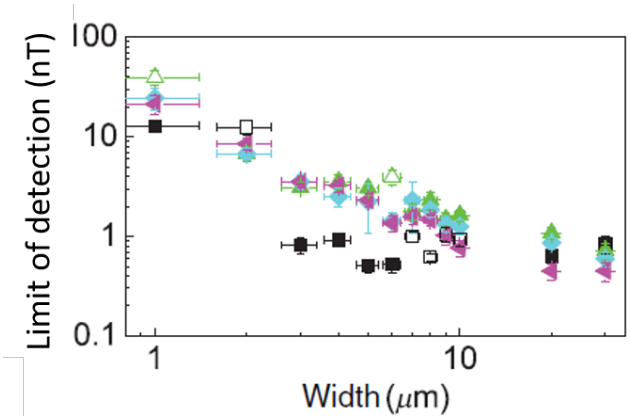

(c) Limit of detection

Figure 2.39: Multi-GMR performances for N=1,4,8,12. (a) Sensitivity, (b) Noise and (c) limit of detection at 1kHz. Open symbols in (b) and (c) represent devices with important magnetic noise (1/f or RTN)

2.6.2 Conclusion

As the limit of detection decreases with N for small width sensor, multi-GMR spin-valve are not suited for *in-vivo* applications. However, multi-GMRs do not present RTN for $N > 4$. For $N = 8$, the limit of detection at 1 kHz decreases with the bias voltage and can reach around 300 pT for a width of 30 µm and a bias voltage of 3 V which is of high interest for high frequencies and low field sensing.

2.7 Conclusion

Three studies on different techniques were reported. They show that reaching a lower limit of detection is a compromise between sensitivity and noise and is strongly limited by RTN. For a single GMR stack, the optimal GMR composition for a width of 4 µm, which is the width of GMR sensor for *in-vivo* recording was selected with a resulting limit of detection of 1 nT at 1kHz. No RTN is expected with this GMR composition so we can increase the voltage on such devices and reach a higher SNR.

In order to perform *in-vivo* recording, GMR sensors need to be fabricated on a probe designed for biological application.

Bibliography

[1] José Pedro Anselmo Amaral. *Measuring Neuronal Activity with High Sensitivity Magnetoresistive Sensors*. PhD thesis, 2014. 40

[2] Jaquelin K Spong, RE Fontana, Moris M Dovek, TL Hylton, et al. Giant magnetoresistive spin valve bridge sensor. *IEEE transactions on magnetics*, 32(2): 366–371, 1996. 48

[3] MT Johnson, PJH Bloemen, FJA Den Broeder, and JJ De Vries. Magnetic anisotropy in metallic multilayers. *Reports on Progress in Physics*, 59(11):1409, 1996. 50

[4] John MD Coey. *Magnetism and magnetic materials*. Cambridge university press, 2010. 50

[5] Zhenghong Qian, Ru Bai, Changmao Yang, Qiliang Li, Yucheng Sun, Dexuan Huo, Lingwei Li, Hongliang Zhan, Yuan Li, and Jianguo Zhu. Effective anisotropy field in the free layer of patterned spin-valve resistors. *Journal of Applied Physics*, 109(10):103904, May 2011. ISSN 0021-8979, 1089-7550. doi: 10.1063/1.3585852. URL http://aip.scitation.org/doi/10.1063/1.3585852. 50

[6] Ana V Silva, Diana C Leitao, João Valadeiro, José Amaral, Paulo P Freitas, and Susana Cardoso. Linearization strategies for high sensitivity magnetoresistive sensors. *The European Physical Journal Applied Physics*, 72(1):10601, 2015. 55

[7] J Moulin, A Doll, E Paul, M Pannetier-Lecoeur, C Fermon, N Sergeeva-Chollet, and A Solignac. Optimizing magnetoresistive sensor signal-to-noise via pinning field tuning. *Applied Physics Letters*, 115(12):122406, 2019. 56

[8] C Fermon, M Pannetier-Lecoeur, Nicolas Biziere, and B Cousin. Optimised gmr sensors for low and high frequencies applications. *Sensors and Actuators A: Physical*, 129(1-2):203–206, 2006. 66

[9] Marília Silva, Diana C Leitao, Susana Cardoso, and Paulo P Freitas. Toward ptesla detectivities maintaining minimum sensor footprint with vertical packaging of spin valves. *IEEE Transactions on Magnetics*, 53(4):1–5, 2016. 72

[10] J Torrejon, A Solignac, C Chopin, J Moulin, A Doll, E Paul, C Fermon, and M Pannetier-Lecoeur. Multiple giant-magnetoresistance sensors controlled by additive dipolar coupling. *Physical Review Applied*, 13(3):034031, 2020. 72

Chapter 3

Magnetrode

Contents

A magnetrode is a probe designed for recording bio-magnetic signals during *in-vivo* experiments. It has at least one GMR sensor in addition to at least one electrode to record electric signals. Electric signals generated by neurons are well known and electrodes are used as a reference and to average magnetic measurements. The limit of detection of a magnetrode's magnetic sensor is around 1nT at 1kHz and we aim at recording the magnetic signature of action potential which is expected between 10 to 100pT.

The previous works from Laure Caruso and Vincent Trauchessec, have proved that GMR sensor can be used at room temperature for recording magnetic activity generated by excitable cells such as muscular cells. L. Caruso has measured the first magnetic signal related to an evoked response field [1]. V. Trauchessec has also made preliminary experiments to record magnetic action potentials (APs) in a cat visual cortex [2]. Since these measurements and in the framework of this thesis, magnetrodes have been improved in three different ways. First, the GMR stack composition has been improved to lower RTN. Then, the probe design has been improved by reducing the tip's thickness from 200 µm to 25 µm. Finally, a magnetrode with two sensors with orthogonal sensitivity have been fabricated to measure a magnetic field in 2-dimensions (2D). It aims at realizing a mapping of magnetic neuronal activity.

First, we will introduce previous works from L. Caruso and V. Trauchessec. Then we will consider the fabrication of magnetrodes and their characterization. Finally, we will see the additional fabrication step for magnetrode designed for 2D recording and a phantom experiment for magnetic field reconstruction in 2D. A short description of electrodes used for *in-vivo* experiment is also presented.

3.1 Proof of concept for biological recording with GMR sensors and first *in-vivo* recording with magnetrodes

Electric potentials generated by different parts of the body are widely used for research or diagnosis (electroencephalography, electrocardiography). In the brain, electric potentials can be recorded at macroscale by electrodes placed on top of the skull, at mesoscale by intracranial electrodes and finally at microscale by intracellular recording. Magnetic field, on the other hand, can only be recorded at macroscale with MEG. Sources of electric potentials are well understood but magnetic sources of the magnetic signal recorded by MEG, on the opposite, are still misunderstood and local recording of the magnetic signal sources would bring knowledge about these magnetic sources.

The absence of technique to record local magnetic field can be explained by the low amplitude of the targeted magnetic field and the need of a bio compatible device in contact with living tissues with a micro-meter size. Working with GMR to record these low magnetic fields is motivated by the possibility to fabricate bio-compatible magnetic sensors (GMR sensors are covered with a bio-compatible passivation layer), to have sensors with a high sensitivity at micrometer scale and a simple measurement set-up as the magnetic information are retrieved by the measurement of a resistive element with a resistance proportional to the external magnetic field.

Several devices with GMR sensors have been developed in the lab for brain imaging and are presented in this section. First a proof of concept on *in-vitro* experiment with mouse

Seed layer	Free layer		Spacer	Hard layer				Cap layer
Ta	NiFe	CoFe	Cu	CoFe	Ru	CoFe	PtMn	Ta
3nm	3.5nm	1.5nm	2.3nm	2.1nm	0.85nm	2nm	18nm	3nm

Table 3.1: GMR composition for the muscle experiment

muscle is studied to validate the use of GMR sensor for biological recording [1, 2, 3], several experiments have also been performed *in-vitro* on rodent hyppocampus slices [2] (not described here). *In-vivo* measurements are realised on cat visual cortex with both planar and sharp probes [2, 4]. The first measurements made with magnetrodes to record a collective magnetic excitation are presented as well as the preliminary recordings of magnetic action potentials generated by several neurons.

3.1.1 *In-vitro* experiment with mouse muscle

In this work, performed in collaboration with the Unité de Neuroscience, Information et Complexité (UNIC) team of CNRS (Gif-sur-Yvette, France), the choice of a mouse skeletal soleus muscle is motivated by its simple organization, the synchronicity of its electrical activity and the parallel positioning of excitable cells. A nerve is connected in the center of the muscle to each fiber composing the muscle. When an action potential (AP) propagates along the nerve and arrives to the muscle, it provokes a post-synaptic AP in opposite directions in every fiber simultaneously. Post-synaptic AP of all fibers inside the muscles sum themselves, thus, the magnitude of the magnetic field is expected to be larger, allowing a magnetic recording with a GMR sensor.

GMR sensors used for this experiment are spin-valves with a composition described in table 3.1. The composition is close to the composition of the reference and optimized stack presented in chapter 2. The GMR stack is a top spin-valve with a SAF for the 3 stacks. However, in this experiment, the anti-ferromagnetic layer is PtMn and not IrMn like the reference and optimized GMR stack. The choice of PtMn instead of IrMn was motivated by its thermal stability [5] due to a higher-blocking temperature than IrMn as well as a high exchange bias which ensures magnetic stability at high-field. However, spin-valves with PtMn layer need a post-deposition annealing to crystallize the PtMn and an annealing with a current pulse under a magnetic field is not possible. PtMn was replaced by IrMn in later GMR sensor to benefit from a lower blocking temperature and the possibility to locally repin a GMR sensor with a pulse of current for 2D magnetrode (cf sec 3.4).

The GMR sensors are rectangular with a length of 1,7mm and a width of 400µm. Three GMR sensors are positioned under the muscle (cf fig 3.1b). They have an MR ratio around 6.5 %, a resistance of 80Ω for a sensitivity of 3.1 %/mT. The recorded magnetic field is averaged over the length of the sensor. A low-pass filter is used on the bandwidth DC-1.2kHz the total noise is 3.5 nT RMS. It has a limit of detection of 1 nT at 10 Hz, 300 pT at 100Hz and 70 pT at 1 kHz. This low LOD is related to the large volume of the sensor.

Muscle fibers are excited from their center by a nerve and two post-synaptic AP propagate along the fiber in opposite directions (cf fig 3.1b). The nerve is introduced inside a suction pipette and a voltage drop in the suction pipette generates an AP. It propagates along the axon of the nerve which triggers post-synaptic AP in every muscle

fiber at the same time. GMR sensors aim at recording the magnetic signature of post-synaptic AP propagation in the muscle fibers. Transmembrane and axial currents can be at the origin of the magnetic field (fig 3.1). However, transmembrane currents are expected to cancel themselves due to the cylindrical symmetry of the fibers, leaving only axial currents as magnetic sources. Axial currents propagate within the muscle in both directions from the center (fig 3.1c) and are partially screened by the return current in the extracellular medium.

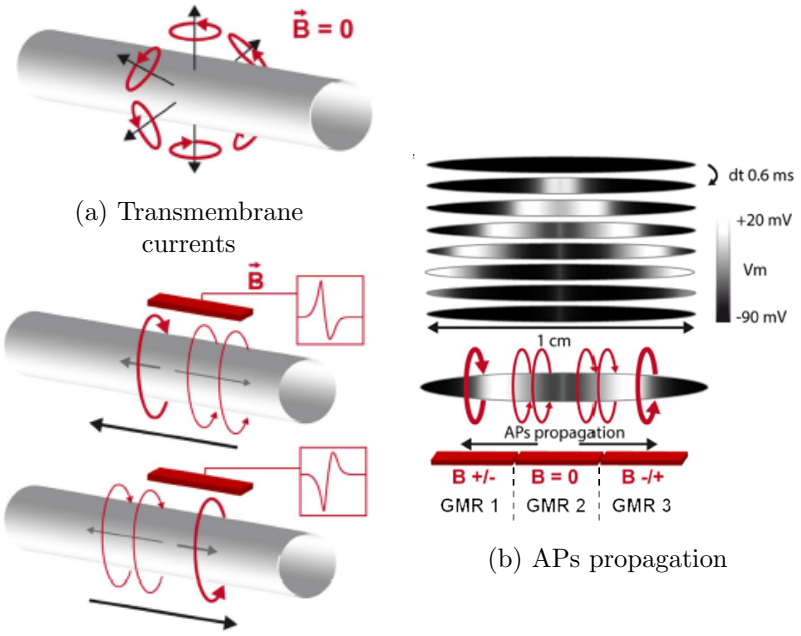

(a) Transmembrane currents

(b) APs propagation

(c) Axial currents

Figure 3.1: (a) Transmembrane currents do not produce a detectable magnetic field at the level of the probe. (b) Axial currents participate to the magnetic field. They are generated at the center of the structure, propagates in both directions with a bipolar signature which appears in the magnetic field component as a signal of opposite polarity (c) APs propagation in the muscle and positions of the three magnetic sensors. From [3]

The sensitive axis of the GMR sensor is perpendicular to its length so GMR sensors are placed parallel to the muscle length in order to be able to record the magnetic fields generated by axial currents. The magnetic fields generated by the AP propagating in opposite directions are supposed to cancel each other at the center so no magnetic field is expected to be recorded by the GMR sensor (GMR 2) positioned under the center of the muscle. GMR 1 and GMR 3 are positioned on both sides of this sensor and are expected to record opposite magnetic field as they are recording AP potentials with opposite directions of propagation.

After averaging (≈10 trials for an SNR of 2 and ≈500 trials for an SNR of 16), two magnetic fields with opposite shapes are recorded on two sensors. The central sensor does not record any significant magnetic field as expected (cf fig 3.2). To ensure the recording of a magnetic post-synaptic AP, three tests are made. First, the current supplying the GMR sensor is decreased down to 0 mA (cf fig 3.2c) to check the quality of the insulating layer of the GMR sensor and to ensure that the recorded signal is purely magnetic and not an artifact from a contact with the conductive medium. Second, curare is used to block the post-synaptic receptors (cf fig 3.2d) and prevent

the AP propagation despite stimulation. This proves that the magnetic signal recorded is the magnetic post-synaptic AP propagation and not an artifact from stimulation. Finally, the GMR sensor is turned by an angle of 90° (cf fig 3.2e), the sensitive axis is perpendicular to the magnetic fields generated by axial currents and should not detect the magnetic field generated by the post-synaptic AP propagation.

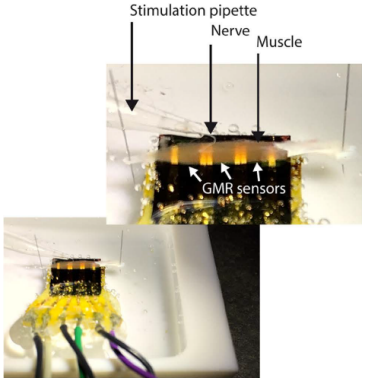

(a) Set-up

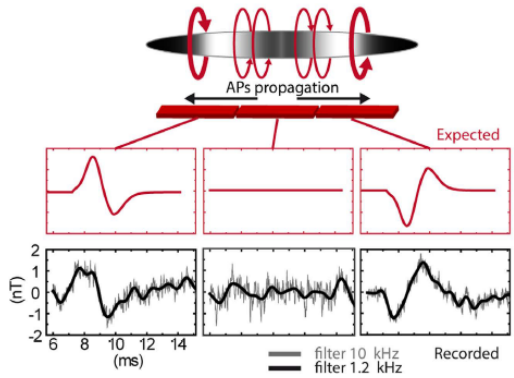

(b) AP propagation

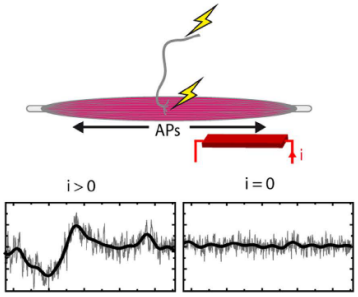

(c) GMR sensors are not supplied.

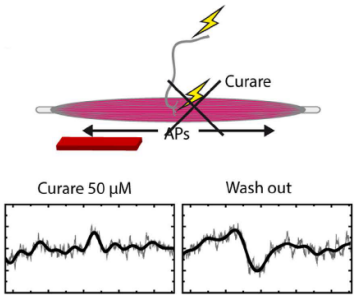

(d) Receptors are blocked by curare.

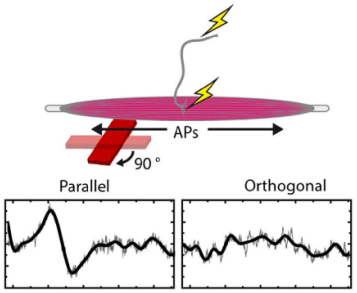

(e) GMR sensor turned by 90°.

Figure 3.2: (a) Photography of the mouse skeletal soleus muscle placed over three GMR sensors. The nerve is placed in a suction pipette. (b) The propagation of the electric AP is pictured on the muscle. The expected and measured magnetic AP are plotted as a function of time. (c) A GMR sensor is not supplied to prove that the recorded signal is purely magnetic. (d) The propagation of the AP in the muscle is stopped by curare to prove that the recorded signal does not come from the electrical stimulus. (e) The GMR sensor is turned by 90° to ensure that the recording signal is along the GMR sensor axis of sensitivity. From [3]

In addition to these tests, the expected magnetic field is calculated by simulation (cf fig 3.3). It takes into account the muscle fibers, the bundle, the sheath and the saline bath. The agreement between simulation and experiment is of good quality and the selected values of bundle and sheath conductivity are coherent with literature.

In conclusion, GMR sensors can be used to record magnetic activity thanks to its biocompatibility, its capacity to be miniaturized without losing in sensitivity and its simple electronics. For *in-vivo* application, GMR sensors need to have a different design, in particular a much smaller size. The next step is to integrate GMR on a sharp probe for insertion in the brain. This probe would be the magnetic counterpart of an electrode, with a similar ease of manipulation.

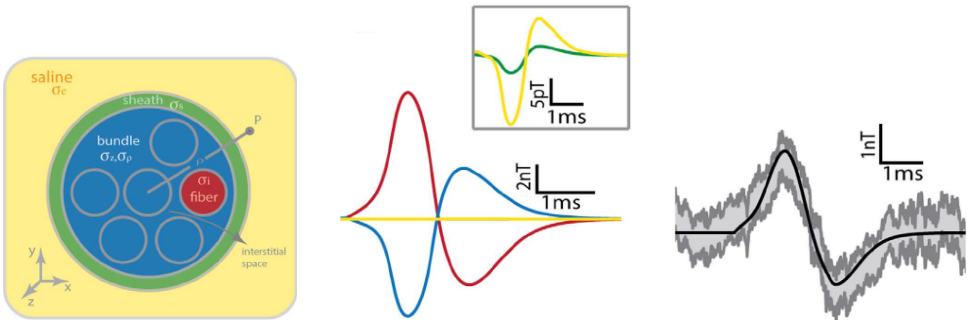

(a) Scheme of all parameters taken into account for the simulation

(b) Magnetic field amplitude

(c) Simulation compared to experiments

Figure 3.3: (a) Scheme of the different parts taken into account for the simulation. The number of muscle fibers is set to about 890 with a diameter of 40µm. (b) Simulated magnetic field generated by each part (yellow: saline bath, green: sheath, blue: bundle and red: muscle fibers). (c) All the magnetic fields computed previously are added (black line). The results are compared to experimental data averaged on 450 trials (grey part). From [3]

3.1.2 *In-vivo* recording with magnetrodes

Recording a magnetic field at local scale has several advantages compared to a measurement of the electric potential variations. First, it is a vectorial measurement providing information both about magnitude and direction of the magnetic field. Also a magnetic sensor is reference free. For electric recording, a reference electrode is placed far from the recording site (in the shoulder for example for *in-vivo* experiment). Finally, the magnetic field only decreases with distance between the magnetic sources and the sensor as there is no distortion of the magnetic signal through brain tissues (the magnetic permeability of the different brain structures is similar to vacuum magnetic permeability). Small SQUID, winded coils, OPM and NV centers are good candidates to record small magnetic field but they cannot be miniaturized to be inserted in the brain or even put in direct contact with living tissues like SQUIDs. Spin electronics based magnetic sensors are then a promising choice as they can be miniaturized down to µm-size, are biocompatible and have a good sensitivity.

In collaboration with Pascal Fries's team at Ernst Strüngmann Institute (Frankfurt, Germany), the first *in-vivo* magnetic recording with magnetrodes has been demonstrated in the visual cortex of a cat. The cortex is in the surface of the brain and thus is easily accessible. In addition, neurons are arranged vertically into columns and can respond collectively to a stimulus. This synchronous response would enhance the magnitude of the recorded signal. Moreover, the visual cortex can easily be stimulated by light. This makes the visual cortex a good choice for magnetic recording.

For this recording, two GMR sensors are placed on the magnetrode (fig 3.4a) but only one is used. GMR sensors are shaped as meanders with 5 segments of 4*30 µm^2. The GMR sensor composition is the same as muscle experiment and is given in table 3.1. They have an MR ratio of 6.1 %, a sensitivity of 1.8 %/mT for a limit of detection of 7 nT at 10 Hz, 2 nT at 100 Hz and 370 pT in the thermal regime above few kHz for a GMR voltage of 0.5V. They are noisier than GMR sensors for muscle experiment but the sensor volume is much lower for magnetrode (21.75µm^3) than GMR sensors for muscle experiment ($\sim 24.10^3$µm^3). This difference has a huge impact on 1/f noise as

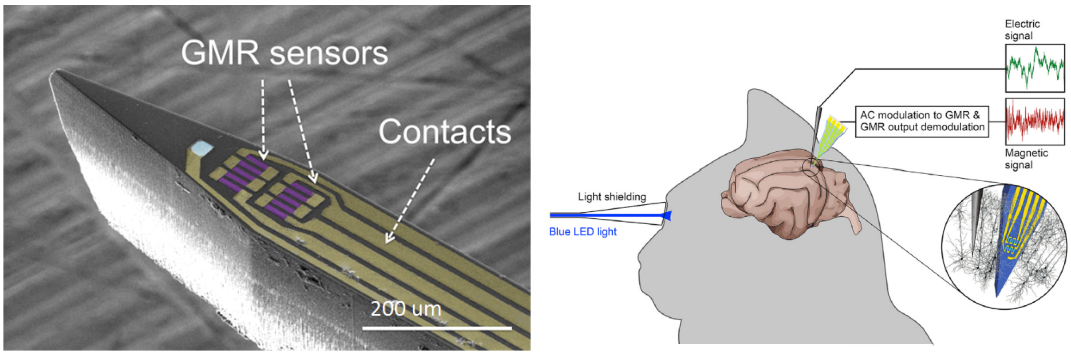

(a) Magnetrode (b) Experiment set-up

Figure 3.4: (a) Colorized SEM image of a magnetrode with GMR sensors in violet, contacts in yellow and electrodes in light blue. (b) Scheme of the experiment set-up. From [4]

we saw in chapter 2 and thus on the limit of detection.

Platinum electrodes are deposited close to the GMR sensors to record both electric and magnetic signals at the same time. As the electric signal is well known, it is interesting to record simultaneously both components of neuronal activity. However, the platinum electrodes were faulty and could not be used because of a noisy signal compared to commercial electrodes. Additional tungsten electrodes placed close to the magnetrode (less than 1 mm) were used instead. The angle of the tip is set to 18° to optimize the insertion in the brain. The thickness of the silicon substrate is 200µm (fig 3.4a). The etching of the silicon wafer is made by a Bosch process described later (section 3.2.2). GMR sensors and contacts are separated from the conductive medium of the brain by a passivation layer composed by a bi-layer of Al_2O_3 (150nm)/Si_3N_4 (150nm).

During *in-vivo* recording, a magnetrode is inserted about 1 mm inside the visual cortex, the total thickness of the cat visual cortex being 1.6 mm. The GMR axis of sensitivity is parallel to the cortex surface. As the brain is a conductive medium, a capacitive coupling can arise between GMR sensors and the extra cellular medium *via* the insulating layer. To separate the electric and magnetic components, the GMR sensor is powered by an AC voltage supply and then the output voltage is demodulated. The magnetic signal is expected to be in-phase and the electric part to be out-of-phase.

The cat is anesthetized during all the experiment. A light is presented to one eye to stimulate an evoked response in the visual cortex. The light stimulation lasts either 100ms or 500ms and is presented 1 000 times. To avoid any adaptation to the light stimulation the time between 2 stimulus varies from 0.9 to 1.5s.

In fig 3.5, one can see that both for the Evoked Related Potential (ERP) and Evoked Response Field (ERF), a signal is detected 20ms after the stimulation. It corresponds to the biological conduction delay between the retina and the visual cortex. Then a strong negative peak followed by a positive peak occurs. In total, 3 similar recordings are reported on two different animals.

The curves from ERP and ERF are exhibiting the same behavior, only the peak's magnitudes are different. The recorded magnetic field is supposed to be a summation of local field potential magnetic counterparts.

The following step is to record a magnetic action potential. An action potential is a

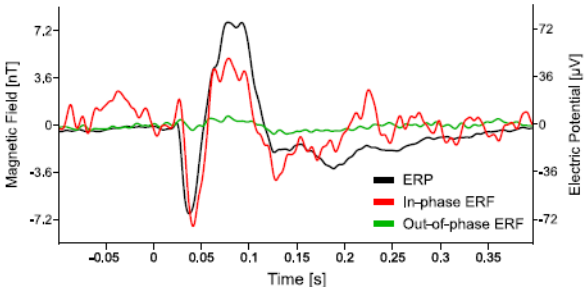

Figure 3.5: In-vivo electrical and magnetic recordings. Event related potentials (ERP) come from a tungsten electrode, Evoked Response Field (ERF) in-phase and out of phase are recorded by GMR sensors. Both outputs are averaged over 1 000 stimulus. From [4]

response from a single neuron with a frequency range around 1 kHz for an estimated amplitude between 10 to 100 pT [6].

3.1.3 *In-vivo* recording of magnetic action potentials

This experiment has been performed also in collaboration with the ESI team, in a cat visual cortex with the same set-up as described in section 3.1.2 and the same type of magnetrode is used. This time GMR sensors are powered by a DC supply and to prevent any electric contamination of the signal by capacitive coupling, experiments are made a second time without supplying the magnetic sensor as control experiment.

A light is used for stimulation. The magnetic field is recorded by a magnetrode and the electric potential is measured by both a tungsten electrode and the platinum electrode of the magnetrode. Two steps are critical to extract electrical spikes (AP temporal signature). First the signal is filtered by a band pass filter [500Hz-8kHz]. This step is important because filtering can alter the AP shape or induce artifacts. Then a threshold is determined to extract spikes from the noise. If the threshold is too low then noise can be interpreted as spikes and if the threshold is too high, then small spikes are not taken into account. Platinum electrode does not detect more spikes during stimulation, which is unexpected [2]. Detected spikes from both electrodes are plotted with the spikes center at 0 ms with a time window of 10 ms. A lot of these spikes with a large amplitude are also detected in a ±3ms window for the platinum electrodes. As it is below the refractory period of a neuron, these spikes are eliminated as considered as irrelevant.

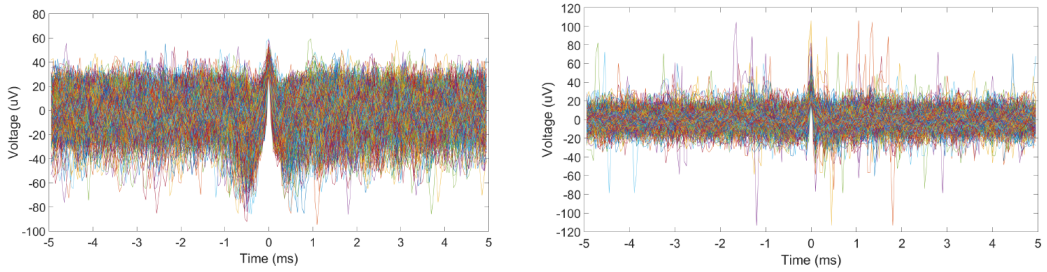

(a) Tungsten electrode (b) Platinum electrode

Figure 3.6: Spikes recorded by the tungsten and platinum electrodes. Each color trace is a single recording. Several spikes appear is the ± 3 ms intervals. These spikes are supposed to be artifact as they appear during the refractory period of a neuron. [2]

To extract a magnetic signal from the noise, recorded magnetic signals are averaged within a small time windows centered on spikes detected by the tungsten electrode. This reduces the magnetic noise level of the GMR sensor down to 0.3 nT and allows the recording of a correlated output on the magnetic channel.

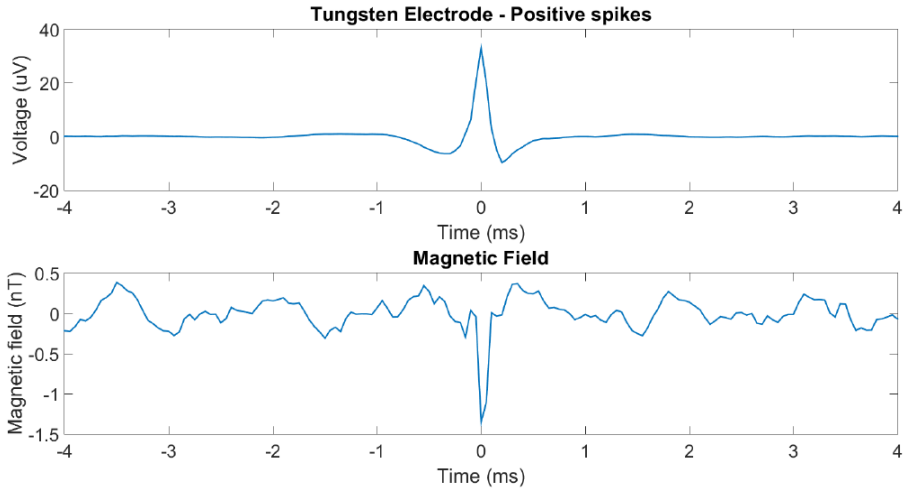

Figure 3.7: Electric and magnetic spikes after averaging of 26 000 positive spikes.[2]

This is the first attempt at recording a magnetic signal correlated to neuronal action potential with a magnetrode. Around 4 000 stimuli have lead to ≈40 000 electric spikes. These spikes were used to extract a corresponding magnetic signal. To verify if the origin of the recorded magnetic signal is magnetic, a similar measurement is made with the same GMR sensor with $I_{GMR} = 0$ mA. The recorded magnetic signal disappears when the GMR sensor is not supplied. These data are from a single shot of measurements and need to be repeated. In the next chapter, we will show further recordings and analyze more in details these measurements which appear correlated to the electrical spikes and disappear under the I=0 control condition.

3.1.4 Conclusion

The previous experiments have proved that small magnetic signals related to biological activity of excitable cells can be recorded *in-vitro* and *in-vivo* by GMR sensors. In order to validate the recording of a magnetic AP, new experiments are performed during this PhD and they are described in the following chapter. The magnetrodes used for these experiments are described in the following sections.

3.2 Magnetrode fabrication

A magnetrode is a sharp probe and its fabrication process is divided in 5 steps: sensors shape definition, contacts deposition, electrodes deposition, passivation and substrate etching. The sensors shape definition, contacts deposition and passivation are the same steps as for the fabrication of GMR sensors in chapter 2. There are three main differences between the fabrication process of regular GMR sensor and magnetrode: first, the silicon substrate is replaced by an SOI substrate, then there is an additional step for platinum electrodes deposition and finally a Bosch process is used to etch the wafer over a thickness of $\sim$ 430 µm.

A great improvement from previous magnetrode generation is the replacement of silicon wafer by Silicon On Insulator (SOI) wafer. SOI wafers are widely used in semiconductor industry as it has several advantages compared to bulk silicon: the lower parasitic capacitance due to the insulation from the silicon substrate by a passivation layer called the buried oxide layer as well as lower leakage current among other advantages. However, we use SOI substrate because it is composed of a superposition of Si/ SiO_2/ Si layers. The first Si layer is called the device layer (the GMR stack is deposited on this layer), the SiO_2layer is called the buried oxide layer and the second Si layer is the handle layer. Different SOI wafers were used and the composition of the last SOI wafer used for magnetrode is pictured in fig 3.8.

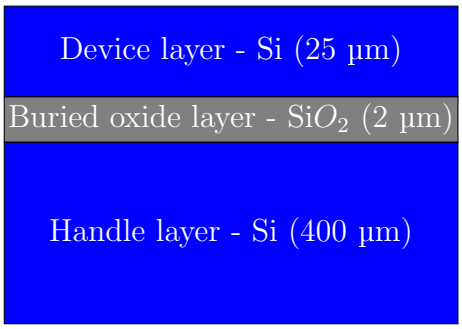

Figure 3.8: Scheme of a SOI wafer (not scaled).

The buried oxide layer is used as an etchant barrier during Deep Reactive Ion Etching (Deep RIE). Deep RIE is a selective etching and allows to etch either silicon or silicate and thus either the device layer/handle layer or buried oxide layer. Depending on the method of fabrication of the SOI wafer, an additional layer of SiO_2can be present under the handle layer. Also, a passivation layer is deposited on top of the device layer to isolate the GMR sensors and contact lines from the device layer.

An SOI substrate allows to have a magnetrode's tip with a thickness of 25 µm and a body with a thickness of $\sim$ 400 µm to facilitate the manipulation of the magnetrode while having a reduced footprint for the tip. The thin tip is inserted into the brain and a reduced thickness is a real asset to prevent damages during insertion while the thick body can support manipulation.

After the fabrication, magnetrode are mounted on Printed Circuit Board (PCB).

3.2.1 GMR sensors and electrodes deposition

Magnetrode designs

On a single 2" wafer, up to 10 magnetrodes can be processed. There are 5 different magnetrode designs and each design is present twice. Each magnetrode is labeled by a number with 3 digits. The first number is the mask version (here it is 7), the second refers to the magnetrode design (from 1 to 5) and the last one is used to differentiate two identical magnetrodes (either 1 or 2).

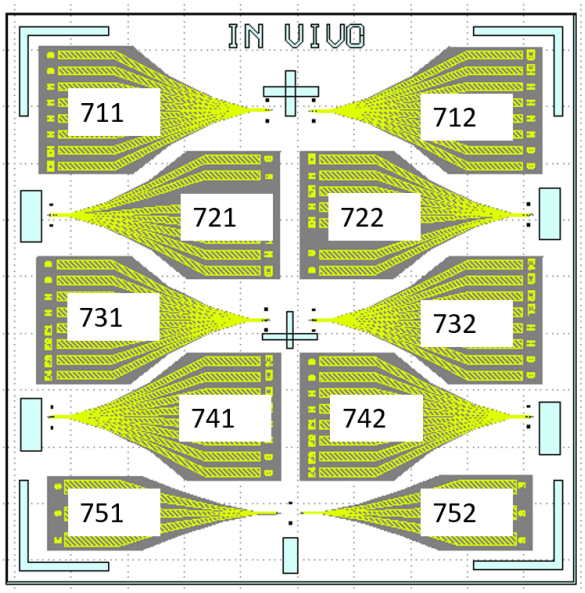

Figure 3.9: Scheme of the mask containing 10 magnetrodes on a single wafer: The contacts lines are in yellow and the shape of the magnetrodes after etching is in gray. All probes are labeled by a number with 3 digits: xyz. x=7, it is the mask version, y is the design of the magnetrode (from 1 to 5) and z differentiates two identical magnetrodes (either 1 or 2).

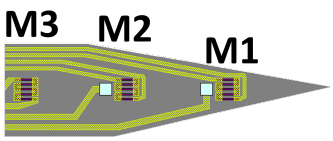

(a) Design 71

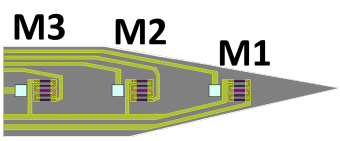

(b) Design 72

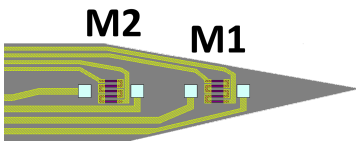

(c) Design 73

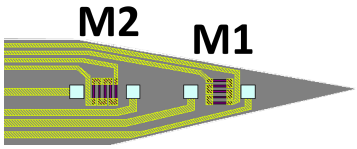

(d) Design 74

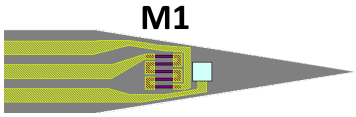

(e) Design 75

Figure 3.10: Zoom on the tip of each 5 designs. Superposition of all masks used for magnetrode fabrication: GMR stack etching (purple), contact deposition (yellow), electrodes deposition (light blue) and thinned substrate (gray). Passivation is deposited over all the wafer except on contact pads and electrodes. GMR sensors are separated center to center by 250 µm and electrodes are at 20 µm from GMR sensor. The GMR sensors are numbered: M1, M2 and M3 with M1 the closest sensor to the tip.

These 5 designs have variations in the number of GMR sensors, GMR sensors axis of sensitivity and number of electrodes:

- **Design 71**: 3 GMR sensors with 2 electrodes at a distance of 10 µm from GMR sensor.
- **Design 72**: To have one electrode for each GMR sensor, all magnetic sensors share a common ground to have more space for an additional electrode. The width of the magnetrode is limited to ∼230 µm and thus the number of contact lines is limited.
- **Design 73**: 2 GMR sensors, each sensor has two electrodes at 20 µm.
- **Design 74**: Same design as 73 but M2 is turned by an angle of 90° for 2D recording. These probes need an additional local repinning step, described in section 3.4.
- **Design 75**: Only 1 GMR sensor with 1 electrode. It allows to reduce the width of the probes down to 130 µm.

Every GMR sensor is a meander with 5 segments, a width of 4 µm, a total length of 50 µm and an active length of 30 µm (not short-circuited by contact). Increasing the number of segments allows to have a higher volume than a single segment, reducing the 1/f noise. The meander shape is used to stabilize magnetic domains and concentrate unstable magnetic domains in the corners (cf fig 2.31). The corners are then short-circuited by contacts. Segments are connected in series, the resistance increases with N, the number of segments, and thus the thermal noise is proportional to $\sqrt{N}$. The probes with several GMR sensors aim to be used either in a laminar way by recording the magnetic field at different depths or as gradiometer to reduce noise. Electrodes are deposited on the probes to record both the electric potential variations and magnetic fields simultaneously. However, designing electrodes is a technical area of its own and it is not a competence developed in our group. Hence, as our electrodes exhibit too much noise, we choose to use commercial electrodes instead. These commercial electrodes and the method to place them close to a GMR sensor is described in section 3.5.3.

All 5 designs are processed as described below.

Substrates used for magnetrodes

As said before, the following steps are similar to previous GMR sensor fabrication process with an additional step for electrodes deposition. The magnetrodes are fabricated in parallel to the optimization of GMR sensors. In 2018, only the reference stack was deposited both on thick silicon substrate and on SOI substrate. In 2019, both the reference stack and the stack composed by free layer with an optimized NiFe thickness were deposited on SOI substrate.

Substrates and GMR stacks used for magnetrode are listed in table 3.2. Si1-ref and Si2-ref are standard silicon wafers with a 2" diameter, a thickness of 270 µm and an insulating layer of 500 nm of SiO_2.

Fabrication

GMR stacks are deposited by sputtering and annealed at 300°C during 1 hour under a magnetic field of 1T to set the hard layer magnetic orientation.

Year	2018			2019			
GMR stack	Reference stack			Reference stack		Optimized stack	
Substrate	Silicon		SOI	SOI 81		SOI 99	
Substrate name	Si1-ref.	Si2-ref.	SOI-ref.	SOI 81-ref.	SOI 99-ref.	SOI 81-opti.	SOI 99-opti.
Tip thickness	270 µm	270 µm	25 µm	25 µm	25 µm	25 µm	25 µm

Table 3.2: List of all substrates and GMR stacks used for magnetrodes fabrication in 2018 and 2019.

Seed layer	Free layer		Spacer	Hard layer				Cap layer	
Ta	NiFe	CoFe	Cu	CoFe	Ru	CoFe	IrMn	Ru	Ta
3.00	x	2.10	2.90	2.10	0.85	2.00	7.50	0.40	5.00

Table 3.3: GMR composition (in nm) with x= 5nm for the reference layer and x=6.3nm for the optimized layer.

GMR stacks are then patterned with optical lithography using a chromium mask for each step of the process. GMR stacks are etched under vacuum by IBE during 24min with a 90° rotation every 6 minutes. After the etching, the resistance of the wafer is measured to test if all the GMR layer has been etched completely. The resistance should be infinite.

Then contacts are deposited by evaporation, it is a trilayer of Ti (15nm)/ Au (150nm)/Ti (15 nm). Platinum electrodes are then deposited on top of squared contacts by evaporation with a thickness of 200 nm. All the wafer is then passivated by a bi-layer of Al_2O_3 (150 nm)/Si_3N_4 (150 nm) except on the contact pads and on the electrodes.

The next step is to etch the device layer to give to the magnetrode its shape and to release the probe by etching all silicon and SiO_2layer around the magnetrodes's tip and body.

3.2.2 Magnetrode etching

To etch an important thickness of material (several microns) IBE is not sufficient and would take too long. We need to use an etching technique called deep Reactive Ion Etching (RIE) which combines physical and chemical etching. We used the Bosch process to etch silicon.

When the chromium masks were designed, magnetrodes were supposed to be released from the wafer by laser cutting. But due to the encountered difficulties [2] and results with a lower quality, we chose to return to Deep RIE. However, the laboratory does not have the equipment to perform a Deep RIE. In 2018, we worked in collaboration with Institut d'Electronique Fondamentale (IEF) in Orsay now Center for Nanoscience and Nanotechnology C2N) which is close to our laboratory. In 2019, we went to Besançon at the Femto-ST, because the clean room of the C2N was not accessible yet. This work has been performed in the framework of the Renatech network. We chose Femto-ST because they have a similar Deep RIE equipment to C2N.

The Bosch process was developed in 1996 [7] to respond to the MEMS industry needs. For MEMS fabrication, vertical sidewalls and a high accuracy are critical parameters. Plasma etching was a good solution to etch silicon but it has a low uniformity. A first improvement was to introduce an aperture between the plasma source and the wafer to select high energy ions and enhance the etching uniformity. However, the selectivity

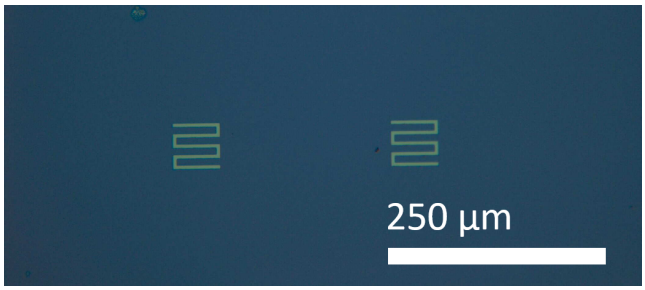

(a) GMR etching

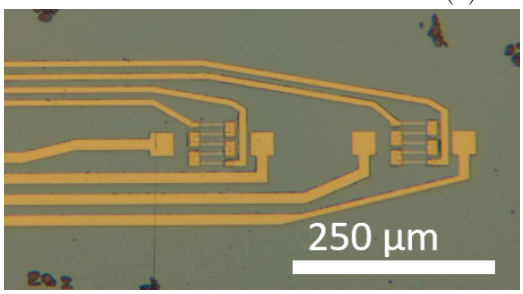

(b) Contacts deposition

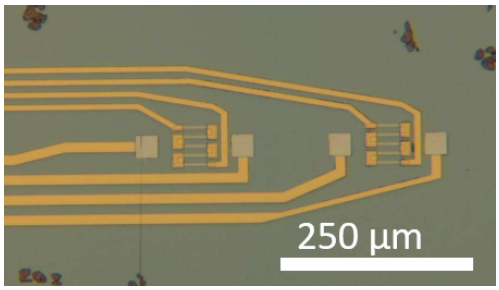

(c) Electrodes deposition

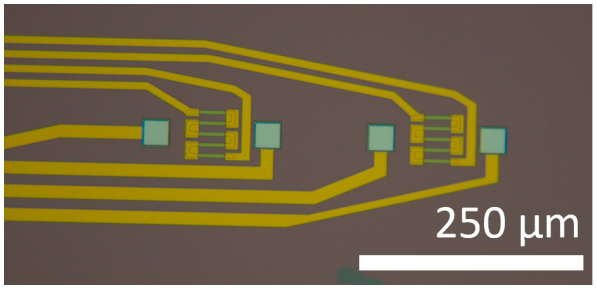

(d) Passivation

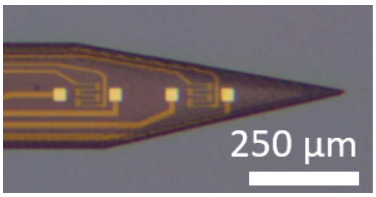

(e) Lithography for cutting

Figure 3.11: Optical image of GMR at each step of fabrication after acetone cleaning.

between material and masking material is too low. To enhance the selectivity, etchant based on fluorine are effective but the etching becomes isotropic, which does not permit to etch with vertical sidewalls. To overcome this issue, the Bosch deep silicon process etching alternates between short etching steps and short passivating steps under plasma etching. During passivation, CF-species are deposited all over the sample (walls and bottom of the structure) and high energy ions from the plasma only etch the bottom of the passivation layer, leaving the sidewalls protected during the etching step. During the etching step, F-species do an isotropic etching but as the sidewalls are more protected than the bottom, the etching is almost anisotropic, leaving a small sidewall roughness.

Bosch deep silicon etching can be realized at room temperature. The selectivity between material and photoresist mask is high, with a ratio of 200:1. Finally an eaching rate of 10 µm/min can be achieved [8].

Deep RIE etching

The SOI wafer is etched in several steps as shown in fig. 3.13 as silicon and $SiO_2$are etched by different reactive species.

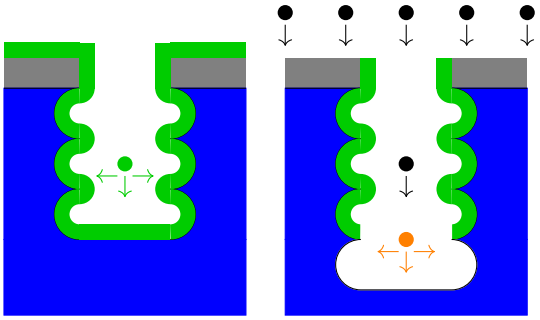

(a) Passivation step. (b) Etching step.

Figure 3.12: Bosch process principle. Black dots are high energy ions (anisotropic) (a) Passivation step with CF-species (green dot) with an isotropic deposition (b) Etching step with F-species, the passivation is etched in the bottom by high-energy ions, and F-species (orange dot) can etch the bottom of the structure.

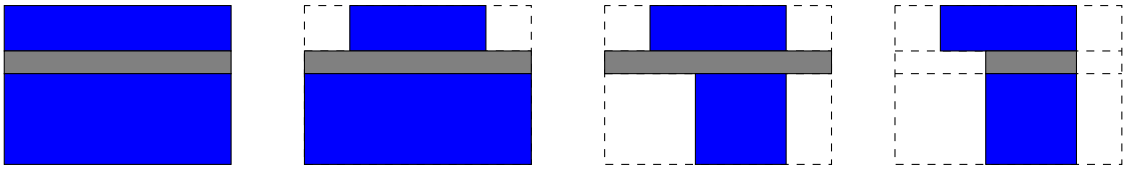

(a) Before Deep RIE (b) After top-side etching (c) After silicon on back-side etching (d) After silica on back-side etching

Figure 3.13: Scheme of Deep RIE steps, silicon is in blue and silica is in grey. (a) The device layer is etched (25 µm) of silicon to shape the final form of the magnetrode. (b) The handle layer (400µm of silicon) is etched under the tip to decrease its thickness down to 25µm and around the magnetrode body. (c) The oxide buried layer (2µm of SiO_2) is etched under the tip and around the magnetrode body. The final thickness of the tip is 25µm while the body is 427µm thick.

Several steps of lithography are needed to define part of the wafer to be etched. A primer is used to enhance the adhesion properties of the wafer before coating the wafer with the photoresist AZ4562. The photoresist is spin-coated and baked during 1 hour at 90 °C. The exposure is made by a laser beam and the mask can be adapted between two exposures. During development, the wafer is immersed in a solution of Az 400k diluted by water with a 3:1 ratio during 3 min and 30 sec. The remaining photoresist has a thickness of 10µm.

The top side etching etches the contour of the magnetrode, including tip and body. It includes etching the GMR passivation (Al_2O_3, Si_3N_4) and the insulating layer (SiO_2) in addition to the device layer (cf fig 3.13b). The back side etching etches the handle layer and the buried oxide under the tip and around the magnetrode body. Before etching the back layer, one must check if there is an additional layer of SiO_2. There are several ways to produce an SOI wafer and one of them grows an additional oxide layer at the bottom during buried oxide layer growth. If there is an additional oxide layer it is important to etch this layer before etching the silicon handle layer. Otherwise, during Bosch process the oxide layer is not etched and during the passivation step, the passivation increases until it cannot be etched anymore.

Once the bottom oxide layer is removed (if needed) the handle and buried oxide layers are etched in two steps (fig 3.13c and fig 3.13d), and magnetrodes can be removed.

Top-side etching The top-side lithography is made with a laser lithography because chromium masks were not made as we first intended to cut magnetrodes with an excimer laser. After lithography, the wafer is placed on a support wafer of silicon. It is maintained by fomblin oil. The wafer is cleaned by an O_2 plasma during 15s. Then the temperature of the platform with the wafer is decreased to $-10\,°C$. The etching of the GMR passivation (270 nm) and oxide layer (500 nm) lasts $\sim$ 23 min.

The etching chamber is then cleaned and the platform temperature is raised to $0\,°C$. The wafer is placed on a SiO_2wafer. To etch the 25 µm of the device layer, 22 cycles with a Bosch process are typically needed.

The fomblin oil is cleaned from the back side with isopropanol. The wafer is finally cleaned with acetone and isopropanol before the next lithography step.

Back-side etching The additional oxide layer at the back is etched in the laboratory by RIE with a plasma of O_2 and CF_4 during 16min. The front side is protected by AZ5214.

The lithography of the back side is more complex. Indeed, there are no marks on the back side. A small hole is drilled with a laser from the front side and through the entire SOI wafer to serve as an alignment mark for the backside lithography. The hole in addition to the edges of the wafer is sufficient to do an alignment for lithography in the back side. The lithography is then made by laser lithography which does not need a chromium mask but takes several hours. For future lithography processing, it would be interesting to have two masks: one for the front-side and a second for the back-side etching. The laboratory has recently acquired an infra-red modulus which added on the MJB4 allows to align the back side of a silicon wafer with a chromium mask.

This will allow the possibility to realize a precise alignment and quick exposure for the back-side lithography.

For the Deep RIE of the handle layer (400 µm), the wafer is placed on a support wafer of SiO_2. The sample is then cleaned by an O_2 plasma and the potential oxide residuals are etched by RIE during 2 min. The handle layer is etched with a Bosch process during 320 cycles.

The oxide buried layer (2 µm of SiO_2) is then etched either in the laboratory or in Femto-ST by conventional RIE.

Probes releasing

After Deep RIE and RIE, magnetrodes are ready to be released from the wafer. The wafer is put in a bath of isopropanol. The unetched parts of the SOI wafer are taken off to facilitate the releasing of magnetrodes. This step is very delicate and can lead to probes breaking. The probes are delicately pushed off the wafer by dragging them from the center of the wafer to the edges.

Probes cleaning

Once the probes are all released from the sample, the fomblin oil needs to be cleaned from the top side on which the GMR sensors and electrodes are. We tried several methods from isopropanol bath, soap cleaning and mechanical cleaning. The best

method is to dip the magnetrode in Novec 7200 to remove the fomblin oil without probes breaking. The results of magnetrode etching is shown in fig. 3.14.

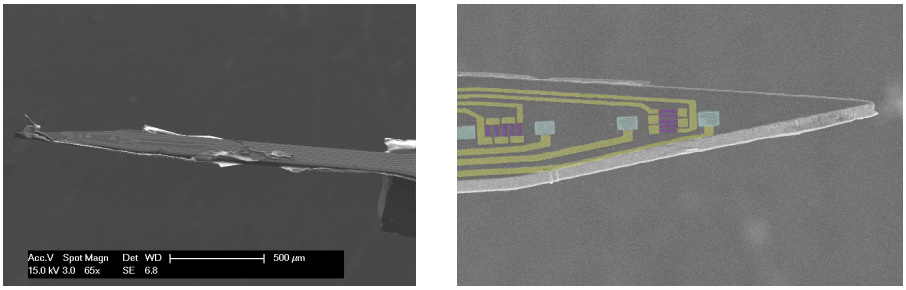

(a) Magnetrode (b) Magnetrode tip

Figure 3.14: SEM image of a magnetrode after deep RIE. (a) The tip has a thickness of 25 µm and the body has a thickness of more than 400 µm. (b) Magnetrode tip with colorized GMR sensor in violet, electrodes in light blue and contacts in yellow.

Problems encountered

We faced several problems during magnetrode etching as shown in fig. 3.15. First, we had an unexpected oxide layer at the back of the SOI wafer, leading to over passivation during Bosch process and resulting in the loss of the sample. Once we had identified the problem, we added an oxide etching step as well as a control after a few cycles of silicon etching to prevent any over passivation issues.

Then we realized that our first mask for front-side etching was too narrow. For some probes, an electrode contacts line is cut by deep RIE etching. We adapt the numeric mask for the laser driven lithography by increasing the width of our final probes.

The alignment for the back-side lithography is not perfect but it does not weaken the probe. A better alignment is expected with the infra-red modulus of the alignment machine (MJB4) and chromium mask with an increased width for the tip.

Finally, there is residual oxide from the oxide buried layer. This is a problem as it can damage neurons during the insertion of the probe.

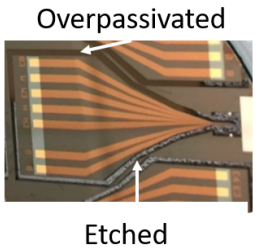

(a) Over passivation

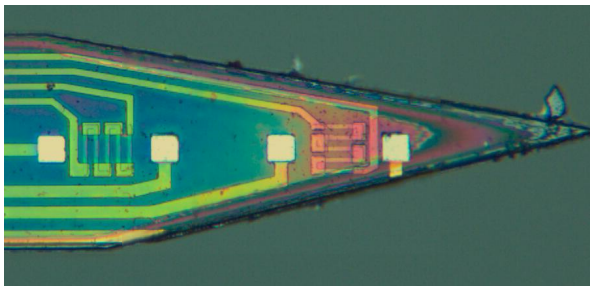

(b) Cut contact line

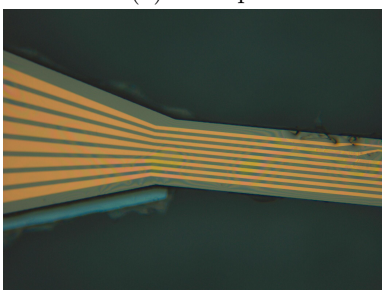

(c) Back-side alignment

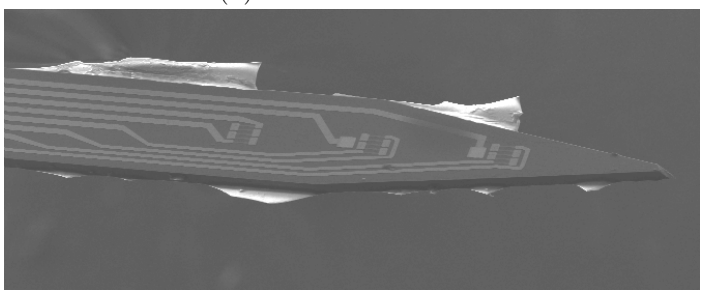

(d) Residual SiO_2

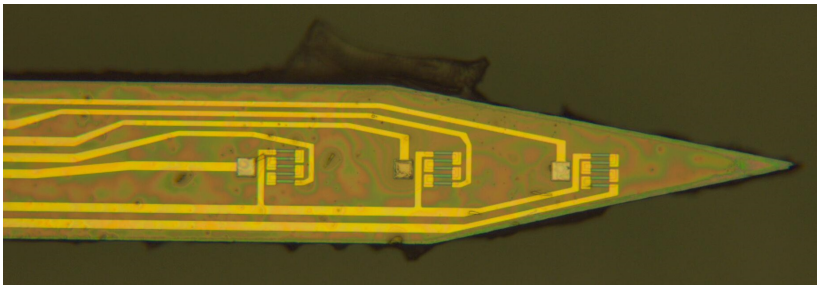

(e) Residual fomblin oil

Figure 3.15: Issues encountered during magnetrodes etching. (a) Overpassivation after Deep RIE: the bottom side of the magnetrode is etched but not the top side. This magnetrodes wafer is lost because the overpassivation cannot be etched to release the probes. (b) The contact line of the first electrode is cut, hence the top electrode cannot be used during *in-vivo* recordings. (c) The back-side alignment is not perfectly align with the top-side. However, it does not does not weaken the probe. (d) The buried oxide layer is not entirely etched. Some residuals are attached to the probe side. (e) In addition to residual SiO_2, the oil used to maintain and thermalized wafer during Deep RIE is not washed away by acetone nor isopropanol.

3.2.3 Magnetrode packaging

After releasing the magnetrodes, a magnetotransport measurement is made. Indeed, at some point in the process, GMR sensors can be heated and the reference layer may have lost its magnetic orientation. In this case, magnetrodes are annealed as described earlier and then they are placed on top of a dedicated PCB. For each magnetrode design, a PCB is made to connect GMR sensors and electrodes to the acquisition chain. A universal electronic system is designed to interface any magnetrodes with up to 3 GMR sensors and up to 4 electrodes with the acquisition chain. This allows to minimize the electronics material and to facilitate the replacement of magnetrodes design during *in-vivo* experiment as the set-up is the same for every magnetrode.

The placement of the magnetrode on the PCB needs to be precise and wax is used to

glue the magnetrode on the PCB. Then magnetrodes are wire-bonded by ultra-sound soldering with an aluminum wire of 25 µm and protected by araldite (cf fig. 3.16). Magnetrodes are then ready to be characterized.

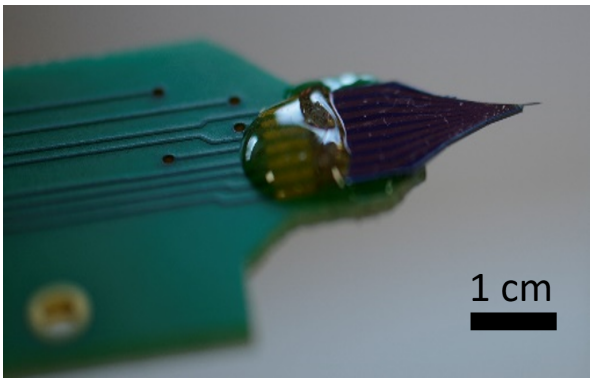

Figure 3.16: Magnetrode mounted on a PCB. The contacts pad of the magnetrode are connected to the PCB by wire-bonding. The thin wires are protected by araldite.

3.3 Characterization

Magnetrodes are characterized by magnetotransport and noise measurements. The characteristics (MR, sensitivity, noise and limit of detection) are compared for each wafer.

3.3.1 Magnetransport

Magnetrodes are placed in Helmholtz coils and the resistance of each GMR sensor depending on the magnetic field is measured. The characteristics of magnetrodes for 2D recording (design 74: 741 and 742) are not shown on R(H) curves. An additional step for the local repinning of the GMR sensors is needed. Both local repinning and characterization are addressed in section 3.4.

First, let's compare R(H) curves for each wafer. In fig. 3.17, R(H) curves from magnetrodes fabricated in 2018 are shown and in fig. 3.18, R(H) curve from magnetrodes fabricated in 2019 are plotted. In fig. 3.17, one can see that for the substrate Si 1, two MR sensors have a lower MR ratio. Also, one GMR sensor of the magnetrode 712 (sensor M3) is broken and cannot be characterized. For the substrate Si 2, two sensors of the probe 722 are not working properly. Indeed, a constant resistance of 200 Ω can be recorded leading to an MR ratio of almost zero. Thus these two sensors cannot be used to record a magnetic field. For the SOI substrate, 5 probes are working with MR ratio between 4.5% to 6%. All working probes seem to have similar properties independently from the substrate (Si or SOI).

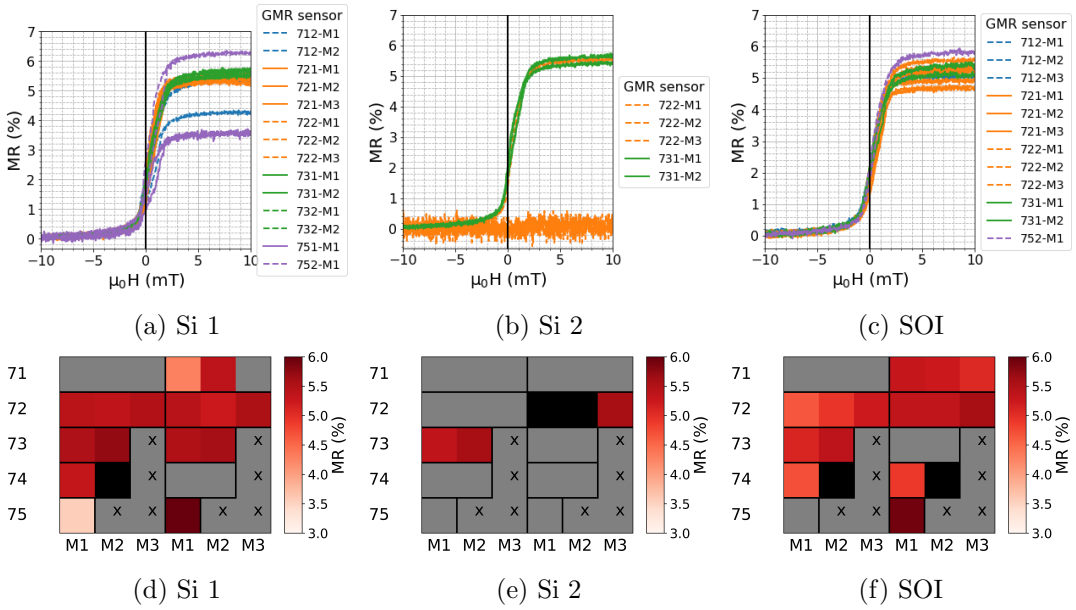

(a) Si 1 (b) Si 2 (c) SOI

(d) Si 1 (e) Si 2 (f) SOI

Figure 3.17: Superposition of R(H) curves of magnetrodes from the same wafer deposited in 2018 (a) - (c) and the corresponding MR values on a colormap (d) -(f). Black squares represent values which are above or below on the scale limit. The gray squares represent an absence of measurement. M1 is the GMR sensor the closest to the tip and M3 the furthest away. The GMR reference stack is deposited on three wafers: (a) a silicon wafer called Si 1, (b) a second silicon wafer called Si 2 and (c) an SOI wafer. In figure (b) two GMR sensors of the probe 722 (M1 and M2) have MR ratio of 0%. This is explained by the resistance of the two GMR sensors. Their resistance is around 200 Ω instead of being around 600 Ω. This can be explained by the GMR sensors being short-circuited by the contacts. MR of all GMR sensors from the same wafer are plotted on a color plot. Gray squares indicate a lack of measurement because the probe is broken. Gray squares with a black cross indicate that there are no sensors to be measured (for example magnetrode with the design 75 have only one sensor which is M1). Black squares mean that the measured MR is not represented on the scale. It is due to a low MR because of short cut like in figure (e) or because the sensor needs a local repinning like in fig (d).

In fig. 3.18, one can see that for the substrate SOI 81-ref., the 5 probes have similar response with an enhanced hysteresis for one sensor of the probes 712 and 722. For the substrate SOI 99-ref. all 6 sensors have a similar R(H) curve. SOI 81-ref. and SOI 99-ref. are two different substrates with GMR sensors composed of the reference GMR stack. The MR ratio is between 5% and 6%.

For the substrate SOI 99-opti., the GMR sensors are composed of the optimized GMR stack. The 3 probes exhibit similar R(H) curve for a MR a bit lower compared to SOI 81-ref. and SOI 99 - ref. around 5%.

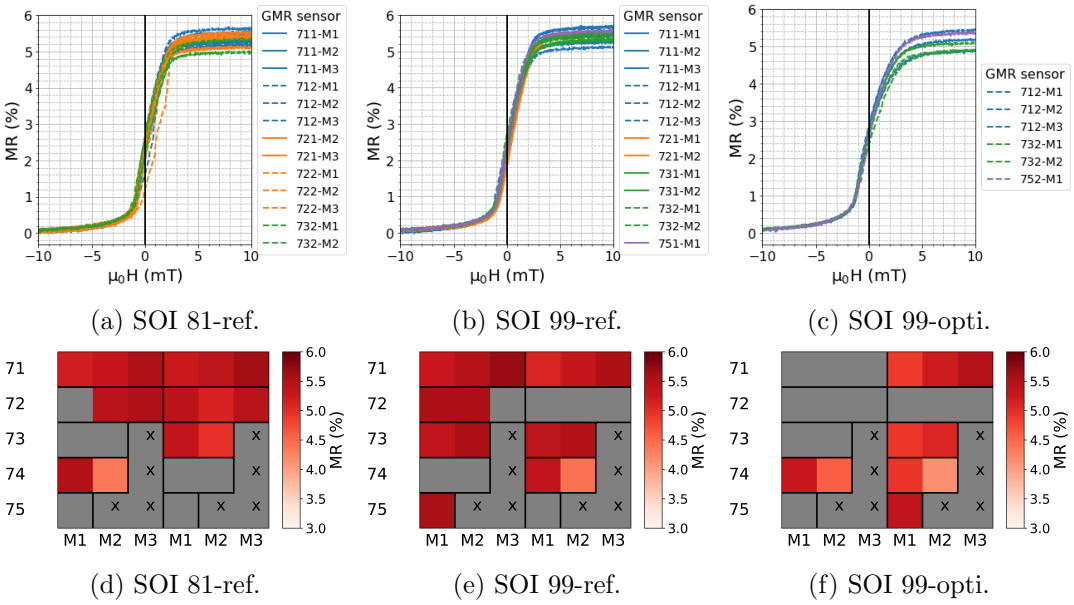

(a) SOI 81-ref. (b) SOI 99-ref. (c) SOI 99-opti.

(d) SOI 81-ref. (e) SOI 99-ref. (f) SOI 99-opti.

Figure 3.18: Superposition of R(H) curves of magnetrodes from the same wafer deposited in 2019 (a) - (c) and the corresponding MR values on a colormap (d) -(f). The GMR reference stack is deposited on two SOI wafers: (a) SOI 81 and (b) SOI 99. The optimized GMR stack is deposited on a SOI wafer called SOI 99. (b) and (c) are deposited on the same wafer cut into several pieces.

The MR for each GMR sensor is plotted in fig 3.19a. The MR is similar for most of the GMR sensors. The MR is a bit lower for the substrate Si 1 -ref., 712-M1 and 752-M1 as expected from R(H) curves. For the substrate Si 2-ref., the sensors M1 and M2 of the probe 721 is almost 0%. The MR for the Si and SOI wafer and for the reference and optimized layer are similar, with an average value of 5.3%. It is below the MR measured for yoke composed of the reference stack or the optimized stack of 4µm (≈6.5%) and lower to meander of 4µm composed of the optimized stack (≈ 6%). This difference can be explained by the fact that the GMR stacks are not deposited at the same time and some parameters can be a bit different (pressure during deposition, ...) or by the impact of the RIE and deep RIE steps.

The resistance for each GMR sensor is shown in fig 3.19b. One can see that the resistance for GMR sensors with the reference stack is a bit higher for silicon wafer than SOI wafer. The MR ratio as well as the sensitivity are good so the 3 sensors are working properly. For the wafer Si 1, the probe 722 shows two sensors (M1 and M2) with a lower resistance. These 2 sensors have an MR close to 0 which means that they are damaged.

The sensitivity for each magnetrode and each GMR sensor are plotted in fig. 3.19c. The sensitivity for the magnetrode with the reference layer is around 1.5%/mT, higher sensitivity comes from resistance jump in the R(H) curve as expected from yokes measurement. Magnetrodes with the optimized layer have a lower sensitivity around 1%/mT. It is lower than expected from yoke and meander measurements (1.5%/mT).

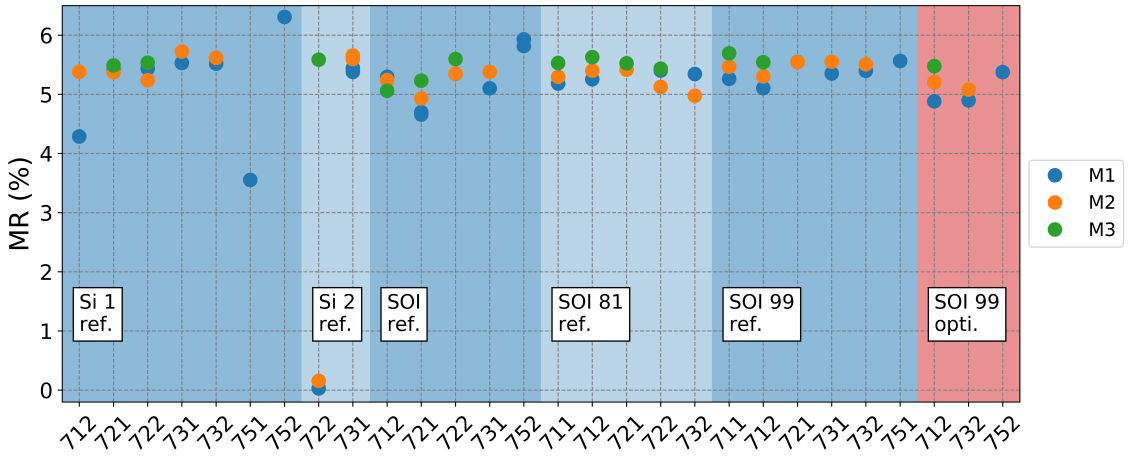

(a) MR

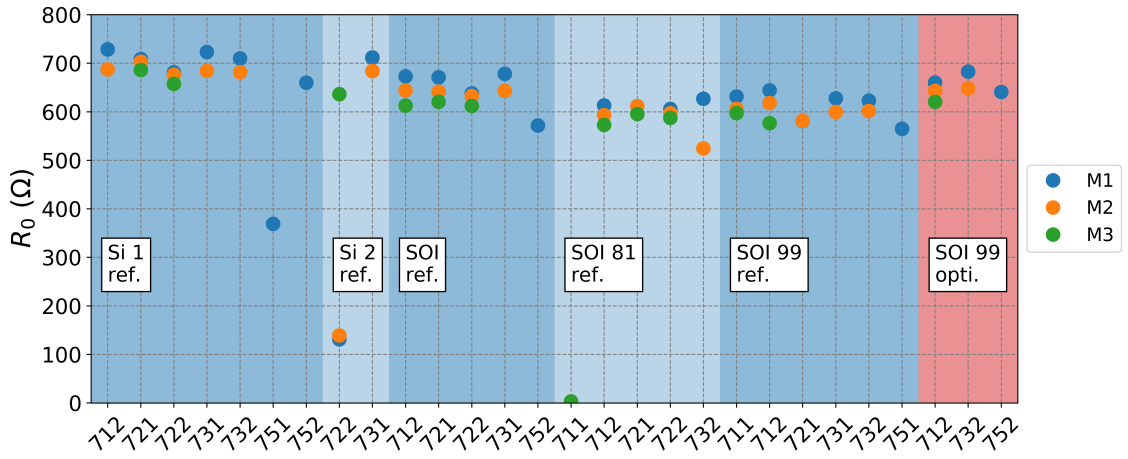

(b) R_0

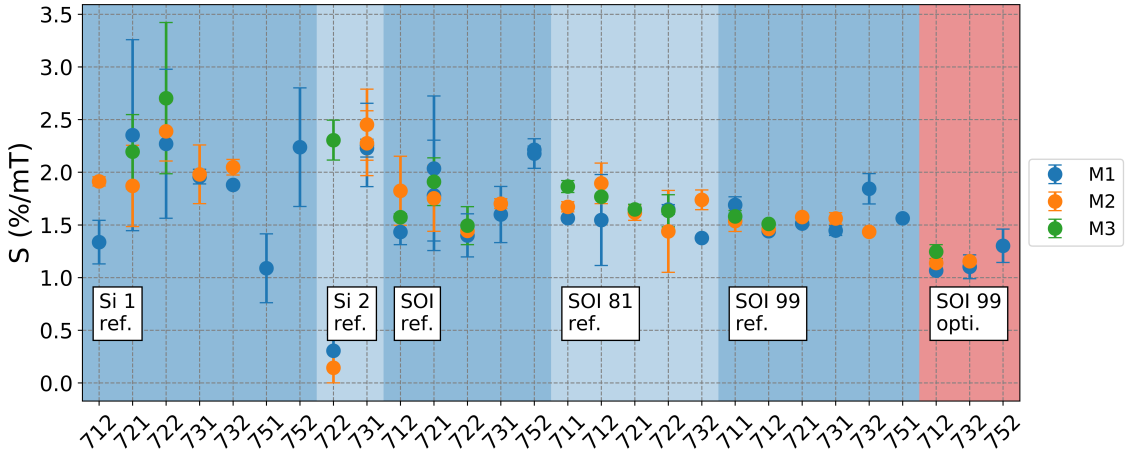

(c) Sensitivity

Figure 3.19: Comparison of GMR sensors characteristics depending on the substrate and GMR stack (blue: reference stack, red: optimized stack). (a) MR (b) $R_0 = \frac{R_{AP}+R_P}{2}$ (c) Sensitivity computed from R(H), error bar is the difference of sensitivity between the two branches.

The fabrication process is reproducible and well controlled. GMR sensors exhibit very similar characteristics. Around half of the magnetrodes exhibit $R_{M1} > R_{M2} > R_{M3}$.

This has an impact on the MR ratio which follows a similar but inverted rule: $MR_{M1} < MR_{M2} < R_{M3}$. This phenomenon is addressed in the annex B. Noise measurements are required to compute the limit of detection around zero field as well as determining the presence of RTN.

3.3.2 Noise measurements

The noise is measured with the same method as described in chapter 2. Magnetrodes with the reference stack have RTN at 1 V in general (cf fig. 3.20) when the optimised stack is stable up to 2-3V. However, as the optimized stack sensitivity is lower than reference stack sensitivity, the limit of detection is impacted and is higher for the optimized stack. For GMR voltage up to 1 V, the best magnetrodes with the reference stack are better than the optimized stack. Magnetrodes with the reference stack are optimal for voltage above 1 V, where magnetrodes with the reference layer start to be unstable due to RTN.

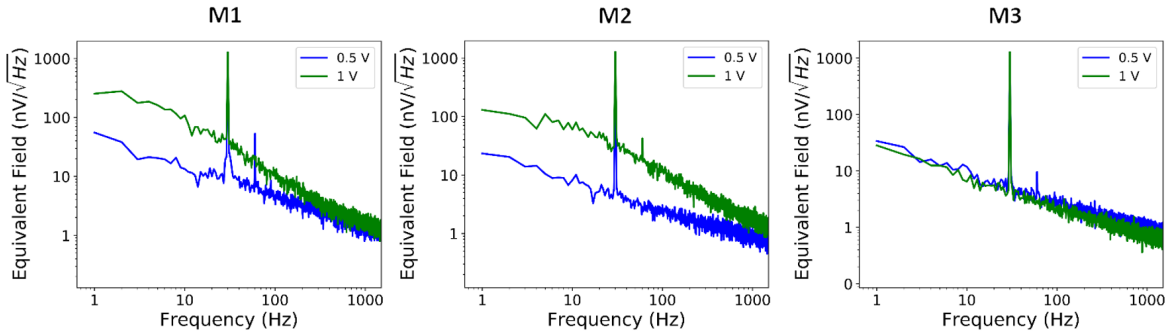

(a) Sensors of a single magnetrode fabricated with the reference stack

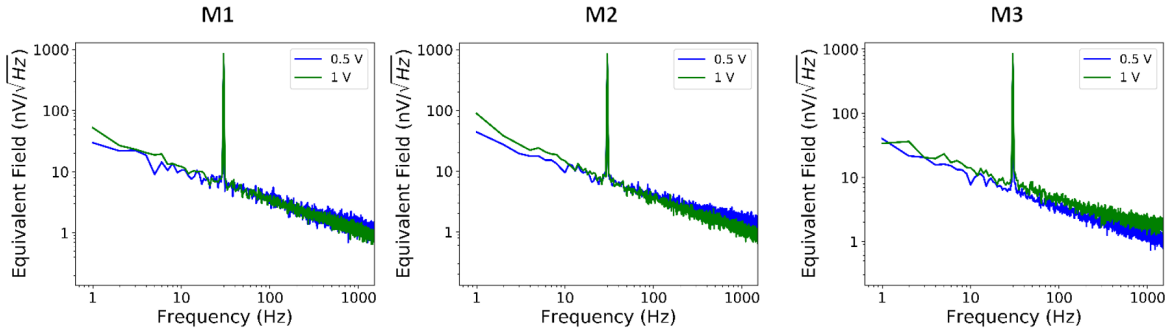

(b) Sensors of a single magnetrode fabricated with the optimized stack.

Figure 3.20: Equivalent field as a function of frequency for a typical magnetrode with (a) the reference stack and (b) the optimized stack. At 1 V, the optimized stack shows less RTN than the reference stack.

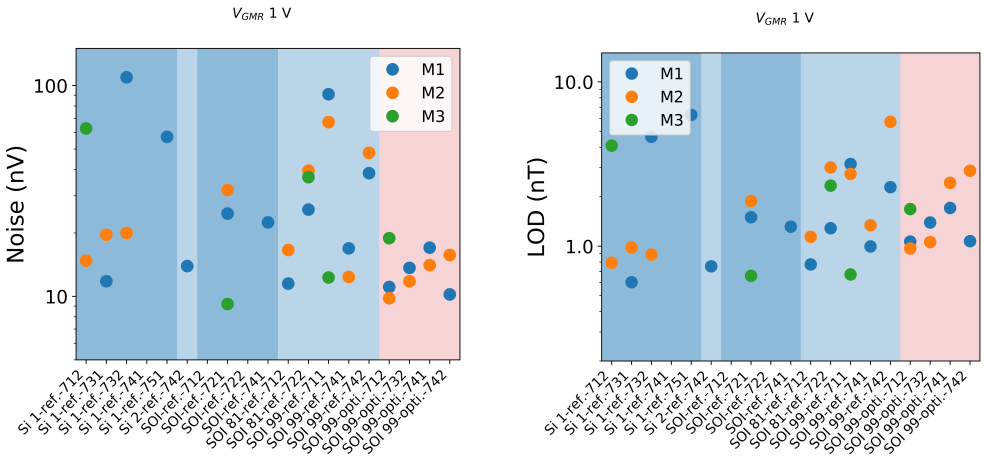

(a) Noise

(b) Limit of detection

Figure 3.21: Noise and limit of detection for each sensor (M1, M2 and M3) of the measured magnetrodes. The blue backgrounds indicate that the magnetrodes sensors are made with the reference layer and the light red is for sensors made with the optimized layer. A change of blue shade means that the magnetrodes have a different substrate than the previous ones. (a) The optimized sensors have a lower dispersion in noise than reference sensors due to almost no RTN (b) The reference layer has a better limit of detection in the absence of RTN due to a higher sensitivity ($\sim$ 1.5 %/mT) compared to optimized sensor with a sensitivity $\sim$ 1 %/mT.

3.3.3 Conclusion

The fabrication process of magnetrodes (developed in the laboratory) is very well controlled and reproducible. Magnetrodes fabricated in 2018 and 2019 have similar properties but despite a lower RTN for optimized stack, up to 1 V, magnetrodes made with the reference stack have a better limit of detection (around or lower than 1 nT). The magnetrode tip thickness has been reduced from 270 µm to 25 µm with a similar sensitivity and noise to thick silicon probes.

3.4 Local repinning for 2D recording

For 2D magnetrodes (design 74), two GMR sensors are designed on the magnetrode as shown on figure 3.22. To realize a 2D recording, the two sensors need to have their axis of sensitivity orthogonal in the plane. The axis of sensitivity is determined by two parameters: the free layer and hard layer magnetization. Also, to have a sensor response, the free layer and the hard layer magnetization of the two GMR sensors need to be perpendicular at zero-field. These two conditions need to be fulfilled for the two GMR sensors but perpendicular axis of sensitivity to have a magnetrode able to do 2D recording. As a reminder, the aim of 2D magnetrodes is to realize a mapping of neuronal activity.

3.4.1 Local repinning method

To have perpendicular axis of sensitivity, one sensor (M2) is turned by an angle of 90° while the other sensor (M1) has a standard orientation (by standard orientation, we mean the same orientation as GMR sensors on magnetrode with designs 71, 72, 73 and 75). The rotation of M2 has an impact on the free layer magnetization as it is controlled by the sensor shape. At this stage, both M1 and M2 have their free layer well oriented. To have both magnetization of the hard layer of both in the proper direction, two steps are needed as described in fig. 3.22.

- **Step 1: global annealing:** all GMR sensors are annealed under a magnetic field during 1 hour (cf fig. 3.22a). M1 and M2 hard layer have the same orientation. M1 is well oriented but M2 hard layer magnetization is parallel to its free layer and needs to be re-annealed without having an impact on M1 hard layer magnetization.
- **Step 2: local repinning:** only M2 is heated with a voltage pulse under a magnetic field (cf fig. 3.22b). M2 hard layer is set perpendicularly to its free layer to have a sensor behavior and at the same time, its magnetization is perpendicular to M1 hard layer magnetization to have two sensors with perpendicular axis of sensitivity.

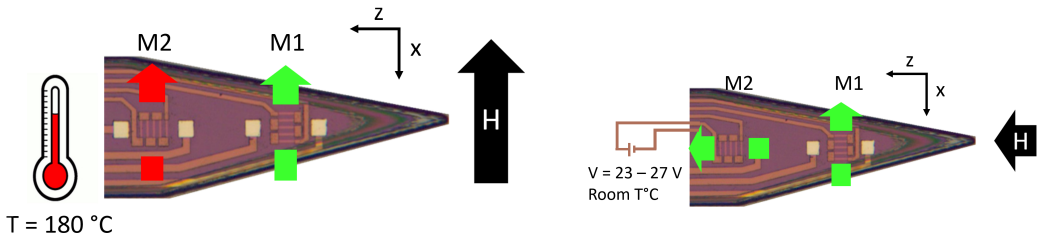

(a) Step 1: global annealing (b) Step 2: local repinning

Figure 3.22: Annealing steps for a 2D magnetrode (The colored arrows represent the magnetization of the hard layers): (a) Step 1: the free layer of M1 and M2 are already orthogonal but after the global annealing M1 and M2 hard layers have the same orientation. M1 is well oriented (green arrow) but M2 needs a local repinning (red arrow). (b) M2 is locally heated by a current pulse under a magnetic field. Only the hard layer of M2 is re-annealed at 90° to have its magnetization perpendicular to both its free layer and M1 hard layer. M1 and M2 have perpendicular axis of sensitivity and can be used to measure a magnetic along x and z axis simultaneously.

Local repinning methods

Several solutions can be used to have GMR sensors with perpendicular axis of sensitivity like the integration of two chips turned by 90° with respect to one another. We chose to use a local heating to only heat M2 over the blocking temperature so M1 hard layer is not impacted by the local repinning method.

Several methods allow to heat a sensor locally: with a laser positioned over one sensor or by Joule heating by sending a voltage pulse to the sensor which needs a local repinning for example. For our local repinning process, we chose to heat M2 locally by Joule heating under a strong magnetic field applied along z due to its simple set-up.

Local repinning process

A magnetic field is generated by an electromagnet (880 mT) and the voltage pulse is delivered by a high-voltage pulse generator (GI SAU-P102). During the local repinning, the MR ratio, sensor's resistance and sensitivity are measured after each pulse to determine the optimal pulse voltage and duration and to prevent sensor degradation due to atomic diffusion. The optimum local repinning parameters are a compromise between exchange bias repinning of the hard layer (the Joule heating needs to be sufficient to achieve a temperature higher than the anti-ferromagnetic blocking temperature) and sensor thermal degradation. The sensor thermal degradation is monitored by change of resistance and we chose to stop the local repinning when the resistance starts to increase.

To study the impact of the local repinning on both M1 and M2, the two sensors are characterized along their sensitive axis (x for M1 and z for M2) as well as perpendicularly to this axis (z for M1 and x for M2, cf fig. 3.23). The MR ratio of M1 and M2 is plotted after the global annealing as a function of the external field for M1 and M2 along x and z. Along its sensitive axis, M1 has a sensor behavior and is well centered. For M2, the free layer is parallel to the hard layer magnetization for ± 10 mT and does

a smooth rotation of 180° but as the hard layer is parallel to the free layer at zero-field, M2 does not have a sensor behavior (cf fig. 3.23). M2 needs to be locally repinned.

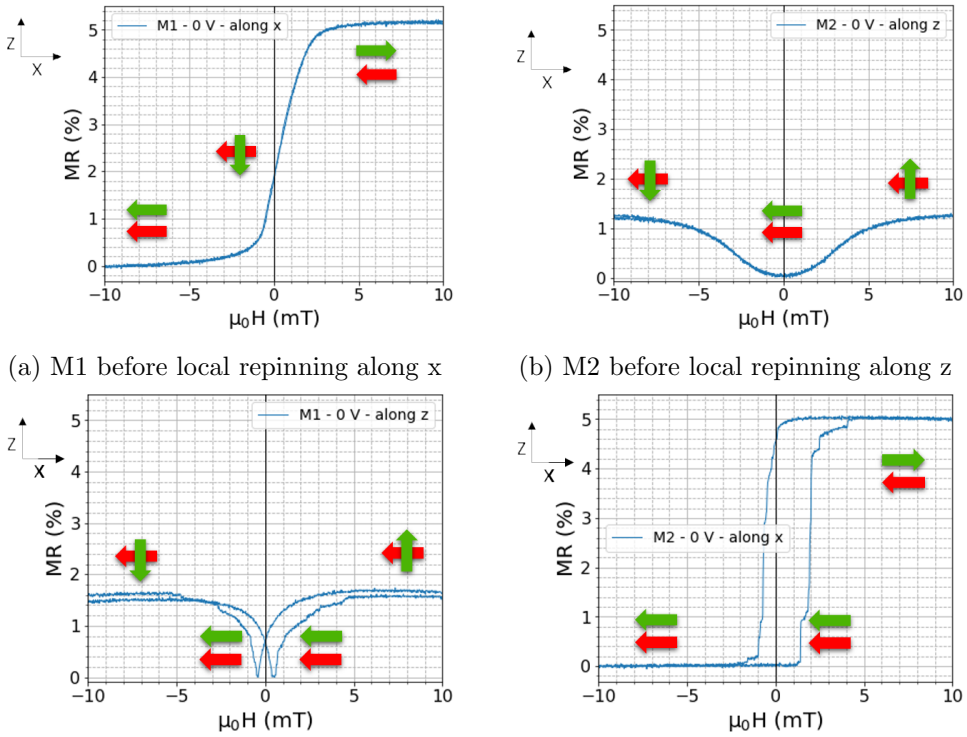

(a) M1 before local repinning along x

(b) M2 before local repinning along z

(c) M1 before local repinning along z

(d) M2 before local repinning along x

Figure 3.23: Sensors responses along their sensitive axis: (a) along x for M1 and (b) along z for M2 and perpendicularly to their sensitivity axis: (c) along z for M1 and (d) along x for M2. The red arrows represent the magnetization direction of the hard layer and the green arrows, the magnetization direction of the free layer. (a) M1 response. The hard layer is well oriented. M1 has a linear response around zero field and two saturation plateaus. (b) M2 response. M2 needs a local repinning because its free layer and hard layer magnetization directions are parallel at zero field. M2 cannot be used as a sensor in this state. (c) M1 response to a field perpendicular to its axis of sensitivity. The butterfly shape comes from the different anisotropy energy (shape anisotropy and magnetocrystalline anisotropy) (d) M2 response to a field perpendicular to its axis of sensitivity.

3.4.2 Results

Magnetotransport

After each voltage pulse, a magnetotransport measurement is made for M2 along x and along z. It allows to follow the evolution of MR ratio, sensitivity and resistance with the amplitude of the voltage pulse and duration. The local repinning starts for a voltage of 20V and stops at 23V for the two examples in figure 3.24. For probe A (magnetrode SOI 99-ref.-742), the figure shows the evolution of the resistance as a function of the external field parallel to the sensitive axis of the sensor depending on the voltage of the pulse used for local repinning. The inset shows the response of the sensor as a function of the external field applied perpendicular to the sensitive axis of the sensor. When the intensity of the voltage pulse increases, the hard layer magnetization starts to

rotate to be parallel to the external field which is along z. When the hard layer is fully magnetized along the z-axis, the hard magnetization is parallel to the free layer. The apparition of two plateaus when an external field is applied in the direction parallel to the sensitive axis of M2, and inversely the disappearing of two plateaus when the field is perpendicular shows the evolution of the hard layer magnetization direction. For probe A, the local repinning is stopped at 23 V because in the P state, the resistance is higher for 23V compared to the resistance at 22 V (cf fig. 3.24). This can mean that the GMR stack composition starts to be degraded by interlayer mixing (atomic diffusion). For probe B (magnetrode SOI 99-ref.-741), the local repinning is also stopped at 23 V because we reached the same MR ratio after the local repinning along the sensitive axis as before the local repinning perpendicularly to the sensitive axis (cf fig 3.25).

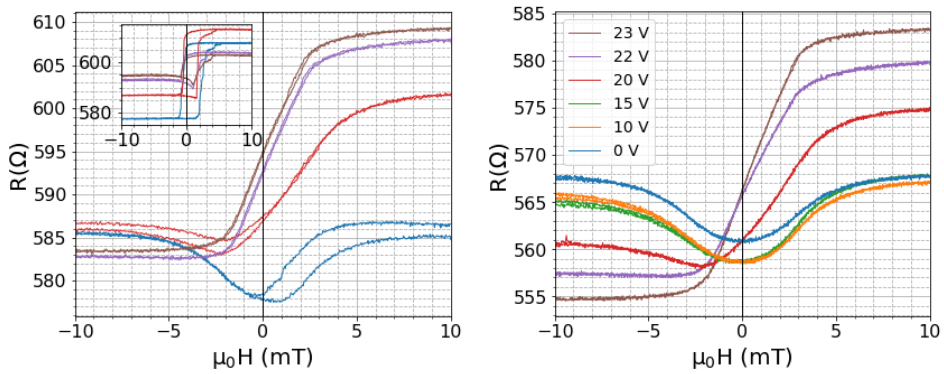

(a) Probe A (b) Probe B

Figure 3.24: Impact of voltage on resistance (a) Probe A: the local repinning is stopped at 23V because the resistance starts to increase, despite a low MR of 4.4%. In comparison, the MR ratio of M1 is 5.4% and before local repinning the MR of M2 was 5.1%. (b) Probe B: the local repinning is stopped at 23V because we reach the maximum MR of all local repinning. The MR ratio of M1 is 5.5% and the MR ratio of M2 is 5.1%.

To estimate the maximal MR ratio of M2 sensor we could expect, we used the MR ratio of M2 before local repinning perpendicularly to its axis of sensitivity. By comparing MR ratio before local repinning perpendicularly to the sensitive axis and after local repinning along the sensitive axis (cf fig 3.25), we can estimate that for probe A, the sensor is not completely repinned because the MR after local repinning is lower than the MR ratio before local repinning. For probe B, the MR after local repinning is similar to the MR after the annealing, thus we can assume that the repinning is complete.

In figure 3.19c (as we saw previously) the sensitivity is around 1.5%/mT for the reference GMR composition. As we saw previously, the sensitivity can be described by the following equation when there is no hysteresis:

$$S = \frac{GMR}{2\mu_0 H_A} \tag{3.1}$$

In figure 3.26, the response of both sensor M1 and M2 along their sensitive axis (respectively along x and along z) is plotted for probe A and probe B. For probe A, M2 is not completely repinned and its MR ratio (4.4 %/mT) is much lower than M1 MR ratio (5.3 %/mT). If we suppose that the anisotropy field ($\mu_0 H_A$) is the same for M1 and M2, then, as the sensitivity of M1 is 1. 5%/mT, we could expect a sensitivity of

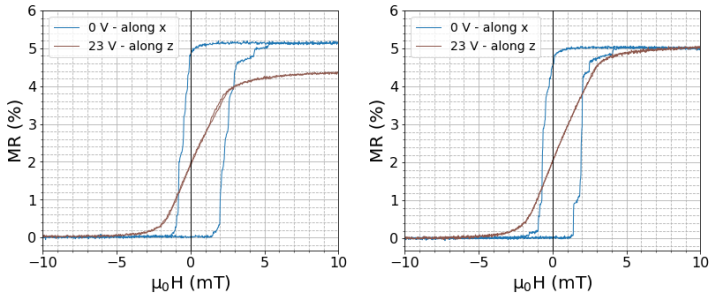

(a) Probe A (b) Probe B

Figure 3.25: MR comparison before local repinning perpendicularly to the sensitive axis (along x) and after local repining along the sensitive axis (along z). (a) The MR after the local repinning is lower. The local repinning must be incomplete. (b) The MR before and after the local repinning is the same. We can consider the local repinning complete.

1.2 %/mT for M2. However,the computed sensitivity of M2 is lower and has a value of 0.9 %/mT. For probe B, with the same hypothesis, the expected sensitivity for M2 is 1.5 %/mT as the sensitivity of M1 is 1.7 %/mT and M1 and M2 MR ratio are 5.5 % and 4.9 %/mT respectively. The measured sensitivity is also lower with a value of 0.9 %/mT which is the same as probe B. The lower sensitivity for M2 sensors after the local repinning cannot be explained by a lower MR as sensitivity does not scale with the MR (probe A and probe B have the same sensitivity and different MR).

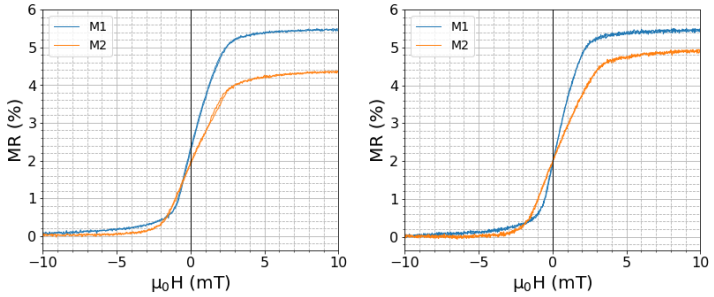

(a) Probe A (b) Probe B

Figure 3.26: Comparison of the response of M1 and M2 along their sensitive axis (respectively x and z) as a function of the external field. (a) The MR ratio of M2 is much lower than M1. Thus a difference of sensitivity is expected. (b) The MR ratio M2 is a bit lower than the MR ratio of M1 (4.9% and 5.5% respectively). The slope of the linear part is higher for M1 than for M2 and thus we can also expect a lower sensitivity for probe B despite a MR ratio of 4.9%.

By comparing M1 and M2 R(H) before and after the local repinning, we can observe that the MR ratio of M1 is slightly increased without having an impact on its sensitivity (cf fig 3.27). From the inset figure, for M1 the two plateaus are well aligned. This indicates that the hard layer is well oriented. For M2, the curves do not superpose and the plateaus are not aligned. This indicates that the hard layer might not be as well aligned as we thought when considering figure 3.25.

The local repinning process was used on 5 probes and the results are summarized in figure 3.28. Magnetrodes with the reference stack composition have a higher sensitivity than the optimized stack as expected. The probe with the maximal MR after local

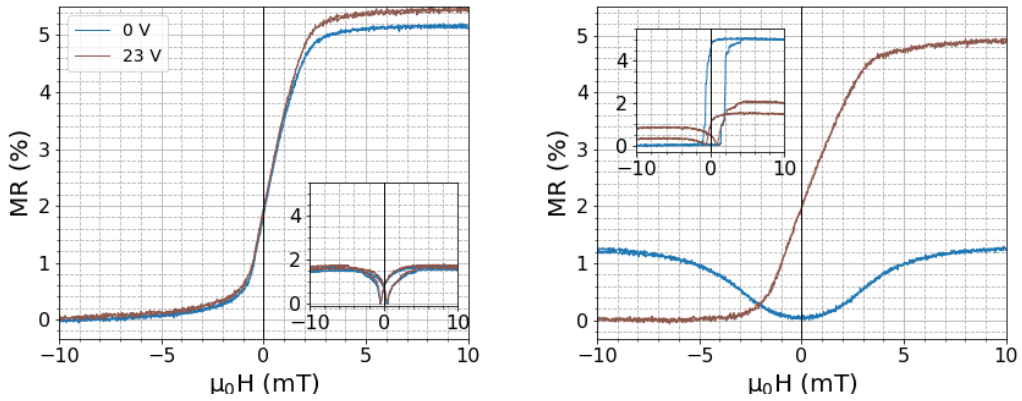

(a) M1 (b) M2

Figure 3.27: Probe B. Response of M1 and M2 along their sensitive axis before local repinning (0 V) and after local repinning (23 V). The inset figures represent the response of M1 and M2 perpendicularly to their sensitive axis.(a) M1 is slightly impacted by the local repinning, its MR ratio is a bit higher after the local repinning. It does not have an impact on M1 sensitivity. The inset figure shows that the hard layer is well oriented because the two plateaus are at the same level. (b) M2 is locally repinned and has a sensor behavior after the local repinning. However, the inset figure shows that, after the local repinning, the hard layer might not be as well repinned as we thought because the two plateaus are not at the same level and the response is different depending on the history of the sensor.

repinning is the magnetrode with the reference layer deposited on the substrate SOI 99 with the name 741 (probe B). It is the only probe with the same MR before local repinning along x and after the local repinning along z. For the probes with the reference stack, the MR ratio of M2 after local repinning is 4.6±0.4% and the sensitivity is 0.9±0.0%/mT as we can see on figure 3.28. For the probes with the optimized GMR stack, the MR ratio of M2 after local repinning is 4.4±0.3% and the sensitivity is 0.7±0.0%/mT. M2 sensitivity is a bit lower for the optimized GMR stack but the difference of sensitivity between M1 and M2 is lower. M1 sensors have a sensitivity of 1.6±0.1%/mT for the reference GMR stack and 1.0±0.1 for the optimized GMR stack.

From magnetotransport measurements, we can preliminarily conclude on the quality of the local repinning procedure (same MR before local repinning along x and after local repinning along z, no hysteresis, sensitivity) but noise measurements in the shielded room are required to measure the limit of detection.

Noise measurements

The noise level of M1 and M2 is measured along their sensitive and non-sensitive axis. We first expected to measure only a sensitivity along x for M1 and z for M2 but, as shown in figure 3.29, M1 and M2 exhibit a sensitivity both along x and z.

First, we compared the sensitivity computed from R(H) and from noise and, as we can see in figure 3.30, they are similar. For M1, the sensitivity along z is 2/3 of the sensitivity along the sensitive axis x (respectively 1.1 %/mT and 1.7 %/mT). For M2, the sensitivity along x is 1/3 of the sensitivity along the sensitive axis z (respectively 0.3 %/mT and 0.9 %/mT). Both sensitivities along x and z need to be taken into

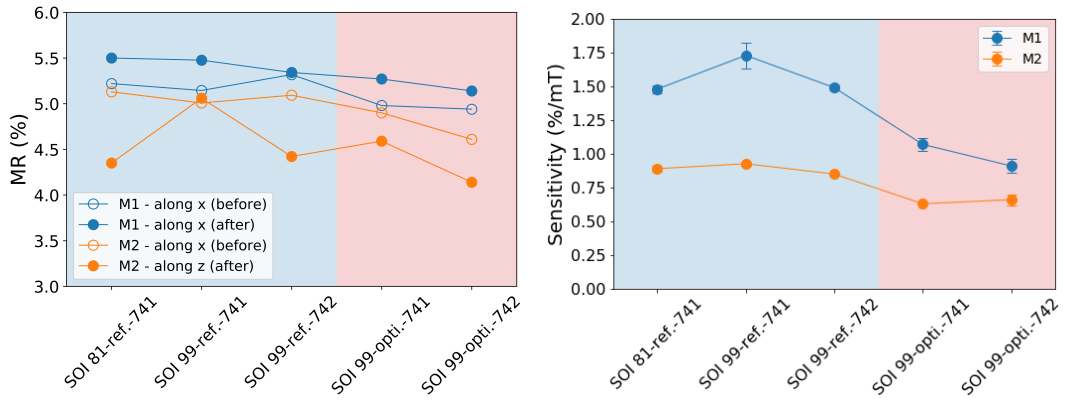

(a) MR ration (b) Sensitivity

Figure 3.28: Summary of MR ratio (before and after repinning) and sensitivity of M1 and M2 along their sensitive axis after local repinning for probes with SOI substrate and GMR stack with the reference or the optimized composition.

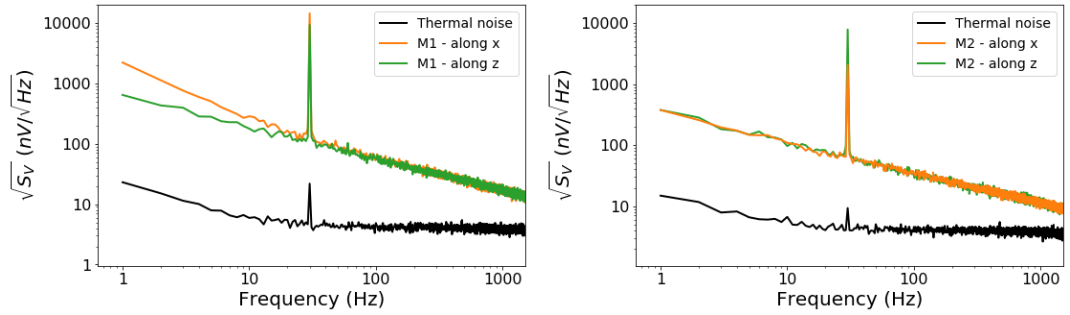

(a) M1 (b) M2

Figure 3.29: Noise measurements of the magnetrode SOI 99-ref.-741. (a) Power spectral density of M1 at 0V (thermal noise) and at 1V along x (sensitive axis) and along z. (b) Power spectral density of M2 at 0V (thermal noise) and at 1V along x and along z (sensitive axis). Perpendicularly to their sensitive axis, M1 and M2 have a peak at 30Hz. M1 and M2 are both sensitive along their sensitive axis and perpendicular to their sensitive axis.

account, the sensitivity perpendicularly to the sensitivity axis is too important to be neglected. This measurement was repeated for each probe (except for magnetrode SOI 81-ref.-741) at different GMR sensor biasing voltages and the results are plotted in figure 3.30. Sensitivity behavior is well defined, depending on the GMR stack (reference or optimized) and axes of measurement (along or perpendicular to the sensitive axis).

As we can see in figure 3.31, the noise level of M1 and M2 of a same probe are close. The LOD is lower for M1 except for the magnetrode SOI 99-ref.-741, because the lower noise level of M2 compensates for its low sensitivity.

Thus, we achieve the local repinning of GMR sensor to have magnetrode able to realize 2D recording. We still need to understand why the sensitivity is lower after a local repinning compared to regular annealing. The next step is to use 2D probe with a phantom to test the reconstruction of a magnetic field with 2 GMR sensors with orthogonal axis of sensitivity.

section2D phantom study To test the response of a 2D magnetrode when exposed to

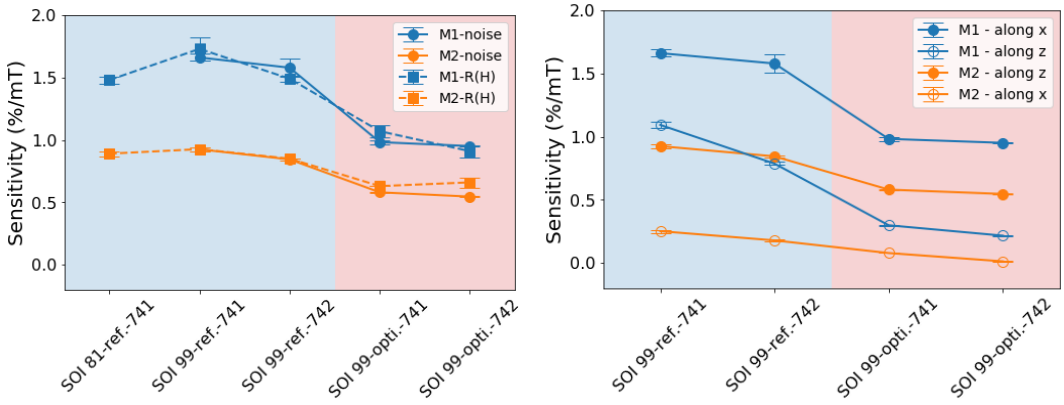

(a) Sensitivity along the sensitive axis of M1 and M2

(b) Sensitivity along x and z

Figure 3.30: (a) Comparison of the sensitivity of M1 and M2 along their sensitive axis (respectively x and z). The results from R(H) and noise measurements are coherent. (b) Comparison of sensitivity of M1 and M2 along their sensitive axis (full circles) and perpendicularly to it (empty circles). For the reference GMR stack, sensitivity of M1 perpendicularly to its sensitivity axis and M2 along its sensitivity axis are very similar. For the optimized GMR stack, each sensitivity is well separated.

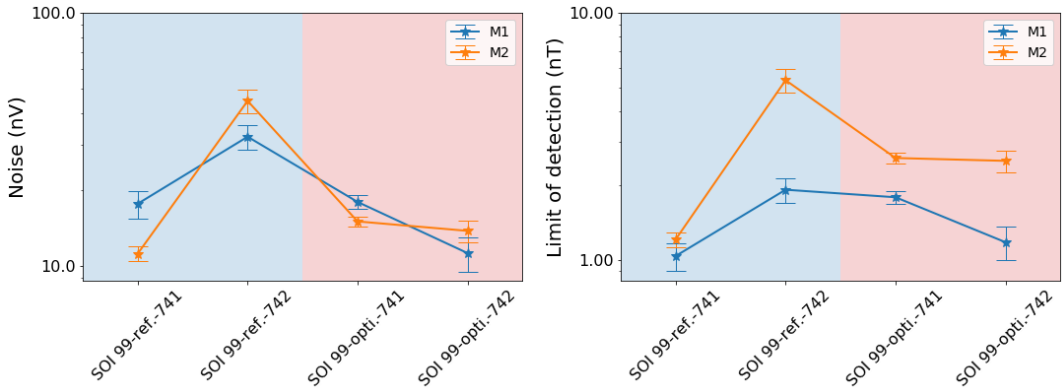

(a) Noise

(b) Limit of detection

Figure 3.31: (a) Noise at 1kHz for a GMR voltage of 1V. The noise level of M1 and M2 is similar, only the magnetrode SOI99-ref.-742 has a noise level both for M1 and M2 higher than the other magnetrodes. (b) Limit of detection at 1kHz for a GMR voltage of 1V. The limit of detection is lower for M1, it is expected as M1 sensitivity is higher than M2. Only the magnetrode SOI 99-ref.-741 has similar limit of detection for M1 and M2. This can be explained by a lower noise for M2 compared to M1 which compensates the difference in sensitivity.

a magnetic field, a phantom has been designed with 3 wires. The wires are made of aluminium and have a thickness of 25 µm. Two of them are placed perpendicularly:

- along z to generate a magnetic field along x
- along x to generate a magnetic field along z.

We use the following convention: a magnetic field generated along x has an angle of 0° and a magnetic field generated along z has an angle of 90°. The third wire is placed with an angle of 45 °.

The objective is to test the reconstruction of the magnetic field from the signal recorded by M1 and M2. By reconstruction we mean computing the magnitude and the angle of the external field.

3.4.3 Set-up

The probe is placed close to the wires (around 2 mm height) with both sensors above the wires (cf fig 3.32). The wires are powered with up to two independent current sources which can deliver a current with various amplitudes and frequency. The output voltage of M1 and M2 are recorded simultaneously and then amplified and filtered with the same set-up as for noise measurement. The generated magnetic field has a sinusoidal shape and the amplitude of the signal recorded by M1 and M2 is extracted for the power spectral density. With this method, we should reach a limit of detection of 1 nT (cf sec. 3.4.5). To reach a limit of detection below the noise level of the GMR sensor *ie* below 1 nT, an averaging over a higher number of events is needed (cf sec. 3.4.6).

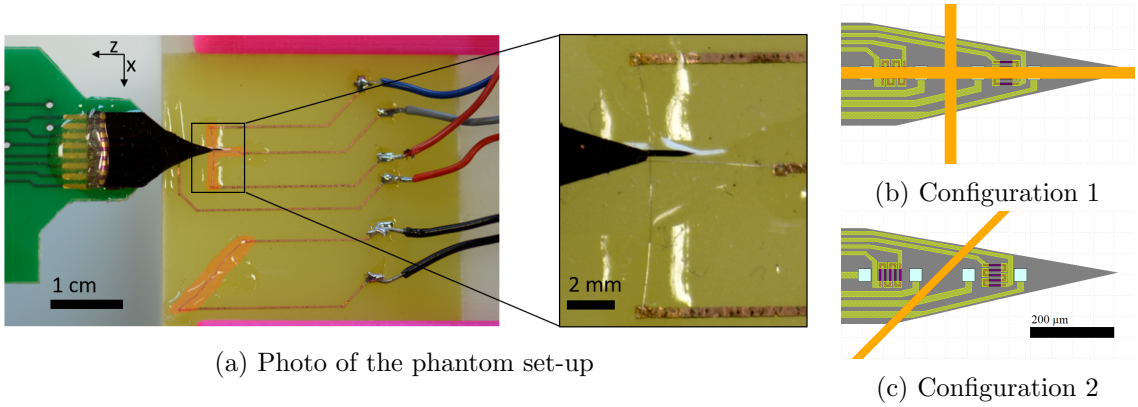

(a) Photo of the phantom set-up

(b) Configuration 1

(c) Configuration 2

Figure 3.32: Phantom set-up used to test the 2D-recording of the magnetrode. (a) Optical picture of the phantom set-up. Wires are highlighted in orange. The probe's tip is placed over the wires. (b) and (c) Schematic of the wire positions relative to sensors M1 and M2 in configuration 1 and 2 respectively.

The outputs of M1 and M2, when the wires are powered, are presented in fig. 3.33. When the magnetrode is placed over the orthogonal wires (configuration 1), a magnetic field can be generated at 0° (fig. 3.33 left) or at 90° (fig. 3.33 middle). As the two wires are not at the same distance from the magnetrode, the second wire is powered with a higher current. In configuration 2 (fig. 3.33 right), M1 and M2 measure a magnetic field which is neither perpendicular nor parallel to their sensitive axis.

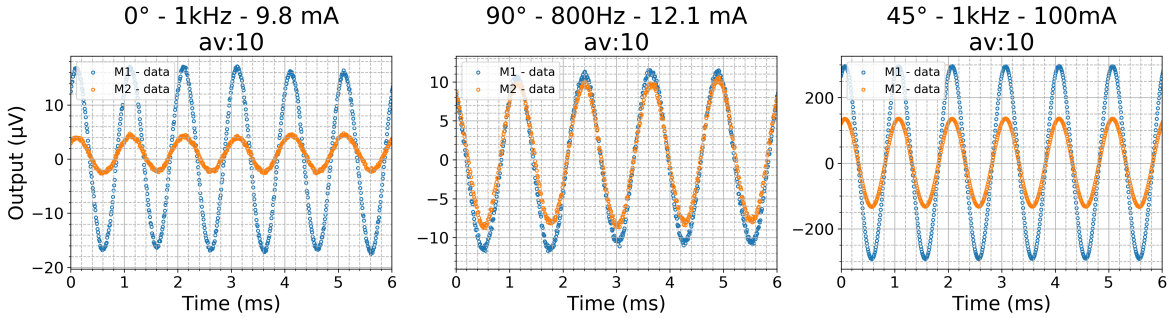

Figure 3.33: Output voltage of M1 and M2 for a magnetic field at 0° *ie* along x (left), at 90° *ie* along z (middle) and at 45° (right)

In configuration 1, both wires can be powered at the same time to generate a magnetic field simultaneously at 0° and 90°. For example, in fig. 3.34, the first wire generates a magnetic field at 0° and is powered with a current amplitude of 9.8 mA at a frequency of 1 kHz and the second wire generates a magnetic field at 90° with a current amplitude of 12.1 mA at a frequency of 800 Hz.

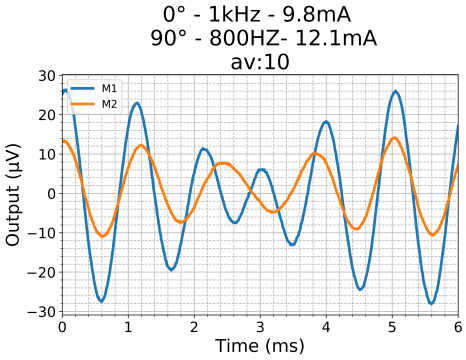

Figure 3.34: Output voltage of M1 and M2 when they are placed over the two orthogonal wires (configuration 1). The two wires are powered and the output of M1 and M2 shows the recording of the two magnetic fields.

The external field is then reconstructed from measurement of M1 and M2 and the sensitivity matrix of the 2D magnetrode.

3.4.4 Method

M1 and M2 are sensitive along x and z and the 2D magnetrode sensitivity matrix is described by:

$$S = \begin{bmatrix} S_{M1,x} & S_{M1,z} \\ S_{M2,x} & S_{M2,z} \end{bmatrix} \tag{3.2}$$

where $S_{i,j}$ if the sensitivity of the sensor Mi along the j axis . The external field along x and z is reconstructed by taking into account the sensitivity along x and z of both M1 and M2:

$$\begin{bmatrix} H_x \\ H_z \end{bmatrix} = S^{-1}. \begin{bmatrix} V_{M1} \\ V_{M2} \end{bmatrix} = \frac{1}{detS}. \begin{bmatrix} S_{M2,z} & -S_{M1,z} \\ -S_{M2,x} & S_{M1,x} \end{bmatrix} . \begin{bmatrix} V_{M1} \\ V_{M2} \end{bmatrix} \tag{3.3}$$

with V_{Mi} the output voltage of Mi for i =1 or 2 and detS=$S_{M1,x}S_{M2,z} - S_{M2,x}S_{M1,z}$. The amplitude of the external field and its angle with respect to the x axis are computed

by:

$$H = \sqrt{H_x^2 + H_z^2} \tag{3.4}$$

$$\theta = \arctan(\frac{H_z}{H_x}) \tag{3.5}$$

3.4.5 Experimental results

We conducted several experiments with the probe SOI 99-ref.-741 (probe B in the previous section). Its sensitivity matrix is:

$$S = \begin{bmatrix} 1.7 & 1.1 \\ 0.2 & 0.9 \end{bmatrix} \tag{3.6}$$

with the values in %/mT. Its characteristics are summarized in table 3.4.

Sensor	M1 main sensitive axis x-0°		M2 main sensitive axis z-90°	
MR(%)	5.5		4.9	
Direction of measurement	0°	90°	0°	90°
Sensitivity (%/mT)	$S_{M1,x}$=1.7	$S_{M1,z}$=1.1	$S_{M2,x}$=0.2	$S_{M2,z}$=0.9
LOD (nT)	1.0±0.1		1.2±0.1	

Table 3.4: Comparison of MR, sensitivity and limit of detection (LOD) at 1kHz

The magnetrode is placed in configuration 1, over the orthogonal wires. Only one wire is powered to generate a magnetic field at 0° *ie* along x *ie* along the sensitive axis of M1. The amplitudes of the magnetic field along x (H_x) and along z (H_z) are computed before retrieving the amplitude of the external field (H) and its angle (θ). The magnetrode is not perfectly parallel to the wire so the computed angle may vary a little from the expected values $\theta = 0°$. The peak-to-peak amplitude of the current is decreased until the value of the angle starts to change. The results are summarized in table 3.5.

The power spectral density of M1 and M2 is averaged 10 times and their amplitude at 1kHz are extracted. To be as close as possible to *in-vivo* condition, we use the amplitude peak-to-peak instead of the amplitude 0-peak. Indeed, we expect a magnetic action potential to have an amplitude peak-to-peak between 10 to 100 pT.

$I_{x,pp}$ (mA)	19.6	9.8	1.964	0.196
$V_{M1,pp}$ (nV)	33 049	16 183	3 283	322
$V_{M2,pp}$ (nV)	6 441	3 206	616	177
$H_{x,pp}$ (nT)	1 796	875	180	8
$H_{z,pp}$ (nT)	232	120	20	17
H_{pp} (nT)	1 810	883	181	19
θ (°)	7.35	7.83	6.34	65.15
R_x (mm)	2.17	2.22	2.16	2.08

Table 3.5: Results for a magnetic field generated along x at 1kHz. $I_{x,pp}$ is the amplitude pp of the current powering the wire. $V_{M1,pp}$ and $V_{M2,pp}$ are the amplitude pp at 1 kHz measured by M1 and M2. H_x, H_z, and H are the amplitude pp of the magnetic field along x, along z and its magnitude. θ is the angle of the magnetic field and R_x is the computed distance between the magnetrode and the wire.

From table 3.5, We can see that the value of the angle starts to change from $\theta = 7.59 \pm 0.24$ ° to $\theta = 6.34$ ° for $I_{x,pp} = 1\ 964$ µA to $\theta = 65.15$ ° for $I_{x,pp} = 196$ µA. This can be explained by the small sensitivity of M2 along x (0.2%/mT). The sensitivity of M2 along x is sufficient to record a magnetic field at 0° with a high amplitude but for lower amplitude, M2 records only noise and the computed H and θ is no longer correct.

3.4.6 Limit of detection

During *in-vivo* recordings, the recorded data can be averaged 40 000 times as we will see later in chapter 4. To estimate the limit of detection for M1 along x, the amplitude pp of $I_{x,pp}$ is decreased until the magnetic signal recorded by M1 has a SNR of 1.

To achieve this, the recorded signal is composed of two parts:

- a sinusoidal signal of 2 periods
- a part without an external magnetic field to record only the noise of M1 and the acquisition chain

To prevent recording a huge amount of data, each acquisition is added to the previously averaged acquisition by using the following equation:

$$\overline{m}_n = \overline{m}_{n-1} * \frac{n-1}{n} + \frac{x_n}{n} \tag{3.7}$$

with n the number of acquisition, x_n the value of the n^{th} acquisition, $\overline{m}_n$ the averaged value of the n^{th} acquisitions, $\overline{m}_{n-1}$ the averaged value of the n-1 acquisitions.

Fig. 3.35 shows the results of the output voltage of M1 being averaged 40 000 times for different magnetic field amplitude pp. For an amplitude of 219 nT, the amplitude of the measured signal by M1 is well above the noise level (around 400 pT peak to peak). When the amplitude pp of the magnetic field decreases the sinusoidal shape can still be seen for an amplitude of 1 nT and 440 pT. As the noise level is also 440 pT, the limit of detection of M1 for 40 000 events is estimated to be 440 pT.

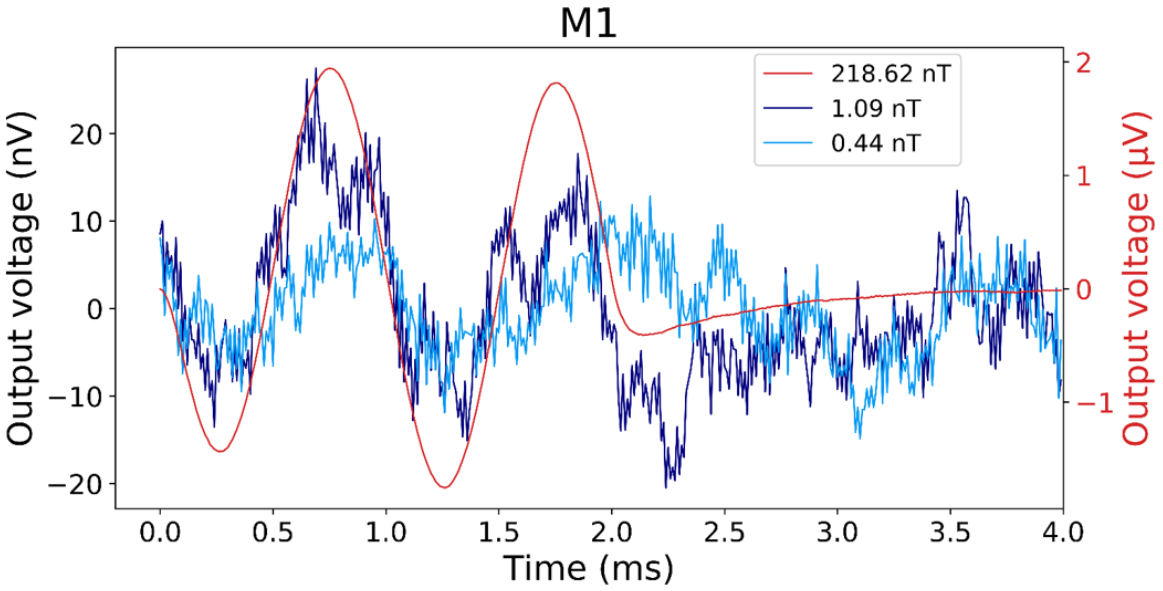

Figure 3.35: Output voltage of M1. The external magnetic field amplitude pp decreases, for Hpp= 219 nT, the amplitude of the output signal (around 4 µV is much higher than the noise (around 30 nT). When the magnetic field decreases down to 1 nT, the output voltage of M1 can still be separated from the noise. Finally, for an amplitude of 440 pT, the output voltage of M1 and the noise amplitude are similar.

To increase the precision of the 2D magnetrode, several issues can be addressed. It would be interesting to suppress the parasitic sensitivity of M1 and M2. Also, the distance between M1 and M2 can be decreased from 250 µm to only 50 µm.

3.5 Electrodes

Electrodes are a key component of magnetrodes as they are used as a reference to detect electrical spikes and average the magnetic signals with a time window centered around these electrical spikes (cf chapter 4). We used several electrodes in addition to GMR sensors of the magnetrode, both home-made platinum electrodes and commercial electrodes. The deposited platinum electrodes are not as good as commercial electrodes so we added commercial electrodes to the magnetrode. First we used tungsten electrodes in close proximity of the magnetrode. Then one or two tungsten electrodes were directly glued on the magnetrode, close to the GMR sensors. To reach high density of electrodes, we used commercial arrays of electrodes with two different types: a dense array which covered only the lower GMR sensor and a less-dense array which covered up to 3 GMR sensors. The ultimate electrode would be designed directly on the magnetrode but as electrodes fabrication is a field of research of its own we chose to use commercial electrodes instead. We did one experiment on increasing our electrode quality before using commercial array electrodes which have the advantages of being specifically developed for neuronal recording, with a higher quality and density than we can provide within a short amount of time.

3.5.1 State of the art

Neural electrodes can be used for recording the neural system to understand its organization and functioning. They can also be used for stimulation.Neural electrodes have to face several challenges such as having a millisecond precision, a high spatial resolution, preventing damages during insertion, discriminating neurons and being able to record neural electric activity during long implantation time in the brain [9, 10, 11, 12].

There are several types of electrodes including penetrating and non penetrating electrodes. The first ones are invasive (microwires, microelectrodes, microelectrodes arrays) when the second ones are non-invasive (planar electrodes or skin electrodes for EEG). As we are using electrodes in addition to a magnetrode which is already invasive, only penetrating electrodes will be presented (non-exhaustive).

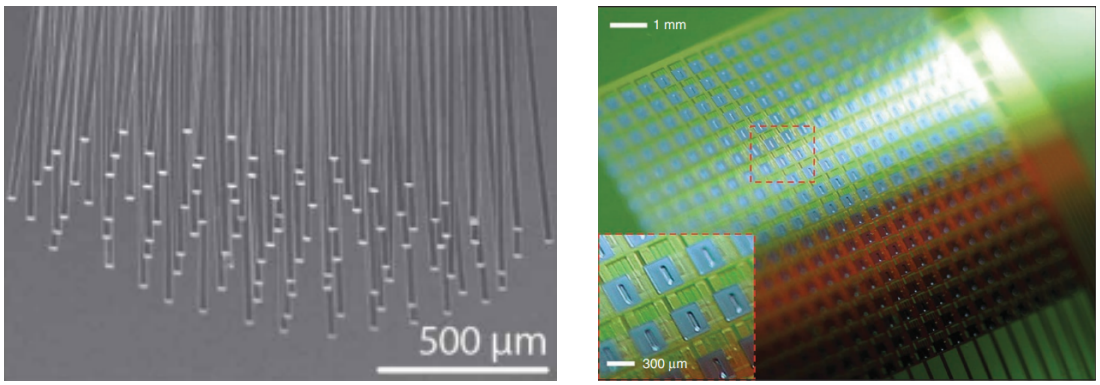

(a) Array of microwires [13] (b) Planar electrode [14]

Figure 3.36: Different types of electrodes

The first electrodes were made with glass or platinum wire. Later, other materials were used for micro wire fabrication: stainless steel, iridium, silicon, tungsten and platinum.

A microwire is a thin metallic wire with a diameter around 10 µm for example. All the length of the wire is covered with a insulator except the tip, leaving the uncovered part in contact with neural tissues which is able to record the electric activity. Microwires are penetrating electrodes and they are passive compared to later active electrodes which can have on-chip preamplifiers [15] or microfluidic system [16] for example.

It can be used alone or with other microwires. Microwires can bend during the insertion leading to imprecise placement in the brain and the difference between the softness of the brain and the microwires rigidity can lead to inflammations of the tissues which limits their operating time [9].

Electrodes have evolved from single sites recording to multiple sites recording [17, 18] either by making an array of microwire like Utah array with 100 electrodes per 16mm^2 of cerebral cortex[19] or by making electrodes with several recording sites at the end of a single shank like Michigan array[17]. This evolution was allowed by silicon microfabrication techniques. The advantages of silicon based neural probes are the possibility to do batch fabrication with a high reproducibility, the CMOS compatibility which allows to have on-chip electronics for silicon based single or multisite recording probes. However, silicon based electrodes have the same drawback as microwires which is its rigidity leading to possible breaking during insertion, damaging the brain during insertion and provoking inflammations.

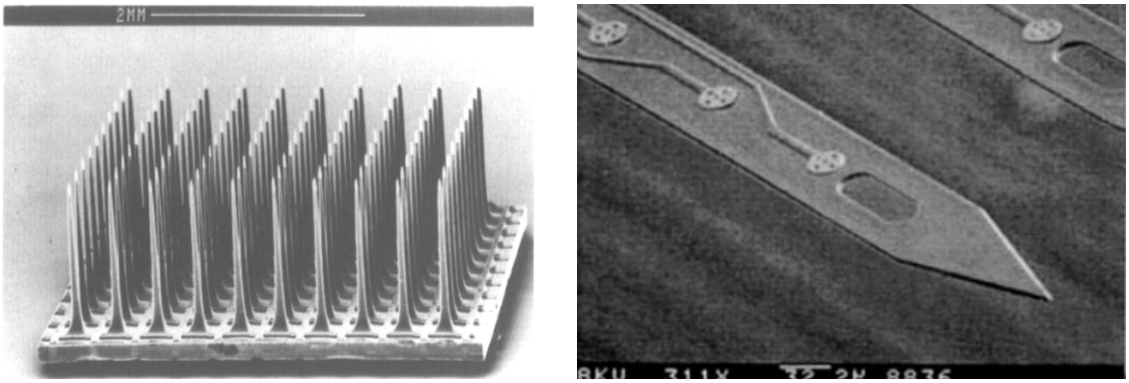

(a) Utah array [20]

(b) Michigan electrodes [21]

Figure 3.37: Different types of electrodes

An other critical aspect of electrodes is their impedance. Indeed, a low impedance is better to have a good recording of neuronal signal [22]. There is a compromise between the size of the electrode which should be small to have a size similar to a neuron body ($\sim$ 10 µm for a cell body) and small enough to be close to neurons but the size has an impact on the impedance and smaller electrodes have a higher impedance. Typically, an electrode's impedance is between 50kΩ to 1MΩ.

In addition to previously mentioned material used for electrodes, iridium oxide, titanium oxide and titanium nitride can be used for electrodes fabrication. An example of multisites recording electrode using TiN is the probe called Neuropixel [10, 11], its objective is to have both a high spatiotemporal resolution and a large volume coverage (cf fig. 3.38a). To achieve this, a shank of 1 cm*70 µm with a thickness of 20 µm is covered by 960 recording sites, 384 can be simultaneously recorded. It allows to discriminate between 20 to 200 neurons per shank depending on the brain structure. Also, to prevent issues due to numerous cables, the outputs are multiplexed so only 2

output wires are needed. Despite being a silicon based probe, Neuropixel can record neural activity during an extended period of time (up to 60 days[12]).

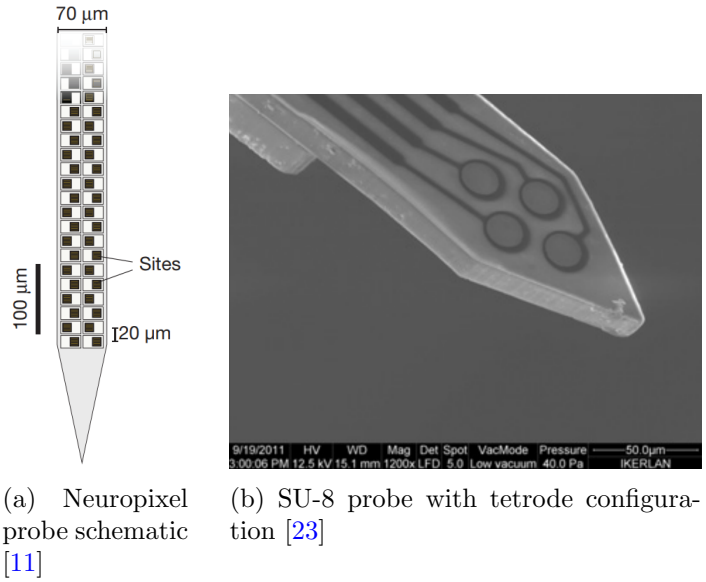

(a) Neuropixel probe schematic [11]

(b) SU-8 probe with tetrode configuration [23]

Figure 3.38: Example of probes with multiple electrodes for neurons identification.

To prevent the tissues inflammations due to rigid neural probes, flexible probes are also under development, with SU-8 based probe [23] for example (cf fig. 3.38b). This flexible electrode also addresses 2 other issues which are neuron discrimination and the gap between the electrode and neural tissues. To be able to discriminate neuron, a tetrode configuration is used with gold electrode (∅ 20 µm) because of its electrical properties and its surface inertness. To prevent any gap between the gold electrode and neural tissue, the fabrication process is adapted by depositing the first SU-8 layers with holes in place of the recording sites, then the holes were filled with metal and finally, several layers of SU-8 were deposited to cover the recording sites and shaped the electrode. The impedance of the electrode at 1kHz is between 0.5-1MΩ. The impedance is high because of the small size of the electrodes.

In conclusion there are several factors to take into account to made electrodes. These factors can be separated in several categories:

- Probe design
  - invasive or non invasive
  - rigid or flexible
  - one or several shanks
  - one or several recording sites on the shank
  - size of the probe
- Recording site design
  - material
  - size (area) of the recording site

  - if planar: gap between electrode and neural tissues
- Electronic read out
  - multiplexed output data
  - wireless

These constraints respond to the challenges of electrodes fabrication and utilization:

- low impedance and low noise level
- high temporal and spatial resolution
- neuron discrimination
- avoid neural tissues damages and inflammations
- long term stability in the brain
- optimized electronic

3.5.2 Electrodes optimization

As we already had an electrode fabrication step in our magnetrode fabrication process, we tried to enhance the platinum electrodes by using titanium nitride instead. The objective is to lower the impedance down to 100 kΩ. We developed a process for depositing TiN by reactive sputtering. We added a gas entry for nitrogen gas to the sputtering chamber. First, the sample is etched by IBE during 30s to clean its surface. Then, it is transferred in the sputtering chamber. The total pressure is keped at 5.10^{-3} mbar and the thickness of the TiN thickness after deposition is measured depending on the partial pressure of nitrogen. The deposition rate decreases when the nitrogen percentage in the sputtering chamber increases as can be seen in fig. 3.39.

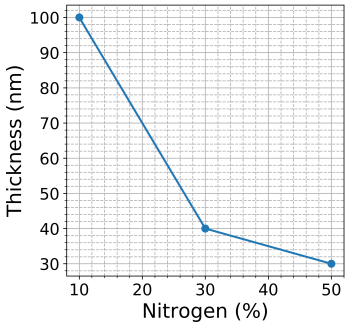

Figure 3.39: Electrode thickness as a function of the percentage of nitrogen in the sputtering chamber. The deposition is made during 1h at 400W.

However, as the deposition rate drops quickly, to reach a thickness of 200 nm of TiN the deposition time is increased (5h for a 200 nm thickness with 30% of Nitrogen).

In addition, the placement of electrode also needed to be adapted with a tetrode configuration to be able to discriminate neurons. In the mean time, two types of commercial electrodes addressing these two issues (good quality electrodes and high density of recording sites) were identified and we chose to use them instead of developing electrodes of our own.

3.5.3 Commercial electrodes

We tried several configurations: magnetrode with 1 tungsten electrode (cf section 3.1.2), magnetrode with 2 tungsten electrodes placed in both sides of the same GMR sensor, magnetrode with an array of electrodes covering the 3 GMR sensors and magnetrode with a dense array of electrodes covering only 1 GMR sensor (cf fig. 3.40).

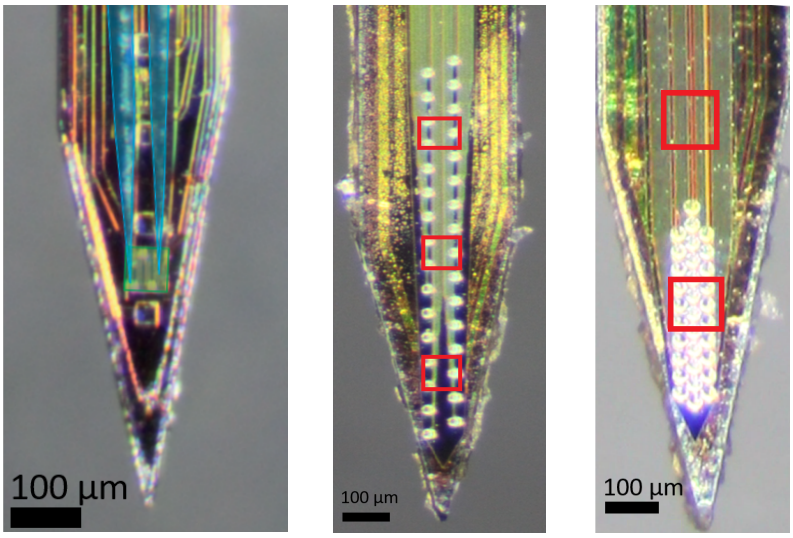

(a) 2 tungsten electrodes (b) Array of electrodes 1 (c) Array of electrodes 2

Figure 3.40: Commercial electrodes used during *in-vivo* experiments. For (b) and (c) The red squares symbolize the position of GMR sensors.

The 2 commercial electrodes arrays have recording sites made of iridium with a diameter of 15 µm. They have 32 recordings electrodes which is supposed to allow neurons discrimination. It is interesting as we would be able to average the magnetic signal from a single neuron. The tip has a thickness of 15 µm and is glued directly on top of the magnetic sensors.

3.6 Conclusion

Magnetrodes have been developed after a successful proof of concept using GMR to record biological signals *in-vitro*. They are fabricated following a very well mastered fabrication process. The thinning process of the magnetrode tip by Deep RIE is mastered and some improvements can be done to prevent residual SiO_2on the edge of the tip. The magnetrodes for 2D recording need an additional step (the local repinning) before being used with a phantom to characterize their limit of detection in 2D mode. The electrodes embedded on the magnetrodes do not match the requirements for *in-vivo* neural recording and commercial electrodes are used instead. Ultimately, magnetrodes will embed the electronics needed to amplify and filter the signal.

In conclusion, magnetrodes are probes with up to 3 magnetic sensors at the state of the art on a probe with a thickness of 25 µm. In addition, 2D magnetrodes can record simultaneously a magnetic field in 2 orthogonal directions. The next step is to use magnetrodes during *in-vivo* recording to try to record magnetic action potentials.

Bibliography

[1] Laure Caruso. *Giant magnetoresistance based sensors for local magnetic detection of neuronal currents*. PhD thesis, 2015. 78, 79

[2] Vincent Trauchessec. *Local magnetic detection and stimulation of neuronal activity*. PhD thesis, Paris Saclay, 2017. 78, 79, 84, 85, 89

[3] Francesca Barbieri, Vincent Trauchessec, Laure Caruso, Josué Trejo-Rosillo, Bartosz Telenczuk, Elodie Paul, Thierry Bal, Alain Destexhe, Claude Fermon, Myriam Pannetier-Lecoeur, et al. Local recording of biological magnetic fields using giant magneto resistance-based micro-probes. *Scientific reports*, 6(1):1–10, 2016. 79, 80, 81, 82

[4] Laure Caruso, Thomas Wunderle, Christopher Murphy Lewis, Joao Valadeiro, Vincent Trauchessec, Josué Trejo Rosillo, Jose Pedro Amaral, Jianguang Ni, Patrick Jendritza, Claude Fermon, et al. In vivo magnetic recording of neuronal activity. *Neuron*, 95(6):1283–1291, 2017. 79, 83, 84

[5] Geoffroy W Anderson, Yiming Huai, and Mahendra Pakala. Spin-valve thermal stability: The effect of different antiferromagnets. *Journal of applied physics*, 87 (9):5726–5728, 2000. 79

[6] Francesca Barbieri. ■ magnetrodes ■ project 600730 - fp7-ict-2011-9, 2015. *unpublished*. 84

[7] Franz Laermer and Andrea Schilp. Method of anisotropically etching silicon, March 26 1996. US Patent 5,501,893. 89

[8] F Laerme, Andrea Schilp, Karsten Funk, and MAOM Offenberg. Bosch deep silicon etching: improving uniformity and etch rate for advanced mems applications. In *Technical Digest. IEEE International MEMS 99 Conference. Twelfth IEEE International Conference on Micro Electro Mechanical Systems (Cat. No. 99CH36291)*, pages 211–216. IEEE, 1999. 90

[9] Anoop C Patil and Nitish V Thakor. Implantable neurotechnologies: a review of micro-and nanoelectrodes for neural recording. *Medical & biological engineering & computing*, 54(1):23–44, 2016. 115, 116

[10] Edward M Callaway and Anupam K Garg. Brain technology: Neurons recorded en masse. *Nature*, 551(7679):172–173, 2017. 115, 116

[11] James J Jun, Nicholas A Steinmetz, Joshua H Siegle, Daniel J Denman, Marius Bauza, Brian Barbarits, Albert K Lee, Costas A Anastassiou, Alexandru Andrei, Çağatay Aydın, et al. Fully integrated silicon probes for high-density recording of neural activity. *Nature*, 551(7679):232–236, 2017. 115, 116, 117

[12] Guosong Hong and Charles M Lieber. Novel electrode technologies for neural recordings. *Nature Reviews Neuroscience*, 20(6):330–345, 2019. 115, 117

[13] Abdulmalik Obaid, Mina-Elraheb Hanna, Yu-Wei Wu, Mihaly Kollo, Romeo Racz, Matthew R Angle, Jan Müller, Nora Brackbill, William Wray, Felix Franke, et al. Massively parallel microwire arrays integrated with cmos chips for neural recording. *Science advances*, 6(12):eaay2789, 2020. 115

[14] Jonathan Viventi, Dae-Hyeong Kim, Leif Vigeland, Eric S Frechette, Justin A Blanco, Yun-Soung Kim, Andrew E Avrin, Vineet R Tiruvadi, Suk-Won Hwang, Ann C Vanleer, et al. Flexible, foldable, actively multiplexed, high-density electrode array for mapping brain activity in vivo. *Nature neuroscience*, 14(12):1599, 2011. 115

[15] Jozsef Csicsvari, Darrell A Henze, Brian Jamieson, Kenneth D Harris, Anton Sirota, Péter Barthó, Kensall D Wise, and Gyorgy Buzsaki. Massively parallel recording of unit and local field potentials with silicon-based electrodes. *Journal of neurophysiology*, 90(2):1314–1323, 2003. 116

[16] Shoji Takeuchi, D Ziegler, Y Yoshida, K Mabuchi, and T Suzuki. Parylene flexible neural probes integrated with microfluidic channels. *Lab on a Chip*, 5(5):519–523, 2005. 116

[17] Kensall D Wise, James B Angell, and Arnold Starr. An integrated-circuit approach to extracellular microelectrodes. *IEEE transactions on biomedical engineering*, (3):238–247, 1970. 116

[18] Bruce L McNaughton, John O'Keefe, and Carol A Barnes. The stereotrode: a new technique for simultaneous isolation of several single units in the central nervous system from multiple unit records. *Journal of neuroscience methods*, 8(4):391–397, 1983. 116

[19] Patrick K Campbell, Kelly E Jones, and Richard A Normann. A 100 electrode intracortical array: structural variability. *Biomedical sciences instrumentation*, 26:161, 1990. 116

[20] Edwin M Maynard, Craig T Nordhausen, and Richard A Normann. The utah intracortical electrode array: a recording structure for potential brain-computer interfaces. *Electroencephalography and clinical neurophysiology*, 102(3):228–239, 1997. 116

[21] Daryl R Kipke, Rio J Vetter, Justin C Williams, and Jamille F Hetke. Silicon-substrate intracortical microelectrode arrays for long-term recording of neuronal spike activity in cerebral cortex. *IEEE transactions on neural systems and rehabilitation engineering*, 11(2):151–155, 2003. 116

[22] Stuart F Cogan. Neural stimulation and recording electrodes. *Annu. Rev. Biomed. Eng.*, 10:275–309, 2008. 116

[23] Ane Altuna, Liset Menendez de la Prida, Elisa Bellistri, Gemma Gabriel, Anton Guimerá, Javier Berganzo, Rosa Villa, and Luis J Fernández. Su-8 based microprobes with integrated planar electrodes for enhanced neural depth recording. *Biosensors and Bioelectronics*, 37(1):1–5, 2012. 117

Chapter 4

In-vivo recording

Contents

During this thesis we aimed at developing and improving magnetrodes to record magnetic action potential from a single neuron in the hippocampus of rats from spontaneous neuronal activity.

To record magnetic action potential (AP), the magnetic signal needs to be averaged multiple times. Indeed, as the limit of detection of the sensor is 20 nT on a 800 Hz-1200 kHz bandwidth, an averaging of over 40 000 events is needed to reduce the limit of detection down to 100 pT which is the highest estimation of a magnetic AP [1]. To realize such an averaging, the spiking activity of neurons is detected by one or several electrodes. The electrical spikes are then used to average the magnetic signal. For all selected electrical spikes, recordings from electric and magnetic signals are extracted and then, averaged.

This leads to choices in the methods to select the electrical spikes used for the averaging. Indeed, a single electrode is needed to detect spikes and differentiate them from noise based on a threshold. However, to select spikes associated to a single neuron at least two electrodes are required. This is expected to increase the quality of the averaging by selecting only spikes associated to a unique neuron and thus decreasing the number of noisy events mistaken as spikes.

4.1 Experimental set-up

Several experiments towards *in-vivo* magnetic recordings have already been made by L. Caruso and V. Trauchessec. They have made a proof of concept with GMR sensors to record magnetic activity from muscle with an *in-vitro* experiment [2] and after reducing the size of the sensors, they have made several *in-vivo* experiments with GMR sensors mounted on a magnetrode [3]. Magnetic LFP have been recorded and a first attempt to record magnetic action potential has been made with preliminary results which will be discussed later.

To investigate more in depth the possibility to detect magnetic signature of action potentials, several experiments were made at the Ernst Strügmann Institute (ESI) for Neuroscience in Frankfurt (Germany) with Pascal Fries's team. The manipulation of the animal and the insertion of the probes were made by Patrick Jendritza and Frederike Klein.

4.1.1 *In-vivo* set-up

The set-up is designed to ensure the well-being of animals (adult male Sprague Dawley rats - Rattus norvegicus domestica) during the experiment while addressing the challenges exposed earlier. The experiments were made in accordance with the animal welfare guidelines of the Regional Board Darmstadt (F149/2004) and the "European Union's Directive 2010/63/EU" [1].

Animals procedure

Animals are sedated at the beginning of the experiment with a mixture of Ketamine (80 mg/Kg) and Medetomidine (0.01 mg/kg). The anaesthesia is maintained with

[1] Article under review at ACS

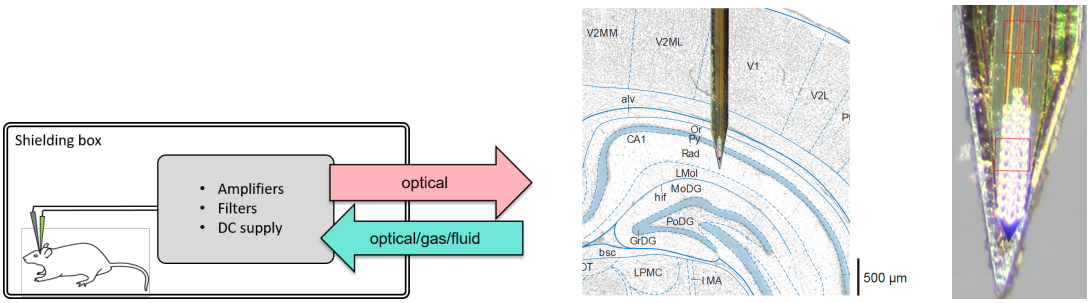

(a) Set-up (b) Probes location (c) Probes

Figure 4.1: Scheme of the whole set-up (a) and probes location in the rat hippocampus with a dense electrodes array (b). (c) Zoom on the magnetrode with electrodes array covering up the GMR sensors. The GMR sensors location is symbolized by red squares. The GMR sensors of the magnetrode records the magnetic signal while the electrodes record the electrical activity of neurons which is used to average the magnetic signal.

Isoflurane (1-2 % in 100 % oxygen) with a custom face mask. Analgesia is maintained with regular injections of Buprenorphine (0.03 mg/kg). To prevent brain swelling, the animals are also injected with Dexamethasone (1 mg/kg). To maintain their physiological state, a mixture of amino acids and glucose is injected to the animals. The rat's vitals are monitored with body temperature, respiration and electrocardiograms. These information are sent *via* an optical fiber.

Probe insertions

After the animals sedation, a craniotomy is made to remove a small piece of the skull to have access to the brain and allow an easy insertion of the recording probes. The recording probes are inserted in the hippocampus to take advantage of its important and spontaneous spiking activity. It prevents the use of an external stimulation (as a reminder to record LFP into the visual cortex, a blue light is sent to one eye of a sedated cat [3]) and allows to record a high number of events in a short period of time. Also the hippocampus contains highly organized pyramidal cells with aligned somata and dendrites which is ideal to record a magnetic field as magnetic fields from different synchronous neurons can be summed.

Data recording

To record electrical activity from neurons, one or several electrodes are glued to the magnetrode close to the GMR sensors or an array of electrodes is directly placed on top of the GMR sensor which is the closest to the end of the tip (M1) or it is placed on top of all GMR sensors. The magnetic activity is directly recorded from GMR sensors with an electronic scheme similar to noise measurement. The recorded signal is amplified by a factor 20x500/9 (2018 recordings) or 5x500/9 (2019 recordings) and filtered with a band-pass from 3 Hz to 30 kHz. Later, a digital filter (300 Hz to 6 kHz) is applied when treating and averaging the data.

Both signals from GMR and electrodes are buffered and digitized at a frequency of 24 414.0625 Hz with a TDT system. GMR sensors are biased with a voltage around 1 V and up to 2 V. The DC on/DC off state is controlled by a TTL signal via an optical fiber which is then converted into an electric signal inside the Faraday cage. Recorded

data and vitals of the rats are sent back to a computer *via* optical fiber (cf fig. 4.1) and are plotted in real time.

Conversion from µV to nT

To convert the output of GMR sensors from µV to nT, the different gain of the acquisition chain, the sensitivity of the magnetrode S and its voltage bias V_{GMR} are taken into account:

$$\mu_0 H = \frac{Output}{Gain * S * V_{GMR}} \tag{4.1}$$

The conversion is detailed in table 4.1 for the blocks presented in this chapter.

Year	Blocks	Probe	Gain	V_{GMR} (V)	S (V/V/T)	V (µV)	μ_0H (nT)
2018	18, 23, 27,29	SOI-ref.-712	20*450/9	1	17	10	0.6
2019	1	SOI 81-ref.-741	5*500/9	1.8	15	10	1.3
2019	7	SOI 81-ref.-741	5*500/9	1	15	10	2.4

Table 4.1: Conversion parameters and results for each block presented in this chapter

4.1.2 Challenges

The challenges are numerous due to the *in-vivo* application and the low amplitude of the targeted magnetic signal (10-100 pT).

Electrical noise, magnetic noise and 50 Hz contamination

To prevent any contamination from outside magnetic and electrical noises, a Faraday cage contains the whole set-up: animal, electrodes, magnetrodes and electronics. It allows to reduce the noise from surrounding environment like noises generated by road traffic and tramway. To prevent 50 Hz contamination from the power line, magnetrodes are powered on dedicated batteries as well as the Tucker-Davis Technologies (TDT) system used to record the electric potential from one or several electrodes (cf fig. 4.1). Also all the data, GMR biasing monitoring, etc. are sent through optical wires.

Artifact tracking

To track artifact due to capacitive coupling with the conductive surrounding medium, the GMR sensors are continuously switched between on (biasing up to 2 V) and off (0 V) during the recording. In previous experiment, GMR were turned on for a long period of time and then switched off. Now they are switched on and off continuously (around 1-2s cycle) with varying interval.The state of the GMR (DC on or DC off) is controlled by optical fibers to suppress any electrical signals from outside the Faraday cage. The recorded electric and magnetic data are sent in real time to a computer outside the Faraday cage to manage the experiment (presence of RTN, amplifier saturation, low spiking activity, rat vitals) also *via* optical fiber (cf fig. 4.1).

Multiple GMR sensors

With the new magnetrode design, up to three GMR sensors can record the neuronal activity simultaneously. This allows to have one GMR for magnetic action potential while another one is used as a control recording as we will see in section 4.3. This is a second method to detect artifact. In the future, one may also use the 2D magnetrode (see chapter 3) for current mapping and reconstruction, though these types of probes have not been implemented in the experiments shown here.

Electrodes selection

To average the magnetic signal and reach a noise level of 100 pT, electrical spikes are detected by electrodes and used as a reference/trigger to average the magnetic signal.

Dedicated electrodes on the magnetrodes are first used to record magnetic action potential. However, the magnetrode's electrodes have a resistance which is too high ($\sim$ 200 kΩ). With a gold electroplating the resistance drops to $\sim$ 160 kΩ which remains too high and we chose to use commercial electrodes instead.

To detect spikes, only one electrode is needed. Indeed, by placing one electrode in the close vicinity of a GMR sensor, the electrical activity of neurons is recorded as well as the magnetic activity and can be used as a reference.

To realize a more precise averaging, it is interesting to be able to discriminate neurons. AP can be sorted out based on their shapes with a single electrode and also by adding a second electrode to record simultaneously the activity of neurons at two different locations. This gives information about the location of the neuron if the two electrodes are placed on both sides of a GMR sensor for example (if the spike amplitude is higher for the left electrode compared to the electrode on the right the neuron is closer to the left).

To localize a neuron with an increased precision, electrodes can be replaced by an electrode array which covers the GMR sensor with a high density. Then, by associating the spikes to a single neuron, it is possible to determine a neuron location and determine if the spiking neuron is centered on the GMR sensor or not.

Spikes sorting

Depending on the numbers of electrodes, the method applied to spikes sorting is different. Here we present methods used during *in-vivo* experiments. With only one electrode, a threshold level is used to select spikes with an amplitude equal or higher than the threshold. There is a compromise between the number of selected spikes (with a lower threshold, more spikes are selected) and the risk to mistake noise for spikes (with a lower threshold, the difference between real spikes and noise is lower).

To refine the spikes selection, a possibility is to compare spike's amplitude on two electrodes to sort them into clusters. With this method, the noise is supposed to be differentiated from spikes. As we will see in sec. 4.3.3, this method is efficient for clusters which are well separated.

Finally, to have an automatic selection based on multiple recordings, an array of electrodes is used. Spikes are sorted into clusters thanks to the electrical recordings made

by the electrodes array and an algorithm called Kilosort [4]. Kilosort has been developed to address the challenge of the increasing number of electrodes on probes for neuronal recordings. It is an algorithm which promises to sort spikes in real time from a huge number of simultaneous recordings.

Duration of the recording

The duration of the recording is determined by several limitation like the stability of the probe, a reasonable duration and recording a sufficient amount of spikes for averaging the magnetic signal. Indeed, if the electrodes or the GMR sensors start to show instabilities then the recording needs to be stopped. Also, the number of recorded spikes is limited by the acquisition time. It is important to record in a brain area with an important spiking activity and to decrease damages made during the insertion of the probes to have a high number of spiking neurons. The selection of spikes have an impact on the number of spikes by clusters. To mitigate all these constraints, we performed recordings over duration of the order of 1-2 hours (i.e. 30-60 mns in ON or OFF conditions).

4.1.3 Conclusion

The experimental set-up is designed to prevent any noise contamination, either from external magnetic noise or from 50 Hz contamination due to power line.

The improvements and changes compared to previous experiments are summarized in fig 4.2 and concern the number and type of electrodes, the GMR sensors and the magnetrode thickness as well as the targeted biological magnetic signal.

Previously, electrodes were only tungsten micro-wires. During this thesis both tungsten micro-wires and electrodes arrays are used. Also the method to select spikes has evolved from a threshold method to a spikes sorting method to associate spikes to a single neuron and thus sort spikes into clusters avoiding noise contamination. The differences between previous and present magnetrodes concern the number of simultaneously recorded GMR sensors, the 2D recording improvement and the thinning of the tip of the magnetrode. Finally, the targeted magnetic signal has changed. Previously, magnetic LFP were recorded in the visual cortex of cats after a visual stimulation, LFP are a collective response and now we aim at recording a magnetic action potential which is spontaneously generated by a single neuron in a rodent hyppocampus.

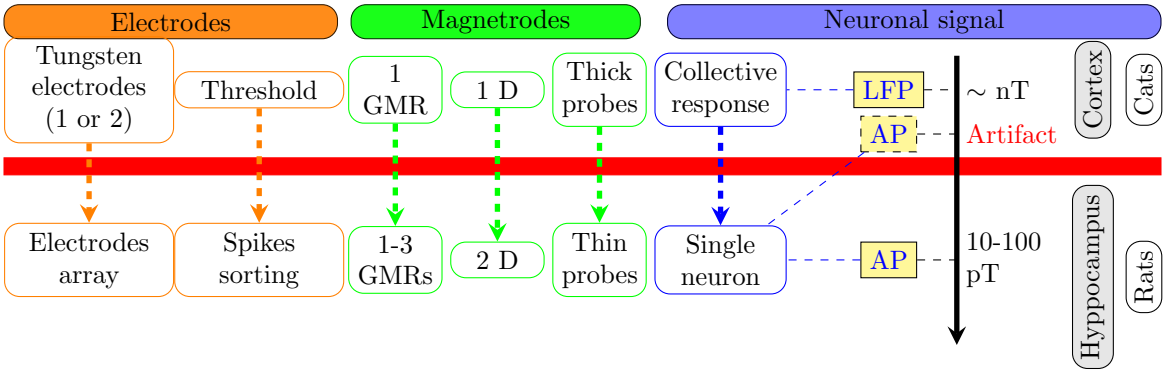

Figure 4.2: Difference between previous experiments and experiments realized during this thesis.

4.2 Recording and extracting the neuronal activity

As explained earlier, the electrodes and the magnetrodes record simultaneously the electrical and magnetic fluctuations in their surroundings, part of which corresponds to the neuronal activity. The electrodes record the electrical activity and the GMR sensors record the magnetic activity. Recording electrical spikes is a well-known technique and it is used here to detect spiking events. These events are then used to average the magnetic signal to decrease the noise level of the recording and possibly extract magnetic AP. The complete method is presented in section 4.2.1.

To enhance the averaging of the magnetic recording, several factors need to be taken into account like the thickness of the magnetrode which has an impact on the spiking rate of neurons (cf sec. 4.2.2) and the biasing voltage of the GMR sensors which can increase the SNR but also has an impact on the neurons surrounding the probes (cf sec. 4.2.3).

4.2.1 Data analysis process

Recorded data

As we can see in fig. 4.3, electrical spikes are clearly visible while the GMR sensor noise level prevents any direct magnetic spike detection and thus an averaging is needed to extract magnetic spikes from the noise.

The electrical spikes are clearly visible when there is only noise in the recorded magnetic signal. The biasing voltage value of the GMR is represented by a dashed line, the DC-on state corresponds to a biasing voltage of 1 V and the DC-off state to a biasing voltage of 0 V. There is a glitch when the GMR is switched on/off, which is removed from the averaging time window. When the GMR is off the noise level is lower and corresponds only to the thermal noise and when the GMR is on, the noise level is increased and corresponds to the 1/f noise in addition to the thermal noise. There is almost no RTN and, if RTN arises, the biasing voltage is decreased until RTN disappears.

GMR sensors are powered on and off continuously (cf sec. 4.1.2), in fig. 4.3, the state of the GMR is symbolized by a dashed line. When the GMR sensor is off (0V), the recorded signal is used as a control experiment. By switching the GMR on and off

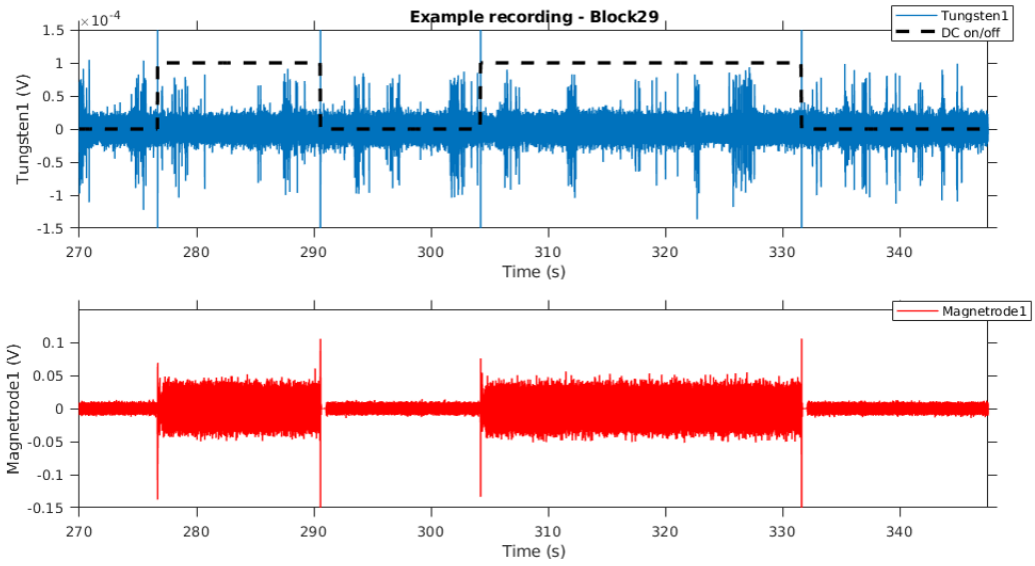

Figure 4.3: Output voltage of the recorded voltage of a tungsten electrode (top) and a GMR sensor (bottom) as a function of time.

regularly, both the control experiment and the recording of the magnetic activity of neurons are made in similar conditions and if slow drifts appear they will be present on both conditions. Monitoring the GMR response with zero voltage is also the main control for capacitive coupling of electrical signal to the sensor, through a leaky passivation, as will be discussed in sec. 4.2.1. It also allows to detect if the GMR operating conditions (such as bias voltage) have an impact on the neuron firing. Indeed, the number of spikes during DC off and DC on needs to be similar. Also, the averaged number of electrical spikes needs to be the same in both cases like in fig. 4.5a.

Example of magnetic signal averaging

Fig. 4.4, shows the averaged electric and magnetic activity over around 12 000 events. In the electrical part, the averaged electrical spikes during DC on and DC off are perfectly superposed. It is important as it means that control recordings made when the GMR sensors are not powered (DC off) and recordings of the magnetic signal when the GMR sensors are powered (DC on) are made in the same conditions.

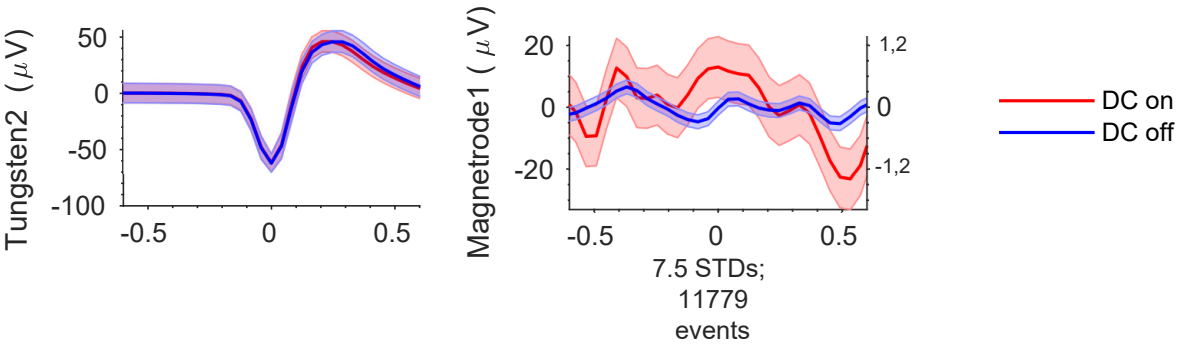

Figure 4.4: Averaged electrical (left) and magnetic (right) signals (2018-block 27-Probe SOI-ref.-712). STDs is the acronym for standard deviation.

When observing the magnetic recording, it appears that the ”on” conditions leads to

higher noise, due to the addition of the 1/f noise of the probe to the thermal noise (which appears when the sensor is off).

Simulation of magnetic signal averaging

To have a toy model of the electrode and magnetic sensor during the experiment, we developed a simulation tool on Python, which generates a simple case of a few neurons firing, on which a white noise or another correlated or uncorrelated perturbation can be added. The modeling of neurons is based on the Python script presented in [5].

According to signal amplitude estimates and phantom study, for a noise amplitude of 20 nT over the bandwidth of interest, the magnetic signal needs to be averaged 40 000 times to reach a noise amplitude as low as 100 pT. To model this case, two neurons are simulated based on the Leaky Integrate-and-Fire (LFI) model. Then, to simulate a recording by an electrode and a magnetrode, a random normal noise is added to the signal. The amplitude of the spike is 100 µV (respectively 100 pT) for the first neuron and 80 µV (respectively 80 pT) for the second neuron. The amplitude of the magnetic neuronal activity is chosen to match the highest amplitude we expect. It does not represent the amplitude nor the shape of a real magnetic action potential. It is used to represent the impact of the noise and the averaging on the averaged recorded magnetic signal. Random noise is also added on the electrode (5 µV) and on the GMR sensor (10 nT) as one can see on fig. 4.5a.

The spikes are detected on the data recorded by the electrode. A time window is extracted with the spike at its center both on the data recorded by the electrode and the GMR sensor (cf fig. 4.5b). Then, all the detected spikes (here 40 000) are used to average the data. A typical result is shown in fig. 4.5c. The noise amplitude is decreased to around 100 pT which is consistent with the expected value presented earlier.

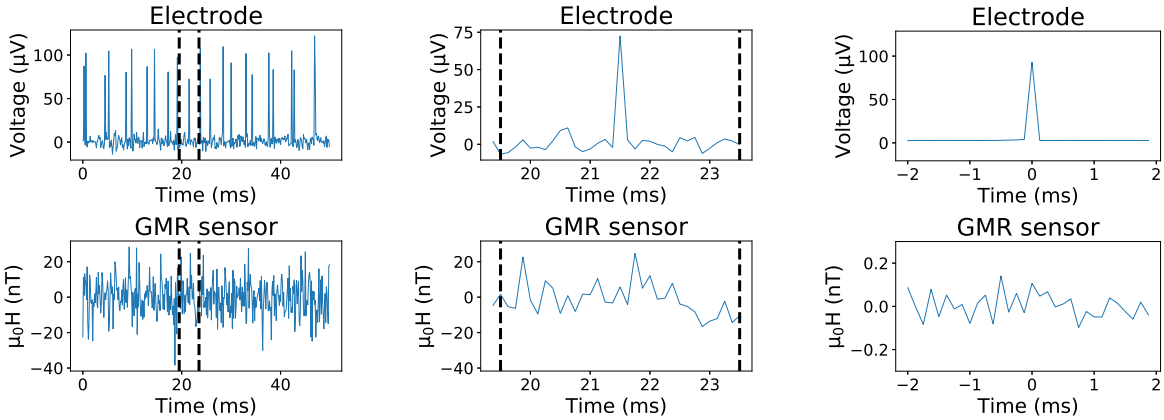

(a) Simulation of recorded signal

(b) Zoom on the selected area

(c) Averaging on 40 000 events

Figure 4.5: Simulation of the recorded signal by an electrode and a GMR sensor. Two neurons are simulated based on the LFI model. A white noise is added to the magnetrode with the mean of the distribution at 5 µV for the electrode and 10 nT for the magnetrode. (a) Simulation of the signal recorded by an electrode (top) and by a GMR sensor (bottom). (b) Zoom on the selected spike presented in (a). (c) Averaging over 40 000 events of the signal recorded by an electrode (top) and by a GMR sensor (bottom)

The resulting averaged magnetic signal depends on the number of spikes detected as we will see in section 4.3.1. To go further it is possible to discriminate spikes and associate them to a neuron based on different method (sec. 4.3.3 and sec. 4.4). When spikes are sorted into clusters, the number of spikes per cluster can be lower and the duration of the experiment might need to be adjusted.

Coupling artifact

A recording session (or block) lasts typically between 30 min and 2 h. For some blocks, there is a signal which is centered at t=0 during DC on and DC off but they are not superposed (cf fig. 4.6). Any signal measured during DC-off do not have a magnetic origin as the GMR sensor is not powered and thus do not measure any external magnetic field. Thus this signal is probably an electrical coupling.

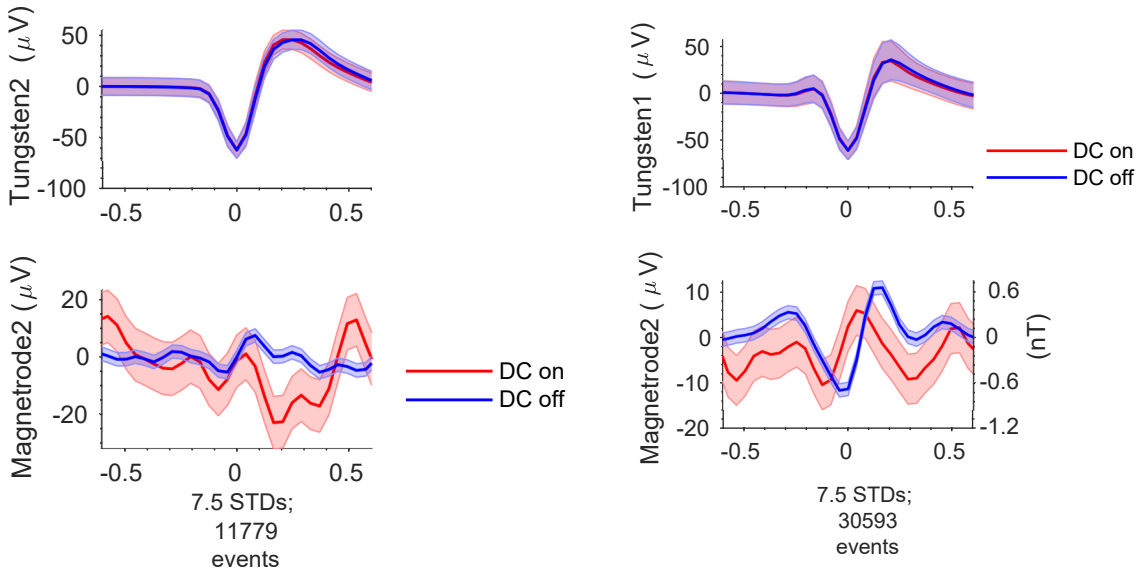

(a) Block 27

(b) Block 29

Figure 4.6: Recordings with a coupling artifact (2018-block 29-Probe SOI-ref.-712)

This coupling might be a capacitive coupling from the electrical spiking signal present in the extracellular medium (which is conducting), through an insulation defect in the passivation layer deposited on top of the GMRs sensors. A bad insulation between the GMR sensors or the contacts and the conductive medium between the brain tissues and the probes will then bring a small electrical change on the GMR resistance, which appears in both DC-on and DC-off conditions, exhibiting roughly the same timing and shape as the signal measured on the electrode. When the passivation is good, no capacitive coupling is observed on the GMR sensors.

4.2.2 Impact of thickness

First magnetrodes were fabricated from usual silicon wafer of 270 µm. This thickness is rather large compared to the diameter of electrode, and insertion of such a large device in the brain tissues leads to local damages to the cells on the path of insertion and in the surrounding of the probe. Therefore, we have developed a much thinner probe (25 µm) based on SOI technology. In order to qualitatively and quantitatively

estimate the benefit of thinning the probe, we have studied the firing signals and rate on a thick and a thin probe in similar conditions otherwise (both in the hippocampus). Fig. 4.7 shows that there are more neurons firing in the vicinity of the thin probe than on the thick probe. We can extract the firing rate (see 4.7), which is 15 times larger on the thin probes. We therefore show experimentally that thinning the probe has a very large impact on the firing rate of neurons compared to the thick probe, which is due to a lower impact of the probe embodiment during insertion and recordings.

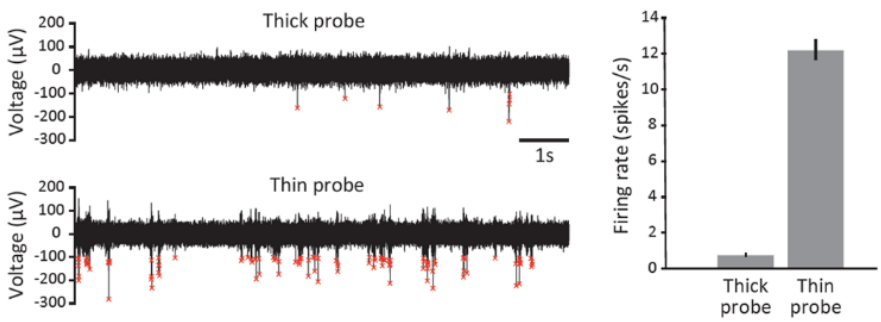

Figure 4.7: Impact of the probe thickness on neuron firing. The left figure shows an electrical recording from a tungsten electrode placed on a thick probe (top) and on a thin probe (bottom). More spikes are detected on the thin probe than on the thick probe on the same amount of time. The figure on the right shows the corresponding firing rates, which is much higher on the thin probe.

4.2.3 Impact of GMR bias voltage

Since the signal of interest is in a frequency range close to the 1/f corner, it might be interesting to consider an increase of bias voltage to enhance the SNR. Indeed, a higher bias voltage will not improve the SNR in the 1/f regime, but will be increased as V in the thermal noise regime. When optimizing the stacks, one goal was the suppression of RTN to allow for higher voltage bias. To evaluate the benefits of this, we tested the probe SOI 81-ref.-741 at 2V bias, and compared it to the usual 1V bias condition over a 2h session each and at the same location in the hippocampus.

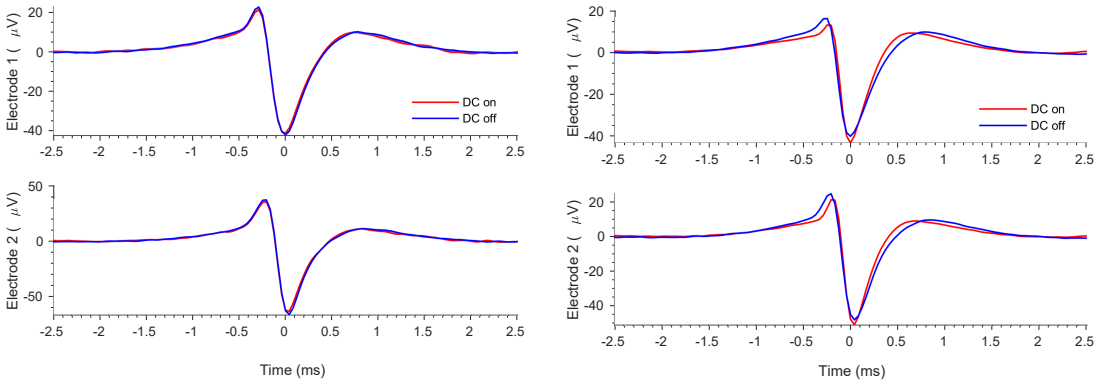

(a) Block 7 - Cluster 66 - 1 V

(b) Block 5 - Cluster 69 - 2 V

Figure 4.8: Averaged electrical (a) and magnetic (b) signal over 8045 events for DC off and 20440 events for DC on with $V_{GMR} = 2$ V. (2019–Probe SOI 81-ref.-741).

Using the Kilosort algorithm, which is presented later in section 4.4, to sort out the various spikes occurring during the recordings, one can see the difference of the averaged

Bias voltage	Averaged nb of spikes		Occurrences percentage	
	ON	OFF	ON	OFF
1 V	8 676	8 173	52 %	48 %
2 V	11 350	8 773	62%	38 %

Table 4.2: Analysis of block 7 (1 V) and block 5 (2V).

electrical signal depending on the on or off state for a bias voltage of 2V in fig. 4.8. In addition, the spiking rate is different in on and off conditions at 2V, compared to the 1V bias (fig. 4.9).

The total number of spikes is clearly higher when the bias is on (10 061 on average vs 8 676), which can also be clearly seen on the percentage of spikes on vs off; 62-38% at 2V compared to 52-48% at 1V (cf fig. 4.10).

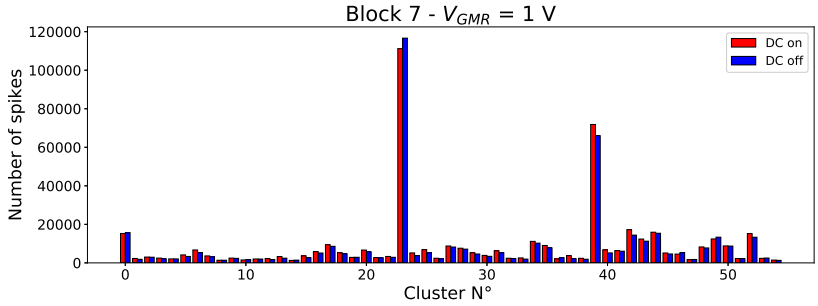

(a) Block 7

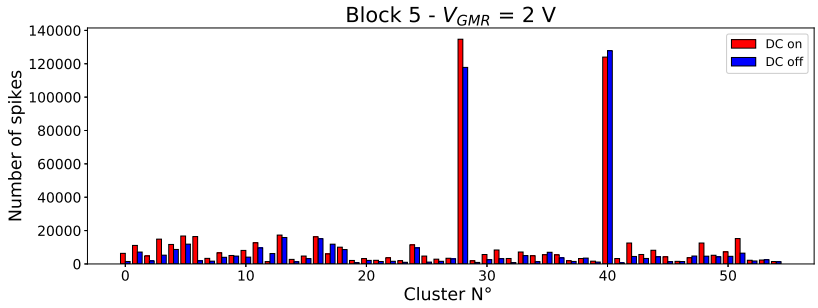

(b) Block 5

Figure 4.9: Number of spikes in on and off conditions for the various neurons spiking identified with Kilosort (cluster number) at 1V bias (block 7) and 2V bias (block 5) (2019-Probe SOI 81-ref.-741).

As neurons are sensitive to heat, their firing rate is increased when local temperature is elevated. We can thus make the hypothesis that by increasing the GMR sensors biasing voltage, we increased the temperature of the sensors by Joule effect and thus the temperature of neurons in vicinity of the GMR sensors was increased as well. One can also notice that in off condition (cf table 4.2) the averaged number of spike per identified neuron is still slightly higher at 2V than on the off conditions at 1V, which might be due to the fact that the switching time (around 1s) is not sufficient to allow the extracellular medium to cool down to its base temperature. We can also observe that at 1V, there is a slightly higher rate (6% higher) when the bias is on.

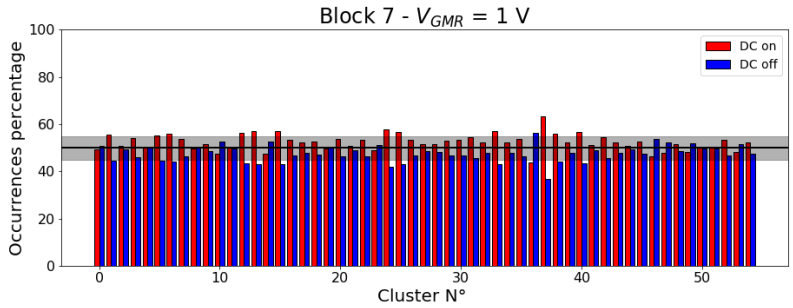

(a) Block 7

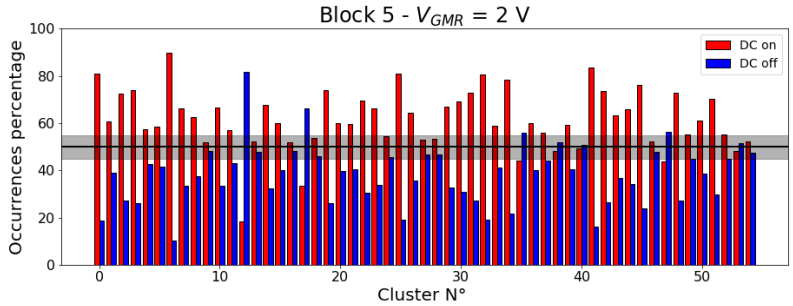

(b) Block 5

Figure 4.10: Percentage of spikes in on and off conditions for the various clusters at 1V bias (block 7) and 2V bias (block 5).The black line is set at 50% and the grey rectangle represents the interval 45%-55%.

As a conclusion on this experiment, we cannot increase the bias voltage to improve the SNR, since it leads to a local temperature elevation, and leads to a control condition which ceases to be comparable in term of spike occurrence and rate to the experiment under bias. To prevent this situation, we decided to limit the GMR sensors biasing voltage up to 1 V to avoid any heating effect on the surrounding neurons.

4.3 Magnetic averaging using tungsten electrodes

In this section, we present the various spike sorting methods applied when the electrical signals is recorded by 1 or 2 tungsten electrodes. From these methods, one can average the magnetic output in a corresponding time window to enhance the SNR.

4.3.1 Threshold method

A first method to select spikes which will be the signal of reference for the magnetic averaging is based on the detection on electrical signal through its amplitude threshold. The threshold is defined by [6]:

$$Thr = 5.5\sigma_n \tag{4.2}$$

$$\sigma_n = median\{\frac{|x|}{0.6745}\} \tag{4.3}$$

with x the signal, σ_n the estimation of the standard deviation (STD) of the background noise.

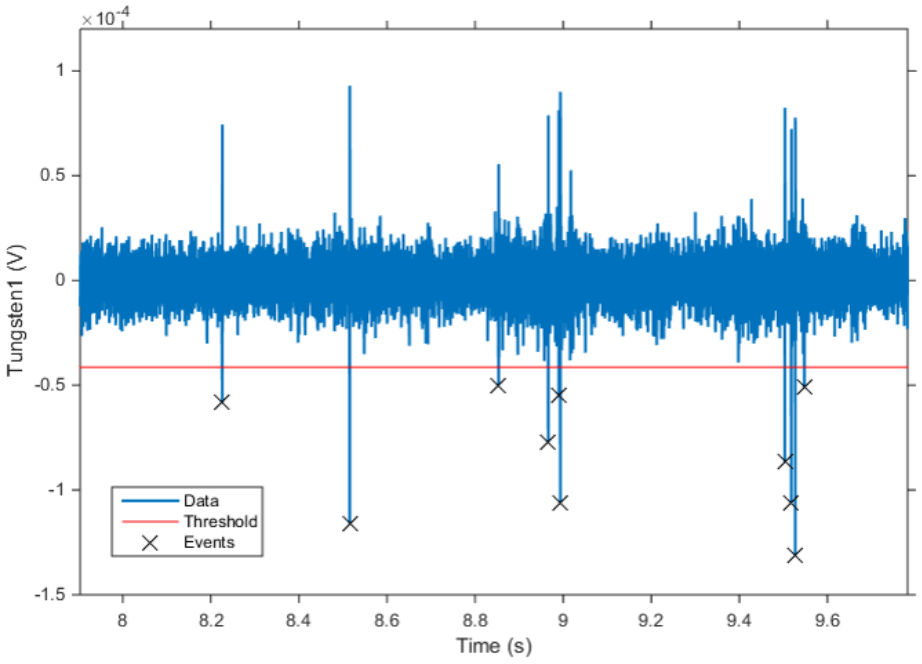

Figure 4.11: Example of spike detection (here negative spikes) with the threshold at 5.5 σ_n symbolized by the red line. The detected spikes are marked with a black crosses.

To prevent artifact from being detected as spikes, several additional parameters are taken into account: the data around DC on/off switching are discarded to prevent switching artifact ; a minimum of 2 ms between 2 spikes is needed ; the outsider events ($> 20\ \sigma_n$) are discarded and different thresholds are studied to measure their impact (from 2.5 σ_n to 12.5 σ_n) on the averaged magnetic signal.

Impact of threshold

The choice of the threshold is crucial for the data analysis. If the threshold is too low then electrical noise is mistaken with real electrical spikes but if the threshold is too high

then some spikes are missed and the number of detected events is artificially decreased. For every detected spike, a time window is extracted from the data with the electrical spike at the center. The magnetic recordings are averaged on the same time window as shown in fig. 4.4. It shows an example of spike detection on a tungsten electrode and the corresponding magnetic averaging on GMR sensors M1 for a threshold of $7.5\sigma_n$. In experiments with one or two tungsten probes, these are located in the close vicinity of the lower sensor on the tip (M1). M2 can be then considered more as a reference probe, since the electrical signals detected by the tungsten electrode(s) are related to neurons located close to M1.

We studied the threshold level impact in fig. 4.12. As first observation, the amplitude of the averaged electrical spike increases from around -20 µV for a threshold $V_{th} = 2.5\sigma_n$ to around -70 µV for $V_{th} = 7.5\sigma_n$. The spike amplitude increases as less noise and spikes with a lower amplitude are taken into account for the averaging. Secondly, for a threshold $\leq 5\sigma_n$, a "spike" shape centered at 0 ms appears for both M1 and M2 in the DC on state. It is different from the coupling artifact present in sec. 4.2.1 as it only appears in DC on state, which indicates a magnetic nature. The amplitude of the signal decreases when the V_{th} increases, for $V_{th} = 2.5\sigma_n$ the amplitude is around 6 nT, then for $V_{th} = 3.75\sigma_n$ it decreases down to around 4.4 nT, for $V_{th} = 5\sigma_n$ the amplitude is only around 1.2 nT and for $V_{th} \geq 6.25\sigma_n$ the signal has completely disappeared for a noise amplitude around 1.2 nT. Thus, this signal is probably only noise and its amplitude decreases with V_{th} as less noise is used for the averaging.

One can also note that the noise level on the magnetrode before averaging is around 85 nT RMS. The noise level is higher than expected from the probe characterization (around 50nT) but as the experiments are not made in a magnetic shielded room, there is additional environmental noise.

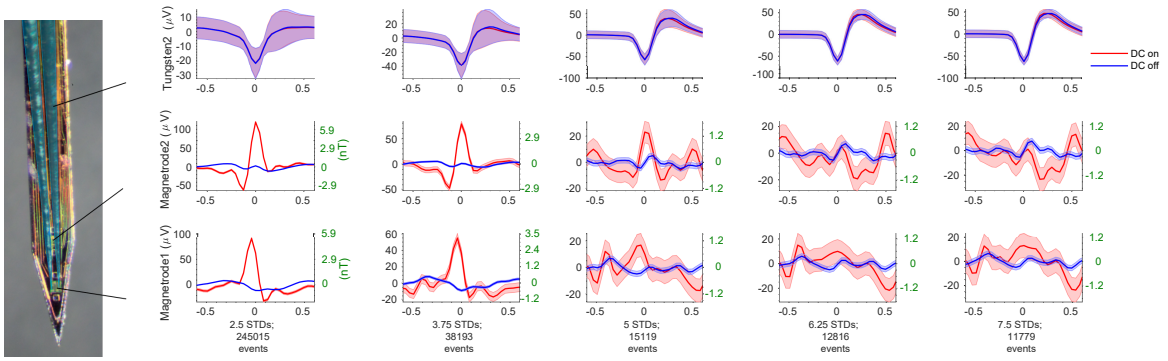

(a) Probes (b) Results from block 7 depending on the threshold level.

Figure 4.12: Impact of threshold level on averaged electrical and magnetic signals (2018-block 27-Probe SOI-ref.-712).

The number of events decreases with the threshold, from 245 015 events for $V_{th} = 2.5\sigma_n$ to 11 779 events for $V_{th} = 7.5\sigma_n$. For a higher threshold, fewer events are selected but they have a higher probability to come from real spikes and not from noise.

Simulation at low threshold

From the simulation model we developed, we can simulate the output averaged signal in presence of noise while varying the threshold level. To simulate this case, a recording

of two neurons which generate spikes with an amplitude of 80 µV (respectively 80 pT) and 100 µV (resp. 100 pT) with a white noise of 5 µV on the electrode (E1) and 20 nT on a magnetrode (M1) is used. With these parameters, we observe noise only on the magnetrode output while the electrode exhibits an increasing spike centered at 0 ms.

We then add correlated noise on both the electrode and the magnetrode with an amplitude of 2 µV on the electrode and 20 nT on the magnetrode. We finally change the threshold level and observe the evolution on the electrical and magnetic outputs. The results are shown in fig. 4.13. For $V_{th} = 1.5\sigma_n$ which corresponds to a V_{th} of 9 µV, a signal exhibiting spike features (biphasic shape centered around t=0) appears on the magnetrode (M1) ; this spike decreases when V_{th} increases until it disappears for $V_{th} = 5\sigma_n = 30$ µV. For $V_{th} = 9$ µV, the overall signal contains real spikes, as well as noise which is only on the electrode and noise correlated on the electrode and the magnetrode.

The magnetic signal is averaged on events from real spikes, correlated noise on E1 and M1 and noise detected on E1 as spikes. Each type of event has an impact on the averaging of the magnetic signal :

- **Uncorrelated noise**: noise events detected as spikes on E1 do not have a counterpart on M1, thus these events are averaged.
- **Real spikes**: the expected amplitude of the magnetic spikes is low (10-100 pT), the noise level should be lower than 100 pT to see a magnetic AP.
- **Correlated noise**: noise events due to correlated noise and detected as spikes on E1 for low threshold levels have a counterpart on M1. The amplitudes of these events are averaged and a ”spike”-like shape appears.

This artifact decreases when V_{th} is increased (fewer noisy events are detected as spikes) and disappears when V_{th} is higher than the noise level of the electrode.

The amplitude of the averaged electrical spike for $V_{th} = 1.5$ µV is low and around 60 µV, when real spikes have an amplitude of either 80 or 100 µV, because noisy events with an amplitude ≥ 9 µV are used to average the electrical signal.

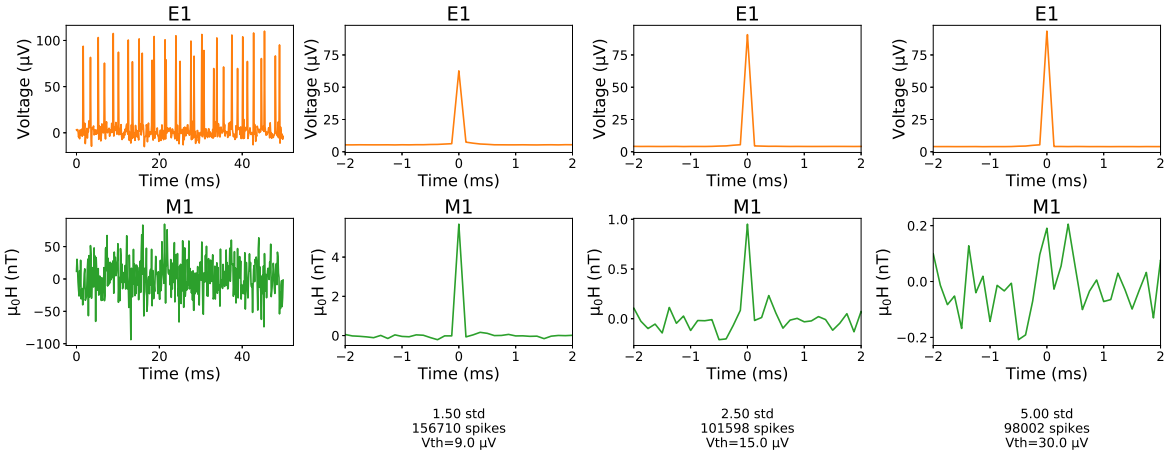

Figure 4.13: Simulation with a white noise on E1 of 5 µV, on M1 of 20 nT and a correlated noise on E1 (2 µV) and M1 (20 nT) with various threshold levels and magnetic spikes amplitude of 80 pT and 100 pT.

When running the simulation with a 500 pT magnetic spike (Fig. 4.14), we observe the same artefact at low threshold but for a threshold of 5 STDs, the real magnetic spike appears.

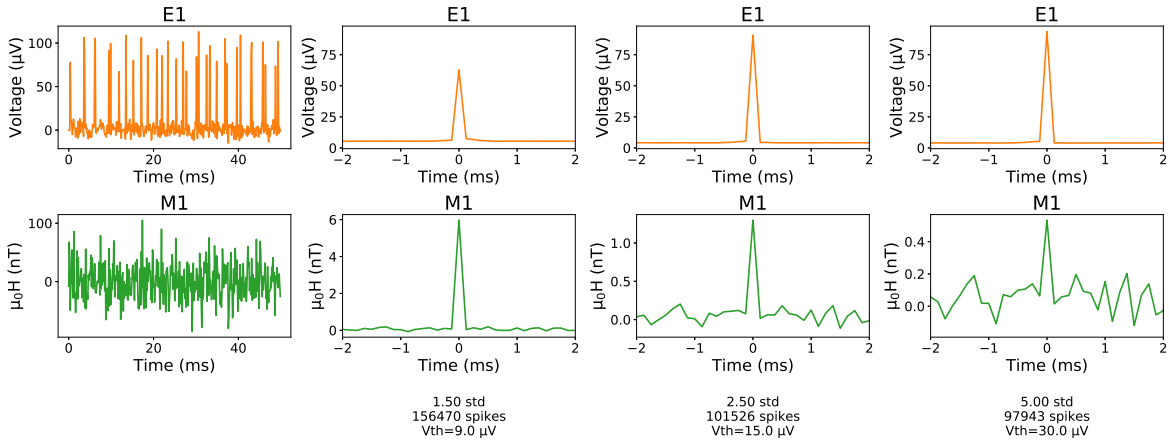

Figure 4.14: Simulation with a white noise on E1 of 5 µV, on M1 of 20 nT and a correlated noise on E1 (2 µV) and M1 (20 nT) with various threshold levels and magnetic spikes amplitude of 500 pT.

4.3.2 Analysis of previously recorded magnetic action potential

In view of the threshold effect, we can attempt to analyze and explain the preliminary results obtained in 2017. The experiments were performed in the former building of ESI, with a higher noise level in the experimental room. We hypothesize that the signal recorded at the end of the experimental session in 2017 was an artifact due to this higher noise level leading to a correlated signal on the electrode and the magnetrode. To test this artifact experimentally, we used a coil placed close to the rat's head (cf fig. 4.15) which generates a square wave with a frequency of 100 Hz. This signal leads to a correlated electromagnetic perturbation on both the electrode and the GMR sensor, at a single frequency.

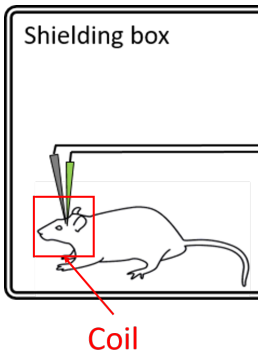

Figure 4.15: Schematic of the set-up used to simulate an electromagnetic artifact

From the averaged electrical signal recorded by the Tungsten1 electrode, we can deduce that below a threshold of $5\sigma_n$, noises and spikes of low amplitudes are selected as the shape of the action potential starts to be well defined for $V_{th} \geq 5\sigma_n$ for an amplitude of around 90 - 100 µV. For $V_{th} = 7.5\sigma_n$, the averaged electrical signal starts to be different

on the DC on and DC off state. Finally, for the higher threshold level selection, only 37 events are selected, which is too low to have a sufficient SNR, as can be seen by the signal deformation on the electrical output. Magnetic output is purely noise.

We also observe that the coupling artifact described in sec. 4.2.1, is present in the DC off state, its amplitude decreases when V_{th} is increased. A magnetic signal appears in the DC on state (cf fig. 4.16) with an amplitude of -2 400 µV (or - 141.2 nT) for a threshold of 2.5 STDs. This signal increases up to -3 200 µV (-188.2 nT) and is reduced down to around -600 µV for V_{th}= 5 STDs. For V_{th} = 6.25 STDs, it disappears. This signal's amplitude is opposite to the coupling artifact and is linked to the magnetic signal generated by the coil.

We suppose that when events are selected on the electrical signal, some of them correspond to noisy peaks in the magnetic signal. As the amplitudes of these peaks are too low, magnetic noises are averaged but when there is an additional magnetic noise, then these noises amplitudes are increased, their averaging results in the shape centered at 0 ms.

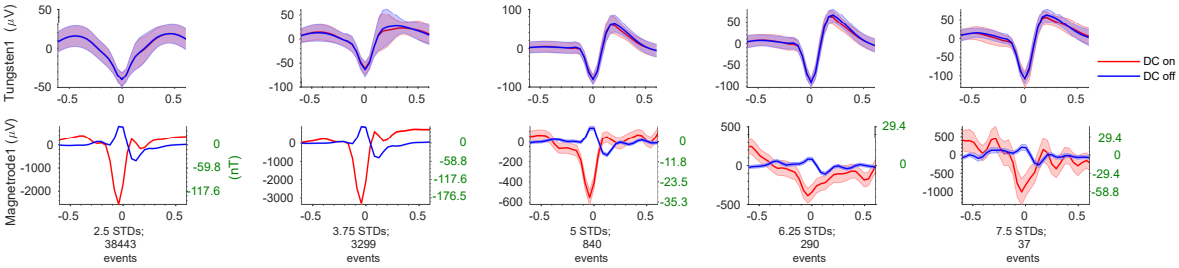

Figure 4.16: Experimental results of the averaged recordings on a tungsten electrode and M1 (2018-Block 23-Probe SOI-ref.712) when an external noise is generated by a coil, and the related effect according to the threshold level.

We experimentally demonstrated that correlated noises can lead to a "spike"-like response in the magnetic averaging at low threshold, which is the most plausible explanation for the observed signal in 2017 (whose amplitude was increasing with low threshold levels).

As a conclusion on the threshold method, it appears that the threshold level selection is a very important parameter, whose choice is a compromise between a level where correlated noises are not leading to spike-like artefact, while keeping a number of events high enough to reach an SNR allowing to be in the range of the expected signal.

In the next sections, we will see how to refine the spike selection and apply techniques which are based on the spike-shape identification rather than a simple amplitude selection.

4.3.3 Discriminating neurons by amplitude correlation

The electrical neuronal activity is recorded on two tungsten electrodes (W1 and W2) at the same time. They are plotted as a function of their amplitude on both tungsten electrodes and then associated to a cluster by a hand-made selection from fig. 4.17a and fig. 4.17c and associated to a cluster. A cluster can regroup spikes from several neurons. The averaging of the electrical and magnetic signal is then made with spikes from a single cluster (cf fig. 4.17b and fig. 4.17d).

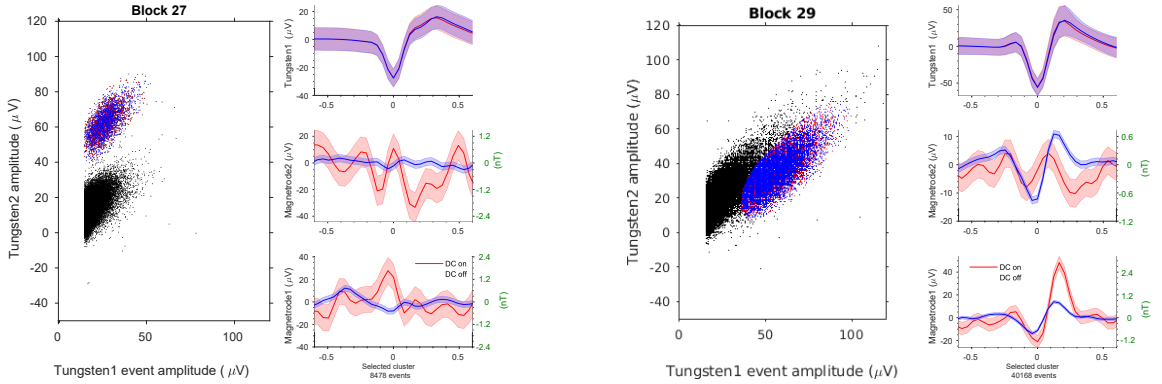

(a) Cluster - block 27 (b) Results - block 27 (c) Cluster - Block 29 (d) Results - block 29

Figure 4.17: Spikes sorting depending on their amplitudes on W1 and W2 (2018 experiments). Blue dots and lines represent data recorded during DC off state while red dots and lines represent data recorded during DC on state. (a) Example of two well defined clusters. The lower one is probably just noise while the upper one is supposed to be only real spikes. (b) The magnetic signal is averaged on 8 478 events which are selected in (a). Only noise is visible on M1 and M2 (c) Example of two clusters which are mixed. (d) A coupling artifact arises on M2 and a higher signal is shown on M1 after an averaging over 40 168 events.

When clusters are well separated, the spike-like artifact does not arise. Thus selecting clusters composed of spikes with amplitudes higher than noise allows to have cleaner recording.

In fig. 4.17d a signal in the DC on state is only recorded on M1 and seems to be different from the coupling artifact. As this signal is higher in the DC on state compared to the DC off state and is only recorded on M1, it might be a recording of a magnetic signal.

4.3.4 Possible magnetic action potential?

Following the identification of the spike-like artefact, we performed several experiments in vivo, varying the threshold to see if a relevant signal may appear in the magnetic output.

In one of the experiments (block 29), we observed a particular feature as is shown in fig. 4.18 and a detailed figure can be found in appendix D.1.

Here the threshold is varied from 1.5 to 7.5 STDs. On the electrical output, the averaged signal reveals the spike with a more precise shape and lower deviation as the threshold is increased. This corresponds to a better selection of relevant spiking events. When observing the magnetic outputs of both sensors (M1, close to the tungsten probe) and M2 (higher towards the probe base), we can distinguish several features. The OFF conditions reveal some slight coupling, which is of electrical nature (for both probes, though of slightly different shape and amplitude). For the ON conditions, at low threshold (<5 STDs), the spike-like artefact appear, on both magnetic probes, which we attribute to correlated electromagnetic noise, as discussed before. The amplitude of this signal decreases when increasing the threshold. For threshold higher than 5 STDS, one observes on M2 a noisy output, which increases as the threshold increases, because fewer events are selected for the averaging. On contrary on M1, one can see a signal

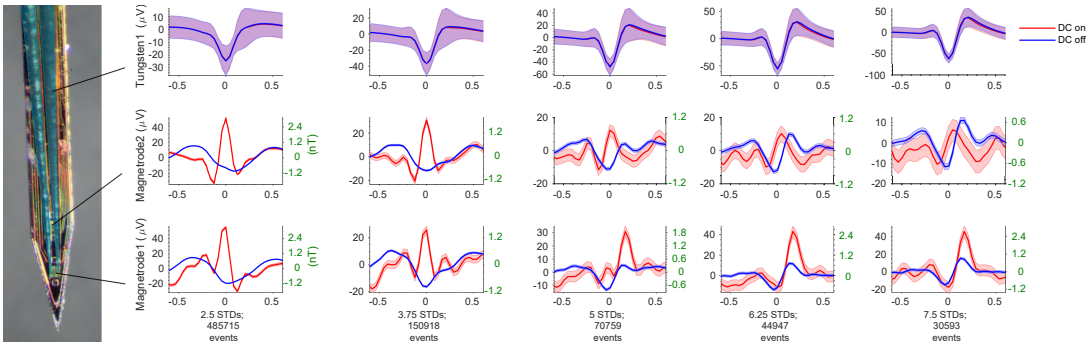

(a) Probe picture

(b) Averaged electrical and magnetic outputs

Figure 4.18: Optical picture of the probe containing the tungsten electrode, the two magnetic sensors location indicated by the arrows. Impact of threshold on recorded electrical and magnetic signals V_{th} for 2.5 STDs, 3.75, 5, 6.25 and 7.5 STDs (2018-block 29-Probe SOI-ref.-712).

pointing out around t=0, with an amplitude of the order of 3-3.5nT peak-to-peak. At higher threshold, the peak is melted in the noise level which increases.

We cannot attribute this signal to a noise-correlated artefact, which would also appear on the M2 probe, which remains without noticeable signal from the noise. This recording has been performed with the best conditions for noise, artefact identification and appears at the state of our knowledge to a magnetically correlated signal with the one measured on the closeby electrode. We did not record another of this signal on another location, but the sensitivity to the probe location in the structure is high and cannot be controlled. In absence of other explanation, this magnetic signal is unexplained by known artefact or capacitive coupling, and could be linked to the magnetic counterpart of the neuronal spiking. Nevertheless, the amplitude is rather high with respect to estimates of single neuron spiking (more in the few hundred pT range).

4.3.5 K-mean clustering

Spikes can also be sorted into clusters by selecting them according to their shape. Here, spikes are sorted based on K-means clustering from a recording on only one tungsten electrode. This type of selection was only used a few times and is reported here to illustrate how spikes can be sorted based on their shapes. Results are shown in fig. 4.19.

Three clusters are identified with a number of events between 1 541 and 2 589.

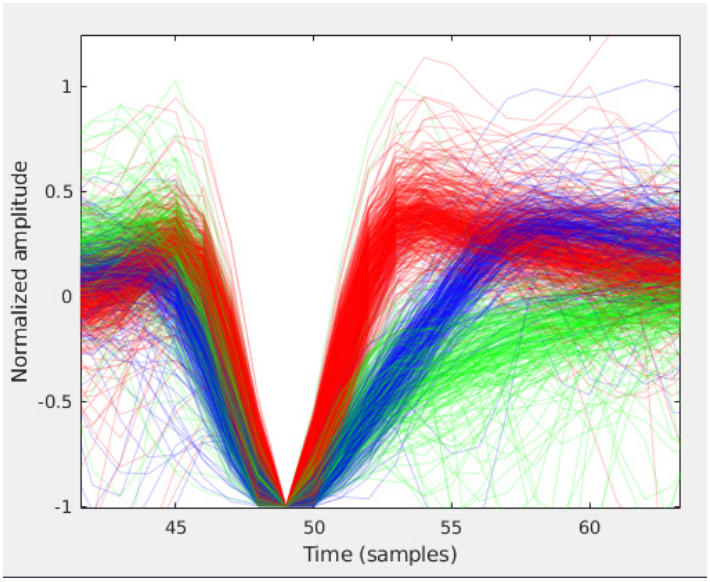

(a) All spikes are plotted at the same time.

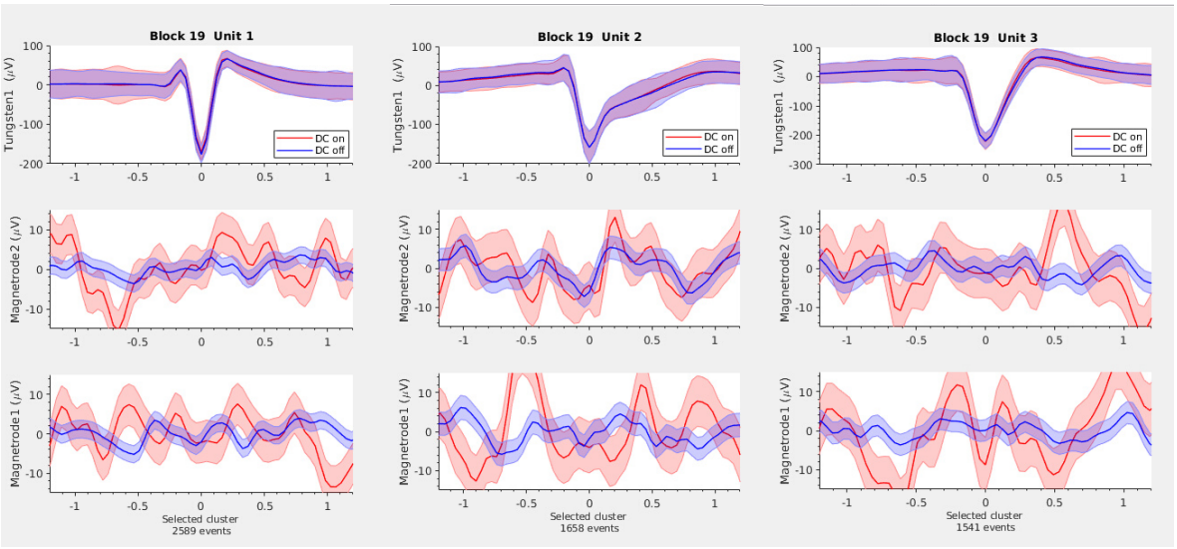

(b) Three units are identified.

Figure 4.19: (a) All spikes are plotted at the same time. Each color correspond to a single unit (unit 1 - red, unit 2 - green, unit 3 - blue). (b) Spikes from a single unit are analysed and plotted as well as the averaged magnetic signal on M1 and M2. (2019-Block 19-Probe SOI-ref.-731)

4.4 Magnetic averaging using arrays of electrodes

Tungsten electrodes are replaced by 2 types of dense array of electrodes. The high density of electrodes allows first to have a better coverage and a better location, which leads to record more electrical signals of interest around the GMR sensors. This should enhance the spikes sorting quality and help to determine the location of a specific neuron (above or close to a magnetic sensor). The sorting method uses the Kilosort algorithm [4] applied to the signals recorded on several electrodes. To reach the challenge of the increasing number of electrodes on probes for neuronal recording, Kilosort [4] is an algorithm which promises to sort spikes in real time from a huge number of simultaneous recordings. In addition, we use a trimmed mean: 10 % of the spikes with the lowest

and highest amplitudes are discarded.

The dense electrode array is only covering the lower GMR sensor (M1) but with a high density of electrodes. The spikes associated to a single neuron and recorded by different electrodes do not have the same amplitude. The position of the neuron can then be deduced. For example, in fig. 4.20 the responding neuron should be located between the electrodes 2, 12 and 17, well centered above M1. To ensure the quality of the recording, the time between 2 spikes is measured. As the refractory period of a neuron is 2 ms, no spikes should be measured in this interval. Otherwise, some spikes fired from another neuron are present in the cluster. Typically, we expect less than 2 % of spikes fired during this interval.

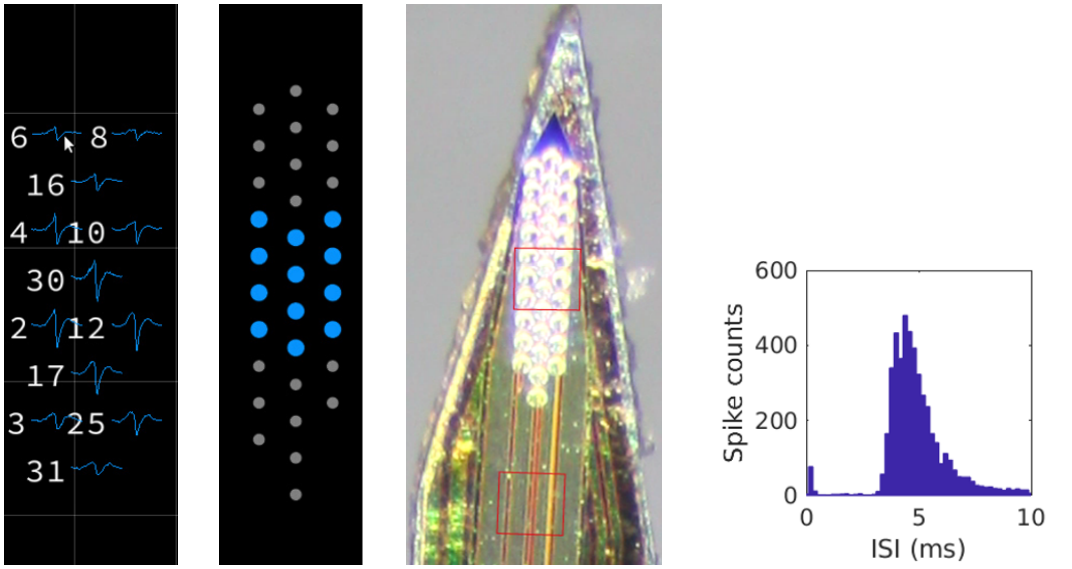

(a) Spikes amplitudes

(b) Electrodes scheme

(c) Picture of a poly3 mounted on a magnetrode

(d) Number of spikes as a function of interval between 2 spikes.

Figure 4.20: Typical recording from a dense array of electrodes.

After the neuronal recording, spikes are sorted into units. Each unit is associated to a unique neuron. The units do not have the same amount of spikes and the number of spikes can be too low to expect any magnetic action potential (less than 40 000 events). For example, unit 1 shown in fig. 4.22 has around 5 000 events with a pretty large noise. On the opposite, unit 2 has 100 000 events but after averaging, the magnetic signal is less noisy than the averaging for unit 1 but there is also no trace of a magnetic action potential. The results are similar on the second type of electrodes array: poly 2.

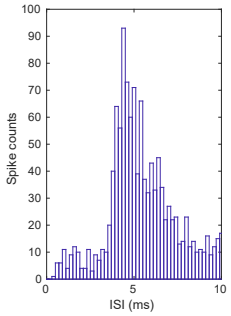

(a) Cluster 57 - ISI

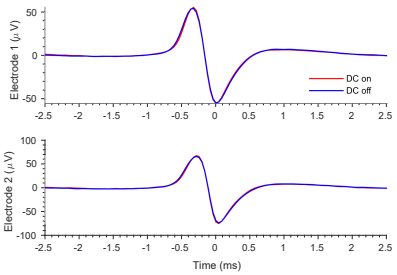

(b) Cluster 57 - averaged electrical signal

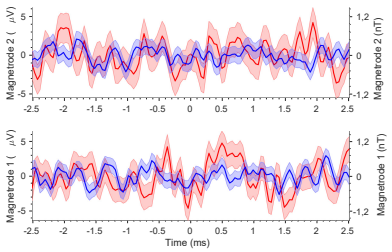

(c) Cluster 57 - averaged magnetic signal

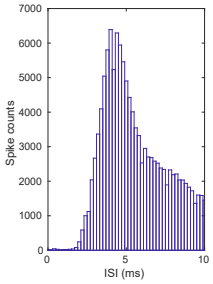

(d) Cluster 36 - ISI

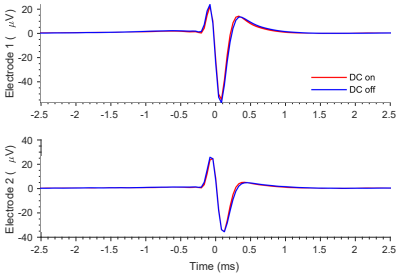

(e) Cluster 36 - averaged electrical signal

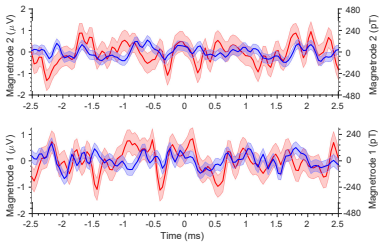

(f) Cluster 36 - averaged magnetic signal

Figure 4.21: (a)-(c) Results computed with Kilosort, from cluster 57 with 6 280 events in DC on state and 5 283 events in DC off state.(2019-block7)-Probe SOI 81-ref.-721) (d)-(f) results from cluster 36 with 111 181 events in DC on state and 116 653 events in DC off state (2019-block7)

.

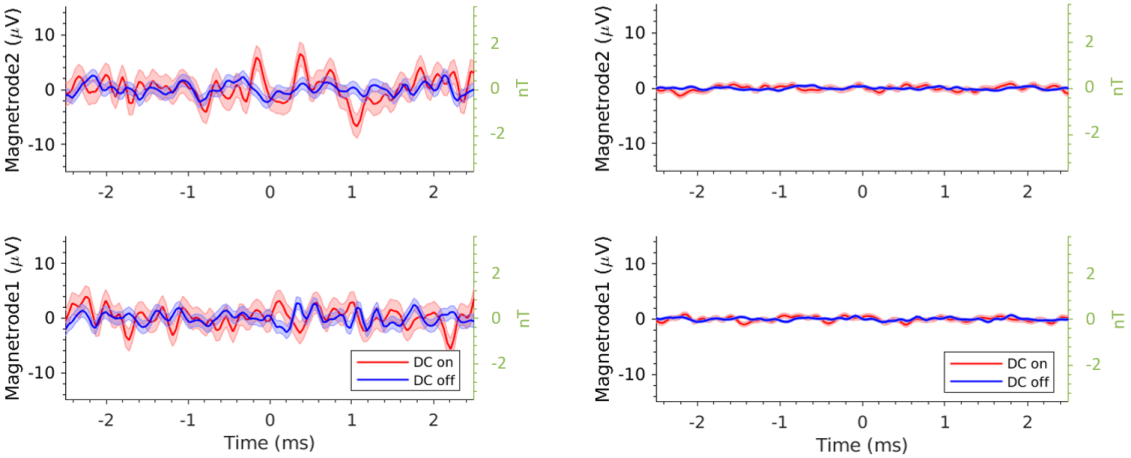

(a) Cluster 55: 5 247 events

(b) Cluster 26 : 113 789 events

Figure 4.22: Example of 2 clusters extracted for the same recording block. For each unit, the number of electrical spike is different (2019-Block 7-Probe SOI 81-ref.-741).

4.5 Conclusion

To summarize on the noise level and limit of detection we reached during the in vivo experiments we report the values in table 4.3. Magnetrodes have a noise amplitude

Figure	Year	Block	Mag.	Elec.	Nb events	Av. noise (nT)	Noise_{RMS}(nT)	$\text{Noise}_{RMS,th}$ (nT)
4.17	2018	27	SOI-ref.-712	W*2	8 478	1.2	78.1	38.7*
4.17	2018	29	SOI-ref.-712	W*2	40 168	0.6	85.0	38.7*
4.21	2019	7	SOI 81-ref.-741	Poly 3	5 283	1.2	61.7	44.6**
4.21	2019	7	SOI 81-ref.-741	Poly 3	116 653	0.24	58.0	44.6**

Table 4.3: Summary of noise amplitude from experimental recordings and noise measured in the magnetic shielded room on a bandwidth of [300 Hz - 6k Hz]. *: Noise computed on probe SOI-ref.-712-M1 at 0.5V. **: Noise computed on probe SOI 81-ref.-712-M1 at 1V.

of respectively 38,7 nT and 44,6 nT for the magnetrode SOI-ref.-712 and SOI 81-ref.-741 in the magnetic shielded room. When extracting the noise level observed during the recording, we can evaluate a single event noise in the frequency band applied, i.e. around 82 and 60nT respectively. These values are higher than the noise extracted from measurement in the best conditions (Magnetic shielding, in air). We can extrapolate some additional noise brought by the remaining noise in the experimental room at ESI, and also from the brain noise itself, which is due to the ionic and therefore electrical activity in the extracellular medium around the probe. This may explain the higher noise value during the experiment.

Nevertheless, in experimental conditions, we have reached a bottom noise floor as low as 240pT. This has not been sufficient yet to record without ambiguity a magnetic action potential, but these values are the best reported in such an experiment.

In conclusion, we have demonstrated that the state of the art thin magnetrode we have developed can allow in vivo recordings with a higher spiking rate than with the former thicker probe. The experiment now presents a very efficient set-up against noise from moving metallic part nearby or from power line contamination. These experiments were made during 2 experimental sessions, the first one in July 2018 and the second in July 2019. 7 magnetrodes were used during these experiments for a total of 62 recording block on 8 rats.

We have also tested several electrodes and spike sorting algorithms. We have therefore improved the method to select the electrical response of a single neuron to perform efficient averaging of the magnetic outputs of the magnetrodes. We have also demonstrated both with a model and experiments that a correlated noise artefact may occur when applying a low level threshold method. This is solved using Kilosort algorithm combined with an array of electrodes to better localize and enhance the signal of interest. In one of the experiments, we observed a magnetic signal correlated with the electrical spike, but this is so far a single observation and with a signal amplitude higher than expected. Also, the location of the magnetrode in the brain is approximate and difficult to control.

Finally, even with the best experimental conditions, we have reached an effective noise level over the frequency band of around 240pT, which gives a lower limit for spike detection.

Bibliography

[1] Francesca Barbieri. ■ magnetrodes ■ project 600730 - fp7-ict-2011-9, 2015. *unpublished*. 124

[2] Francesca Barbieri, Vincent Trauchessec, Laure Caruso, Josué Trejo-Rosillo, Bartosz Telenczuk, Elodie Paul, Thierry Bal, Alain Destexhe, Claude Fermon, Myriam Pannetier-Lecoeur, et al. Local recording of biological magnetic fields using giant magneto resistance-based micro-probes. *Scientific reports*, 6(1):1–10, 2016. 124

[3] Laure Caruso, Thomas Wunderle, Christopher Murphy Lewis, Joao Valadeiro, Vincent Trauchessec, Josué Trejo Rosillo, Jose Pedro Amaral, Jianguang Ni, Patrick Jendritza, Claude Fermon, et al. In vivo magnetic recording of neuronal activity. *Neuron*, 95(6):1283–1291, 2017. 124, 125

[4] Marius Pachitariu, Nicholas Steinmetz, Shabnam Kadir, Matteo Carandini, et al. Kilosort: realtime spike-sorting for extracellular electrophysiology with hundreds of channels. *BioRxiv*, page 061481, 2016. 128, 143

[5] Nosratullah. Modeling the simplest biological neuron with python, 2020. URL https://medium.com/analytics-vidhya/modeling-the-simplest-biological-neuron-with-python-adda892c8384. 131

[6] R Quian Quiroga, Zoltan Nadasdy, and Yoram Ben-Shaul. Unsupervised spike detection and sorting with wavelets and superparamagnetic clustering. *Neural computation*, 16(8):1661–1687, 2004. 136

Conclusion

The aim of this thesis was to optimize a tool called magnetrode, which is the magnetic counterpart of an electrode and is a new tool for neuroscience. The simultaneous recording of neuronal activity by magnetrodes at local scale and by MEG which is a non-invasive method is of great interest. Indeed, the recording of the local activity might push further the understanding of the MEG signals recorded at large scale by establishing the link from micro-scale signals to macroscale recordings. The signal recorded by MEG comes from post-synatic activity which last tens of milliseconds. Thus, the activity of several neurons is summed and can be measured. As the activity of an ensemble of neurons was already measured with magnetrodes [1], the aim of this thesis is to record the magnetic activity of a single neuron called action potential.

The amplitude of a magnetic action potential is expected between 10 and 100 pT at a frequency of a few kHz. To detect these signals, magnetic sensors based on Giant MagnetoResistance (GMR) effect are integrated into a magnetrode. These sensors can detect a magnetic field with an amplitude of 1 nT at 1 kHz. To decrease this detection limit, several axes have been studied.

The width and composition of the GMR sensors have been optimized to reach the best compromise between a low detection limit and stability. Indeed, a stable GMR sensor does not exhibit random telegraph noise (RTN) and allows the biological signal to be recorded and averaged over a long period of time while keeping a limit of detection of 1 nT. To reduce the damage inflicted by the insertion of the magnetrode into the brain, the tip thickness has been reduced from 270 µm down to 25 µm while keeping the same limit of detection, which is around 1nT. It has an important impact on the firing rate of neurons as the spiking rates is increased 10 times when using thin magnetrodes instead of thick magnetrodes. It implies that for the same recording time, more spiking events are detected with the thin probe.

In order to realize a mapping of neuronal currents, a magnetrode designed to measure a magnetic field in two dimensions has been developed. The technique of local repining has been adapted to a magnetrode with two sensors having perpendicular axis of sensitivity. This work has highlighted the existence of a parasitic sensitivity perpendicularly to the main sensitive axis; hence to reconstruct a magnetic field in two dimensions, a sensitivity matrix which takes into account both the main and parasitic sensitivities of the two GMR sensor is needed. An improvement would be to suppress the parasitic sensitivity while having a single sensitive axis between 1.5 %/mT and 2 %/mT. To go further, the local repining method can be optimized : the GMR sensor currently reoriented by local heating with a voltage pulse can be instead heated with a laser to

to avoid sensitivity degradation during repinning. In addition, the distance between the two sensors can be reduced for a better localization of the neuron whose signal is detected.

Finally, magnetrodes have been applied to *in-vivo* recordings under well-controlled conditions at the Ernst Strüngmann Institute (ESI). Indeed, both electrical and magnetic noises are reduced thanks to a Faraday cage, the use of external batteries to supply all the electronics inside the cage and the use of optical fibers to communicate between the inside and the outside of the Faraday cage. Two batches of magnetrodes were made, the first one in 2018 and second one in 2019 and they were used during two experimental sessions. During both sessions, 25 µm thin magnetrodes have proved their robustness after repeated insertions and withdrawals and their stability over a period of one year. In addition, the electrodes used to detect spiking events were upgraded from one or two tungsten electrodes to dense electrodes arrays in order to refine the spikes selection and increase the localization of neurons. The detection and understanding of artifacts has been improved thanks to the increased numbers of electrodes and also with simulations which have explained an artifact.

In conclusion, we have succeded in decreasing the magnetic noise level of magnetrode and of the experimental setup down to 240 pT or 480 pT peak-to-peak. Unfortunately, this amplitude is still too high for in vivo magnetic action potential recording without ambiguities. However, in one session we observed a magnetic signal correlated to the electrical spike. Its amplitude is pretty high compared to the expected magnetic amplitude (2.4 nT instead of the 100 pT estimation) but all the control experiments are in favor of a real magnetic signal. This signal is recorded neither when the GMR sensor is not powered nor by the second GMR sensor.

To go further and decrease the magnetrode limit of detection, one possibility is to replace GMR sensors by sensors based on Tunnel Magnetoresistance (TMR). TMR sensors have a higher magnetoresistance ratio than GMR sensors but their 1/f noise at low frequency is also higher which limits the performance of TMR at low frequencies presently, but makes TMR potentially more interesting at a few kHz. Moreover, in the laboratory, the noise of TMR is studied to have a better understanding of the mechanisms behind noise. TMR would be a great improvement, as in addition to a lower limit of detection, the size of the magnetic sensors can be reduced from 50*50 μm^2 to an array of dots with a diameters of 5 µm for example, leading to a better spatial resolution. In addition, to optimize the neuronal detection and localization, one can imagine a magnetrode, which alternates TMR sensors and electrodes with similar diameters (5 µm for example) covering up the entire magnetrode tip.

To reduce the noise, the first level of electronics (filtering and amplification) can be directly integrated onto the silicon wafer before the magnetrode fabrication. Leading to an optimized magnetrode with a high density of electrodes and TMR sensors as well as an optimized integrated electronics. Collaborators from Institute of Smart Sensors in Stuttgart are currently developing an ASIC (application-specific integrated circuit) to integrate the electronics in the silicon substrate.

This thesis has been the opportunity to push the magnetrode technology further in several ways: GMR composition, substrate thinning and 2D sensing. There is room for further improvements which require interesting research to be done with the exciting perspectives of recording a magnetic action potential to push further our understanding

of the working principles of the brain.

Bibliography

[1] Laure Caruso, Thomas Wunderle, Christopher Murphy Lewis, Joao Valadeiro, Vincent Trauchessec, Josué Trejo Rosillo, Jose Pedro Amaral, Jianguang Ni, Patrick Jendritza, Claude Fermon, et al. In vivo magnetic recording of neuronal activity. *Neuron*, 95(6):1283–1291, 2017. 149

Appendix A

GMR sensor fabrication

Step		
step 1	**Etching**	
Lithography	photoresist	1813 (2s-500 rpm/60s-4000 rpm/2s-6000 rpm)
	baking	3 min at 110°C
	exposure	20 s
	developing	MF319, 45 s
Etching (IBE)	current	6.4 mA
	pressure	1×10^4 mbar
	power	90 W
	time	24 min (rotation 90° / 6 min)
Lift-off		acetone and isopropanol with ultra-sound
step 2	**Contact deposition**	
Lithography	photoresist	AZ5214E (2s-500 rpm/60s-4000 rpm/2s-6000 rpm)
	baking	3 min à 110°C
	exposure	20 s, hard contact (MJB4)
	developing	MF319, , 45 s
Evaporation	cleaning (IBE)	30s, 90W
	deposition	Ti: 65 mA, 2min , 4-5nm
		Au: 400 mA, 2min, 120-150 nm
		Ti: 65 mA, 2min, 4-5 nm
Lift-off		acetone and isopropanol with ultra-sound
step 3	**Passivation**	
Lithography	photoresist	AZ5214E (2s-500 rpm/60s-4000 rpm/2s-6000 rpm)
	baking	3 min à 110°C
	exposure	20 s, hard contact (MJB4)
	developing	MF319, 45s
Sputtering	cleaning (IBE)	30s 90 W
	deposition	Al_2O_3, 2 h, 200 W, 5.3×10^3 mbar
		Si_3N_4, 2 h, 200 W , 5.3×10^3 mbar
Lift-off		acetone and isopropanol with ultra-sound

Appendix B

Resistance and MR variation between M1, M2 and M3

AS we have seen in section 3.3.1, for almost half of the magnetrode we have: $R_{M1} > R_{M2} > R_{M3}$ and $MR_{M1} < MR_{M2} < R_{M3}$ (cf fig.B.1a).

The increase of resistance between M1, M2 and M3 can be partly explained by the increase of contact resistance which lower the MR of the GMR sensors as shown in fig.B.1b.

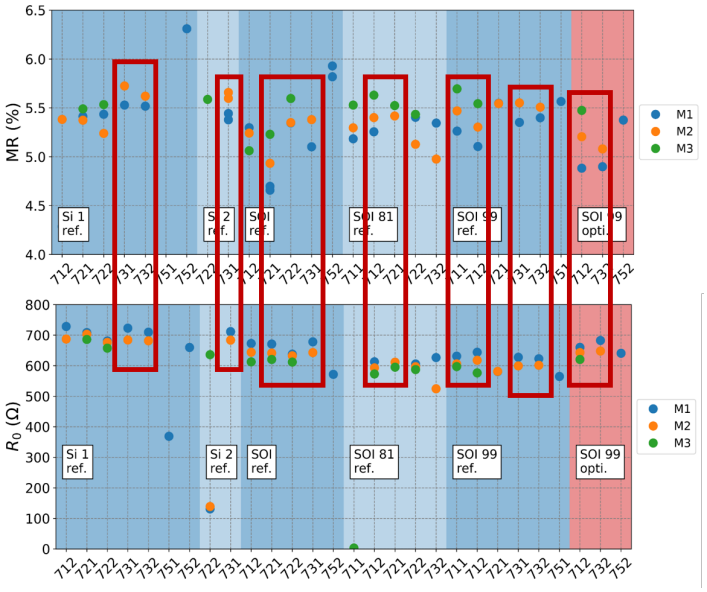

(a) Comparison MR and R

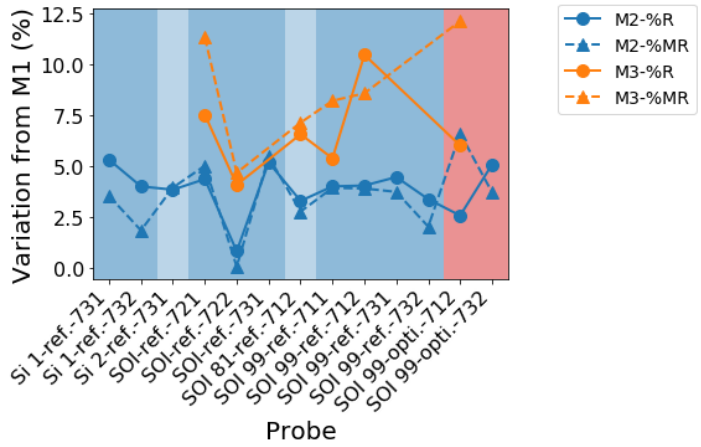

(b) Percentage variation

Figure B.1: Comparison of the MR and R of the selected magnetrode.

Appendix C

Code for the simulation

C.1 Neuron simulation

```
# -*- coding: utf-8 -*-

import numpy as np

class NeuronV2:
    Nb_neurons=0

    def _set_Hm(self,check=False):
        self.Hm=[ i*self.H_spike/self.V_spike for i in self.Vm]
        print('set_Hm')
    def _set_Vm(self,check=False):
        I = self.Iamp * np.ones(len(self.time))         # input current
                                                (A)

        print('set_Vm')
        # ---------------iterate over each time step
        compt=0
        for i, t in enumerate(self.time):

            if t > self.t_rest:
        #         randomTerm = np.random.normal(0,1)
                randomTerm=0
                self.Vm[i] = self.Vm[i-1] + (-self.Vm[i-1] + I[i]*self
                                                    .Rm + randomTerm) /
                                                     self.tau_m * self.
                                                    dt

                compt+=1

                if self.Vm[i] >= self.Vth:
#                     print('SPIKE')
        #             print(Vm[i-compt:i+1])
                    self.Vm[i] += self.V_spike
                    self.t_rest = t + np.random.randint(2,4)
                    self.compt=copy.deepcopy(compt)
                    if check:
                        print(compt)
                    compt=0
```

```
        self._set_Hm(check=check)

    def __init__(self,T,V_spike,Vth,Iamp,dt):
        self.T=T                                    # total time to
                                                    simulate (msec)
        self.Rm=1                                   # resistance (
                                                    kOhm)
        self.Cm=10                                  # capacitance (
                                                    uF)
        self.V_spike=V_spike                        # spike delta (V
                                                    )
        self.Iamp=Iamp
        self.dt = dt                                # simulation
                                                    time step (msec)
        self.time = np.arange(0, self.T+self.dt, self.dt) # time array
        self.t_rest = np.random.randint(0,4)        # initial
                                                    refractory time
        self.Vm = np.zeros(len(self.time))          # potential (V)
                                                    trace over time
        self.tau_m = self.Rm*self.Cm                # time constant
                                                    (msec)
        self.tau_ref = np.random.randint(2,4)       # refractory
                                                    period (msec)
        self.Vth = Vth                              # spike
                                                    threshold (V)
        self.compt=0
        self.Hm=np.zeros(len(self.time))            # mag fieldl (T)
                                                     trace over time
        self.H_spike=V_spike *1e-6                  #  mag spike
                                                    amplitude (pT)


        self._set_Vm()

        NeuronV2.Nb_neurons+=1
```

C.2 E1 simulation

```
# -*- coding: utf-8 -*-

import numpy as np

class electrode:
    def _set_noise(self):
        self.noise=[n+np.random.normal(0,1)*self.noiseAmp for n in
                                                    self.noiseElectro]


    def _set_Vrecorded(self):
        for i in range(len(self.time)):
            self.Vrecorded.append(self.Vm[i]+self.noise[i])

    def __init__(self,noise,electromag,Vm,time,dt):
        self.time=time
        self.dt= dt
        self.noiseAmp=noise
        self.noiseElectro=electromag
        self.Vm=Vm
```

```
        self.noise=[]
        self.Vrecorded=[]

        self._set_noise()
        self._set_Vrecorded()

    def detect_spike(self,Vth):
        spike_index=[]
        for index,v in enumerate(self.Vrecorded):
            if v >= Vth:
                spike_index.append(index)
        return spike_index

    def average_spikes(self,spike_index,t):
         spikes=[]
         di=int(t/self.dt)
         for i in spike_index:
             if i-di>0 and i+di<len(self.Vrecorded)-2:
                 spikes.append(self.Vrecorded[i-di:i+di])
         time_av=np.arange(-t, t, self.dt)
         return time_av,np.mean(spikes,axis=0)
```

C.3 M1 simulation

```
# -*- coding: utf-8 -*-

import numpy as np

class magnetrode:
    def _set_noise(self):
        self.noise=[n+np.random.normal(0,1)*self.noiseAmp*self.
                                            sensitivity/self.Vgmr for n
                                             in self.noiseElectro]

    def _set_Hrecorded(self):
        for i in range(len(self.time)):
            self.Hrecorded.append(self.Hm[i]*self.sensitivity/self.
                                                Vgmr+self.noise[i])
    def __init__(self,sensitivity,Vgmr,noiseAmp,noiseElectro,Hm,time,
                                            dt):
        self.time=time
        self.dt=dt
        self.sensitivity=sensitivity
        self.Vgmr=Vgmr
        self.noiseAmp=noiseAmp
        self.noiseElectro=noiseElectro
        self.noise=[]
        self.Hm=Hm
        self.Hrecorded=[]

        self._set_noise()
        self._set_Hrecorded()

    def average_spikes(self,spike_index,t):
         spikes=[]
         di=int(t/self.dt)
```

```
        for i in spike_index:
            if i-di>0 and i+di<len(self.Hrecorded)-2:
                spikes.append(self.Hrecorded[i-di:i+di])
        time_av=np.arange(-t, t, self.dt)
        return time_av,np.mean(spikes,axis=0)
```

C.4 Artifact stimulation

```
# -*- coding: utf-8 -*-

from scipy import signal
import numpy as np
import matplotlib.pyplot as plt
from matplotlib import rcParams
import neuron
import magnetrode
import electrode

plt.style.use('C:/Users/admin-local/Documents/script_Python/
                                    Graph_thesis/RH.mplstyle')
plt.rc('lines', linewidth=2)

list_color=plt.rcParams['axes.prop_cycle'].by_key()['color']
# define neurons
T=150000
dt= 0.125

#neurone 1
V_spike=100*1e-6
Vth=2*1e-6
Iamp=4*1e-5
#neurone2
V_spike2=80*1e-6
Vth2=1*1e-6
Iamp2=3*1e-5
# create neuron
neuron1=neuron.NeuronV2(T,V_spike,Vth,Iamp,dt)
neuron2=neuron.NeuronV2(T,V_spike2,Vth2,Iamp2,dt)

time=neuron1.time
Vm_total=[neuron1.Vm[i] +neuron2.Vm[i]   for i in range(len(time))]
Hm_total=[neuron1.Hm[i]   +neuron2.Hm[i]  for i in range(len(time))]

##----------------------Noise electro mag

noiseElectromag_phase=-125
noiseElectromag_duty=0.5
noiseElectromag_freq=1/10   # 100 Hz
electromagnoise0=np.random.normal(0,1,size=len(time))
electromagnoise1=np.zeros(len(time))
#electromagnoise1=signal.square(2 * np.pi * noiseElectromag_freq *
                                    time+noiseElectromag_phase*np.pi/
                                    180,duty=noiseElectromag_duty)
electromagnoise=[electromagnoise0[i] +electromagnoise1[i] for i in
                                    range(len(time))]
```

```
#----------------------define electrodes, magnetrodes
v=2 #Correlated noise

#E1
Vnoise=5*1e-6
Vnoise_electro=v*1e-6
E1=electrode.electrode(Vnoise,[noisei*Vnoise_electro for noisei in
                                    electromagnoise],Vm_total,time,dt)
#M1
S=1 #V/V/T
Vgmr=1 #V
Hnoise=20*1e-9 #T
Hnoise_electro=v*10*1e-9
M1=magnetrode.magnetrode(S,Vgmr,Hnoise,[noisei*Hnoise_electro for
                                    noisei in electromagnoise],Hm_total
                                    ,time,dt)

#-----Plot
tmax=50
imax=int(tmax//dt)

fig,ax=plt.subplots(2,len(Vth_list)+1,figsize=(5*(len(Vth_list)+1),7.5
                                    ),constrained_layout=True)
ax[0,0].plot(time[:imax],[v*1e6 for v in E1.Vrecorded[:imax]],color=
                                    list_color[1])
ax[1,0].plot(time[:imax],[v*1e9 for v in M1.Hrecorded[:imax]],color=
                                    list_color[2])

ax[0,0].set_title('E1')
ax[0,0].set_xlabel('Time (ms)')
ax[0,0].set_ylabel(r'Voltage ($\mu$V)')

ax[1,0].set_title('M1')
ax[1,0].set_xlabel('Time (ms)')
ax[1,0].set_ylabel(r'\mu$_0$H (nT)')

#-----detect spike
sigma=np.median([abs(i)/0.6745 for i in E1.Vrecorded]) # Computed
                                    standard noise deviation for
                                    Vthreshold

Vth_list=[1.5,2.5,5]

Hmin,Hmax,Vmin,Vmax=[],[],[],[]
for i,std in enumerate(Vth_list[::-1]):
    Vth=std*sigma

    spike_index=E1.detect_spike(Vth)
    spike_time=[]
    spike_amp=[]
    for j in spike_index: # to plot spikes detection
        spike_time.append(time[j])
        spike_amp.append( E1.Vrecorded[j])

    #averaged spike
    t=4
    time_av,E1_av=E1.average_spikes(spike_index,t)
    time_av,M1_av=M1.average_spikes(spike_index,t)
```

```
    tmax=50
    imax=int(tmax//dt)

    #-----------------plot
    k=len(Vth_list)-i
    ax[0,k].plot(time_av,[v*1e6 for v in E1_av],color=list_color[1])
    ax[1,k].plot(time_av,[v*1e9 for v in M1_av],color=list_color[2])

    yminV,ymaxV=ax[0,k].get_ylim()
    Vmin.append(yminV)
    Vmax.append(ymaxV)
    yminH, ymaxH=ax[1,k].get_ylim()
    Hmin.append(yminH)
    Hmax.append(ymaxH)

    ax[0,k].set_title(f'E1')
    ax[0,k].set_xlabel('Time (ms)')
    ax[0,k].set_ylabel(r'Voltage ($\mu$V)')

    ax[1,k].set_title(f'M1')
    ax[1,k].set_xlabel('Time (ms)')
    ax[1,k].set_ylabel(r'$\mu_0$H (nT)')

    ax[1,k].text(0.5,-0.8,f'{std:.2f} std\n{len(spike_index)} spikes\
                                        nVth={Vth*1e6:.1f}'+r'$\mu$V',
                                        transform=ax[1,k].transAxes,
                                        horizontalalignment='center',
                                        fontsize=16)

ymin_V=min(Vmin)
ymax_V=max(Vmax)
ymin_H=min(Hmin)
ymax_H=max(Hmax)

for i in range(len(Vth_list)):
    ax[0,i+1].set_ylim(ymin=ymin_V,ymax=ymax_V)
#     ax[1,i+1].set_ylim(ymin=ymin_H,ymax=ymax_H)

    ax[0,i+1].set_xlim(xmin=-2,xmax=2)
    ax[1,i+1].set_xlim(xmin=-2,xmax=2)
```

Appendix D

Impact of threshold

Detailed figure of the possible magnetic action potential described in section 4.3.4.

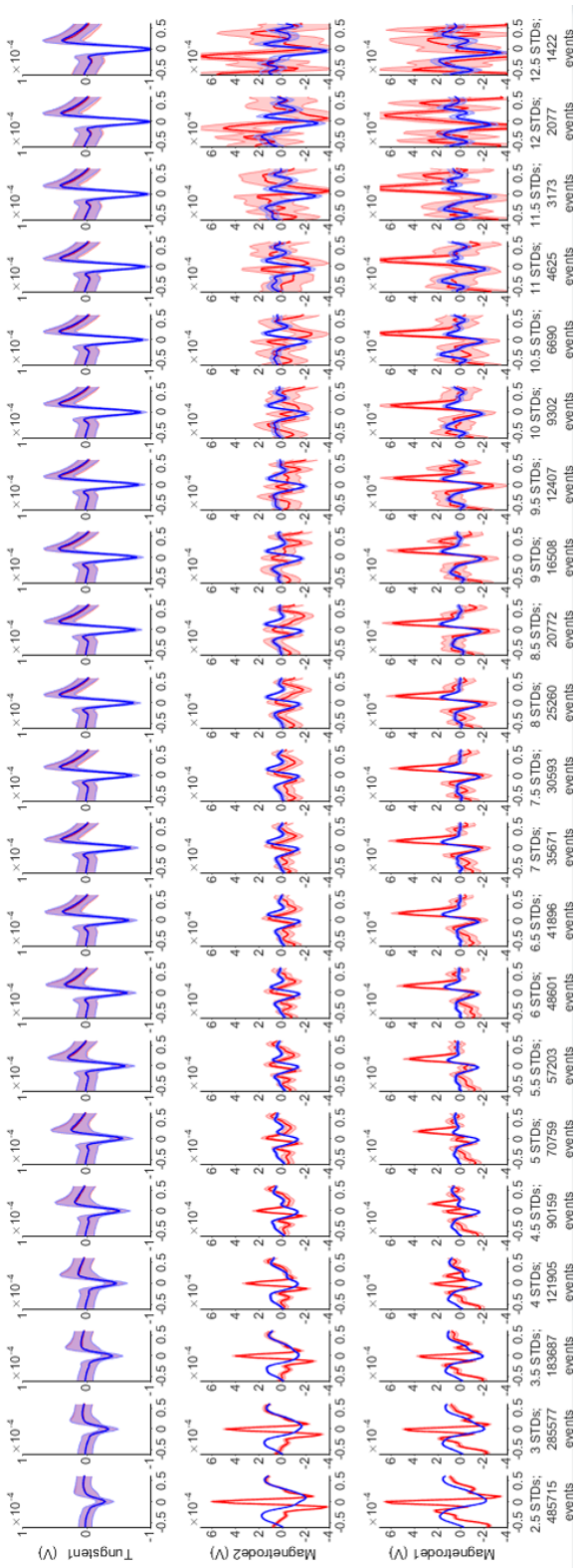

Figure D.1: Impact of threshold on recorded electrical and magnetic signals for V_{th} between 2.5 STDs and 12.5 STDs (2018-block 29-Probe SOI-ref.-712).

université PARIS-SACLAY

ÉCOLE DOCTORALE
Physique en l'Île-de-France (PIF)

Titre : Enregistrements biomagnétiques avec des capteurs à électronique de spin

Mots clés : capteur, spintronique, biomagnétisme, GMR

Résumé : L'effet de magnétorésistance géante (GMR) permet de fabriquer des capteurs magnétiques avec une bonne sensibilité dont la résistance est proportionnelle au champ magnétique. De plus, ils sont sensibles à petite taille (quelques microns), à température ambiante et selon une direction de sensibilité unique. Ce sont donc des capteurs intéressants pour mesurer les champs magnétiques générés par l'activité électrique des neurones à l'échelle locale, comme les potentiels d'action, dont l'amplitude est attendue entre 10 et 100 pT à 1 kHz. Comme les capteurs GMR ont une limite de détection (LOD) de l'ordre du nT à basse fréquence, plusieurs études ont été menées, notamment sur la taille et la composition du capteur GMR pour l'améliorer. La sonde qui implémente ces capteurs pour les mesures in-vivo, appelée magnétrode, a également été optimisée selon deux axes particuliers : sa pointe est affinée pour en limiter l'invasivité d'une part et intègre plusieurs capteurs GMR qui peuvent notamment réaliser des mesures en 2D d'autre part. Ces magnétrodes ont ainsi été appliquées à la mesure in-vivo sur des rongeurs. Les sondes ainsi développées et optimisées conservent une LOD de 1 nT autour de 1 kHz et ont gagné en stabilité ce qui a permis de réduire le niveau de bruit pendant les expériences in-vivo en moyennant sur un nombre important d'évènements. De plus, une magnétrode permettant de mesurer un champ magnétique en 2D a été développée. Enfin, les capteurs GMR sont à l'état de l'art sur une magnétrode dont la pointe a été affinée pour une épaisseur finale de 25 µm. Les sondes réalisées permettent de mesurer in-vivo des signaux magnétiques d'une amplitude de l'ordre de 250 pT.

Title : Biomagnetic sensors based on spin electronics.

Keywords : sensor, spintronics, biomagnetism, GMR

Abstract : Magnetic sensors based on the Giant Magnetoresistance (GMR) effect have a good sensitivity with a resistance which is proportional to the external magnetic field. In addition, they are sensitive at small scale (a few microns), at room temperature and along a unique axis of sensitivity. Thus, they are good candidates to measure the magnetic fields generated by the electrical activity of neurons at local scale like action potentials which have an amplitude expected between 10 and 100 pT at 1 kHz. As GMR sensors have a limit of detection (LOD) in the nT range at low frequency, several studies were conducted, including on the size and composition of the GMR sensor, to improve it. A probe that implements GMR sensors to conduct in-vivo experiments, called magnetrode, was also optimized in two ways. First, the tip thickness is reduced to decrease its invasiveness. Second, several GMR sensors are embedded on the magnetrode and in particular for 2D measurements. The optimized magnetrodes were then used for in-vivo recordings on rodents. They keep a limit of detection of 1 nT around 1 kHz for an increased stability which enables the reduction of the noise level of in-vivo experiments thanks to an averaging over a large number of events. In addition, a magnetrode for 2D measurements was developed. Finally, GMR sensors at the state of the art are implemented on a magnetrode with a tip thickness decreased down to 25 µm. Magnetrodes are able to detect an in-vivo signal with an amplitude around 250 pT.

Maison du doctorat de l'Université Paris-Saclay
2ème étage aile ouest, Ecole normale supérieure Paris-Saclay
4 avenue des Sciences,
91190 Gif sur Yvette, France